CREEP OF HI-NICALON™ S CERAMIC FIBER TOWS AT 1100°C IN AIR AND IN SILICIC ACID-SATURATED STEAM

THESIS

Logan M. Gumucio

AFIT-ENY-MS-18-J-072

DEPARTMENT OF THE AIR FORCE
AIR UNIVERSITY

AIR FORCE INSTITUTE OF TECHNOLOGY

Wright-Patterson Air Force Base, Ohio

DISTRIBUTION STATEMENT A.
APPROVED FOR PUBLIC RELEASE; DISTRIBUTION UNLIMITED.

The views expressed in this thesis are those of the author and do not reflect the official policy or position of the United States Air Force, Department of Defense, or the United States Government. This material is declared a work of the U.S. Government and is not subject to copyright protection in the United States.

AFIT-ENY-MS-18-J-072

CREEP OF HI-NICALON™ S CERAMIC FIBER TOWS AT 1100°C IN AIR AND IN SILICIC ACID-SATURATED STEAM

THESIS

Presented to the Faculty

Department of Aeronautics and Astronautics

Graduate School of Engineering and Management

Air Force Institute of Technology

Air University

Air Education and Training Command

In Partial Fulfillment of the Requirements for the

Degree of Master of Science in Aeronautical Engineering

Logan M. Gumucio, B.S.

June 2018

DISTRIBUTION STATEMENT A.
APPROVED FOR PUBLIC RELEASE; DISTRIBUTION UNLIMITED.

AFIT-ENY-MS-18-J-072

CREEP OF HI-NICALON™ S CERAMIC FIBER TOWS AT 1100°C IN AIR AND IN SILICIC ACID-SATURATED STEAM

Logan M. Gumucio, B.S.

Committee Membership:

Dr. Marina B. Ruggles-Wrenn
Chair

Dr. Randall S. Hay
Member

Dr. Thomas Eason, III
Member

AFIT-ENY-MS-18-J-072

Abstract

Innovations in SiC based ceramic matrix composites (CMCs) have yielded exceptional high-temperature properties and performance in aggressive oxidizing environments. These material characteristics provide potential avenues for future advancements in many applications where current metallic alloys perform near their operating temperature limits in a harsh environment. As steam (typically present in these types of environments) enters through cracks in the matrix of a SiC/SiC composite, it leaches Si and becomes saturated with silicic acid, $Si(OH)_4$, prior to attacking the reinforcing SiC fibers. Therefore, it is paramount that a thorough understanding of the performance and durability of SiC fibers be obtained under these conditions. This research effort investigated the creep behavior of Hi-Nicalon™ S SiC fibers at 1100°C in air and in silicic acid-saturated steam. The fiber tows that were tested consist of approximately 500 fiber filaments with an average diameter of 12 µm. Creep tests were performed with creep stresses ranging from 3.5 to 650 MPa in both air and in silicic acid-saturated steam. Regions of primary and secondary creep were observed in all tests, with the transition from primary to secondary creep occurring within the first hour of each test. Creep run-out was defined as 100 hours at creep stress and was achieved at 600 MPa in air, but only at 3.5 MPa in saturated steam. The steady-state creep rates achieved in saturated steam were approximately an order of magnitude higher than those achieved in air. Post-test microstructural analysis revealed passive oxidation of the fibers tested in air and in saturated steam. Evidence of crystallized scale growth was found on fibers tested in saturated steam.

Acknowledgments

First, I would like to thank my advisor, Dr. Ruggles-Wrenn. She has provided vital instruction and advice that has guided me throughout my research. She always found time to answer my questions and provide me with the information I needed along the way. I would like to extend a big thank you to the very supportive lab technicians and maintenance team here at AFIT, J.S., M.R., J.D. and K.L. I would not have been able to gather all of my research data, let alone get through the headaches and issues that I experienced in the laboratory without their expertise and training. They were always available and willing to help out where they could. M.V. spent countless hours training and helping me with my post-test analysis work. Even with my very tight time table, he went out of his way to ensure I acquired my SEM imagery and achieve the results that I needed. Dr. R.H. provided me with helpful instruction and analysis of microscopy images. I would also like to thank my Mother and Father for helping me understand the importance of education early on in life. They taught me the value of hard work and perseverance, and have always been there for me cheering on the sidelines. To my children, thank you for your daily reminders of love that sustained me over the years. Finally, I would like to thank and acknowledge the love and support of my beautiful wife, who has always been by my side encouraging me to do my best and accomplish my goals.

Thank you all for getting me here and being part of my journey.

Logan M. Gumucio

Table of Contents

Page

Abstract iv
Table of Contents vi
List of Figures viii
List of Tables xl
I. Introduction 1
1.1 Problem 5
1.2 Purpose 6
1.3 Overview 7
II. Literature Review 8
2.1 Ceramic Matrix Composites 8
2.2 Non-Oxide Silicon Carbide (SiC) Fibers 12
2.3 Creep 19
2.4 Previous Work 22
III. Methodology 29
3.1 Theory 29
3.2 Material and Equipment 31
3.3 Specimen Preparation Procedure 34
3.4 Experimental Facility Operation 36
IV. Analysis and Results 42
4.1 Temperature Profiles 42
4.2 Engineering Strain Measurement 45
4.3 Creep of Hi-Nicalon™ S Fiber Tows at 1100°C 49
4.4 Post-Test Microstructural Analysis of Hi-Nicalon™ S fiber tows 69

4.4.1 Optical Microscopy 69

4.4.2 Scanning Electron Microscopy (SEM).....72

V. Conclusions and Recommendations 88

5.1 Conclusions 88

5.2 Recommendations 89

Appendix A. Representative SEM Images 91

Bibliography 173

List of Figures

Figure 1 – Different types of composites based on reinforcement. Modified with permission by Springer Nature [3], pg. 1, Figure 1.1, Copyright © 1998 by Springer Science & Business Media. 2

Figure 2 – Use of composites in commercial transport aircraft. Note the dramatic increase in the past 50 years. The Boeing 787 did reach 50% composites by weight. Reproduced from [11]. 4

Figure 3 – Strength to weight ratio as a function of temperature. Reproduced from [19], pg. 410, Figure 1, Copyright © 2004, with permission from Elsevier. 6

Figure 4 – Comparison of the stress-strain behaviors of a monolithic ceramic, discontinuous, and continuous CMCs. Reproduced from [22], pg. 119, Figure 4.1, Copyright © 1999, with permission from Elsevier. 11

Figure 5 – Failure of CFCCs showing crack propagation for strong and weak interfacial bond strengths. Reproduced with permission by Springer Nature [3], pg. 148, Figure 5.6, Copyright © 1998 by Springer Science & Business Media. 12

Figure 6 – The Yajima process of making SiC from a polycarbosilane (PCS). Reproduced with permission by Springer Nature [3], pg. 81, Figure 3.20, Copyright © 1998 by Springer Science & Business Media. 15

Figure 7 – Microstructures of three generations of Nicalon^{TM} fibers. Reproduced with permission from Springer Nature [12], pg. 118, Figure 9, Copyright © 2005 by Springer-Verlag Berlin Heidelberg. 19

Figure 8. Typical creep curve showing the different regions of creep. Reproduced from Robertson [15]. 21

Figure 9 – A spool of Hi-Nicalon™ S fiber tow. Reproduced by Nippon Carbon Co., Ltd. [44] 31
Figure 10 – MHI HGA-S-CX1300 heater (a) and controller (b). Reproduced from Mitchell [17]..... 34
Figure 11 – Layout of the three tab method used in fiber tow testing. Reproduced from Mitchell [17]..... 35
Figure 12 - Test specimen preparation process..... 36
Figure 13 – Fiber tow specimen mounted in creep testing apparatus. Reproduced from Piper [15]..... 38
Figure 14 – Alumina susceptor and steam feed tube assembled in one half of the furnace. Reproduced from Armani [13]..... 39
Figure 15 – Silica wool inserted into alumina tube acting as saturation chamber for silicic acid-saturated steam. Reproduced from Robertson [15]..... 40
Figure 16 – Bleed-off assembly located just prior to the feeding tube of the test chamber. 41
Figure 17 – Creep test facility configured for saturated steam tests. Reproduced from Robertson [15]..... 41
Figure 18 – Temperature profile obtained in laboratory air at 1100°C. 43
Figure 19 – Temperature profiles obtained in saturated steam at 1100°C. Profile (a) was used for specimens S1-S3, while profile (b) was used for specimens S4-S12. 44
Figure 20 - Creep strain vs time for Hi-Nicalon™ S fiber tows at 1100°C in laboratory air..... 52

Figure 21 – Creep strain vs time for Hi-Nicalon™ S fiber tows at 1100°C in laboratory air..... 53
Figure 22 - Creep strain vs. time for Hi-Nicalon™ S fiber tows at 1100°C in silicic acid-saturated steam. 54
Figure 23 - Creep strain vs. time for Hi-Nicalon™ S fiber tows at 1100°C in silicic acid-saturated steam. 55
Figure 24 - Steady-state creep rate vs. applied stress for Hi-Nicalon™ S fiber tows at 1100°C in laboratory air, steam, and silicic-acid saturated steam. Results from Shillig [14] in air and steam are included for comparison. 57
Figure 25 - Creep stress vs. time of rupture for Hi-Nicalon™ S fiber tows at 1100°C in air, steam, and saturated steam. Data at 1100°C in air and steam from Steffens [2] and Shillig [14] are included for comparison. Arrow indicates that specimen failure did not occur when the test was completed. 58
Figure 26 - Steady-state creep rate vs. applied stress for Hi-Nicalon™ S fiber tows at 800°C, 900°C, 1000°C, and 1100°C in laboratory air. Results from Shillig [14], Robertson [15], Mitchell [17], and Kroeger [18] are included for comparison. 60
Figure 27 - Steady-state creep rate vs. applied stress for Hi-Nicalon™ S fiber tows at 800°C, 900°C, 1000°C, and 1100°C in steam, as obtained by Shillig [14]. 60
Figure 28 - Steady-state creep rate vs. applied stress for Hi-Nicalon™ S fiber tows at 800°C, 900°C, and 1100°C in saturated steam. Results from Robertson [15] and Mitchell [17] are included for comparison. 61
Figure 29 - Creep stress vs. time to rupture for Hi-Nicalon™ S fiber tows at 800°C, 900°C, 1000°C, and 1100°C in laboratory air. Results from Shillig [14], Robertson

[15], Mitchell [17], and Kroeger [18] are included for comparison. Arrow indicates that specimen failure did not occur when the test was completed. 62

Figure 30 - Steady-state creep rate vs. applied stress for Hi-Nicalon™ S fiber tows at 800°C, 900°C, 1000°C, and 1100°C in laboratory air and steam. Results from Shillig [14], Robertson [15], Mitchell [17], and Kroeger [18] are included for comparison. 63

Figure 31 - Creep stress vs. time to rupture for Hi-Nicalon™ S fiber tows at 800°C, 900°C, 1000°C, and 1100°C in laboratory air and steam. Results from Shillig [14], Robertson [15], Mitchell [17], and Kroeger [18] are included for comparison. Arrow indicates that specimen failure did not occur when the test was completed. 64

Figure 32 – Steady-state creep rate vs. applied stress for Hi-Nicalon™ S fiber tows at 800°C, 900°C, and 1100°C in laboratory air and saturated steam. Results from Shillig [14], Robertson [15], and Mitchell [17] are included for comparison. 65

Figure 33 - Creep stress vs. time to rupture for Hi-Nicalon™ S fiber tows at 800°C, 900°C, 1000°C, and 1100°C in laboratory air and saturated steam. Results from Shillig [14], Robertson [15], Mitchell [17], and Kroeger [18] are included for comparison. Arrow indicates that specimen failure did not occur when the test was completed. 65

Figure 34 - Steady-state creep rate vs. applied stress for Hi-Nicalon™ S fiber tows at 800°C, 900°C, 1000°C, and 1100°C in laboratory air, steam, and saturated steam. Results from Shillig [14], Robertson [15], and Mitchell [17] are included for comparison. 67

Figure 35 - Creep Stress vs. time to rupture for Hi-Nicalon™ S fiber tows at 800°C, 900°C, 1000°C, and 1100°C in laboratory air, steam, and saturated steam. Results

from Shillig [14], Robertson [15], Mitchell [17], and Kroeger [18] are included for comparison. Arrow indicates that specimen failure did not occur when the test was completed. 68
Figure 36 - Keyence VHX Digital microscope in the Air Force Research Laboratory (AFRL) Materials and Manufacturing Directorate. 69
Figure 37 - Optical image of Hi-Nicalon™ S fiber tow specimen "Air 3" at 1000x magnification, examining the center part of the gage section of two fibers subjected to creep in laboratory air. 71
Figure 38 - Optical image of Hi-Nicalon™ S fiber tow specimen "Air 9" at 1000x magnification, examining the center part of the gage section of a fiber subjected to creep in laboratory air. 71
Figure 39 - Optical image of Hi-Nicalon™ S fiber tow specimen "Steam 12" subjected to creep in silicic acid-saturated steam (1000x magnification), examining the section of the fiber located below the fracture surface. The circular “rainbow” patches on the surface of the fiber suggest that the oxide layer has begun to crystallize. 72
Figure 40 - Quanta 650 scanning electron microscope (SEM) in the Air Force Research Laboratory (AFRL) Materials and Manufacturing Directorate. 73
Figure 41 - EMS 150T ES coating machine in the Air Force Research Laboratory (AFRL) Materials and Manufacturing Directorate. 74
Figure 42 - SEM micrograph of the Hi-Nicalon™ S fiber tow specimen “Steam 4” subjected to 255 MPa at 1100°C in silicic acid-saturated steam for 38.04 hrs. Oxide scale is visible. 77

Figure 43 - SEM micrograph of the Hi-Nicalon™ S fiber tow specimen “Steam 1” subjected to 3.5 MPa at 1100°C in silicic acid-saturated steam achieving creep run-out of 100 hours at creep stress. Note regions along the length of the fibers welded together with oxide scale..... 77
Figure 44 - SEM micrograph of the Hi-Nicalon™ S fiber tow specimen “Air 3” subjected to 353 MPa at 1100°C in laboratory air achieving creep run-out of 100 hours at creep stress. Oxide scale is visible..... 78
Figure 45 - SEM micrograph from Hi-Nicalon™ S fiber tow specimen “Air 1” subjected to 3.5 MPa at 1100°C in laboratory air achieving creep run-out of 100 hours at creep stress. The dark line along the fiber is indicative of contact between fibers. 81
Figure 46 - SEM micrograph of Hi-Nicalon™ S fiber tow specimen “Air 9” subjected to 600 MPa at 1100°C in laboratory air achieving creep run-out of 100 hours at creep stress. The gouged line along the fiber is indicative of contact between fibers..... 82
Figure 47 – SEM micrograph of Hi-Nicalon™ S fiber tow specimen “Air 3” subjected to 353 MPa at 1100°C in laboratory air achieving creep run-out of 100 hours at creep stress. The pitted line and remnants of oxide scale along the fiber is indicative of contact between fibers..... 82
Figure 48 - SEM micrograph of Hi-Nicalon™ S fiber tow specimen “Steam 12” subjected to 450 MPa at 1100°C in silicic acid-saturated steam for 13.53 hours. The pitted lines along the length of the fibers are indicative of contact between fibers... 83
Figure 49 - SEM micrograph of Hi-Nicalon™ S fiber tow specimen “Air 10” examining the fracture surface of a fiber subjected to 650 MPa at 1100°C in laboratory air for 2.24 hrs..... 84

Figure 50 - SEM micrograph of Hi-Nicalon™ S fiber tow specimen “Steam 12” examining the fracture surface of multiple fibers subjected to 450 MPa at 1100°C in silicic acid-saturated steam for 13.53 hrs. 84
Figure 51 - SEM micrograph of Hi-Nicalon™ S fiber tow specimen “Steam 11” examining the fracture surface of a fiber subjected to 650 MPa at 1100°C in silicic acid-saturated steam. Note the early stages of crystallized scale growth. 85
Figure 52 - SEM micrograph of Hi-Nicalon™ S fiber tow specimen “Steam 4” examining the varying degrees of crystallization along the surface of a group of fibers subjected to 255 MPa at 1100°C in silicic acid-saturated steam..... 86
Figure 53 - SEM micrograph of Hi-Nicalon™ S fiber tow specimen “Steam 4” examining the fracture surface of a fiber subjected to 255 MPa at 1100°C in silicic acid-saturated steam. Note the defined amorphous and crystallized scale growth. 87
Figure 54 - SEM micrograph of Hi-Nicalon™ S fiber tow specimen “Air 1” examining the silica scale thickness of a fiber along the lower portion of the fiber tow (σ_{cr} = 3.5 MPa, t_f = 100† hrs). 91
Figure 55 - SEM micrograph of Hi-Nicalon™ S fiber tow specimen “Air 1” examining the silica scale thickness of a fiber along the lower portion of the fiber tow (σ_{cr} = 3.5 MPa, t_f = 100† hrs). 91
Figure 56 – SEM electron backscatter deflection micrograph of Hi-Nicalon™ S fiber tow specimen “Air 1” examining the silica scale thickness of a fiber along the lower portion of the fiber tow (σ_{cr} = 3.5 MPa, t_f = 100† hrs). 92

Figure 57 - SEM micrograph of Hi-Nicalon™ S fiber tow specimen “Air 1” examining evidence of fiber to fiber contact along the lengths of a fiber along the lower portion of the fiber tow (σ_{cr} = 3.5 MPa, t_f = 100† hrs)..... 92

Figure 58 - SEM micrograph of Hi-Nicalon™ S fiber tow specimen “Air 1” examining the silica scale thickness of a fiber along the midpoint of the fiber tow (σ_{cr} = 3.5 MPa, t_f = 100† hrs). 93

Figure 59 - SEM micrograph of Hi-Nicalon™ S fiber tow specimen “Air 1” examining the silica scale thickness of a fiber along the midpoint of the fiber tow (σ_{cr} = 3.5 MPa, t_f = 100† hrs). 93

Figure 60 - SEM micrograph of Hi-Nicalon™ S fiber tow specimen “Air 1” examining the silica scale thickness of a fiber along the midpoint of the fiber tow (σ_{cr} = 3.5 MPa, t_f = 100† hrs). 94

Figure 61 - SEM electron backscatter deflection micrograph of Hi-Nicalon™ S fiber tow specimen “Air 1” examining the silica scale thickness of a fiber along the midpoint of the fiber tow (σ_{cr} = 3.5 MPa, t_f = 100† hrs)..... 94

Figure 62 - SEM micrograph of Hi-Nicalon™ S fiber tow specimen “Air 1” examining evidence of fiber to fiber contact on multiple fibers along the midpoint of the fiber tow (σ_{cr} = 3.5 MPa, t_f = 100† hrs). 95

Figure 63 - SEM micrograph of Hi-Nicalon™ S fiber tow specimen “Air 1” examining the silica scale thickness of a fiber along the upper portion of the fiber tow (σ_{cr} = 3.5 MPa, t_f = 100† hrs)..... 95

Figure 64 - SEM electron backscatter deflection micrograph of Hi-Nicalon™ S fiber tow specimen “Air 1” examining the silica scale thickness of a fiber along the upper portion of the fiber tow (σ_{cr} = 3.5 MPa, t_f = 100† hrs). 96

Figure 65 - SEM micrograph of Hi-Nicalon™ S fiber tow specimen “Air 1” examining the silica scale thickness of a fiber along the upper portion of the fiber tow (σ_{cr} = 3.5 MPa, t_f = 100† hrs). 96

Figure 66 - SEM electron backscatter deflection micrograph of Hi-Nicalon™ S fiber tow specimen “Air 1” examining the silica scale thickness of a fiber along the upper portion of the fiber tow (σ_{cr} = 3.5 MPa, t_f = 100† hrs). 97

Figure 67 - SEM micrograph of Hi-Nicalon™ S fiber tow specimen “Air 3” examining the silica scale thickness of a fiber along the lower portion of the fiber tow (σ_{cr} = 353 MPa, t_f = 100† hrs). 97

Figure 68 - SEM micrograph of Hi-Nicalon™ S fiber tow specimen “Air 3” examining the silica scale thickness of a fiber along the lower portion of the fiber tow (σ_{cr} = 353 MPa, t_f = 100† hrs). 98

Figure 69 - SEM micrograph of Hi-Nicalon™ S fiber tow specimen “Air 3” examining the silica scale thickness of a fiber along the midpoint of the fiber tow (σ_{cr} = 353 MPa, t_f = 100† hrs). 98

Figure 70 - SEM electron backscatter deflection micrograph of Hi-Nicalon™ S fiber tow specimen “Air 3” examining the silica scale thickness of a fiber along the midpoint of the fiber tow (σ_{cr} = 353 MPa, t_f = 100† hrs) 99

Figure 71 - SEM micrograph of Hi-Nicalon™ S fiber tow specimen “Air 3” examining the silica scale thickness of a pair of fibers along the midpoint of the fiber tow (σ_{cr} = 353 MPa, t_f = 100† hrs). 99
Figure 72 – SEM electron backscatter deflection micrograph of Hi-Nicalon™ S fiber tow specimen “Air 3” examining the silica scale thickness of a pair of fibers along the midpoint of the fiber tow (σ_{cr} = 353 MPa, t_f = 100† hrs). 100
Figure 73 - SEM electron backscatter deflection micrograph of Hi-Nicalon™ S fiber tow specimen “Air 3” examining a fiber surface where contact between fibers has ripped off a portion of the silica scale along the upper portion of the fiber tow (σ_{cr} = 353 MPa, t_f = 100† hrs). 100
Figure 74 - SEM micrograph of Hi-Nicalon™ S fiber tow specimen “Air 3” examining the silica scale thickness of a fiber along the upper portion of the fiber tow (σ_{cr} = 353 MPa, t_f = 100† hrs). 101
Figure 75 - SEM electron backscatter deflection micrograph of Hi-Nicalon™ S fiber tow specimen “Air 3” examining the silica scale thickness of a fiber along the upper portion of the fiber tow (σ_{cr} = 353 MPa, t_f = 100† hrs). 101
Figure 76 - SEM micrograph of Hi-Nicalon™ S fiber tow specimen “Air 9” examining the silica scale thickness and traces of fiber to fiber contact on a fiber along the lower portion of the fiber tow (σ_{cr} = 600 MPa, t_f = 100† hrs). 102
Figure 77 - SEM micrograph of Hi-Nicalon™ S fiber tow specimen “Air 9” examining traces of fiber to fiber contact on fibers along the lower portion of the fiber tow (σ_{cr} = 600 MPa, t_f = 100† hrs). 102

Figure 78 - SEM micrograph of Hi-Nicalon™ S fiber tow specimen “Air 9” examining the silica scale thickness on a fiber along the lower portion of the fiber tow (σ_{cr} = 600 MPa, t_f = 100† hrs). 103
Figure 79 - SEM electron backscatter deflection micrograph of Hi-Nicalon™ S fiber tow specimen “Air 9” examining the silica scale thickness on a fiber along the lower portion of the fiber tow (σ_{cr} = 600 MPa, t_f = 100† hrs). 103
Figure 80 - SEM micrograph of Hi-Nicalon™ S fiber tow specimen “Air 9” examining the silica scale thickness on a fiber along the lower portion of the fiber tow (σ_{cr} = 600 MPa, t_f = 100† hrs). 104
Figure 81 - SEM electron backscatter deflection micrograph of Hi-Nicalon™ S fiber tow specimen “Air 9” examining the silica scale thickness on a fiber along the lower portion of the fiber tow (σ_{cr} = 600 MPa, t_f = 100† hrs). 104
Figure 82 - SEM micrograph of Hi-Nicalon™ S fiber tow specimen “Air 9” examining traces of fiber to fiber contact on a small bundle of fibers along the lower portion of the fiber tow (σ_{cr} = 600 MPa, t_f = 100† hrs). 105
Figure 83 - SEM micrograph of Hi-Nicalon™ S fiber tow specimen “Air 9” examining the silica scale thickness on a fiber along the lower portion of the fiber tow (σ_{cr} = 600 MPa, t_f = 100† hrs). 105
Figure 84 - SEM electron backscatter deflection micrograph of Hi-Nicalon™ S fiber tow specimen “Air 9” examining the silica scale thickness on a fiber along the lower portion of the fiber tow (σ_{cr} = 600 MPa, t_f = 100† hrs). 106

Figure 85 - SEM micrograph of Hi-Nicalon™ S fiber tow specimen “Air 9” examining the silica scale thickness on a fiber along the midpoint of the fiber tow (σ_{cr} = 600 MPa, t_f = 100† hrs)..... 106
Figure 86 - SEM electron backscatter deflection micrograph of Hi-Nicalon™ S fiber tow specimen “Air 9” examining the silica scale thickness on a fiber along the midpoint of the fiber tow (σ_{cr} = 600 MPa, t_f = 100† hrs)..... 107
Figure 87 - SEM micrograph of Hi-Nicalon™ S fiber tow specimen “Air 9” examining the silica scale thickness on a fiber along the midpoint of the fiber tow (σ_{cr} = 600 MPa, t_f = 100† hrs)..... 107
Figure 88 - SEM electron backscatter deflection micrograph of Hi-Nicalon™ S fiber tow specimen “Air 9” examining the silica scale thickness on a fiber along the midpoint of the fiber tow (σ_{cr} = 600 MPa, t_f = 100† hrs)..... 108
Figure 89 - SEM micrograph of Hi-Nicalon™ S fiber tow specimen “Air 9” examining evidence of fiber to fiber contact on a fiber along the midpoint of the fiber tow (σ_{cr} = 600 MPa, t_f = 100† hrs)..... 108
Figure 90 - SEM micrograph of Hi-Nicalon™ S fiber tow specimen “Air 9” examining the silica scale thickness on a fiber along the midpoint of the fiber tow (σ_{cr} = 600 MPa, t_f = 100† hrs)..... 109
Figure 91 - SEM micrograph of Hi-Nicalon™ S fiber tow specimen “Air 9” examining the surfaces on multiple fibers along the upper portion of the fiber tow (σ_{cr} = 600 MPa, t_f = 100† hrs)..... 109

Figure 92 - SEM micrograph of Hi-Nicalon™ S fiber tow specimen “Air 9” examining the surface of a fiber along the upper portion of the fiber tow (σ_{cr} = 600 MPa, t_f = 100† hrs)..... 110
Figure 93 - SEM micrograph of Hi-Nicalon™ S fiber tow specimen “Air 9” examining the silica scale thickness of multiple fibers along the upper portion of the fiber tow. Note the locations where these fibers had been bonded to other fibers and pulled away (σ_{cr} = 600 MPa, t_f = 100† hrs)..... 110
Figure 94 - SEM micrograph of Hi-Nicalon™ S fiber tow specimen “Air 9” examining the silica scale thickness of a fiber along the upper portion of the fiber tow (σ_{cr} = 600 MPa, t_f = 100† hrs)..... 111
Figure 95 - SEM electron backscatter deflection micrograph of Hi-Nicalon™ S fiber tow specimen “Air 9” examining the silica scale thickness of a fiber along the upper portion of the fiber tow (σ_{cr} = 600 MPa, t_f = 100† hrs)..... 111
Figure 96 - SEM micrograph of Hi-Nicalon™ S fiber tow specimen “Air 9” examining the silica scale thickness of a fiber along the upper portion of the fiber tow. Note differences in fiber surface content (σ_{cr} = 600 MPa, t_f = 100† hrs)..... 112
Figure 97 - SEM micrograph of Hi-Nicalon™ S fiber tow specimen “Air 10” examining the fracture surface of a fiber along the upper portion of the fiber tow (σ_{cr} = 650 MPa, t_f = 2.24 hrs)..... 112
Figure 98 - SEM micrograph of Hi-Nicalon™ S fiber tow specimen “Air 10” examining features on the fracture surface of a fiber along the upper portion of the fiber tow (σ_{cr} = 650 MPa, t_f = 2.24 hrs)..... 113

Figure 99 - SEM micrograph of Hi-Nicalon™ S fiber tow specimen “Air 10” examining features on the fracture surface of a fiber along the upper portion of the fiber tow (σ_{cr} = 650 MPa, t_f = 2.24 hrs)..... 113
Figure 100 - SEM micrograph of Hi-Nicalon™ S fiber tow specimen “Air 10” examining the fracture surface of a fiber along the upper portion of the fiber tow (σ_{cr} = 650 MPa, t_f = 2.24 hrs). 114
Figure 101 - SEM micrograph of Hi-Nicalon™ S fiber tow specimen “Air 10” examining features on the surface of a fiber along the lower portion of the fiber tow (σ_{cr} = 650 MPa, t_f = 2.24 hrs). 114
Figure 102 - SEM micrograph of Hi-Nicalon™ S fiber tow specimen “Air 10” examining features on the surface of a fiber along the lower portion of the fiber tow (σ_{cr} = 650 MPa, t_f = 2.24 hrs). 115
Figure 103 - SEM micrograph of Hi-Nicalon™ S fiber tow specimen “Air 10” examining features on the surface of a fiber along the lower portion of the fiber tow (σ_{cr} = 650 MPa, t_f = 2.24 hrs). 115
Figure 104 - SEM micrograph of Hi-Nicalon™ S fiber tow specimen “Air 10” examining the fracture surface of a fiber along the lower portion of the fiber tow (σ_{cr} = 650 MPa, t_f = 2.24 hrs). 116
Figure 105 - SEM micrograph of Hi-Nicalon™ S fiber tow specimen “Air 10” examining the fracture surface of a fiber along the lower portion of the fiber tow (σ_{cr} = 650 MPa, t_f = 2.24 hrs). 116
Figure 106 - SEM electron backscatter deflection micrograph of Hi-Nicalon™ S fiber tow specimen “Steam 1” examining a group of fibers along the lower portion of the

fiber tow. Note the considerable buildup of what appears to be silica scale due to duration of saturated steam exposure (σ_{cr} = 3.5 MPa, t_f = 100† hrs). 117
Figure 107 - SEM electron backscatter deflection micrograph of Hi-Nicalon™ S fiber tow specimen “Steam 1” examining fibers along the lower portion of the fiber tow. Note the considerable buildup of what appears to be silica scale due to duration of saturated steam exposure (σ_{cr} = 3.5 MPa, t_f = 100† hrs). 117
Figure 108 - SEM micrograph of Hi-Nicalon™ S fiber tow specimen “Steam 1” examining fibers along the lower portion of the fiber tow. Note the some of the fibers have almost been completely consumed by silica scale due to duration of saturated steam exposure (σ_{cr} = 3.5 MPa, t_f = 100† hrs)..... 118
Figure 109 - SEM micrograph of Hi-Nicalon™ S fiber tow specimen “Steam 1” examining a fiber along the lower portion of the fiber tow. Note the thick amount of oxide scale as well as the “mushroom” like nodules along the fiber length (σ_{cr} = 3.5 MPa, t_f = 100† hrs)..... 118
Figure 110 - SEM micrograph of Hi-Nicalon™ S fiber tow specimen “Steam 1” examining a fiber along the lower portion of the fiber tow. Note the buildup along the fibers exterior surface (σ_{cr} = 3.5 MPa, t_f = 100† hrs). 119
Figure 111 - SEM micrograph of Hi-Nicalon™ S fiber tow specimen “Steam 1” examining fibers along the lower portion of the fiber tow. Note the excessive buildup of silica scale as well as cavitation present (σ_{cr} = 3.5 MPa, t_f = 100† hrs)..... 119
Figure 112 - SEM electron backscatter deflection micrograph of Hi-Nicalon™ S fiber tow specimen “Steam 1” examining fibers along the lower portion of the fiber tow.

Note the excessive buildup of silica scale as well as cavitation present (σ_{cr} = 3.5 MPa, t_f = 100† hrs). 120

Figure 113 - SEM electron backscatter deflection micrograph of Hi-Nicalon™ S fiber tow specimen “Steam 1” examining a group of fibers along the lower portion of the fiber tow. Note the nodules and pitting along the fibers surfaces (σ_{cr} = 3.5 MPa, t_f = 100† hrs)..... 120

Figure 114 - SEM electron backscatter deflection micrograph of Hi-Nicalon™ S fiber tow specimen “Steam 1” examining a group of fibers along the lower portion of the fiber tow. Note the nodules along the fibers surfaces (σ_{cr} = 3.5 MPa, t_f = 100† hrs). 121

Figure 115 - SEM electron backscatter deflection micrograph of Hi-Nicalon™ S fiber tow specimen “Steam 1” examining a fiber along the lower portion of the fiber tow. Note the cavitation within the silica scale (σ_{cr} = 3.5 MPa, t_f = 100† hrs). 121

Figure 116 - SEM micrograph of Hi-Nicalon™ S fiber tow specimen “Steam 1” examining a fiber along the lower portion of the fiber tow. Note the cavitation within the silica scale (σ_{cr} = 3.5 MPa, t_f = 100† hrs). 122

Figure 117 - SEM micrograph of Hi-Nicalon™ S fiber tow specimen “Steam 1” examining fibers along the lower portion of the fiber tow. Note the thickness of the silica scale as well as cavitation (σ_{cr} = 3.5 MPa, t_f = 100† hrs). 122

Figure 118 - SEM micrograph of Hi-Nicalon™ S fiber tow specimen “Steam 1” examining a fiber along the lower portion of the fiber tow. Note the thickness of the silica scale (σ_{cr} = 3.5 MPa, t_f = 100† hrs). 123

Figure 119 - SEM electron backscatter deflection micrograph of Hi-Nicalon™ S fiber tow specimen “Steam 1” examining a fiber along the lower portion of the fiber tow. Note the thickness of the silica scale (σ_{cr} = 3.5 MPa, t_f = 100† hrs). 123

Figure 120 – SEM electron backscatter deflection micrograph of Hi-Nicalon™ S fiber tow specimen “Steam 1” examining fibers along the lower portion of the fiber tow. Note the thickness of the silica scale and cavitation present along the fiber surface (σ_{cr} = 3.5 MPa, t_f = 100† hrs). 124

Figure 121 - SEM micrograph of Hi-Nicalon™ S fiber tow specimen “Steam 1” examining fibers along the midpoint of the fiber tow. Note the excessive silica scale growth, welding multiple fibers together (σ_{cr} = 3.5 MPa, t_f = 100† hrs)..... 124

Figure 122 - SEM micrograph of Hi-Nicalon™ S fiber tow specimen “Steam 1” examining fibers along the midpoint of the fiber tow. Note the thickness of the silica scale (σ_{cr} = 3.5 MPa, t_f = 100† hrs). 125

Figure 123 – SEM electron backscatter deflection micrograph of Hi-Nicalon™ S fiber tow specimen “Steam 1” examining fibers along the midpoint of the fiber tow. Note the thickness of the silica scale (σ_{cr} = 3.5 MPa, t_f = 100† hrs). 125

Figure 124 - SEM micrograph of Hi-Nicalon™ S fiber tow specimen “Steam 1” examining fibers along the midpoint of the fiber tow. Note the thickness of the silica scale that has welded the fibers together (σ_{cr} = 3.5 MPa, t_f = 100† hrs). 126

Figure 125 - SEM micrograph of Hi-Nicalon™ S fiber tow specimen “Steam 1” examining fibers along the midpoint of the fiber tow. Note the thickness of the silica scale that has welded the fibers together (σ_{cr} = 3.5 MPa, t_f = 100† hrs). 126

Figure 126 - SEM micrograph of Hi-Nicalon™ S fiber tow specimen “Steam 1” examining a fiber along the midpoint of the fiber tow. Note the thickness of the silica scale that has almost consumed the fiber (σ_{cr} = 3.5 MPa, t_f = 100† hrs)..... 127
Figure 127 - SEM electron backscatter deflection micrograph of Hi-Nicalon™ S fiber tow specimen “Steam 1” examining a fiber along the midpoint of the fiber tow. Note the thickness of the silica scale that has almost consumed the fiber (σ_{cr} = 3.5 MPa, t_f = 100† hrs). 127
Figure 128 - SEM micrograph of Hi-Nicalon™ S fiber tow specimen “Steam 1” examining a fiber along the midpoint of the fiber tow. Note the thickness of the silica scale (σ_{cr} = 3.5 MPa, t_f = 100† hrs). 128
Figure 129 - SEM electron backscatter deflection micrograph of Hi-Nicalon™ S fiber tow specimen “Steam 1” examining a fiber along the midpoint of the fiber tow. Note the thickness of the silica scale (σ_{cr} = 3.5 MPa, t_f = 100† hrs)..... 128
Figure 130 - SEM micrograph of Hi-Nicalon™ S fiber tow specimen “Steam 1” examining a fiber along the upper portion of the fiber tow (σ_{cr} = 3.5 MPa, t_f = 100† hrs)..... 129
Figure 131 - SEM micrograph of Hi-Nicalon™ S fiber tow specimen “Steam 1” examining a fiber along the upper portion of the fiber tow. Note signs of dewetting along the fiber surface (σ_{cr} = 3.5 MPa, t_f = 100† hrs). 129
Figure 132 - SEM micrograph of Hi-Nicalon™ S fiber tow specimen “Steam 1” examining a group of fibers along the upper portion of the fiber tow. Note signs of dewetting and nodules along the fiber surfaces (σ_{cr} = 3.5 MPa, t_f = 100† hrs)..... 130

Figure 133 - SEM micrograph of Hi-Nicalon™ S fiber tow specimen “Steam 1” examining a group of fibers along the upper portion of the fiber tow. Note signs of dewetting and nodules along the fiber surfaces (σ_{cr} = 3.5 MPa, t_f = 100† hrs). 130
Figure 134 - SEM micrograph of Hi-Nicalon™ S fiber tow specimen “Steam 1” examining a group of fibers along the upper portion of the fiber tow. Note signs of dewetting along the fiber surfaces (σ_{cr} = 3.5 MPa, t_f = 100† hrs). 131
Figure 135 - SEM electron backscatter deflection micrograph of Hi-Nicalon™ S fiber tow specimen “Steam 1” examining a group of fibers along the upper portion of the fiber tow. Note signs of dewetting along the fiber surfaces (σ_{cr} = 3.5 MPa, t_f = 100† hrs)..... 131
Figure 136 - SEM micrograph of Hi-Nicalon™ S fiber tow specimen “Steam 1” examining a fiber surface along the upper portion of the fiber tow. Note signs of dewetting present (σ_{cr} = 3.5 MPa, t_f = 100† hrs). 132
Figure 137 - SEM micrograph of Hi-Nicalon™ S fiber tow specimen “Steam 1” examining a fiber along the upper portion of the fiber tow. Note the asymmetrical thickness of oxide scale around the fiber (σ_{cr} = 3.5 MPa, t_f = 100† hrs)..... 132
Figure 138 - SEM micrograph of Hi-Nicalon™ S fiber tow specimen “Steam 1” examining the fiber surfaces of a group of fibers along the upper portion of the fiber tow. Note signs of dewetting along the fiber surfaces (σ_{cr} = 3.5 MPa, t_f = 100† hrs). 133
Figure 139 - SEM micrograph of Hi-Nicalon™ S fiber tow specimen “Steam 4” examining the fracture surfaces of a group of fibers along the lower portion of the

fiber tow. Note areas of silica amorphous and crystallized scale growth (σ_{cr} = 255 MPa, t_f = 38.04 hrs). 133
Figure 140 - SEM electron backscatter deflection micrograph of Hi-Nicalon™ S fiber tow specimen “Steam 4” examining the fracture surfaces of a group of fibers along the lower portion of the fiber tow. Note areas of silica amorphous and crystallized scale growth (σ_{cr} = 255 MPa, t_f = 38.04 hrs). 134
Figure 141 - SEM micrograph of Hi-Nicalon™ S fiber tow specimen “Steam 4” examining the fracture surfaces of a group of fibers along the lower portion of the fiber tow. Note crystallized scale growth along the fiber surfaces (σ_{cr} = 255 MPa, t_f = 38.04 hrs)..... 134
Figure 142 - SEM electron backscatter deflection micrograph of Hi-Nicalon™ S fiber tow specimen “Steam 4” examining the fracture surfaces of a group of fibers along the lower portion of the fiber tow. Note crystallized scale growth along the fiber surfaces (σ_{cr} = 255 MPa, t_f = 38.04 hrs). 135
Figure 143 - SEM micrograph of Hi-Nicalon™ S fiber tow specimen “Steam 4” examining the fracture surfaces of a group of fibers along the lower portion of the fiber tow. Note areas of silica amorphous and crystallized scale growth (σ_{cr} = 255 MPa, t_f = 38.04 hrs). 135
Figure 144 – SEM electron backscatter deflection micrograph of Hi-Nicalon™ S fiber tow specimen “Steam 4” examining the fracture surfaces of a group of fibers along the lower portion of the fiber tow. Note areas of silica amorphous and crystallized scale growth (σ_{cr} = 255 MPa, t_f = 38.04 hrs). 136

Figure 145 - SEM electron backscatter deflection micrograph of Hi-Nicalon™ S fiber tow specimen “Steam 4” examining the fracture surface of a fiber along the lower portion of the fiber tow. Note the thickness of the silica scale (σ_{cr} = 255 MPa, t_f = 38.04 hrs)..... 136
Figure 146 - SEM micrograph of Hi-Nicalon™ S fiber tow specimen “Steam 4” examining the fracture surfaces of a group of fibers along the lower portion of the fiber tow. Note areas of silica scale thickness (σ_{cr} = 255 MPa, t_f = 38.04 hrs). 137
Figure 147 - SEM electron backscatter deflection micrograph of Hi-Nicalon™ S fiber tow specimen “Steam 4” examining the fracture surfaces of a group of fibers along the lower portion of the fiber tow. Note areas of silica scale thickness (σ_{cr} = 255 MPa, t_f = 38.04 hrs). 137
Figure 148 - SEM micrograph of Hi-Nicalon™ S fiber tow specimen “Steam 4” examining the fracture surfaces of a fiber along the lower portion of the fiber tow. Note the thickness of the silica scale (σ_{cr} = 255 MPa, t_f = 38.04 hrs). 138
Figure 149 - SEM micrograph of Hi-Nicalon™ S fiber tow specimen “Steam 4” examining the fracture surfaces of a group of fibers along the lower portion of the fiber tow. Note the thickness and areas of silica amorphous and crystallized scale growth (σ_{cr} = 255 MPa, t_f = 38.04 hrs). 138
Figure 150 - SEM micrograph of Hi-Nicalon™ S fiber tow specimen “Steam 4” examining the fracture surfaces of a group of fibers along the lower portion of the fiber tow. Note the thickness and areas of silica amorphous and crystallized scale growth (σ_{cr} = 255 MPa, t_f = 38.04 hrs). 139

Figure 151 - SEM micrograph of Hi-Nicalon™ S fiber tow specimen “Steam 4” examining the fracture surfaces of a group of fibers along the upper portion of the fiber tow. Note the thickness and areas of silica amorphous and crystallized scale growth (σ_{cr} = 255 MPa, t_f = 38.04 hrs). 139
Figure 152 - SEM electron backscatter deflection micrograph of Hi-Nicalon™ S fiber tow specimen “Steam 4” examining the fracture surfaces of a group of fibers along the upper portion of the fiber tow. Note the thickness and areas of silica amorphous and crystallized scale growth (σ_{cr} = 255 MPa, t_f = 38.04 hrs). 140
Figure 153 - SEM electron backscatter deflection micrograph of Hi-Nicalon™ S fiber tow specimen “Steam 4” examining the fiber and fracture surfaces of a group of fibers along the upper portion of the fiber tow. Note the areas of silica amorphous and crystallized scale growth (σ_{cr} = 255 MPa, t_f = 38.04 hrs). 140
Figure 154 - SEM micrograph of Hi-Nicalon™ S fiber tow specimen “Steam 4” examining the fiber and fracture surfaces of a group of fibers along the upper portion of the fiber tow. Note the areas of silica amorphous and crystallized scale growth (σ_{cr} = 255 MPa, t_f = 38.04 hrs) 141
Figure 155 - SEM electron backscatter deflection micrograph of Hi-Nicalon™ S fiber tow specimen “Steam 4” examining the fiber and fracture surfaces of a group of fibers along the upper portion of the fiber tow. Note the areas of silica amorphous and crystallized scale growth (σ_{cr} = 255 MPa, t_f = 38.04 hrs). 141
Figure 156 - SEM micrograph of Hi-Nicalon™ S fiber tow specimen “Steam 4” examining a group of fibers along the upper portion of the fiber tow. Note the areas of silica amorphous and crystallized scale growth (σ_{cr} = 255 MPa, t_f = 38.04 hrs). 142

Figure 157 - SEM micrograph of Hi-Nicalon™ S fiber tow specimen “Steam 4” examining the fracture surfaces of multiple fibers along the upper portion of the fiber tow. Note the thickness of the silica scale (σ_{cr} = 255 MPa, t_f = 38.04 hrs). 142
Figure 158 - SEM electron backscatter deflection micrograph of Hi-Nicalon™ S fiber tow specimen “Steam 4” examining the fracture surfaces of multiple fibers along the upper portion of the fiber tow. Note the thickness of the silica scale (σ_{cr} = 255 MPa, t_f = 38.04 hrs). 143
Figure 159 - SEM micrograph of Hi-Nicalon™ S fiber tow specimen “Steam 4” examining the fracture surfaces of a group of fibers along the upper portion of the fiber tow. Note the thickness of the silica scale (σ_{cr} = 255 MPa, t_f = 38.04 hrs)..... 143
Figure 160 - SEM micrograph of Hi-Nicalon™ S fiber tow specimen “Steam 4” examining the fracture surfaces of multiple fibers along the upper portion of the fiber tow. Note the unknown growth on the fracture surface of the fiber, suggesting progressive fiber failure (σ_{cr} = 255 MPa, t_f = 38.04 hrs). 144
Figure 161 - SEM electron backscatter deflection micrograph of Hi-Nicalon™ S fiber tow specimen “Steam 4” examining the fracture surfaces of multiple fibers along the upper portion of the fiber tow. Note the unknown growth on the fracture surface of the fiber, suggesting progressive fiber failure (σ_{cr} = 255 MPa, t_f = 38.04 hrs). 144
Figure 162 – SEM micrograph of Hi-Nicalon™ S fiber tow specimen “Steam 12” examining the fracture surfaces of multiple fibers along the lower portion of the fiber tow (σ_{cr} = 450 MPa, t_f = 13.53 hrs). 145

Figure 163 - SEM electron backscatter deflection micrograph of Hi-Nicalon™ S fiber tow specimen “Steam 12” examining the fracture surfaces of multiple fibers along the lower portion of the fiber tow (σ_{cr} = 450 MPa, t_f = 13.53 hrs). 145
Figure 164 - SEM micrograph of Hi-Nicalon™ S fiber tow specimen “Steam 12” examining rogue fibers along the lower portion of the fiber tow. Note the unknown growth along the exterior surface of the fibers (σ_{cr} = 450 MPa, t_f = 13.53 hrs). 146
Figure 165 - SEM electron backscatter deflection micrograph of Hi-Nicalon™ S fiber tow specimen “Steam 12” examining rogue fibers along the lower portion of the fiber tow. Note the unknown growth along the exterior surface of the fibers (σ_{cr} = 450 MPa, t_f = 13.53 hrs). 146
Figure 166 - SEM micrograph of Hi-Nicalon™ S fiber tow specimen “Steam 12” examining the exterior surface along a rogue fiber along the lower portion of the fiber tow (σ_{cr} = 450 MPa, t_f = 13.53 hrs). 147
Figure 167 - SEM electron backscatter deflection micrograph of Hi-Nicalon™ S fiber tow specimen “Steam 12” examining the exterior surface along a rogue fiber along the lower portion of the fiber tow (σ_{cr} = 450 MPa, t_f = 13.53 hrs). 147
Figure 168 - SEM micrograph of Hi-Nicalon™ S fiber tow specimen “Steam 12” examining the exterior surface of fractured fibers along the lower portion of the fiber tow. Note the crystallized silica scale along the fiber surface (σ_{cr} = 450 MPa, t_f = 13.53 hrs)..... 148
Figure 169 - SEM micrograph of Hi-Nicalon™ S fiber tow specimen “Steam 12” examining the exterior surface of fractured fibers along the lower portion of the fiber

tow. Note the crystallized silica scale along the fiber surface (σ_{cr} = 450 MPa, t_f = 13.53 hrs)..... 148
Figure 170 - SEM micrograph of Hi-Nicalon™ S fiber tow specimen “Steam 12” examining the exterior surfaces of a group of fractured fibers along the lower portion of the fiber tow. Note the rogue fiber present (σ_{cr} = 450 MPa, t_f = 13.53 hrs)..... 149
Figure 171 - SEM electron backscatter deflection micrograph of Hi-Nicalon™ S fiber tow specimen “Steam 12” examining the exterior surfaces of a group of fractured fibers along the lower portion of the fiber tow. Note the rogue fiber present (σ_{cr} = 450 MPa, t_f = 13.53 hrs)..... 149
Figure 172 - SEM micrograph of Hi-Nicalon™ S fiber tow specimen “Steam 12” examining the fracture surfaces of a pair of fibers along the lower portion of the fiber tow. Note the thickness of silica scale (σ_{cr} = 450 MPa, t_f = 13.53 hrs)..... 150
Figure 173 - SEM electron backscatter deflection micrograph of Hi-Nicalon™ S fiber tow specimen “Steam 12” examining the fracture surfaces of a pair of fibers along the lower portion of the fiber tow. Note the thickness of silica scale (σ_{cr} = 450 MPa, t_f = 13.53 hrs)..... 150
Figure 174 - SEM micrograph of Hi-Nicalon™ S fiber tow specimen “Steam 12” examining the fracture surface of a fiber along the lower portion of the fiber tow. Note the thickness of silica scale (σ_{cr} = 450 MPa, t_f = 13.53 hrs)..... 151
Figure 175 - SEM electron backscatter deflection micrograph of Hi-Nicalon™ S fiber tow specimen “Steam 12” examining the fracture surface of a fiber along the lower portion of the fiber tow. Note the thickness of silica scale (σ_{cr} = 450 MPa, t_f = 13.53 hrs)..... 151

Figure 176 – SEM micrograph of Hi-Nicalon™ S fiber tow specimen “Steam 12” examining the fracture surface of a fiber along the lower portion of the fiber tow. Note the different features present along the exterior fiber surface (σ_{cr} = 450 MPa, t_f = 13.53 hrs)..... 152
Figure 177 - SEM electron backscatter deflection micrograph of Hi-Nicalon™ S fiber tow specimen “Steam 12” examining the fracture surface of a fiber along the lower portion of the fiber tow. Note the different features present along the exterior fiber surface (σ_{cr} = 450 MPa, t_f = 13.53 hrs)..... 152
Figure 178 - SEM micrograph of Hi-Nicalon™ S fiber tow specimen “Steam 12” examining the fracture surface of a fiber along the lower portion of the fiber tow. Note the thickness of silica scale (σ_{cr} = 450 MPa, t_f = 13.53 hrs). 153
Figure 179 - SEM electron backscatter deflection micrograph of Hi-Nicalon™ S fiber tow specimen “Steam 12” examining the fracture surface of a fiber along the lower portion of the fiber tow. Note the thickness of silica scale (σ_{cr} = 450 MPa, t_f = 13.53 hrs)..... 153
Figure 180 - SEM micrograph of Hi-Nicalon™ S fiber tow specimen “Steam 12” examining the fracture surface of a fiber along the upper portion of the fiber tow. Note the thickness of silica scale (σ_{cr} = 450 MPa, t_f = 13.53 hrs). 154
Figure 181 - SEM electron backscatter deflection micrograph of Hi-Nicalon™ S fiber tow specimen “Steam 12” examining the fracture surface of a fiber along the upper portion of the fiber tow. Note the thickness of silica scale (σ_{cr} = 450 MPa, t_f = 13.53 hrs)..... 154

Figure 182 - SEM electron backscatter deflection micrograph of Hi-Nicalon™ S fiber tow specimen “Steam 12” examining the fracture surfaces of a group of fibers along the upper portion of the fiber tow (σ_{cr} = 450 MPa, t_f = 13.53 hrs). 155
Figure 183 - SEM micrograph of Hi-Nicalon™ S fiber tow specimen “Steam 12” examining the fracture surface and exterior surfaces of a group of fibers along the upper portion of the fiber tow. Note the crystallized scale growth along the fiber surface (σ_{cr} = 450 MPa, t_f = 13.53 hrs). 155
Figure 184 - SEM micrograph of Hi-Nicalon™ S fiber tow specimen “Steam 12” examining the fracture surfaces of a group of fibers along the upper portion of the fiber tow. Note the crystallized scale, scale thickness, and fiber to fiber contact (σ_{cr} = 450 MPa, t_f = 13.53 hrs). 156
Figure 185 - SEM electron backscatter deflection micrograph of Hi-Nicalon™ S fiber tow specimen “Steam 12” examining the fracture surfaces of a group of fibers along the upper portion of the fiber tow. Note the crystallized scale, scale thickness, and fiber to fiber contact (σ_{cr} = 450 MPa, t_f = 13.53 hrs)..... 156
Figure 186 – SEM micrograph of Hi-Nicalon™ S fiber tow specimen “Steam 12” examining the fracture surface of a pair of fibers along the upper portion of the fiber tow (σ_{cr} = 450 MPa, t_f = 13.53 hrs). 157
Figure 187 - SEM electron backscatter deflection micrograph of Hi-Nicalon™ S fiber tow specimen “Steam 12” examining the fracture surface of a pair of fibers along the upper portion of the fiber tow (σ_{cr} = 450 MPa, t_f = 13.53 hrs). 157
Figure 188 - SEM micrograph of Hi-Nicalon™ S fiber tow specimen “Steam 12” examining the fracture surface of a fiber along the upper portion of the fiber tow.

Note the features growing on the exterior fiber surface (σ_{cr} = 450 MPa, t_f = 13.53 hrs)..... 158
Figure 189 - SEM electron backscatter deflection micrograph of Hi-Nicalon™ S fiber tow specimen “Steam 12” examining the fracture surface of a fiber along the upper portion of the fiber tow. Note the features growing on the exterior fiber surface (σ_{cr} = 450 MPa, t_f = 13.53 hrs)..... 158
Figure 190 - SEM micrograph of Hi-Nicalon™ S fiber tow specimen “Steam 12” examining the fracture surfaces of a group of bonded fibers along the upper portion of the fiber tow (σ_{cr} = 450 MPa, t_f = 13.53 hrs)..... 159
Figure 191 - SEM electron backscatter deflection micrograph of Hi-Nicalon™ S fiber tow specimen “Steam 12” examining the fracture surfaces of a group of bonded fibers along the upper portion of the fiber tow (σ_{cr} = 450 MPa, t_f = 13.53 hrs)..... 159
Figure 192 - SEM micrograph of Hi-Nicalon™ S fiber tow specimen “Steam 12” examining the fracture surface of a fiber along the upper portion of the fiber tow (σ_{cr} = 450 MPa, t_f = 13.53 hrs)..... 160
Figure 193 - SEM electron backscatter deflection micrograph of Hi-Nicalon™ S fiber tow specimen “Steam 12” examining the fracture surface of a fiber along the upper portion of the fiber tow (σ_{cr} = 450 MPa, t_f = 13.53 hrs)..... 160
Figure 194 - SEM micrograph of Hi-Nicalon™ S fiber tow specimen “Steam 11” examining the fracture surface of a fiber along the lower portion of the fiber tow (σ_{cr} = 650 MPa, t_f = 6.19 hrs)..... 161

Figure 195 - SEM electron backscatter deflection micrograph of Hi-Nicalon™ S fiber tow specimen “Steam 11” examining the fracture surface of a fiber along the lower portion of the fiber tow (σ_{cr} = 650 MPa, t_f = 6.19 hrs). 161
Figure 196 - SEM micrograph of Hi-Nicalon™ S fiber tow specimen “Steam 11” examining the fracture surface of a fiber along the lower portion of the fiber tow (σ_{cr} = 650 MPa, t_f = 6.19 hrs)..... 162
Figure 197 - SEM electron backscatter deflection micrograph of Hi-Nicalon™ S fiber tow specimen “Steam 11” examining the fracture surface of a fiber along the lower portion of the fiber tow (σ_{cr} = 650 MPa, t_f = 6.19 hrs). 162
Figure 198 - SEM micrograph of Hi-Nicalon™ S fiber tow specimen “Steam 11” examining the fracture surface of a fiber along the lower portion of the fiber tow (σ_{cr} = 650 MPa, t_f = 6.19 hrs)..... 163
Figure 199 - SEM electron backscatter deflection micrograph of Hi-Nicalon™ S fiber tow specimen “Steam 11” examining the fracture surface of a fiber along the lower portion of the fiber tow (σ_{cr} = 650 MPa, t_f = 6.19 hrs). 163
Figure 200 - SEM micrograph of Hi-Nicalon™ S fiber tow specimen “Steam 11” examining the fracture surface of a fiber along the lower portion of the fiber tow (σ_{cr} = 650 MPa, t_f = 6.19 hrs)..... 164
Figure 201 - SEM electron backscatter deflection micrograph of Hi-Nicalon™ S fiber tow specimen “Steam 11” examining the fracture surface of a fiber along the lower portion of the fiber tow (σ_{cr} = 650 MPa, t_f = 6.19 hrs). 164

Figure 202 - SEM micrograph of Hi-Nicalon™ S fiber tow specimen “Steam 11” examining the fracture surfaces of bonded fibers along the lower portion of the fiber tow (σ_{cr} = 650 MPa, t_f = 6.19 hrs). 165
Figure 203 - SEM micrograph of Hi-Nicalon™ S fiber tow specimen “Steam 11” examining the fracture surface of a fiber along the upper portion of the fiber tow. Note growths on the fiber fracture surface (σ_{cr} = 650 MPa, t_f = 6.19 hrs). 165
Figure 204 - SEM electron backscatter deflection micrograph of Hi-Nicalon™ S fiber tow specimen “Steam 11” examining the fracture surface of a fiber along the upper portion of the fiber tow. Note growths on the fiber fracture surface (σ_{cr} = 650 MPa, t_f = 6.19 hrs). 166
Figure 205 - SEM micrograph of Hi-Nicalon™ S fiber tow specimen “Steam 11” examining the fracture surface of a fiber along the upper portion of the fiber tow (σ_{cr} = 650 MPa, t_f = 6.19 hrs)..... 166
Figure 206 - SEM electron backscatter deflection micrograph of Hi-Nicalon™ S fiber tow specimen “Steam 11” examining the fracture surface of a fiber along the upper portion of the fiber tow (σ_{cr} = 650 MPa, t_f = 6.19 hrs). 167
Figure 207 - SEM micrograph of Hi-Nicalon™ S fiber tow specimen “Steam 11” examining the fracture surface of a fiber along the upper portion of the fiber tow. Note the unknown growth on the fracture surface and formation of crystallized scale on the exterior fiber surface (σ_{cr} = 650 MPa, t_f = 6.19 hrs). 167
Figure 208 - SEM micrograph of Hi-Nicalon™ S fiber tow specimen “Steam 11” examining the fracture surface of a fiber along the upper portion of the fiber tow. Note the unknown growth on the fracture surface (σ_{cr} = 650 MPa, t_f = 6.19 hrs).... 168

Figure 209 - SEM micrograph of Hi-Nicalon™ S fiber tow specimen “Steam 11” examining the fracture surface of a fiber along the upper portion of the fiber tow. Note the unknown growth on the fracture surface (σ_{cr} = 650 MPa, t_f = 6.19 hrs).... 168
Figure 210 - SEM micrograph of Hi-Nicalon™ S fiber tow specimen “Steam 11” examining the fracture surface of a fiber along the upper portion of the fiber tow. Note the unknown growth on the fracture surface (σ_{cr} = 650 MPa, t_f = 6.19 hrs).... 169
Figure 211 - SEM micrograph of Hi-Nicalon™ S fiber tow specimen “Steam 11” examining the fracture surface of a fiber along the upper portion of the fiber tow (σ_{cr} = 650 MPa, t_f = 6.19 hrs)..... 169
Figure 212 - SEM electron backscatter deflection micrograph of Hi-Nicalon™ S fiber tow specimen “Steam 11” examining the fracture surface of a fiber along the upper portion of the fiber tow (σ_{cr} = 650 MPa, t_f = 6.19 hrs). 170
Figure 213 - SEM electron backscatter deflection micrograph of Hi-Nicalon™ S fiber tow specimen “Steam 11” examining the fracture and exterior surfaces of fibers along the upper portion of the fiber tow. Note different stages of crystallization along the exterior fiber surface (σ_{cr} = 650 MPa, t_f = 6.19 hrs). 170
Figure 214 - SEM micrograph of Hi-Nicalon™ S fiber tow specimen “Steam 11” examining the fracture surface of a fiber along the upper portion of the fiber tow (σ_{cr} = 650 MPa, t_f = 6.19 hrs)..... 171
Figure 215 - SEM electron backscatter deflection micrograph of Hi-Nicalon™ S fiber tow specimen “Steam 11” examining the fracture surface of a fiber along the upper portion of the fiber tow (σ_{cr} = 650 MPa, t_f = 6.19 hrs). 171

Figure 216 - SEM micrograph of Hi-Nicalon™ S fiber tow specimen “Steam 11” examining the fracture surface of a fiber along the upper portion of the fiber tow (σ_{cr} = 650 MPa, t_f = 6.19 hrs)..... 172
Figure 217 - SEM electron backscatter deflection micrograph of Hi-Nicalon™ S fiber tow specimen “Steam 11” examining the fracture surface of a fiber along the upper portion of the fiber tow (σ_{cr} = 650 MPa, t_f = 6.19 hrs). 172

List of Tables

Table 1 – Characteristics of different types of CMCs. Adapted from [19], pg. 44, Table 2.1. 10

Table 2 – Manufacturer, elemental composition, and approximate cost of all three generations of SiC based fibers. Reprinted from [24], pg. 826, Table 3, Copyright © 2006, with permission by Springer Nature. 16

Table 3 – Mechanical and thermal properties of all three generations of SiC based fibers. Reprinted from [24], containing data from [27], pg. 826, Table 4, Copyright © 2006, with permissions by Springer Nature. 16

Table 4 – Creep mechanisms in fine-grained polycrystalline ceramics. Adapted from Armani [12]. 22

Table 5 – Typical properties of Hi-Nicalon™ S fiber. Data reproduced from NGS Advanced Fibers Co., Ltd. [45] 32

Table 6 - Effective gauge lengths of Hi-Nicalon™ S fibers at 1100°C 49

Table 7 – Summary of tensile creep test results for Hi-Nicalon™ S fiber tows at 1100°C in laboratory air and in silicic acid-saturated steam. 51

Table 8 - Hi-Nicalon™ S fiber tow specimens used for analysis with optical microscope. 70

Table 9 - Hi-Nicalon™ S fiber tow specimens analyzed using scanning electron microscopy (SEM). 75

Table 10 – Predictions of the oxide scale thickness for creep tests in air and in saturated steam obtained using Deal-Grove kinetics. 79

I. Introduction

Scientists and engineers have arrived at a point where many new technologies are limited by the materials available. Press states, “The classical model of materials application has been inverted. We once sought applications for materials. We now have applications driving the creation of materials. We now design materials for what we need” [1]. To establish access to materials whose properties can meet the ever growing demands of current, as well as future innovations, a large focus on material development has emerged within the last century for the science and engineering communities. As research for this effort increased, it would eventually lead to the investigation of combining multiple materials to yoke each of their respective properties into one collaborative form. Just as past eras were represented by the materials that had defined them, this current era some refer to as “The Composite Age” [2].

A composite is a material that has a chemically and/or physically distinct phase distributed within a continuous phase [3]. The distinct phase that is distributed throughout the composite material is also known as a reinforcement phase, often consisting of particles, fibers, whiskers, or sheets, as seen in Figure 1. This phase is ultimately responsible for the strength and stiffness of the composite material. The continuous phase, also known as the matrix, forms the body of the composite. Its purpose is to transfer the encountered loads amongst the reinforcement phase of the composite, and act as an adhesive to bind and protect the reinforcement phase from abrasion or environmental attack. The attractive features of composites mainly stem from their physical properties such as high strength, high stiffness, and light weight, as well as their ability to be designed

specifically for a certain task. Composites are highly sought after for a variety of modern applications ranging from aerospace, aircraft, automotive, marine, energy, infrastructure, armor, biomedical, and sports [4].

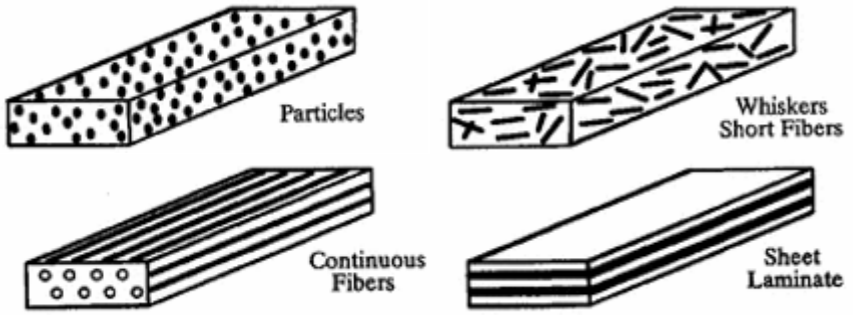

Figure 1 – Different types of composites based on reinforcement. Modified with permission by Springer Nature [3], pg. 1, Figure 1.1, Copyright © 1998 by Springer Science & Business Media.

While research and development of composite materials has increased dramatically throughout the 20th century, the concept of utilizing fibrous reinforcement itself is not necessarily a new endeavor, as it can be traced back to ancient Egypt where straw was used to reinforce clay bricks [5]. Other early instances such as the use of composites by the Mongols of Genghis Khan in the 12th century AD highlighted the effectiveness of using composite materials. Their bows were constructed by utilizing a combination of wood, animal horn/bone and sinew, bonded with natural pine resin, and secured with wrappings of silk and birch bark [6], [7]. It can be seen that the design and use of composites were well understood by the Mongols, as recently some of the surviving bows were restrung and tested, exhibiting approximately 80% of the strength of modern composite bows [7].

While other examples of composite use exist throughout early history, ultimately it was the growth of the aircraft industry following World War II that initiated the fervently

increasing pace of composite material development to what it is today. In the 1950s the Boeing 707 was the first commercial passenger jet that was built with composite materials, comprising about 2% of the overall structure [8]. By the 1960s, as composite use on aircraft was proving successful and more advanced composite materials (such as boron and graphite) became available, the United States Air Force (USAF) began researching these materials for use on aircraft control surfaces [9]. After 1965, the USAF became largely invested in the cause, as it would go on to lead the majority of the ongoing research and development efforts to bring high performance fiber composites into reality for future industry platforms [10].

Since 1965, the use of composites in the aerospace industry has continually increased, ultimately yielding what is now deemed the next generation of both fighter (F-22 and F-35) and commercial (Boeing 787 Dreamliner) aircraft. The structural weight for both the F-22 and F-35 fighter consist of approximately 30% composite, while the commercial 787 Dreamliner boasts its structure at approximately 50% composite [9]. From the rapid growth, advancements, and successful use of composite materials on aircraft platforms over the last 50 years, as shown in Figure 2, it can be said that composites are the future of aerospace.

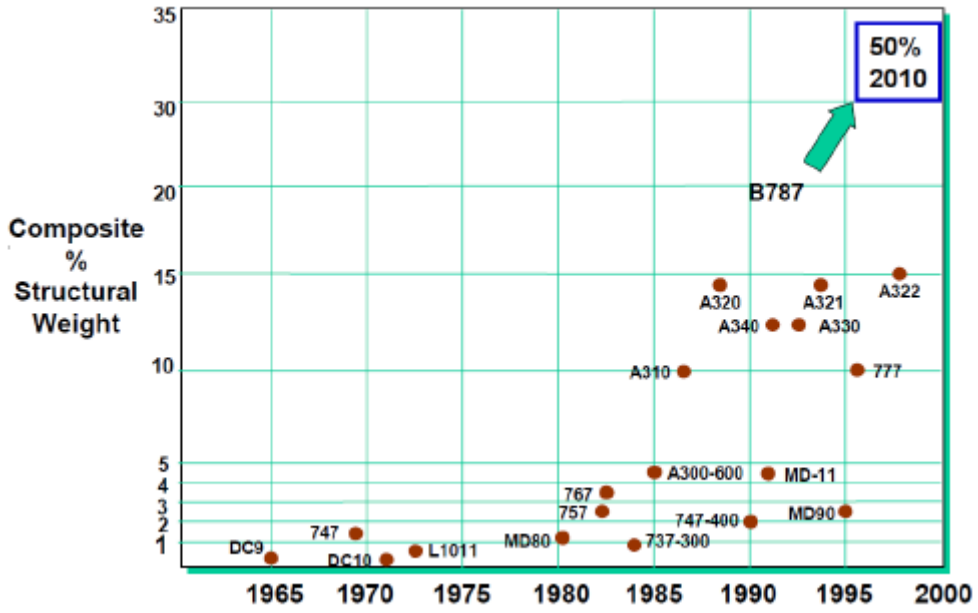

Figure 2 – Use of composites in commercial transport aircraft. Note the dramatic increase in the past 50 years. The Boeing 787 did reach 50% composites by weight. Reproduced from [11]**.**

However, like all other materials, composites also come with their disadvantages. Recalling the limitations placed upon modern design, one of such limitations for a materials consideration revolves around its service temperature (the maximum temperature that a material can be used for an extended period of time). Composites are no exception in this regard, as all materials fail to maintain their strength at high temperatures. However, a substantial amount of research has been completed over the last 50 years to improve upon this weakness of composite materials [12].

In order to improve upon this drawback of composites being unable to retain their strength at high temperatures, new materials would need to be considered and utilized for the different phases of the composite. Ceramics are primarily known for their ability to maintain high strength at elevated temperatures. Their own weakness however is due to their lack of plasticity or ability to deform before fracture. This lack of deformation causes

ceramics to catastrophically fail without warning. Similar to composites, this problem has also generated a substantial interest from the materials community, and over the last quarter of the 20th century research efforts have been directed towards developing an energy-dissipation method for ceramics. This has been accomplished by combining the benefits of both composite and ceramic materials into what is known as a ceramic matrix composite (CMC) [3].

1.1 Problem

The main objective of CMCs is to improve upon the toughness/durability of ceramic materials, thus allowing it to be utilized in applications that demand high strength but whose environments are too demanding for traditional materials. Currently, the materials of some structural aircraft sections are operating at or near their respective service temperature limits. In addition to this, some of these applications operate in highly-corrosive environments. When comparing the strengths and temperature limits of other traditional metal alloys currently used in high-temperature structural applications, CMCs have shown that they can surpass the specific strengths of traditional materials at elevated temperatures, as seen in Figure 3. CMCs could potentially replace the current materials being used for these high-temperature structural applications. However, for CMCs to be considered for such implementation, a thorough understanding of their performance and durability must be assured at both elevated temperatures and harsh service environments.

1.2 Purpose

To build upon that understanding, this research investigates the creep performance (a material's ability to resist permanent deformation under constant mechanical stress) of Hi-Nicalon™ S Silicon Carbide (SiC) fibers at 1100°C in air and silicic acid-saturated steam ($Si(OH)_4$). The results of this effort strive to support the validation of ceramic fibers and CMCs as materials for future advanced aerospace applications. It also supplements previously recorded data and phenomena reported in similar research [2], [13]–[18].

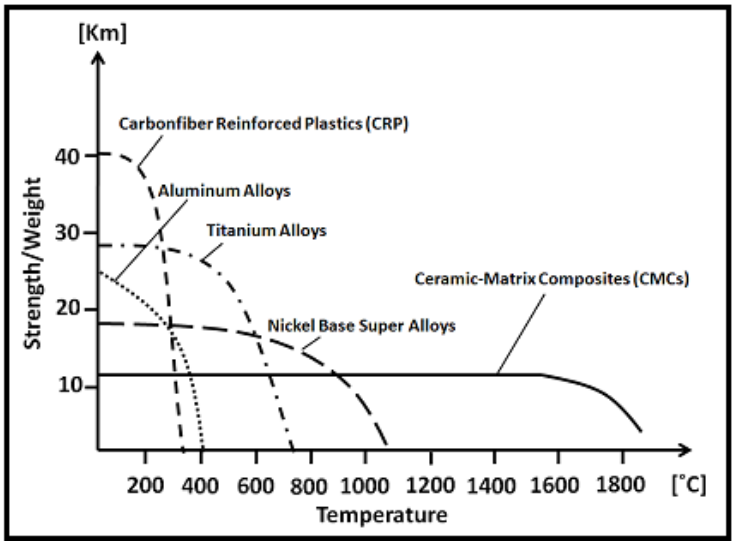

Figure 3 – Strength to weight ratio as a function of temperature. Reproduced from [19]***, pg. 410, Figure 1, Copyright © 2004, with permission from Elsevier.***

The questions/phenomena further addressed by this effort are regarding the growth of silica scale found on the fibers at different elevated temperatures after testing, as well as the increase in fiber strength that this silica scale provides at these higher temperatures. Also, fiber creep rates will be compared and examined against previous efforts for air and steam (both saturated and unsaturated) environments at this higher temperature of 1100°C,

so as to build upon the overall creep performance of the Hi-Nicalon™ S fiber at various elevated temperatures.

1.3 Overview

Chapter I provided a history of composite materials, along with the rationale and purpose of this research. Chapter II provides a detailed overview of CMCs, silicon carbide fibers, creep, and previous research efforts. Chapter III presents detailed information about the material being used, along with the experimental methodology of this work regarding specimen preparation and facility operation. Chapter IV presents the obtained experimental results as well as their analysis. Lastly, Chapter V closes with a discussion of the overall conclusions of this effort, as well as providing recommendations should ongoing work surrounding this effort be pursued/modified in the future.

II. Literature Review

The 21st century has brought about unthinkable breakthroughs and advances in technology. But as those technologies are applied in varying applications throughout the world and industry, ultimately they will be limited by the performance of the very materials of their construction. An example of this would be the aerospace industry, as it has seen incredible advancements throughout history, yet even with the next generation of aircraft in our midst, the persistent motto of "Faster, Higher, Farther" used throughout the industry has yet to be satisfied. New materials are being developed and evaluated to prove they are capable of meeting the growing needs of future aerospace applications.

One such material is that of ceramics, particularly its adaptation and involvement in the realm of composites known as Ceramic Matrix Composites (CMCs). The development of this material has granted engineers the ability to utilize the primary benefits of ceramic materials and improve upon their weakness. But for CMCs to be safely considered for future aerospace applications, their capabilities must be tested and verified in the very environmental conditions that they will operate. Chapter II further discusses the evolution of CMCs materials as well as the ongoing work being done to more thoroughly understand their behavior for such applications.

2.1 Ceramic Matrix Composites

Monolithic ceramic materials are often simply associated with pottery and tiles. However, when utilized properly, the properties of ceramic materials can actually allow them to be employed in far more advanced applications than one's average house pot. The properties they typically can provide are high strength, high hardness, low density, low

thermal expansion coefficients, and low electrical and thermal conductivities. But the characteristic that separates them from other materials, such as metals and polymers, is their high melting point, which grants them the ability to operate at extreme temperatures over extended periods of time. However, ceramics also have their own shortcomings, the greatest of which stems from their brittle nature. Ceramics have an extremely low toughness or ability to deform, which ultimately results in the sudden catastrophic failure of the material when stressed past its limits. Even the smallest of flaws will bring this demise, as ceramics are extremely sensitive to even the smallest crack, void, or inclusion [3].

Ceramic matrix composites (CMCs) are the result of extensive research and development focused on overcoming this primary downfall of monolithic ceramic materials. The sole purpose behind CMCs is to increase the toughness of ceramic materials, thus granting them the ability to exhibit more graceful failure, all the while still providing their attractive weight, strength, and high-temperature properties. By introducing varying forms of reinforcement, energy-dissipating mechanisms have become plausible, granting an increase in toughness and providing damage-tolerant behavior to ceramic materials.

Two types of CMCs exist: discontinuous and continuous fiber ceramic composites (DFCCs and CFCCs). The reinforcement phase of DFCCs typically consists of particulate, platelet, whisker, fiber, or in situ second phases. While these DFCCs can provide high yield and ultimate strengths up to 1000 MPa, their fracture toughness is about one third that of CFCCs [20].

CFCCs incorporate a continuous reinforcement phase of fibers that span the entire length of the composite. This network of continuous fibers acts as a load carrier and helps maintain the structural integrity of the composite during matrix cracking [21]. These fibers are what give CFCCs a higher toughness compared to DFCCs. Table 1 displays and compares the characteristics of these different types of CMCs.

Table 1 – Characteristics of different types of CMCs. Adapted from [20]***, pg. 44, Table 2.1.***

Continuous CMCs	Discontinuous CMCs
Excellent High Temp Mech. Properties	Excellent High Temp Mech Properties
High Specific Strength and Stiffness High Fracture Toughness	High Specific Strength and Stiffness Higher Useful Strengths.
Dimensional Stability Low Thermal Expansion	Fracture Toughness Good but Inferior to Continuous CMCs
Good Thermal Shock Resistance Graceful Failure Mode	Thermal Shock Resistance Inferior to Continuous CMCs
Oxidation Resistance Machining More Difficult Processing More Complicated and Expensive	Amenable to Cheaper Conventional Processes Machining Expensive

Figure 4 compares the stress-strain behavior of each of these materials, with the area under each curve being representative of the fracture toughness of each material respectively. While this DFCC material being represented utilizes a particulate form of reinforcement and is able to achieve a higher strength, as seen in Figure 4, it still suffers from brittle fracture similar to that of the monolithic ceramic material. It can be seen that the CFCC is able to still demonstrate a fair amount of load carrying capacity in order to prolong the effects of failure, thus providing enhanced toughness as compared to its counterparts [22]. This enhanced fracture toughness of CFCCs over both monolithic

ceramics and DFCCs is ultimately achieved by how cracks interact with these continuous fibers and propagate through the composite matrix.

As cracks grow through the matrix, they are deflected by the continuous fibers that are reinforcing the composite. This deflection isolates the crack growth, thus restricting the ability for multiple cracks to combine and cause sudden catastrophic failure. This is largely dependent on the interface (bond) between the fibers and the matrix, with a weak matrix interface being required for it to behave as a crack arrestor, as portrayed in Figure 5. This weak fiber/matrix interface is what provides opportunity for toughness enhancement behavior, such as fiber/matrix debonding, crack deflection, and fiber pullout [3].

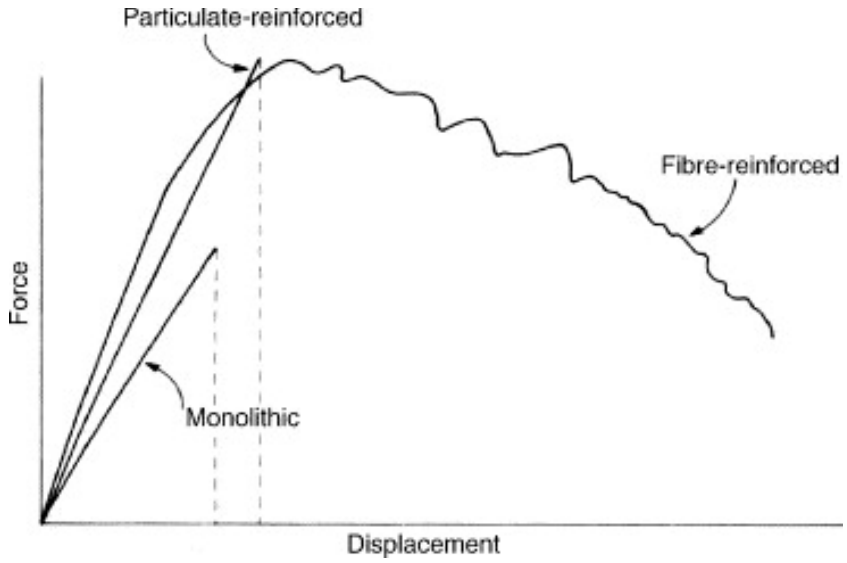

Figure 4 – Comparison of the stress-strain behaviors of a monolithic ceramic, discontinuous, and continuous CMCs. Reproduced from [22]***, pg. 119, Figure 4.1, Copyright © 1999, with permission from Elsevier.***

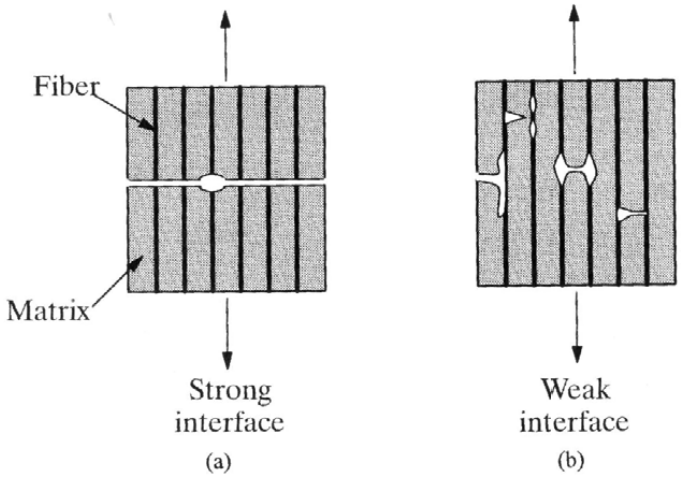

Figure 5 – Failure of CFCCs showing crack propagation for strong and weak interfacial bond strengths. Reproduced with permission by Springer Nature [3], pg. 148, Figure 5.6, Copyright © 1998 by Springer Science & Business Media.

2.2 Non-Oxide Silicon Carbide (SiC) Fibers

Seeing that the strength and load carrying capacity of a CMC is largely dependent on the fibers that it consists of, it is important to understand the very materials of the fibers themselves and how they are linked to the overall properties of the CMC. The most studied CMCs are those consisting of non-oxide materials for both the matrix and the fibers (non-oxide/non-oxide) [23]. Non-oxide materials lack oxygen in their crystal structure. While this matrix/fiber combination of non-oxide materials is used in CMCs for matrix/fiber compatibility, the main purpose is to utilize their combined properties that are maintained at high temperatures.

Non-oxide fibers, while having comparable Young's moduli (tensile elasticity) and diameters to oxide fibers, display superior tensile strength and creep resistance. Even under high stresses, non-oxide fibers have demonstrated lower creep rates at temperatures greater than 1200℃, whereas oxide fibers have barely exceeded 1000℃ [23]. As such, non-oxide

fibers are being considered for a variety of applications. The only non-oxide fibers that have shown their general applicability for advanced CMC use are those based on silicon carbide (SiC) [24].

The properties of bulk SiC are highly sought after, being the second hardest material known with a Young's modulus twice that of steel (approx. 400 GPa), a density half that of steel ($3.15\ g/cm^3$), as well as a maximum service temperature of 1600°C [25]. However, being able to realistically produce these in fiber form at the degree of quality required for the fibers to obtain these bulk characteristics has proved to be a challenging task. Nevertheless, this has led to the development and production of three generations of fibers, with the latest one approaching the very physical limits of SiC [25].

The production of SiC fibers first came about by means of chemical vapor deposition (CVD) in the 1960s. CVD is a chemical process that exposes a wafer or substrate to a precursor which reacts on the substrate and produces a deposit of the desired material. Initially for SiC, this process would typically result in producing thick fibers, with diameters ranging from 100-150 μm. But fibers of those large diameters were too thick, inflexible, and difficult to handle to be considered for CMC use [3], [25].

It was not until later in the 1970s that research conducted by Yajima et al. [26] would alter the process in order to produce SiC fibers of usable smaller diameters. This was accomplished by melt spinning a polymer precursor (Polycarbosilane (PCS)) into a precursor fiber, followed by using curing and controlled pyrolysis to cross link the polymer chains and produce a fine ceramic fiber [3]. This process would produce SiC fibers with

diameters of approximately 15 μm [25]. Further details surrounding this process can be seen in Figure 6.

The availability of small SiC fibers lead to the commercial production of the first generation of SiC fibers. These first generation fibers were commercially produced by a Japanese company named Nippon Carbon in the early 1980s and consisted of the Nicalon 100 series, eventually replaced by the Nicalon 200 series a few years later. The Nicalon 200 series had a diameter around 15 μm and consisted of approximately 56.6 wt% silicon (Si), 31.7 wt% carbon (C), and 11.7 wt% oxygen (O) [25].

Later in the 1980s another Japanese company, Ube Industries, also started producing their own series of first generation SiC fibers known as the Tyranno Fiber. The Tyranno LOX-M was different in the fact that it utilized the addition of titanium in the polymer precursor (known as polytitanocarbosilane (PTC)) used in the manufacturing process of the fiber. This was reported to yield better thermal and chemical stability compared to the first generation Nicalon fibers [27], all the while retaining a fairly similar composition, as seen in Table 2.

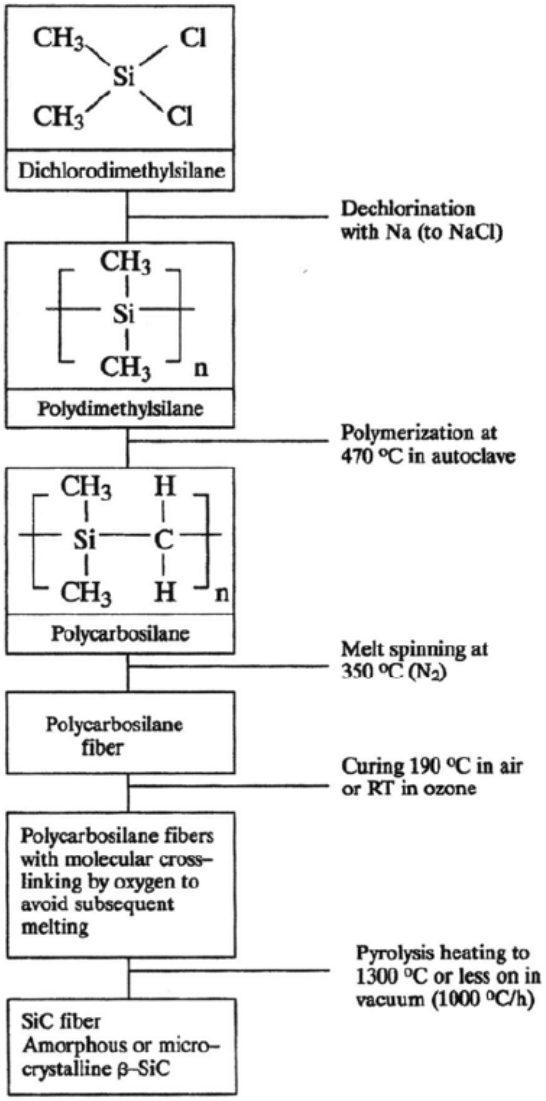

Figure 6 – The Yajima process of making SiC from a polycarbosilane (PCS). Reproduced with permission by Springer Nature [3], pg. 81, Figure 3.20, Copyright © 1998 by Springer Science & Business Media.

When comparing the properties of these first generation fibers produced by Nippon Carbon and Ube Industries, as shown in Table 3, it can be observed that these first generation fibers failed to reach the expected properties of bulk SiC. It was found that the limiting factor was due to the non-stoichiometric (elements lacking expected proportions)

composition of the fibers, with both the Nicalon and Tyranno fibers containing excess carbon and oxygen, roughly 32 and 12 wt%, respectively. This excess amount of oxygen caused the fibers to be thermally unstable and significantly degraded their strength properties [23].

Table 2 – Manufacturer, elemental composition, and approximate cost of all three generations of SiC based fibers. Reprinted from [25]***, pg. 826, Table 3, Copyright © 2006, with permission by Springer Nature.***

	Trade mark	Manufacturer	Cross linking method	Approximate maximum production temperature	Elemental composition (wt%)	Density (g/cm^3)	Average diameter (μm)	Cost (US $/kg)
First Gen.	Nicalon 200	Nippon Carbon	Oxygen	1200°C	56Si + 32C + 12O	2.55	14	2000
	Tyranno LOX-M	Ube Ind.	Oxygen	1200°C	54Si + 32C +12O + 2Ti	2.48	11	1250
Second Gen.	Hi-Nicalon	Nippon Carbon	Electron irradiation	1300°C	62.5Si + 37C +O.5O	2.74	12	8000
	Tyranno LOX-E	Ube Ind.	Electron irradiation	1300°C	55Si + 37.5 +5.5O + 2Ti	2.39	11	N/A
	Tyranno ZM	Ube Ind.	Oxygen	1300°C	57Si + 34.5C + 7.5O + 1Zr	2.48	11	1500
	Tyranno ZE	Ube Ind.	Electron irradiation	1300°C	58.5Si + 38.5C + 2O + 1Zr	2.55	11	N/A
Third Gen.	Tyranno SA 1	Ube Ind.	Oxygen	>1700°C	68Si + 32C +0.6Al	3.02	11	N/A
	Tyranno SA 3	Ube Ind.	Oxygen	>1700°C	68Si + 32C +0.6Al	3.1	7.5	5000
	Sylramic	COI ceramics	Oxygen	>1700°C	67Si + 29C +0.8O + 2.3B +0.4N +2.1Ti	3.05	10	10000
	Sylramic iBN	COI Ceramics	Oxygen	>1700°C	N/A	3.05	10	>10000
	Hi-Nicalon Type-S	Nippon Carbon	Electron irradiation	>1500°C	69Si + 31C + 0.2O	3.05	12	13000

Table 3 – Mechanical and thermal properties of all three generations of SiC based fibers. Reprinted from [25]***, containing data from*** [28]***, pg. 826, Table 4, Copyright © 2006, with permissions by Springer Nature.***

	Trade mark	Manufacturer	Thermal expansion coefficient, ppm/°C (to 1000°C) [15]	Room temperature axial thermal conductivity W/m K [15]	Room temperature strength (GPa)	Room temperature Young's modulus (GPa)
First Gen.	Nicalon 200	Nippon Carbon	3.2	3	3	200
	Tyranno LOX-M	Ube Ind.	3.1	1.5	3.3	185
Second Gen.	Hi-Nicalon	Nippon Carbon	3.5	8	2.8	270
	Tyranno LOX-E	Ube Ind.	NA	NA	2.9	200
	Tyranno ZM	Ube Ind.	NA	2.5	3.4	200
	Tyranno ZE	Ube Ind.	NA	NA	3.5	233
Third Gen.	Tyranno SA1	Ube Ind.	NA	65	2.8	375
	Tyranno SA3	Ube Ind.	NA	65	2.9	375
	Sylramic	COI Ceramics	5.4	46	3.2	400
	Sylramic iBN	COI Ceramics	5.4	>46	3.5	400
	Hi-Nicalon Type-S	Nippon Carbon	NA	18	2.5	400

While the presence of oxygen in the fibers was identified as a limiting factor, it also served as a vital part of the process used to produce the fiber itself. To overcome this issue and improve the properties of the first generation fibers, new methods of cross-linking the polymer precursors had to be developed [25].

In 1990 Nippon Carbon developed a new method to overcome these limiting factors in the first generation of SiC fibers by utilizing electron radiation to interact with the polymer precursors [23], [25]. This new cross-linking process successfully reduced the oxygen content of the fibers produced from PCS precursors to 0.5 wt%, resulting in the second generation of SiC fibers, the Hi-Nicalon fiber produced by Nippon Carbon [29], [30]. These Hi-Nicalon fibers boasted better strength retention at elevated temperatures [31] and were roughly 35% stiffer than the first generation fibers, remaining linear elastic up to 1350°C [25].

This newly developed process didn't have the same results for the PTC precursor fibers, causing the second generation Tyranno LOX-E fibers made by Ube Industries to still contain a high oxygen content and not be commercially produced. Instead, Ube Industries began investigating the use of zirconium as a replacement. This new zirconium fiber was the Tyranno ZM fiber, yielding a reduction in oxygen content to approximately 8 wt% and was more stable than the first generation Tyranno LOX-M fibers [25]. While this second generation of fibers served as an improvement over their first generation counterparts, their compositions still contained a large excess of carbon, which negatively affects the creep and oxidation resistance of the fiber [23].

Thus further improvements of the second generation SiC fibers were desired, and both Nippon Carbon and Ube Industries expounded upon the lessons learned from the behavior control processes of the first and second generation fibers. Ube Industries implemented another metal, aluminum, into their polymer precursor, resulting in their third generation SiC fiber, Tyranno SA fibers. Nippon Carbon focused on improving the stoichiometric composition of their Hi-Nicalon fiber and found a way to reduce the excess amount of carbon present by using a radiation cured precursor as an intermediate step. They also thermally treated the fibers at high temperature in a hydrogen-rich environment [23], [25]. This successfully reduced the amount of excess carbon to a C/Si ratio of 1.05, resulting in Nippon Carbon's third generation of SiC fiber, the Hi-Nicalon^{TM} S or Type-S [25].

As shown in Table 3, the properties of Hi-Nicalon^{TM} S strongly resemble those of bulk SiC. The Young's modulus of Hi-Nicalon^{TM} S is approximately 400 GPa, and it is capable of maintaining both its stiffness and strength up to 1400°C. This high level of strength retention is attributed to its polycrystalline structure containing small grains roughly 50 nm in size, a vast improvement over the previous amorphous structures of older generations of Nicalon^{TM} fibers [12], [25]. A comparison of the microstructures for each generation of Nicalon^{TM} fibers is presented in Figure 7. The Hi-Nicalon^{TM} S along with other third generation SiC fibers, also exhibit higher creep resistance than the second

generation Hi-Nicalon^{TM} fibers. The Hi-Nicalon^{TM} S particularly has displayed less than 0.5% creep strain after 60 hours at 1350°C and 850 MPa stress [23].

After many years of research and development, Hi-Nicalon^{TM} S and other nearly stoichiometric third generation fibers now possess the characteristics similar to bulk SiC and are continuing to be optimized to fulfill industry requirements [25].

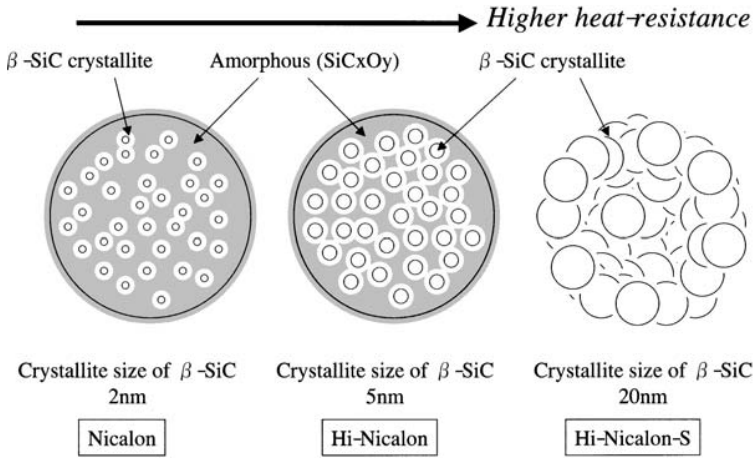

Figure 7 – Microstructures of three generations of Nicalon^{TM} fibers. Reproduced with permission from Springer Nature [12]***, pg. 118, Figure 9, Copyright © 2005 by Springer-Verlag Berlin Heidelberg.***

2.3 Creep

When considering a material to fulfill the design requirements of an advanced application, several material properties must be understood so as to avoid catastrophic failure. One such material property for this type of application is that of creep resistance. Creep is a phenomenon in which material experiences inelastic (permanent) deformation under a constant stress [32], [33]. Considering ceramic materials, creep generally occurs at high temperatures with moderate stress levels and low strain rates [33].

To examine the creep resistance of a material one may perform a creep test. These tests typically apply a constant force to a test specimen in a relatively high temperature environment while measuring the dimensional changes that occur over time. The results of these tests provide a better understanding of creep characteristics and their respective stages or regions for a given material. This data is typically presented by a creep curve displaying the strain the material specimen had experienced over time, as seen in Figure 8. In this figure, while the initial strain (the strain immediately experienced upon loading) occurs over a very brief time interval, it may be considered an instantaneous response.

Creep is broken down into three stages or regions: primary creep, secondary creep, and tertiary creep. The primary creep region is characterized by a decreasing strain rate. This region is typically related to changes in the materials structure (e.g., grain size, dislocation density) or redistribution of stresses. This strain rate will eventually level out to a constant rate, transitioning into the secondary or steady-state region. Within the secondary creep region, the straight line signifying this constant rate of strain is generally the dominant interval of the overall creep curve. At this secondary stage, creep is occurring due to deformation of the materials microstructure. This secondary region will transition into the final tertiary creep region. Tertiary creep is characterized by an increasing strain rate due to structural damage that has occurred in the material, often initiated by voids and crack formation, which ultimately leads to the failure or rupture of the test specimen. This final stage is typically very short or entirely missing for ceramic materials due to their brittle nature [34], [35].

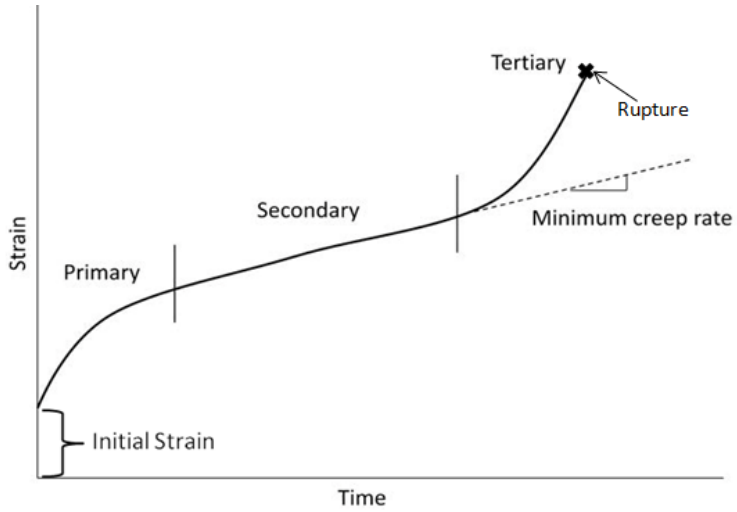

Figure 8. Typical creep curve showing the different regions of creep. Reproduced from Robertson [15]**.**

For CMCs the secondary or steady-state creep region is the area of most interest and can be subject to a variety of creep mechanisms at elevated temperatures [13]. These different mechanisms can be seen in Table 4. To identify these creep mechanisms that are present in a tested material, a link between the experimental data and the mechanism must first be established. The creep rate of materials can be expressed by a commonly known form of the Arrhenius rate equation [33]:

$$\dot{\varepsilon} = B\frac{D\mu b}{kT}\left(\frac{b}{d}\right)^{p}\left(\frac{\sigma}{\mu}\right)^{n} \quad (1)$$

where $\dot{\varepsilon}$ is the strain rate, B is a constant, μ is the shear modulus, b is the Burgers vector, k is the Boltzmann constant, T is the absolute temperature, d is the grain size diameter, σ is the applied stress, p is the grain size power law exponent, and n is the stress power law exponent. The diffusion coefficient D, is the result of another equation:

$$D = D_o \exp\left(\frac{-Q}{RT}\right) \quad (2)$$

where D_o is a frequency factor, Q is the creep activation energy, R is the universal gas constant, and T is the absolute temperature.

From Equation (1), the values of p and n are associated with different creep mechanisms, as presented in Table 4. Upon completion of a creep test, these p and n values can be determined from the experimental creep data and ultimately used to identify the creep mechanisms that are present in the test specimen.

Table 4 – Creep mechanisms in fine-grained polycrystalline ceramics. Adapted from Armani [13]**.**

n **stress exponent**	***p*** **grain size exponent**	**Mechanism**
1	2	Diffusional creep through lattice (Nabarro-Herring creep)
1	3	Diffusional creep along grain boundaries (Coble creep)
2	1	Grain boundary sliding and interface-reaction controlled creep
4	3	GBS and cavity growth
3-5	0	Dislocation creep: 3 –glide controlled, 5 –climb controlled
>5	-	Cavity growth controlled creep

2.4 Previous Work

Hay and associates [36]–[38] have investigated oxidation and scale crystallization kinetics of Hi-Nicalon^{TM} S fibers for a variety of temperatures ranging from 500 – 1600°C in dry and wet air, as well as steam environments. In dry air at temperatures of 700 – 1400°C, Hay et al. [36] found that oxidation of the fibers initially produced an amorphous

silica scale which would begin to crystallize around temperatures of 1000°C. The crystalline scales were found to be thinner than the amorphous scales, except for locations where growth cracks had allowed for more rapid oxidation to occur.

The growth kinetics of the amorphous scale were analyzed using the modified Deal-Grove relationship [36][39], which predicts the growth rate of silicon dioxide ($SiO_{2)}$ scale [36]–[38], [40]–[42]. This model is represented in Equations (3) - (5). Within these equations, variables A_0 and B_0 are constants, Q_a and Q_b are activation energies, B is the parabolic rate constant, B/A is the linear rate constant, A is the SiO_2 thickness at which crossover from linear to parabolic kinetics occurs, R is the universal gas constant, and T is the absolute temperature.

$$\frac{dx}{dt} = \frac{B}{(A + 2x)} \tag{3}$$

$$A = A_0 \exp\left(-\frac{Q_a}{RT}\right) \tag{4}$$

$$B = B_0 \exp\left(-\frac{Q_b}{RT}\right) \tag{5}$$

When an initial thickness of SiO_2 scale (x_i) is used, the solution to the model shown in (3) may be obtained. This solution is shown in (6), where Equation ((7) displays the time shift variable, $\boldsymbol{\tau}$, which corrects for the initial state of the oxide layer [36][37].

$$\mathrm{x} = \frac{1}{2}\,\mathrm{A}\left\{\left[1 + \frac{(\mathrm{t} + \tau)}{\frac{A^2}{4B}}\right]^{1/2} - 1\right\} \tag{6}$$

$$\tau = \frac{(x_i^2 + Ax_i)}{B} \tag{7}$$

Hay and Corns [38] utilized this model in conjunction with other methods to determine the parabolic rate constants for SiO_2 glass ($B_{G)}$ and crystalline (B_C) scale formation during passive oxidation of SiC fibers in steam. This was done for Hi-Nicalon™ S fibers tested in saturated steam at temperatures ranging from 500 – 1600°C. They found that the glass scale formed faster than crystalline scale at temperatures less than or equal to 1500°C. However, this trend reversed at 1600°C, as the crystalline scales would form more rapidly than the glass scales due to a change in oxidation mechanism. These discoveries should prove to be a valuable resource for future efforts modeling SiC oxidation in steam environments [38].

Armani [13] designed and developed the facility and test method originally used at the Air Force Institute of Technology (AFIT) for analyzing the creep of oxide fiber tows at elevated temperatures in both air and steam environments. With this facility, Armani investigated the influence these types of environments would have on the creep behavior of Nextel™610 and Nextel™720 ceramic fiber tows at elevated temperatures ranging from 1100 - 1300°C. Results revealed that the presence of steam had a degrading effect on the creep lifetimes and steady-state creep rates of both the Nextel™610 and Nextel™720 fiber tows at elevated temperatures.

Shortly thereafter Steffens [2] modified the test facility and methods created by Armani to investigate the mechanical performance of higher strength SiC-based fiber tows, particularly Hi-Nicalon™ S, in both air and steam environments at 800 and 1100°C. The results showed in the presence of steam at 800°C, the creep rate and lifetime of the Hi-Nicalon™ S fiber tow specimens decreased. However, when the temperature was increased

from 800 to 1100°C in the steam environment, it had a favorable effect on the creep performance of the Hi-Nicalon^{TM} S fiber tows, increasing their lifetime by at least one order of magnitude. This improvement of life was predicted to be a result of the formation of a protective silicon oxide layer on the fibers that occurred during testing. This silicon oxide layer yielded a delay in the growth of surface defects on the fiber tow specimens and ultimately a delay in fiber failure.

The creep behavior of these particular Hi-Nicalon^{TM} S fibers continued to be evaluated at different elevated temperatures, as Shillig [14] would go on to investigate the fiber tows at temperatures of 800°C, 900°C, 1000°C, and 1100°C in both air and steam environments. Again, it was found that the presence of steam had negative effects on the creep performance of the fiber tows at all temperatures evaluated; however, it was noted that these effects would become less pronounced as the temperature increased. Looking further into this matter, upon completion of the creep tests within a steam environment it was found that the degraded fiber tows contained different signs of oxidation for their lower and upper regions along the fiber tow, those being active and passive oxidation, respectively.

Considering the methods used to apply steam to the fiber tow specimens, it was realized that as the steam was being fed through the feeding tube at the bottom of the susceptor which housed the fiber tow specimen, the steam would gradually leach silicon from the SiC fibers as it traveled up to the top of the susceptor, eventually becoming saturated with silicic acid ($Si(OH)_4$). This gradual chemical change of steam would yield different oxidation mechanisms in the lower and upper regions of the fiber tow specimen

within the susceptor as it would travel upward throughout the duration of testing. This decrease in the amount of degradation regarding creep performance at high temperature steam environments was attributed to the transition from passive oxidation (occurring at 800-1000°C) to active oxidation (occurring at 1100°C) of the Hi-Nicalon^{TM} S fiber tow specimens.

These irregularities would later be investigated by Robertson [15], who in a collaborative effort with Sprinkle [43], further modified the test facility originally developed by Armani. These modifications were completed to preheat the steam to a desired test temperature and saturate the steam with silicic-acid prior to it reaching the fiber tow specimen. This in turn resulted in a more uniform temperature distribution as well as more consistent oxidation mechanisms experienced throughout the entirety of the fiber tow specimen, and would be successfully validated by Sprinkle as he performed creep tests of Sylramic-iBN fiber tows at 400 and 500°C in air and silicic-acid saturated steam ($Si(OH)_4$) [43].

Utilizing the modified test facility to evaluate the mechanical behavior of Hi-Nicalon^{TM} S fiber tows at 800°C in air and now, silicic-acid saturated steam, Robertson found that the silicic-acid saturated steam environment still degraded the creep performance of the fiber tows, but to a lesser extent when compared to the unsaturated steam environments investigated in the years prior. Additionally, it was also found that the Hi-Nicalon^{TM} S fiber tows showed five times the load carrying capacity in silicic-acid saturated steam as compared to the fiber tows used in previous tests of unsaturated, unheated steam. These findings were determined to be a direct result of the uniform oxide

layer that was able to form on the fiber tow specimens due to the modifications that were made to the test facility [15].

The evaluation of Hi-Nicalon^{TM} S fiber tows continued as Piper [16] investigated their mechanical behavior at 700°C in air and silicic-acid saturated steam. Similar to the results of Robertson's testing at 800°C, it was again found that exposure to silicic-acid saturated steam had negative effects on the creep performance of the fiber tow specimens, although not as severe as what had been caused by unsaturated steam in previous research. The fiber tow specimens also displayed consistent layers of silicon scale growth along their respective lengths, once again validating the testing facility modifications by Sprinkle and Robertson.

Mitchell [17] contributed to the evaluation of Hi-Nicalon^{TM} S fiber tows by studying their creep behavior at 900°C in air and silicic-acid saturated steam. The results concurred with previous efforts, as the presence of silicic-acid saturated steam significantly degraded creep performance of the fiber tows, however not as severely as previous work tested at similar temperatures in unsaturated steam. It was noted that when the tested fiber tows were compared against previous efforts done at 700°C and 800°C in silicic acid-saturated steam, the silicon scale growth on these fiber tow specimens tested at 900°C were more pronounced.

Kroeger [18] then continued the investigation of creep behavior on the Hi-Nicalon™ S fiber tows at 1000°C in air and in silicic acid-saturated steam. He found that the presence of silicic acid-saturated steam continued to have a detrimental impact on the creep performance of the fibers, with creep lifetimes decreasing by one order of magnitude

and steady-state creep rates increasing by one order of magnitude. He also observed an increase in the oxide scale thickness, with both amorphous and crystallized oxide scale appearing on the fracture surfaces of the fibers tested in saturated steam, and not in fibers tested in laboratory air.

Kroeger also used the Deal-Grove model (Equation (3)) to predict the oxide scale thickness for tests in laboratory air and in saturated steam. After completing post-test analysis using scanning electron microscopy (SEM), he found that the model predictions appeared to be more accurate for the fiber tows subjected to saturated steam than the predictions made for the fiber tows tested in laboratory air. When performing SEM analysis of the fracture surfaces of the fibers that were tested, he also polished cross-sections of the fibers and viewed them using the electron backscatter deflection detector on the SEM. This was an attempt to get improved fidelity of the oxide scale thickness, however the composition of the oxide scale and that of the fibers were too similar to be detected in the SEM.

III. Methodology

Due to the high temperatures and aggressive environments that some materials must endure in advanced engineering applications, it is imperative that their capability is satisfactory so as to avoid catastrophic failure. By evaluating the effects that air and saturated steam environments may have on creep behavior, that capability may be better understood. The purpose of evaluating the creep behavior of Hi-Nicalon^{TM} S fibers at elevated temperatures in air and saturated steam environments is to develop a better understanding of how these ceramic fibers would perform under similar circumstances found in engineering applications. The data acquired by this effort not only provides benefit to the exploration of this particular ceramic fiber's performance, but also serves as a stepping stone for the validation of ceramic fiber based materials developed for future high temperature applications currently limited to traditional alloys.

3.1 Theory

The main advantage of the CMCs is their ability to retain their strength to weight ratio at elevated temperatures. By utilizing a continuous ceramic fiber reinforcement coupled with a ceramic distributed phase, not only are CMCs able to possess excellent high temperature mechanical properties, but ultimately they are capable of exhibiting a more graceful failure mode than monolithic ceramics. Silicon carbide (SiC) fibers are non-oxide fibers that have shown promise for advanced CMC use, and their latest generations are being evaluated to ensure their capability in high temperature applications. An important consideration for use of a material, especially in high temperature environments, is its creep resistance. This deformation characteristic may be examined and analyzed by performing

creep tests. These types of tests are invaluable, as they provide a wealth of information which aids in determining failure modes and overall life expectancy of a given material prior to introducing it into service.

Creep tests for fibers, however, are problematic. In these experiments it is difficult to determine whether the strain accumulation is in fact due to creep deformation of the fibers or due to progressive failure of individual fibers within the fiber tow throughout the duration of the creep test. When individual fibers fail during the test, the load is redistributed amongst the remaining fibers, thus causing the stress carried by them to increase for the remainder of the test. Thus it is difficult to isolate creep deformation from deformation caused by the continuously increasing stress.

This particular effort evaluates the creep performance of Hi-Nicalon^{TM} S fiber tows, the latest generation of SiC fibers made by Nippon Carbon Co, Ltd, and seeks to assess that behavior in air and silicic acid-saturated steam environments at 1100°C. To carry out the analysis of the creep tests some assumptions are needed. While it may not actually be the case, it is assumed that each of the fiber tows being tested has the same number of intact fibers. It is also assumed that the silicic acid-saturated steam is free of contaminates. At elevated temperatures, oxidation of the fiber tow ensues, which causes a change in the cross sectional area of the fibers. While these changes may occur, a constant cross sectional area of the fiber tow is assumed for stress calculations.

3.2 Material and Equipment

This research effort evaluated the creep behavior of Hi-Nicalon™ S fiber tows at 1100°C in laboratory air and silicic acid-saturated steam. Hi-Nicalon™ S fiber tows (Figure 9) are the third generation of SiC fibers produced by Nippon Carbon Co Ltd of Tokyo, Japan [44]. By utilizing de-carbonization pyrolysis and electron-beam curing, this stoichiometric β-SiC fiber is near-oxygen free and yields higher modulus, better creep resistance, and improved oxidation resistance compared to the second generation fiber, Hi-Nicalon™ [45].

Figure 9 – A spool of Hi-Nicalon™ S fiber tow, manufactured by Nippon Carbon Co., Ltd. [44]

The Hi-Nicalon™ S fiber tows being used in this research consist of approximately 500 individual fibers with diameters averaging 12 μm, providing an average cross-sectional area of 5.655×10^{-8} m^2. The typical properties of Hi-Nicalon™ S fibers are presented in Table 5.

Table 5 – Typical properties of Hi-Nicalon™ S fiber. Data reproduced from NGS Advanced Fibers Co., Ltd. [46]

Number of filaments	500
Filament diameter (μm)	12
Product Form	Tow
Sizing Agent	PVA
Linear density, tex (g/km)	195
Oxygen content (wt%)	0.8
Modulus of Elasticity (GPA)	380

The Hi-Nicalon™ S fiber tows were tested at AFIT in the Mechanics of Advanced Aerospace Materials Laboratory, Department of Aeronautics and Astronautics, using a fiber tow testing facility originally built by Armani [13], and later modified by Steffens [2], Shillig [14], Robertson [15], and Sprinkle [43]. This facility is capable of examining the creep behavior of fiber tows at various temperatures in air or in steam (saturated or unsaturated) environments. The facility itself utilizes various pieces of equipment in order to accurately examine the creep behavior of the fiber tow.

A compact two-zone resistance-heated furnace (Model 653.03A, MTS Systems Corporation, Eden Prairie, MN) with two temperature controllers (MTS 409.83) provide the high temperature environment. A ceramic susceptor (alumina tube with end caps) designed to fit inside the furnace is used to achieve a more uniform and repeatable temperature distribution along the fiber tow. The gauge section of the fiber tow specimen is located inside the susceptor with the specimen ends passing through slots in the susceptor end caps. The total length of the furnace is 124 mm and the length of the susceptor is 90 mm. Temperature profiles are measured throughout the length of the furnace in air and in steam with a K-type thermocouple.

A cold gripping method is used in all tests in order to avoid high-temperature contact and thus a possible thermo-chemical interaction between the fiber and other materials. Hence, specimen elongation is measured outside the furnace with an LVDT (Schaevitz M12-30) attached to the bottom tab of the fiber tow specimen. The dead weight is attached to the rod extending from the bottom of the LVDT. Displacement data is recorded using an MTS FlexTest 40 digital controller.

For testing in steam, steam is generated using a steam generator (Model HGA-S-01, MHI, Cincinnati, OH) capable of delivering steam at temperatures up to approximately 500°C and deionized water. The testing facility employs two CX1300 heating units (see Figure 10(a)) connected in series. These units are powered by an IBPAN controller (see Figure 10(b)). Both heating units were redesigned to provide faster response to setting adjustments and to generate enough heat to produce steam temperatures up to 1200°C. The original $MoSi_2$ resistance heating coil was replaced with an $MoSi_2$ coil of smaller thickness that also included an additional complete turn. The new heating coil was encased in insulation (KVS 174/400, RATH, Newark, DE) prior to mounting in the CX1300 shell.

The heating chamber contains an alumina tube that acts as a reducing nozzle. At one end the diameter of the tube reduces sharply from 50 mm to 6 mm. The reduced end of this alumina tube is fitted into an alumina supply tube, which delivers steam to the test chamber. An R-type thermocouple in alumina sheathing inserted through a tight-fit hole into the supply tube monitors the steam temperature just before it enters the test chamber. To saturate steam with the silicic acid, silica wool (Hereaus Quartz, LLC USA, Austin TX) is placed inside the alumina tube that passes through the heating chamber of the modified

CX1300 heating unit. The high surface area of the fibrous silica wool allows for a faster reaction with the steam as it passes through, assuring steam saturation with silicic acid.

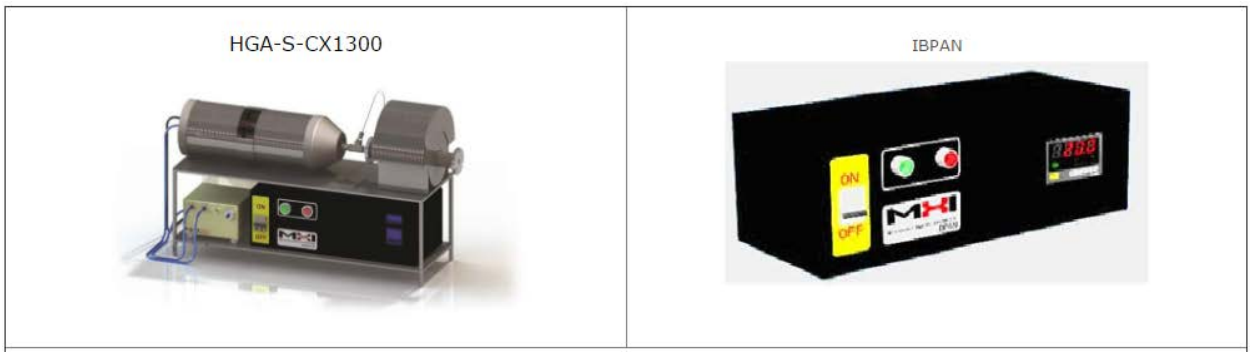

(a) ***(b)***

Figure 10 – MHI HGA-S-CX1300 heater (a) and controller (b). Reproduced from Mitchell [17]**.**

3.3 Specimen Preparation Procedure

The Hi-Nicalon™ S fiber tow specimens were prepared using the three tab method developed by Steffens [2]. The three tab method utilizes a layout of three fiberglass tabs (primary, secondary, and tertiary), to house each end of the fiber tow specimen. The dimensions of the primary, secondary, and tertiary tabs are 1.0 in x 1.5 in (0.0254 m x 0.0381 m), 1.0 in x 1.0 in (0.0254 m x 0.0254 m), and 0.75 in x 0.75 in (0.0191 m x 0.0191 m), respectively.

These three fiberglass tabs are cut to size and arranged according to the schematic shown in Figure 11. The primary tab contains a hole punched along the centerline, which is used to suspend the fiber tow specimen from the hook fixture in the test facility. The

primary and secondary tabs are sanded to alleviate sharp edges from possibly damaging the fiber tow specimen during sample preparation and testing.

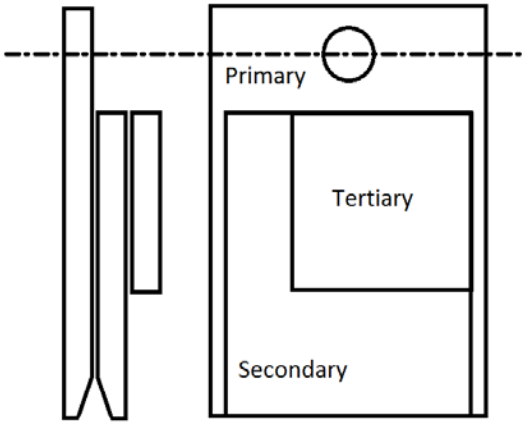

Figure 11 – Layout of the three tab method used in fiber tow testing. Reproduced from Mitchell [17]**.**

A board marked with grid lines was used to prepare each fiber tow specimen with the three tab method (Figure 12). The primary tabs were secured to a sample preparation board with tape, having a 7 in (0.178 m) gap between tabs and a grid line bisecting the hole of each tab (Step 1 in Figure 12). A length of Hi-Nicalon™ S fiber was cut from the spool, aligned along the gridline, and attached to the primary tabs with tape (Step 2 in Figure 12). The secondary tab was then attached using a two part epoxy (Step 3 in Figure 12). Upon drying, the excess fiber was folded over and secured with the tertiary tab using the same epoxy (Step 4 in Figure 12). Lastly, excess fiber protruding from the tertiary tab was removed using a razor blade (Step 5 in Figure 12). By preparing the test specimens utilizing the three tab method, we ensure that the fiber tows are secure and subjected to only axial loading throughout the duration of the creep test.

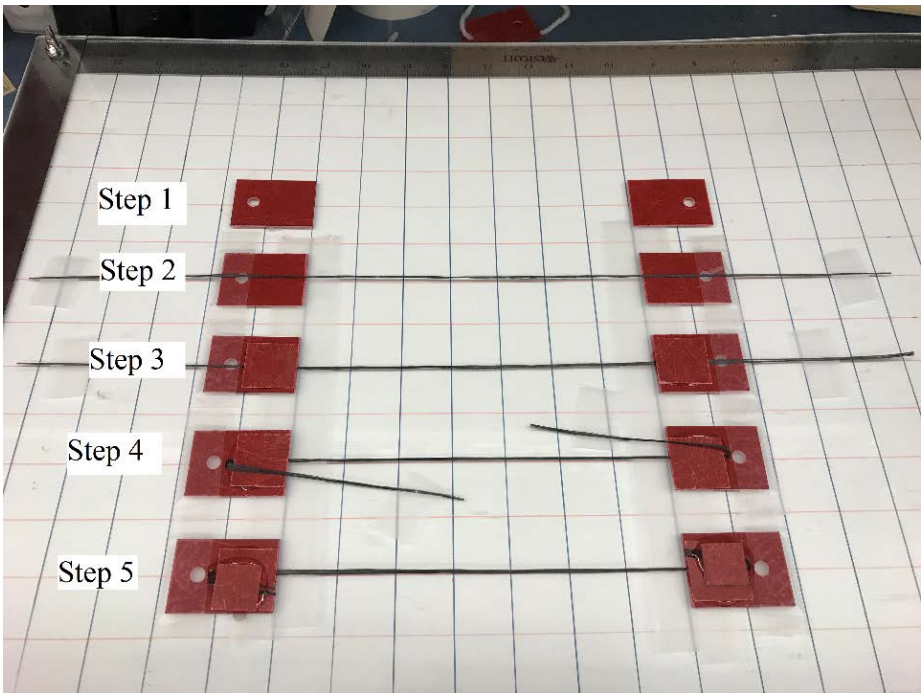

Figure 12 - Test specimen preparation process.

3.4 Experimental Facility Operation

This effort will test Hi-Nicalon™ S fiber tows at the Air Force Institute of Technology (AFIT) in the Mechanics of Advanced Aerospace Materials Laboratory, Department of Aeronautics and Astronautics. The test facility was originally built by Armani [13], who tested oxide fiber tows at elevated temperature in air and in steam environments. Steffens [2] and Shillig [14] then modified the facility to perform creep tests of SiC fiber tows. From these experiments, Shillig discovered that the nature of the steam delivery system was causing the steam to be chemically altered as it traveled along the fiber tow specimen within the test chamber.

This problem sparked a need for further modifications to the facility, which were then completed by Robertson [15] and Sprinkle [43]. These modifications enabled delivery of silicic-acid saturated steam directly to the test chamber. Other modifications included the capability to preheat the steam to the test temperature prior to entering the test chamber. The modified test facility permits evaluation of SiC fibers in a realistic service environment. Testing SiC fiber tows at elevated temperature in silicic acid-saturated steam simulates conditions experienced by SiC fibers reinforcing a SiC/SiC composite. As the steam found within a combustion environment enters the matrix cracks of a SiC/SiC composite, it leaches Si from the SiC matrix and becomes saturated with silicic acid before it reaches the reinforcing SiC fibers of the composite [17].

Tensile creep tests were performed using a dead-weight creep rig. The creep testing apparatus, as seen in Figure 13, utilizes an alumina susceptor, a tube with end caps that resides within an MTS 653.03A two-zone resistance furnace. The prepared fiber tow specimen is hung from a supporting hook and passes through slots in the susceptor end caps. The use of the susceptor tube allows for a more uniform temperature distribution along the enclosed portion of the test specimen. The elongation of the fiber tow specimen was measured with an LVDT (Schaevitz M12-30) connected to the bottom tab of the fiber tow specimen, which resides outside the furnace. The rod extending from the bottom of the LVDT core holds the dead weight. The creep test apparatus also utilizes a K-type thermo-couple on a hydraulic ram actuator to obtain temperature profiles along the length of the furnace.

The steam generating apparatus described above is used when testing in steam. The steam (saturated or unsaturated) is delivered into the bottom of the susceptor via a feeding tube as seen in Figure 14. The steam is delivered continuously with a slight positive pressure expelling the dry air and creating a uniform steam environment inside the susceptor.

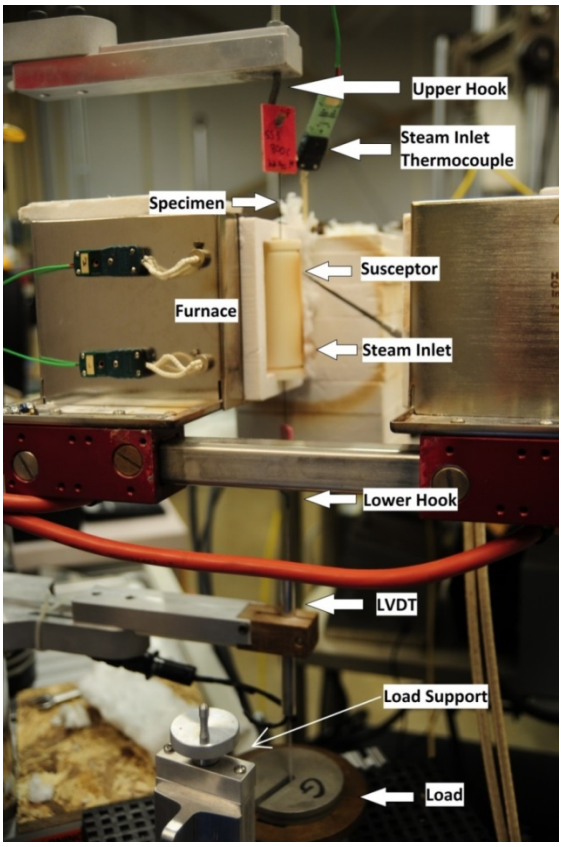

Figure 13 – Fiber tow specimen mounted in creep testing apparatus. Reproduced from Piper [15].

Figure 14 – Alumina susceptor and steam feed tube assembled in one half of the furnace. Reproduced from Armani [13]***.***

The steam is produced by a Micropyretics Heaters International model HGA-S steam generator, while a Cole Parmer ® model 7518-10 peristaltic pump delivers 7.5 ml/min of de-ionized water from a 50 gallon reservoir. The generated steam flows through an alumina tube within two MHI CX1300 heaters, where it is heated to the desired temperature prior to being delivered to the test chamber. This alumina tube may also be loaded with silica wool, as seen in Figure 15, to saturate the steam with silicic acid prior to reaching the test chamber.

Figure 15 – Silica wool inserted into alumina tube acting as saturation chamber for silicic acid-saturated steam. Reproduced from Robertson [15]**.**

A relatively high steam flow rate (~4700 ml/min) is needed to maintain the desired steam temperature (800-1200°C) in the test chamber. However, steam entering the test chamber at such a high flow rate will aerodynamically damage the fiber tow specimen. In order to transition from a higher steam flow rate in the heating unit to a desired low flow rate in the test chamber, an alumina bleed-off tube is inserted into a hole cut in the side of the feeding tube. Before inserting the bleed-off tube into the feeding tube, its end was cut at a 45° angle. The outer diameter of the bleed-off tube was nearly the same as the inner diameter of the feeding tube to insure a tight fit. The flow is regulated by simply rotating the bleed-off tube (see Figure 16). The overall configuration of the test facility is shown in Figure 17.

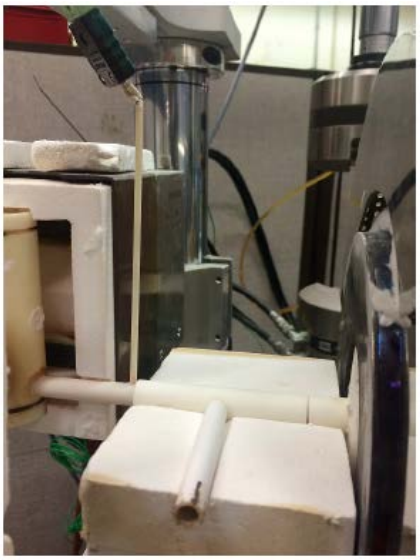

Figure 16 – Bleed-off assembly located just prior to the feeding tube of the test chamber. Reproduced from Robertson [15]**.**

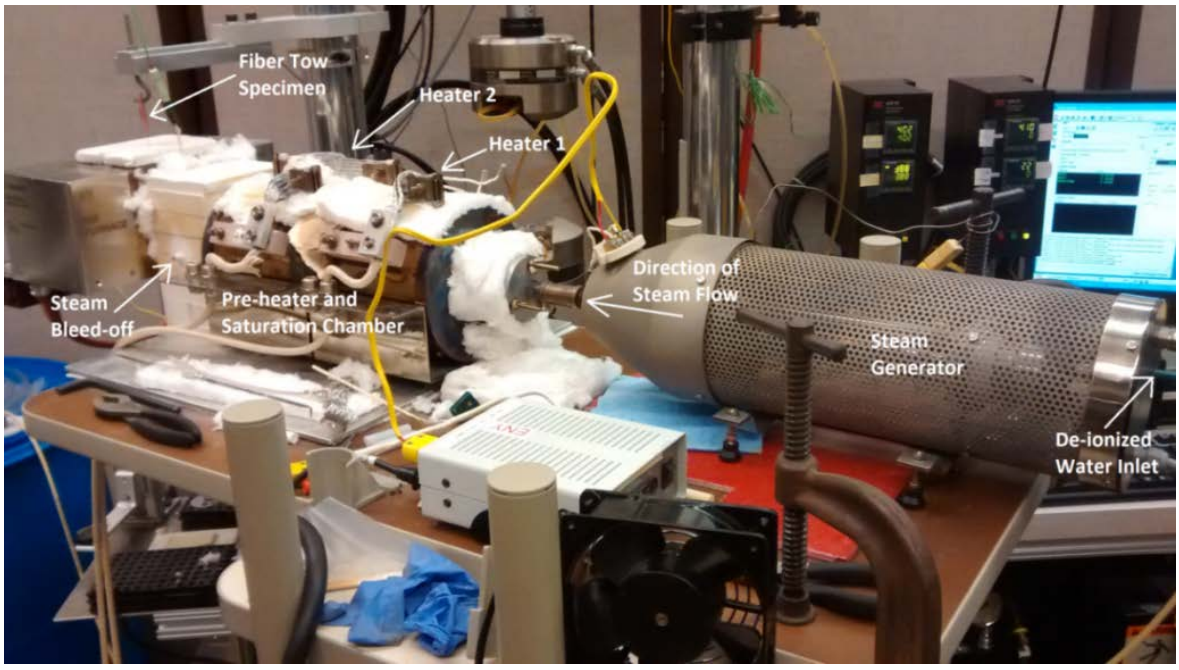

Figure 17 – Creep test facility configured for saturated steam tests. Reproduced from Robertson [15]**.**

IV. Analysis and Results

4.1 Temperature Profiles

Temperature profiles were measured throughout the length of the furnace in air and in steam in order to verify that uniform test temperature was achieved inside the susceptor. Additionally, temperature profiles were employed to determine the effective gauge lengths in air and in steam, which were subsequently used to calculate creep strain and creep strain rate from the displacement values measured by the LVDT throughout each test. The method used to determine the effective gauge length and to calculate the engineering strain is discussed in section 4.2.

The temperature profiles for both the air and saturated steam environments were determined by utilizing the ram actuator of an MTS machine to vertically move a K-type thermocouple (±3°C accuracy) along the centerline of the susceptor housed within the furnace and recording the temperature readings with the MTS software. The temperature profiles obtained at 1100°C in air and saturated steam are shown in Figure 18 and Figure 19, respectively.

Note that the zero position in Figure 18 and Figure *19* corresponds to the middle of the susceptor, while the positions of + 60 mm and -60 mm correspond to the top and bottom of the susceptor, respectively. When the furnace heating elements were replaced in the course of this research effort, the temperature profile for testing in saturated steam had to be accomplished anew (see Figure 19(b)). The temperature profile in Figure 19(b) was used for specimens S4-S12, while the temperature profile in Figure 19(a) was used for specimens S1-S3.

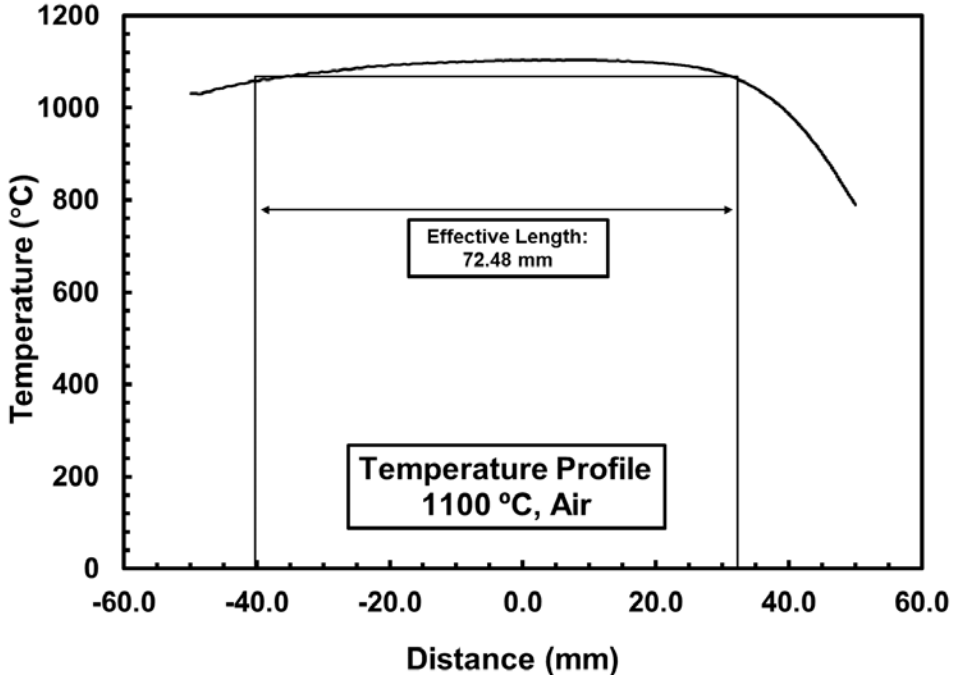

Figure 18 – Temperature profile obtained in laboratory air at 1100°C.

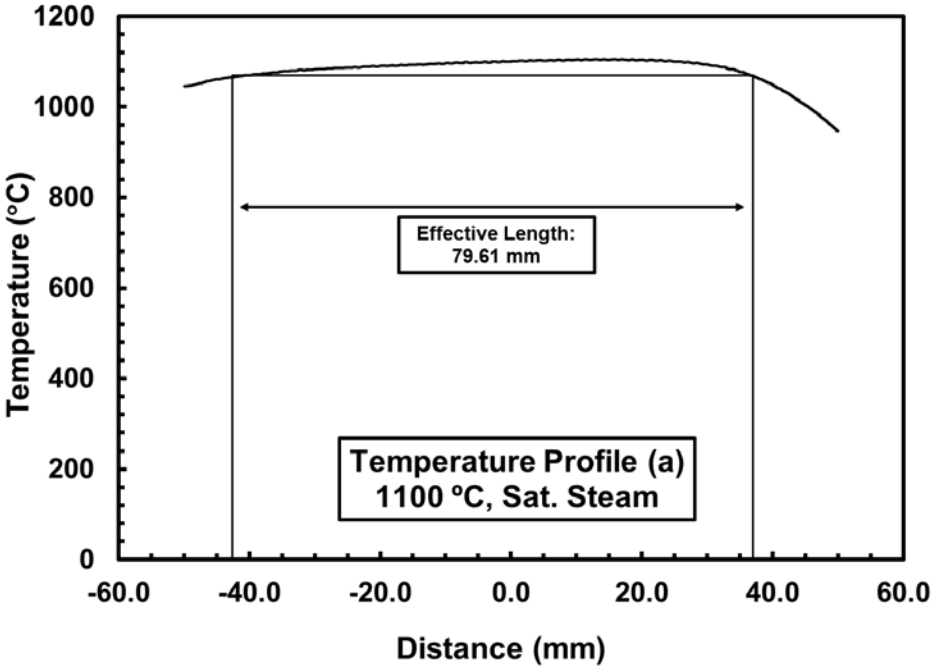

(a)

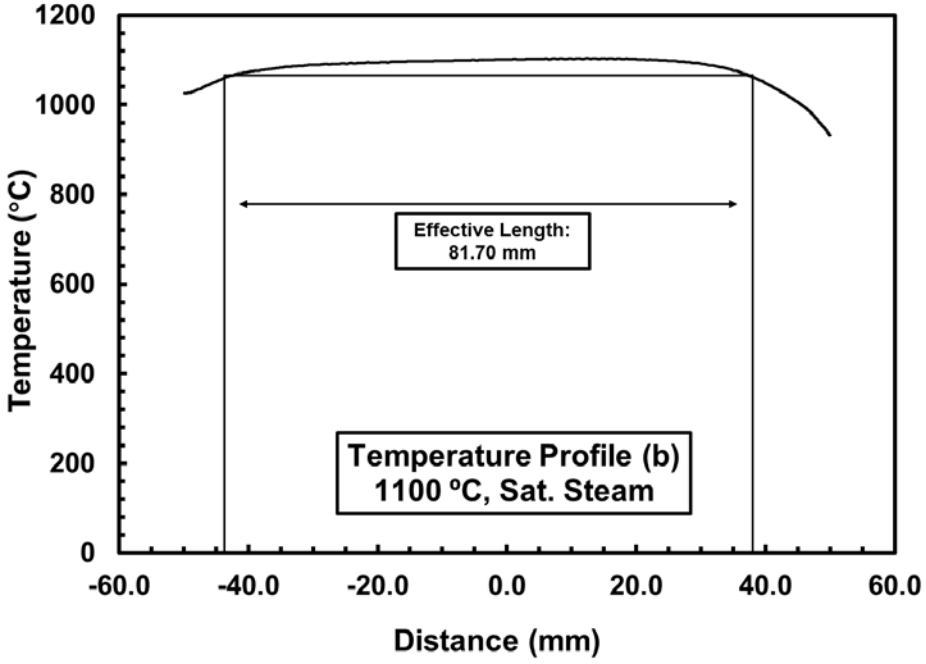

(b)

Figure 19 – Temperature profiles obtained in saturated steam at 1100°C. Profile (a) was used for specimens S1-S3, while profile (b) was used for specimens S4-S12.

4.2 Engineering Strain Measurement

Typically a direct measurement of strain may be obtained by using extensometry. However in the case of fiber tow testing this method of measuring strain is not possible. Therefore, a method that permits strain calculation from displacement data is required.

Recall the setup of the fiber tow testing facility used in this work, mentioned previously in section 3.4. In this work the elongation of each fiber tow specimen was measured with an LVDT (Schaevitz M12-30) connected to the bottom tab of the fiber tow specimen outside of the furnace. Thus the total recorded specimen elongation was the sum of contributions from parts of the specimen located in three different temperature zones: the hot zone (at uniform temperature of 1100°C), the temperature gradient zone and the cold zone. The hot zone is the portion of the specimen near the middle of the furnace which is at the target test temperature of 1100°C. The temperature gradient zone refers to the transitional portions of the specimen, which are located inside of the furnace but outside of the hot zone. The cold zone refers to the regions of the fiber tow specimen that are exposed to room temperature above and below the furnace. The sizes of these temperature zones are determined by the temperature profile, discussed previously in section 4.1. Strain and strain rate were calculated from the displacement data by using a method proposed by Armani [13], which is similar to that proposed by DiCarlo [47], Morrell [48], and Kandil and Dyson [49]. A brief description of the method is given below.

Given a fiber tow test specimen of length 2L and taking the midpoint of the specimen to be defined as the zero position, the creep that is experienced by the specimen occurs along its length from –L to L. For the regions outside of these bounds, creep is

considered negligible due to the lower temperature. The creep strain and creep strain rate can then be calculated as:

$$\varepsilon_m = \frac{\Delta l}{2L} = \int_0^t \dot{\varepsilon}_m \, dt \tag{8}$$

$$\dot{\varepsilon}_m = \frac{measured\ extension\ rate}{2L} = \frac{1}{2L}\int_{-L}^{L} \dot{\varepsilon} dl \tag{9}$$

The total measured strain, ε_m, and strain rate, $\dot{\varepsilon}_m$, calculated by Equations (8) and (9) account for the variations in strain and strain rate along the length of the fiber tow, 2L. These variations are caused by the variation in temperature along the length of the fiber tow, with the largest amounts of strain being produced in the hottest sections. The desired test temperature is located at the center of the furnace and is denoted in the following equations with subscript *0*. By taking the time integral of the strain rate at the center of the furnace one can determine the strain at the center of the furnace. This may also be obtained by using the overall change in length of the specimen, Δl, and dividing by a hypothetical length, $(2L)_{eff}$. This hypothetical length is the effective gauge length of the fiber tow and is described as the length obtained under a temperature profile where all of the strain is accumulated under the peak temperature, with zero strain obtained under the lower temperature. The strain at the desired maximum temperature can then be calculated:

$$\varepsilon_o = \int_0^t \dot{\varepsilon_o} dt = \frac{\Delta l}{(2L)_{eff}} \tag{10}$$

Likewise, the strain rate at the maximum temperature at the center of the furnace can be expressed in terms of effective gauge length as:

$$\dot{\varepsilon_o} = \frac{measured\ extension\ rate}{(2L)_{eff}} = \frac{1}{(2L)_{eff}} \int_{-L}^{L} \dot{\varepsilon} dl \tag{11}$$

Taking the ratio of Equations (9) and (11) yields:

$$\frac{\dot{\varepsilon}_m}{\dot{\varepsilon}_o} = \frac{\Delta l}{(2L)_{eff}} \tag{12}$$

Since stress is uniform along the length of the fiber tow specimen and temperature is a function of location along the fiber tow specimen, the general power-law creep equation can be applied:

$$\dot{\varepsilon} = A\sigma^n \exp\left(\frac{-Q}{RT(l)}\right) \tag{13}$$

Combining Equation (9), Equation (12), and Equation (13), the ratio of the measured strain rate to the actual strain rate can be reduced to a function of temperature:

$$\frac{\dot{\varepsilon}_m}{\dot{\varepsilon}_o} = \frac{1}{2L}\int_{-L}^{L} exp\left\{\frac{-Q}{R}\left(\frac{1}{T(l)} - \frac{1}{T_o}\right)\right\} dl \tag{14}$$

This ratio of measured strain to actual strain can then be expressed as a summation of increments of length, h, where L = hk and k is an integer:

$$\frac{\dot{\varepsilon}_m}{\dot{\varepsilon}_o} = \frac{1}{2k}\sum_{i=-k}^{k} exp\left\{\frac{-Q}{R}\left(\frac{1}{T(l)} - \frac{1}{T_o}\right)\right\} \tag{15}$$

Using this numerical approach, the effective gauge length can now be calculated:

$$(2L)_{eff} = 2L\left(\frac{\dot{\varepsilon}_m}{\dot{\varepsilon}_o}\right) \tag{16}$$

Because the effective gauge length accounts for the variation in temperature along the fiber tow, it can be used to calculate strain and strain rate for the fiber tow specimen using the displacement data measured by the LVDT. By utilizing this approach in conjunction with the temperature profiles previously mentioned in section 4.1, as well as creep activation energy of 177 kj/mol for Hi-Nicalon^{TM} S fibers from literature [50], the effective length of the fiber tow specimen was determined at 1100°C in air and in saturated steam. These effective length values are presented in Table 6. Again, it should be noted that for saturated steam, two effective lengths were obtained corresponding to two

temperature profiles. Effective length (a) was used for saturated steam specimens S1-S3, and effective length (b) was used for saturated steam specimens S4-S12.

Table 6 - Effective gauge lengths of Hi-Nicalon^{TM} S fibers at 1100°C

	Air	Saturated Steam
Effective Length (mm)	72.48	(a) 79.61 (b) 81.70

It should be noted that there are different approaches to determining the effective length of fiber tow specimens. Some methods, such as those used by Hammand [51] and Yun et al.[52], make the assumption that the majority of creep deformation occurs solely within the hot zone of the furnace, thereby using only the flattest portion of the temperature profile nearest the target temperature in order to calculate the effective gauge length. This method is subjective however, as it relies on human determination of the flat zone, and is dependent on the overall flatness of the temperature profile as well as on the sharpness of the temperature drop off near the boundaries of the hot zone.

4.3 Creep of Hi-Nicalon™ S Fiber Tows at 1100°C

Before we examine the experimental data obtained in this effort, it is important to reiterate the assumptions made in section 3.1 Theory. We assume that all 500 fibers of the fiber tow are initially intact, have the same cross-sectional area, and are loaded equally. Furthermore, we assume that the cross-sectional area of the fibers remains unchanged despite the oxidation of the fibers which would occur at elevated temperature. While employing these assumptions, we also recognize that any production defects, specimen

preparation damage, and oxidation experienced by the fiber tow could in actuality alter its effective cross-sectional area and consequently increase the creep stress during testing.

Additionally we assume that the steam which is saturated with silicic acid and delivered to the test chamber is contaminant free, although it is likely to have experienced some contamination from the alumina tubing in the test facility. Finally, we note that it is difficult to determine whether the progressive deformation of the fibers during the test is in fact due to creep mechanisms. It is possible that individual fibers or small groups of fibers will fail during the creep test prior to the complete rupture of the fiber tow. Such progressive failures of individual fibers would lead to the transfer of the applied load to the remaining fibers that are intact resulting in a higher stress being experienced by the remaining fibers. In this case the continual deformation of the fiber tow is due to an increase in stress rather than creep.

Tensile creep tests of Hi-Nicalon™ S fiber tows were performed at 1100°C in laboratory air and in silicic acid-saturated steam. Creep run-out was established as 100 hours at creep stress. The results of the creep tests are summarized in Table 7. The rupture time, steady-state creep rate, and creep strain are shown for each creep stress level and test environment.

Table 7 – Summary of tensile creep test results for Hi-Nicalon™ S fiber tows at 1100°C in laboratory air and in silicic acid-saturated steam.

Specimen ID	Test Environment	Creep Stress (MPa)	Creep Lifetime (hrs)	Steady-State Creep Rate (s^{-1})	Creep Strain (%)
A1	Air	3.5	100†	2.18E-10	0.026
A3	Air	353	100†	1.70E-09	0.128
A4	Air	450	100†	4.30E-09	0.208
A7	Air	500	100†	2.36E-09	0.220
A9	Air	600	100†	3.61E-09	0.261
A10	Air	650	2.24	4.08E-08	0.230
S1	Sat. Steam	3.5	100†	2.20E-09	0.114
S4	Sat. Steam	255	38.04	3.92E-09	0.133
S7	Sat. Steam	353	19.89	8.23E-09	0.140
S6	Sat. Steam	400	5.24	1.17E-08	0.100
S12	Sat. Steam	450	13.53	1.67E-08	0.144
S9	Sat. Steam	500	15.39	1.85E-08	0.196
S10	Sat. Steam	600	8.84	2.89E-08	0.214
S11	Sat. Steam	650	6.19	5.62E-08	0.239

† Creep run-out defined as 100 hours at creep stress. Failure of specimen did not occur when the test was terminated.

Creep strain vs. time curves obtained for Hi-Nicalon™ S fiber tows at 1100°C in laboratory air are shown in Figure 20 and Figure 21. Creep run-out (defined as 100 hours at creep stress) was achieved at stress levels of 3.5 MPa, 353 MPa, 450 MPa, 500 MPa, and 600 MPa. By isolating the time interval to the first few hours of the test, as shown in Figure 21, it can be seen that primary and secondary creep regimes were achieved, with the transition from primary to secondary creep occurring within the first hour of each test. Tertiary creep was not observed. While it may appear that the 600 MPa test shows the

beginning of tertiary creep, the increasing strain rate towards the end of this test is likely due to failures of individual fibers preceding the ultimate tow failure.

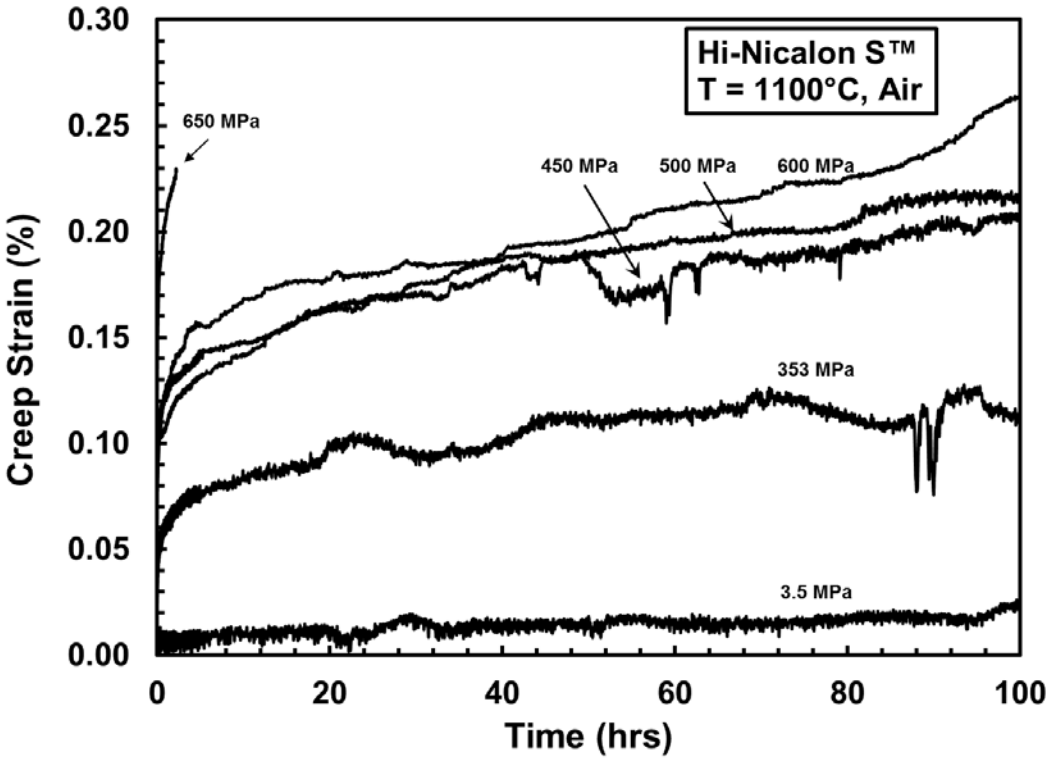

Figure 20 - Creep strain vs time for Hi-Nicalon™ S fiber tows at 1100°C in laboratory air.

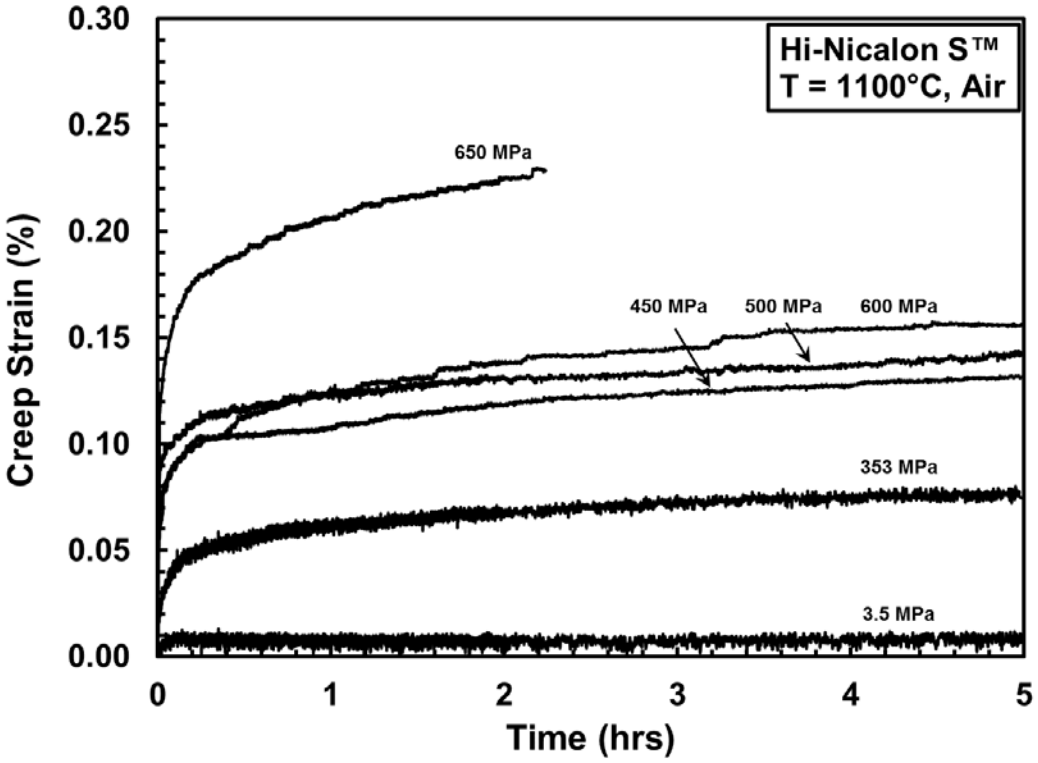

Figure 21 – Creep strain vs time for Hi-Nicalon™ S fiber tows at 1100°C in laboratory air.

Creep strain vs. time curves obtained for Hi-Nicalon™ S fiber tows at 1100°C in silicic acid-saturated steam are shown in Figure 22 and Figure 23. A comparison of the creep strain vs. time curves obtained in silicic acid-saturated steam (Figure 22 and Figure 23) to those produced in laboratory air (Figure 20 and Figure 21) reveals that the presence of saturated steam has a significant negative impact on the creep lifetime of the fiber tow. In saturated steam creep run-out of 100 hours was achieved only at 3.5 MPa. Primary and secondary creep regimes were observed in all tests, with the transition from primary to secondary creep occurring within the first hour of each test.

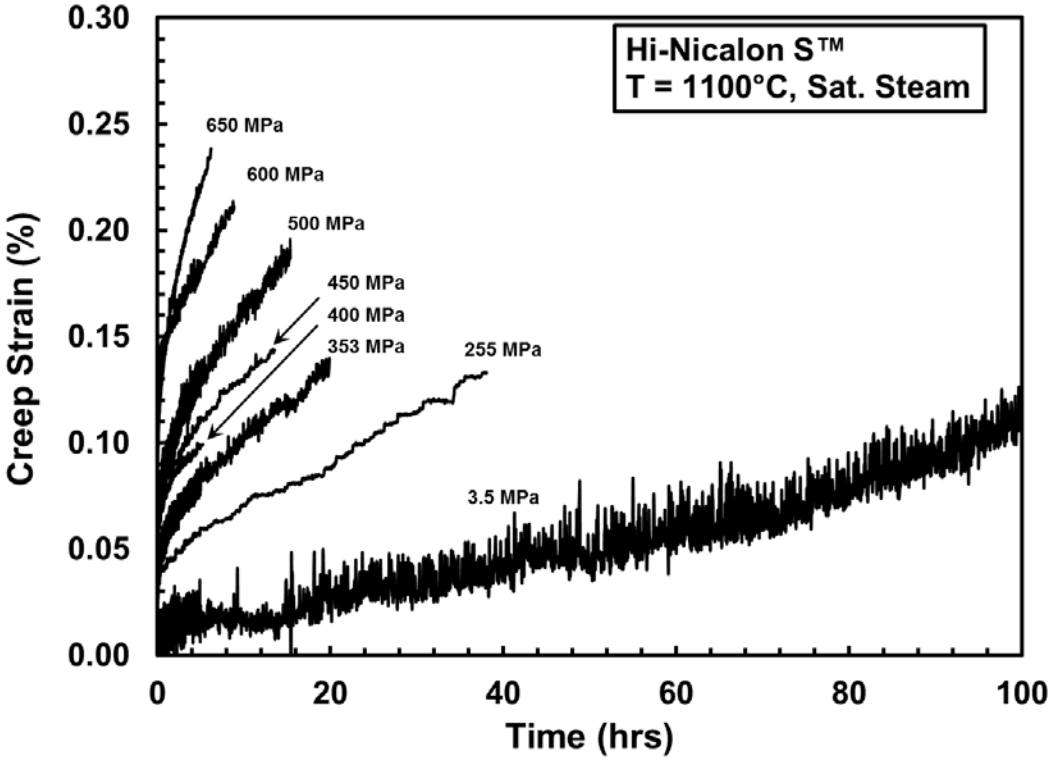

Figure 22 - Creep strain vs. time for Hi-Nicalon™ S fiber tows at 1100°C in silicic acid-saturated steam.

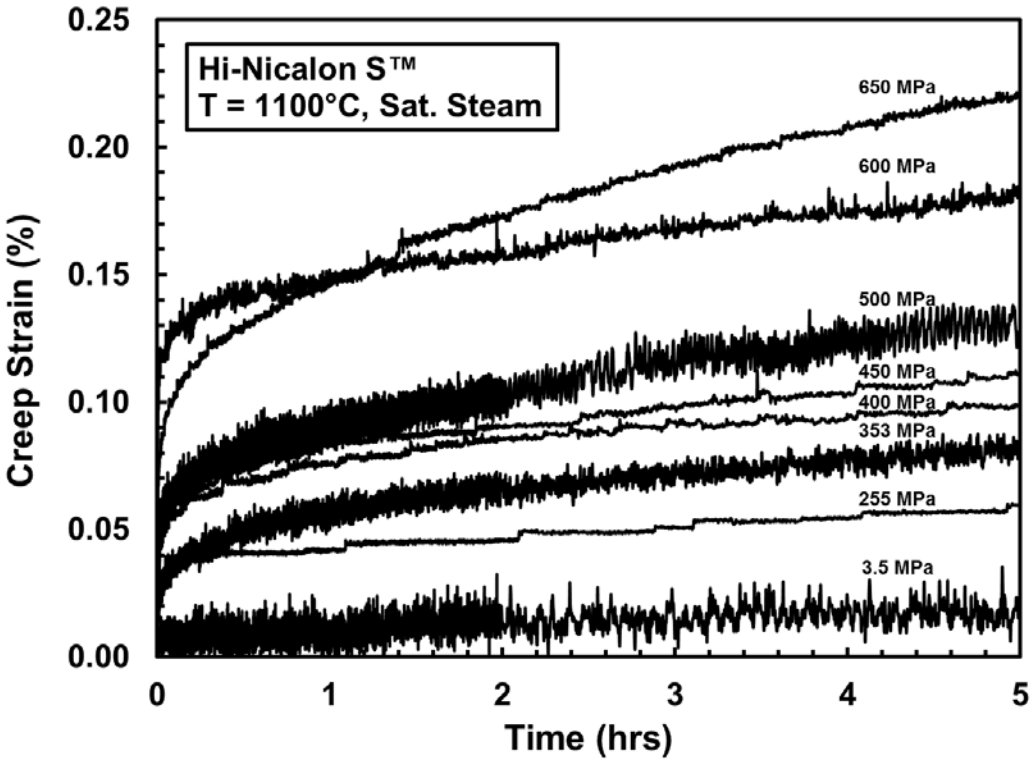

Figure 23 - Creep strain vs. time for Hi-Nicalon™ S fiber tows at 1100°C in silicic acid-saturated steam.

Steady-state creep was observed throughout the majority of each test. The steady-state creep rates as a function of applied stress are presented in Figure 24. The data obtained for Hi-Nicalon™ S fiber tows at 1100°C in air and in silicic acid-saturated steam show an increase in creep rates in the presence of silicic acid-saturated steam. The creep rate data in Figure 24 were fitted with a Norton-Bailey power law equation:

$$\dot{\varepsilon} = A\sigma^n \tag{17}$$

In this equation $\dot{\varepsilon}$ is the minimum creep rate, A is a temperature-dependent coefficient which accounts for the activation energy and other variables, σ is the applied stress, and n is the creep stress exponent. Fitting the data obtained in this effort and the data obtained at 1100°C in laboratory air and steam by Shillig [14] with this power law equation

yielded stress exponents of n ≈ 3.64 for laboratory air, n ≈ 0.99 for steam, and n ≈ 2.64 for saturated steam. Assuming that the fiber tow deformation is due to creep and not due to progressive failure of individual filaments, we can assess the controlling creep mechanisms. A stress exponent of n ≈ 2.64 obtained at 1100°C in saturated steam indicates that the controlling creep mechanism falls between the bounds of grain boundary sliding and interface-reaction controlled creep (for n = 2) and the dislocation glide controlled creep (for n = 3).

Piper [16] found a stress exponent of n ≈ 5.3 at 700°C in saturated steam. Robertson [15] obtained a stress exponent of n ≈ 4.1 at 800°C in saturated steam. Mitchell [17] determined a stress exponent of n ≈ 5.7 at 900°C in saturated steam. Kroeger [18] found a stress exponent of n ≈ 6.9 at 1000°C in saturated steam. Comparing these results to the stress exponent obtained in this work, it appears that the creep mechanism changes as the temperature rises above 1000°C. Sauder and Lamon [53] tested Hi-Nicalon™ S fibers at temperatures ranging from 1300°C to 1500°C in vacuum ($\sim 10^{-4} Pa$) and reported stress exponents ranging from 2.4 to 2.9.

It should be noted that if the deformation accumulated by the fiber tow is due to progressive failure of individual fibers and not creep, these stress exponents would not represent creep mechanisms. For these reasons, it is recommended that future efforts focus on assessing the extent (if not the actual number) of failures of individual fibers occurring during the creep test, but prior to the ultimate failure of the fiber tow.

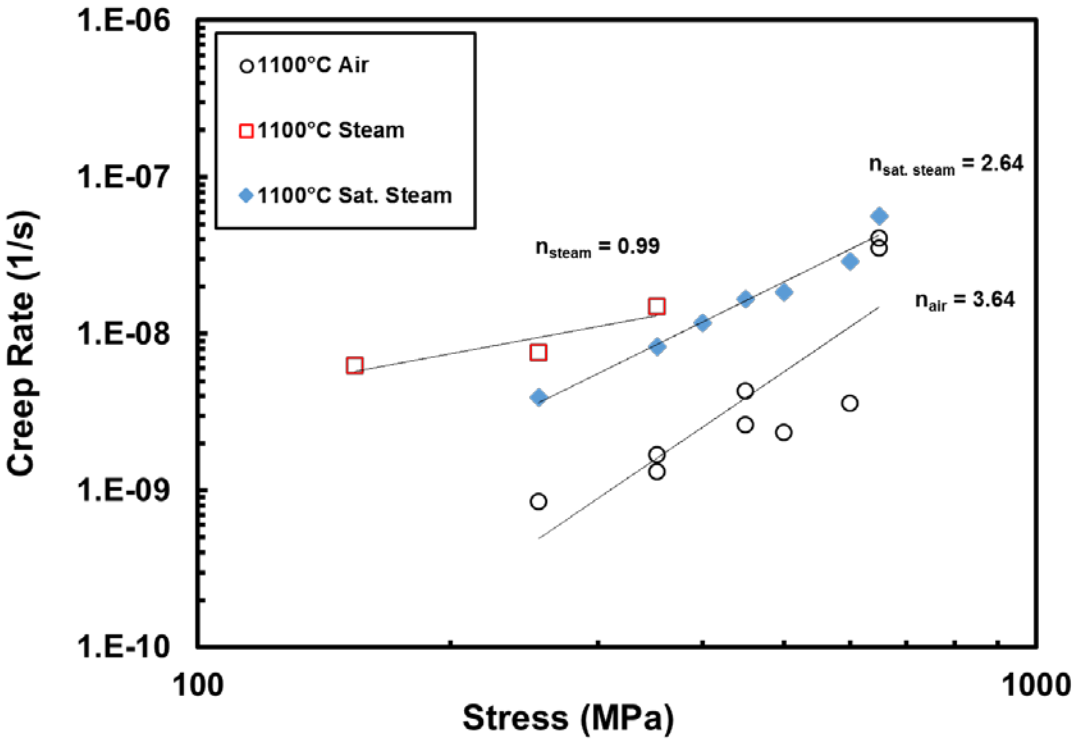

Figure 24 - Steady-state creep rate vs. applied stress for Hi-Nicalon™ S fiber tows at 1100°C in laboratory air, steam, and silicic-acid saturated steam. Results from Shillig [14] ***in air and steam are included for comparison.***

The creep lifetime as a function of creep stress is displayed in Figure 25, where the results obtained at 1100°C in laboratory air and in steam by Steffens [2] and Shillig [14] are included for comparison. The creep lifetime decreases with increasing applied stress in all tests. This trend is more noticeable for fiber tows tested in saturated steam and steam. Although only a small amount of steam data is available for comparison, it appears that steam is the most damaging environment. For a given creep stress, the shortest creep lifetimes are produced in steam. The majority of fiber tow specimens tested in laboratory air in this work had the longest lifetimes for a given creep stress, with all but the 650 MPa test achieving creep run-out of 100 hours. Previous efforts by Steffens [2]and Shillig [14]

showed decreased lifetimes at 467 MPa and 450 MPa at 1100°C in laboratory air compared to that achieved at 450 MPa in laboratory air in this effort.

Fiber tow specimens tested in saturated steam were still capable of achieving creep stress levels similar to those used in laboratory air tests. Nevertheless, the presence of saturated steam significantly reduced the creep lifetime of each fiber tow. Long creep lifetimes were produced at lower creep stresses and short lifetimes, at higher creep stresses. However, transition from long lifetimes at low creep stresses to very short lifetimes at high creep stresses was not as abrupt as transitions observed at 700°C by Piper [16], 800°C by Robertson[15], 900°C by Mitchell [17], and 1000°C by Kroeger [18].

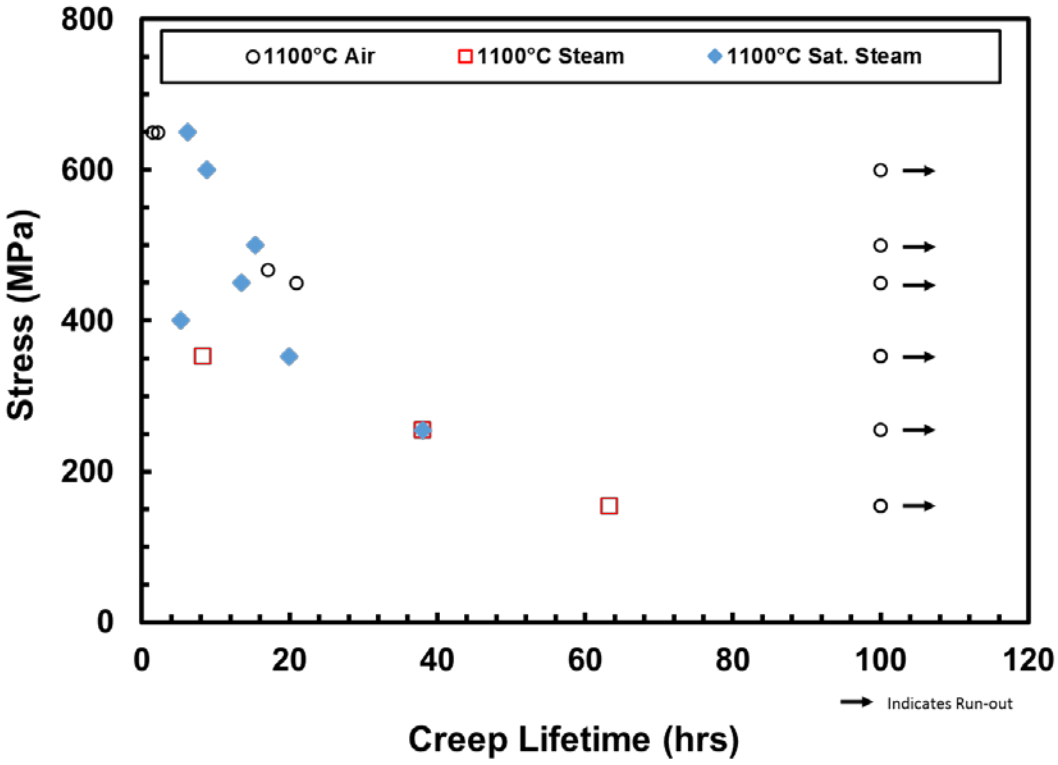

Figure 25 - Creep stress vs. time of rupture for Hi-Nicalon™ S fiber tows at 1100°C in air, steam, and saturated steam. Data at 1100°C in air and steam from Steffens [2] ***and Shillig*** [14] ***are included for comparison. Arrow indicates that specimen failure did not occur when the test was completed.***

Remarkably the creep lifetime of the specimen tested at 650 MPa in saturated steam was almost three times that achieved at 650 MPa in laboratory air. The longer creep lifetime in saturated steam could be due to the increased growth of the protective oxide scale. We also note that the first two attempts to perform a 650 MPa creep test in air were unsuccessful, the test specimens failed upon loading. The creep lifetime at 650 MPa in air presented in Figure 25 was obtained during the third attempt.

It is important to understand the effects that different temperatures and environments have on the creep performance of the fiber tow. The creep strain rate vs. applied stress results obtained at different temperatures are presented in Figure 26-Figure *28*. Results at 800°C are from Shillig [14] and Robertson [15], while results at 900°C and 1000°C are from Mitchell [17] and Kroeger [18] respectively. In laboratory air (Figure 26), in steam (Figure 27) and in saturated steam (Figure 28) – the creep rates increase with temperature. The results in Figure 26-Figure 28 also reveal that increasing temperature had a negative impact on the level of stress which the fibers could endure in all three environments.

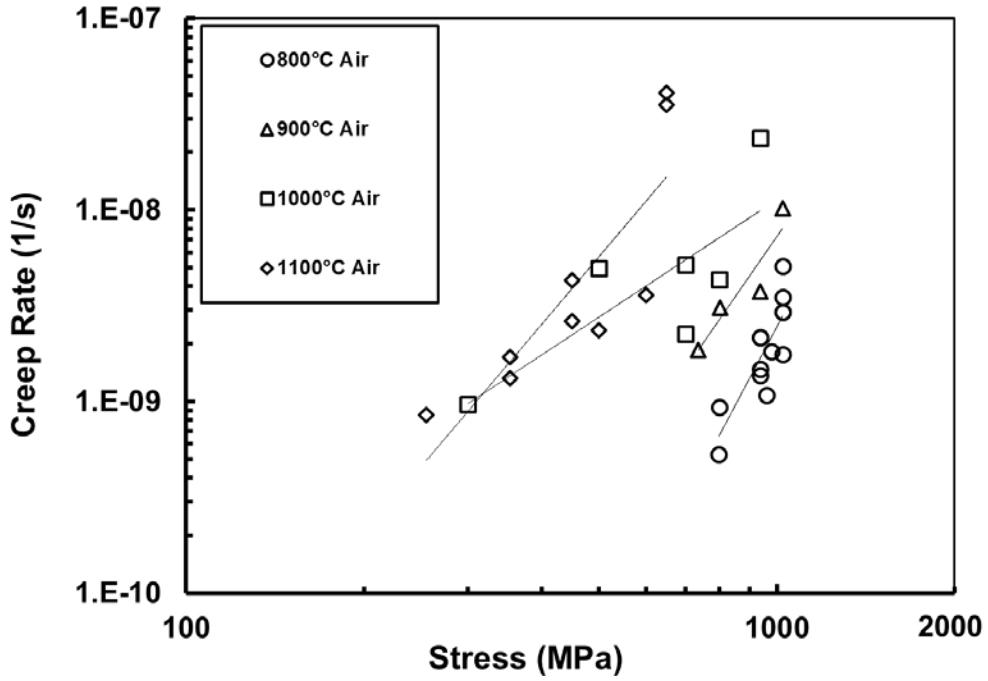

Figure 26 - Steady-state creep rate vs. applied stress for Hi-Nicalon™ S fiber tows at 800°C, 900°C, 1000°C, and 1100°C in laboratory air. Results from Shillig [14]*, Robertson* [15]*, Mitchell* [17]*, and Kroeger* [18] *are included for comparison.*

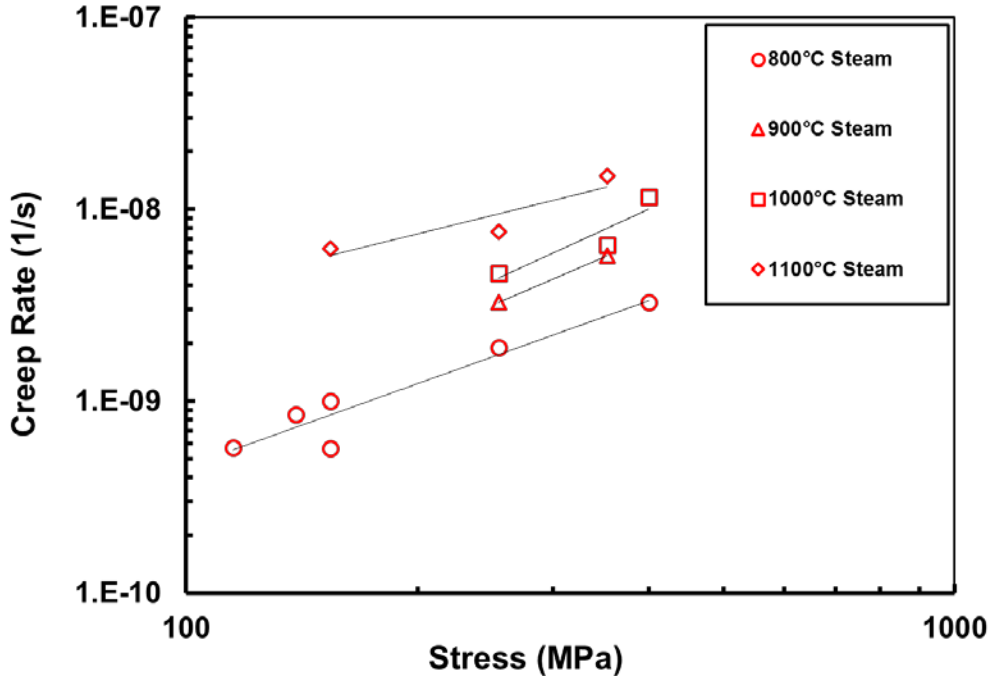

Figure 27 - Steady-state creep rate vs. applied stress for Hi-Nicalon™ S fiber tows at 800°C, 900°C, 1000°C, and 1100°C in steam, as obtained by Shillig [14]*.*

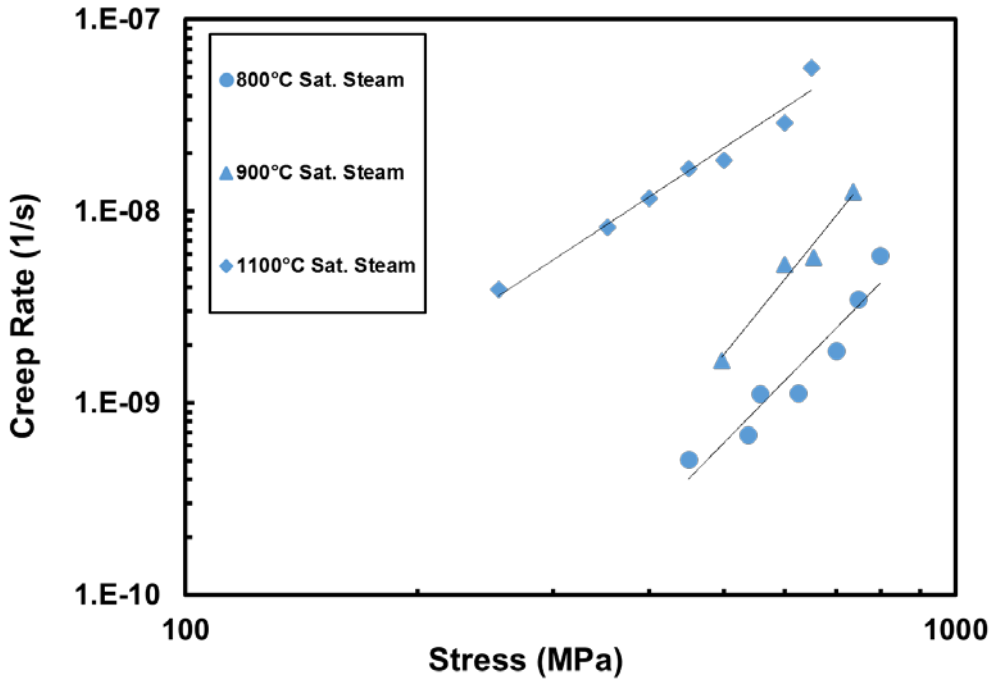

Figure 28 - Steady-state creep rate vs. applied stress for Hi-Nicalon™ S fiber tows at 800°C, 900°C, and 1100°C in saturated steam. Results from Robertson [15] ***and Mitchell*** [17] ***are included for comparison.***

The effect of temperature on creep lifetime in laboratory air is shown in Figure 29. In laboratory air, creep lifetimes decrease with increasing temperature. The longest creep lifetimes were obtained at lower temperatures, while the shortest creep lifetimes were obtained at higher temperatures.

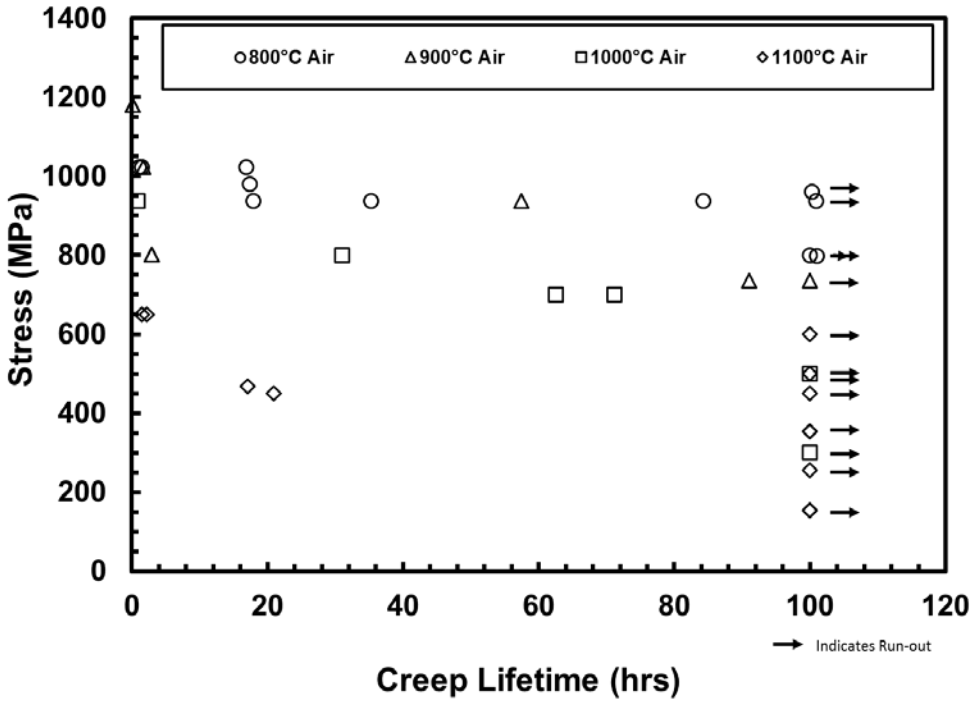

Figure 29 - Creep stress vs. time to rupture for Hi-Nicalon™ S fiber tows at 800°C, 900°C, 1000°C, and 1100°C in laboratory air. Results from Shillig [14]***, Robertson*** [15]***, Mitchell*** [17]***, and Kroeger*** [18] ***are included for comparison. Arrow indicates that specimen failure did not occur when the test was completed.***

The data presented in Figure 30-Figure 35 demonstrate the effects of different environments on creep of the fiber tows at 800-1100°C. Results of prior work [14], [15], [17], [18] are included in Figure 30 - Figure 35 for comparison. The effects of unsaturated steam are seen in Figure 30 and Figure 31. Figure 30 shows the steady-state creep rate vs. applied stress at 800-1100°C in air and in steam. It is seen that for a given creep stress, higher creep rates are produced in steam than in laboratory air. Moreover, it is evident that steam has a negative effect on the level of creep stress that could be sustained by the fiber tow. These trends are even more apparent in Figure 31, which shows the creep stress vs. time to rupture at 800-1100°C in air and in steam. The creep rupture data in Figure 31 show

that at all temperatures studied, the longest creep lifetimes and highest applied stresses were obtained in air, while the shortest lifetimes and the lowest applied stresses were obtained in steam.

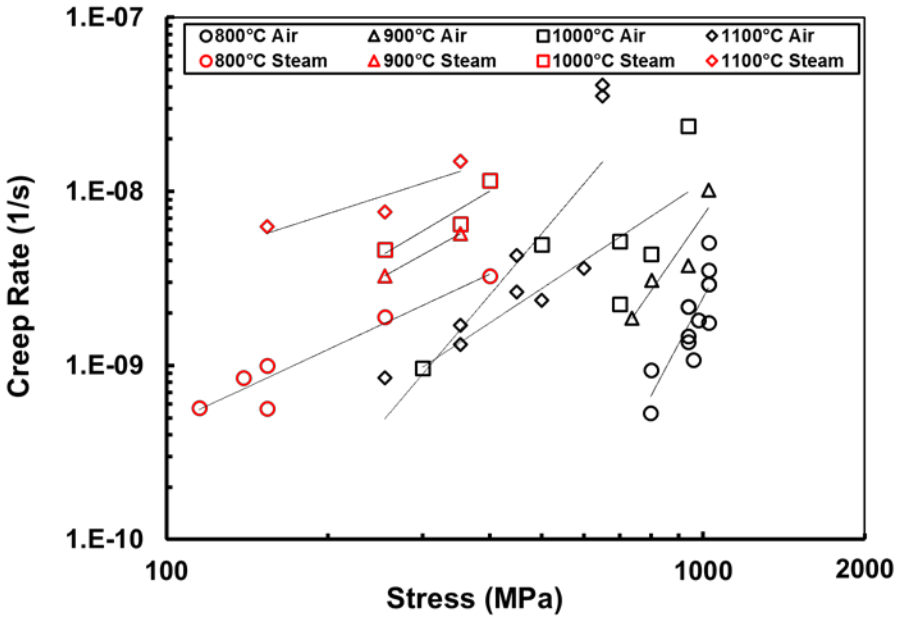

Figure 30 - Steady-state creep rate vs. applied stress for Hi-Nicalon™ S fiber tows at 800°C, 900°C, 1000°C, and 1100°C in laboratory air and steam. Results from Shillig [14]***, Robertson*** [15]***, Mitchell*** [17]***, and Kroeger*** [18] ***are included for comparison.***

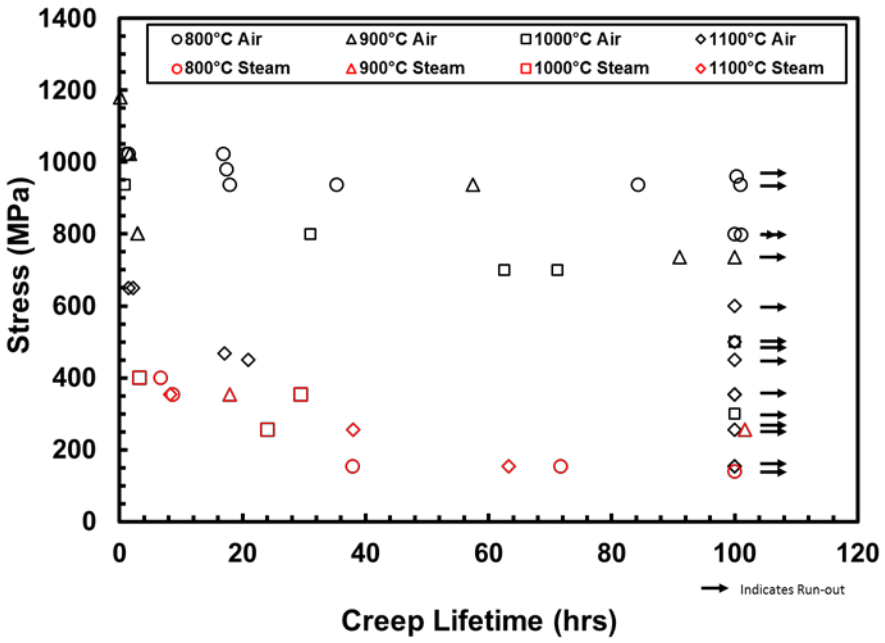

Figure 31 - Creep stress vs. time to rupture for Hi-Nicalon™ S fiber tows at 800°C, 900°C, 1000°C, and 1100°C in laboratory air and steam. Results from Shillig [14]***, Robertson*** [15]***, Mitchell*** [17]***, and Kroeger*** [18] ***are included for comparison. Arrow indicates that specimen failure did not occur when the test was completed.***

The effects of saturated steam on creep of fiber tows at 800 - 1100°C are shown in Figure 32 and Figure 33. Figure 32 shows that for a given creep stress, higher creep rates are produced in saturated steam than in laboratory air. It is also evident that saturated steam had a negative impact on the level of creep stress that can be applied to the fiber tow.

The creep stress vs. time to rupture results obtained at 800 - 1100°C in air and in saturated steam are presented in Figure 33. Once again we note that the longest lifetimes and the highest applied stresses were obtained in air, while shorter lifetimes and smaller applied stresses were obtained in saturated steam. However, the reductions in creep lifetime and in applied stress caused by saturated steam are not as severe as those found caused by unsaturated steam.

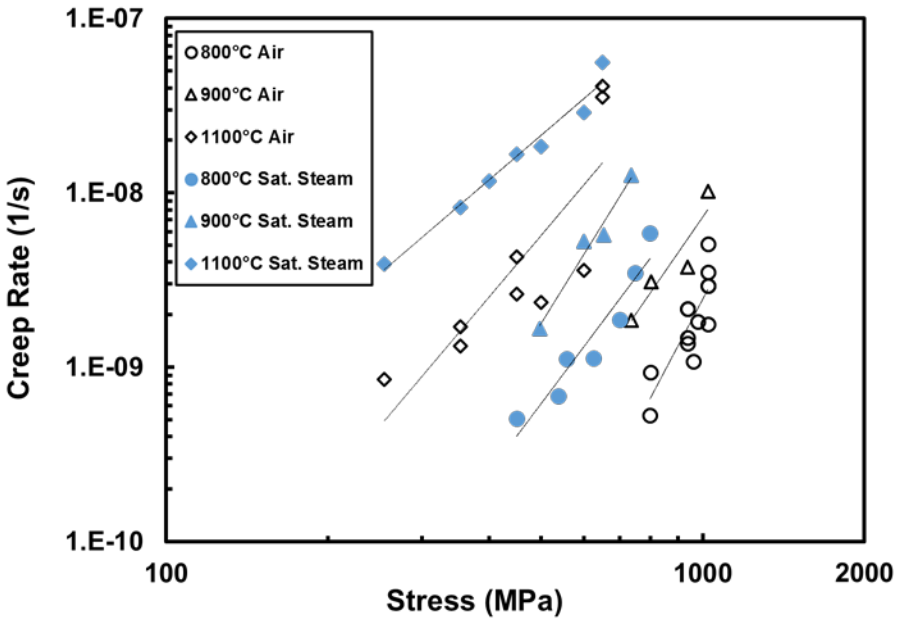

Figure 32 – Steady-state creep rate vs. applied stress for Hi-Nicalon™ S fiber tows at 800°C, 900°C, and 1100°C in laboratory air and saturated steam. Results from Shillig [14]*, Robertson* [15]*, and Mitchell* [17] *are included for comparison.*

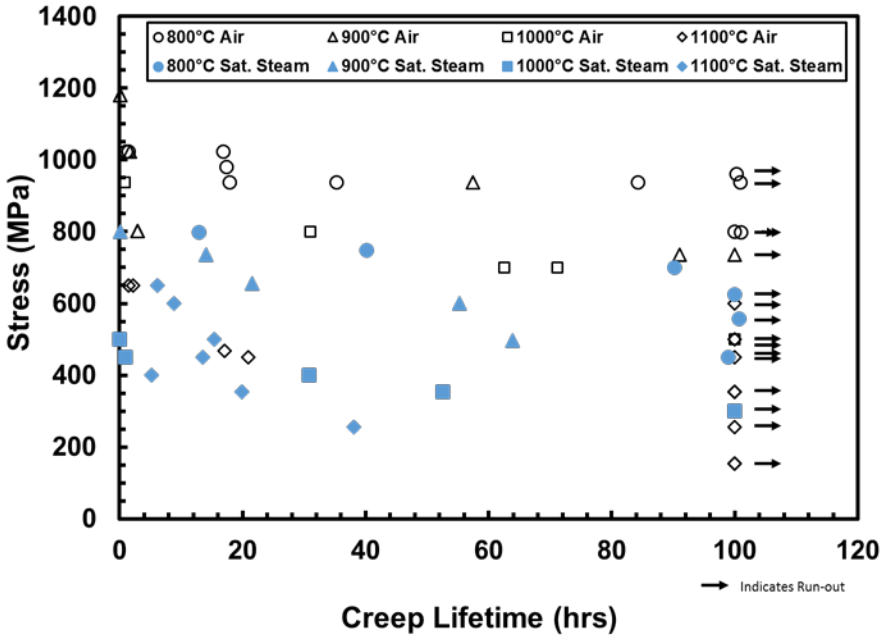

Figure 33 - Creep stress vs. time to rupture for Hi-Nicalon™ S fiber tows at 800°C, 900°C, 1000°C, and 1100°C in laboratory air and saturated steam. Results from Shillig [14]*, Robertson* [15]*, Mitchell* [17]*, and Kroeger* [18] *are included for comparison. Arrow indicates that specimen failure did not occur when the test was completed.*

Creep strain rate vs. applied stress results obtained in laboratory air, steam, and saturated steam at 800 - 1100°C are presented in Figure 34. It is evident that, for a given creep stress the highest steady-state creep rates were produced in steam, followed by those produced in saturated steam. The lowest steady-state creep rates were produced in laboratory air. The creep rates obtained in saturated steam are approximately one order of magnitude higher than those produced in laboratory air. At temperatures below 800 and 900°C, creep rates produced in saturated steam are approximately one order of magnitude lower than the creep rates produced in unsaturated steam. However, as the temperature rises above 1000°C, the difference between the creep-rates obtained in unsaturated steam and those obtained in saturated steam becomes less severe. At 1100°C the creep rates produced in saturated steam are approximately five times lower than those obtained in unsaturated steam. Still only a limited amount of creep data has been obtained in unsaturated steam at and above 1100°C. Additional tests should be performed at temperatures $\geq$ 1100°C in steam and in saturated steam to further evaluate the effects of temperature and environment on creep of Hi-Nicalon™ S fiber tow.

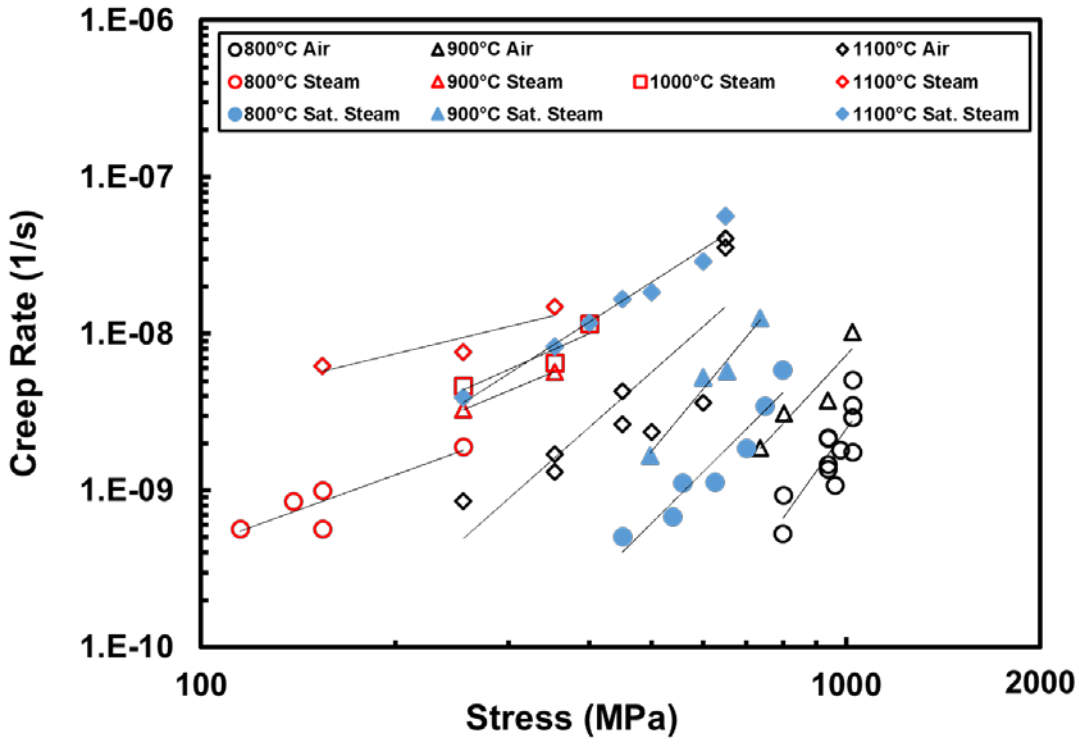

Figure 34 - Steady-state creep rate vs. applied stress for Hi-Nicalon™ S fiber tows at 800°C, 900°C, 1000°C, and 1100°C in laboratory air, steam, and saturated steam. Results from Shillig [14]***, Robertson*** [15]***, and Mitchell*** [17] ***are included for comparison.***

Creep-rupture results obtained in laboratory air, steam, and saturated steam at 800 - 1100°C are presented in Figure 35. Recall that creep run-out is defined at 100 hours at creep stress. It is evident that at all temperatures investigated, creep lifetimes were reduced due to saturated steam and further reduced due to steam. The longest creep lifetimes as well as the highest applied stresses were obtained in laboratory air, followed by those obtained in saturated steam. The shortest creep lifetimes and the lowest applied stresses were observed in steam.

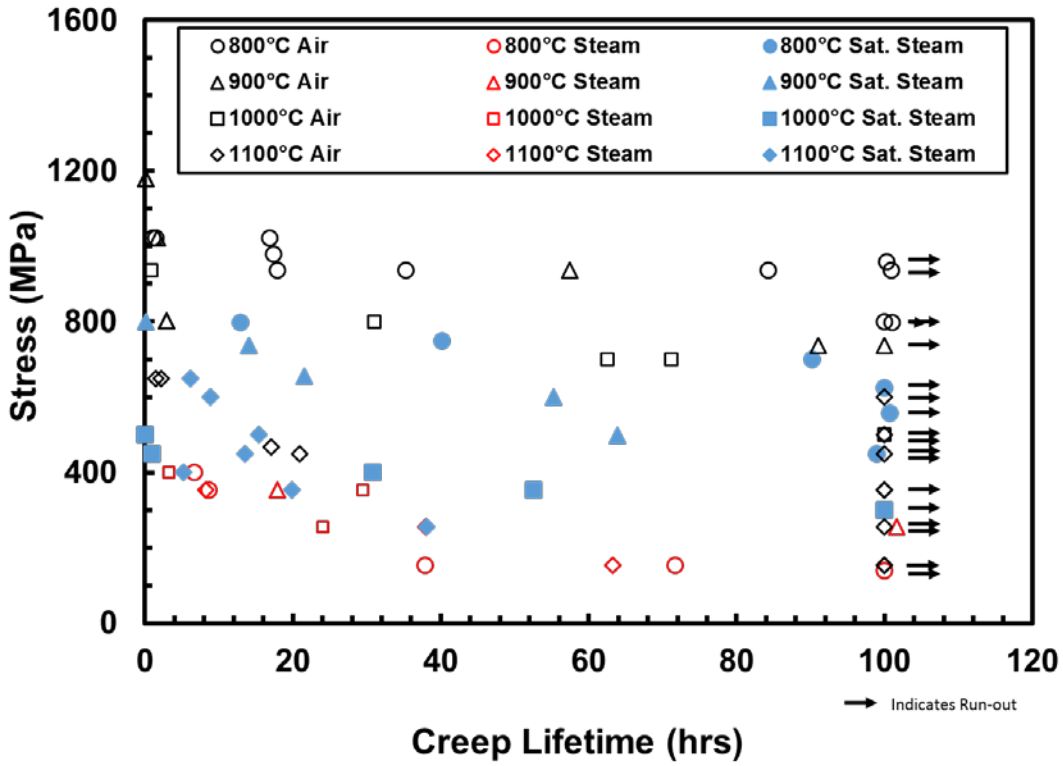

Figure 35 - Creep Stress vs. time to rupture for Hi-Nicalon™ S fiber tows at 800°C, 900°C, 1000°C, and 1100°C in laboratory air, steam, and saturated steam. Results from Shillig [14]***, Robertson*** [15]***, Mitchell*** [17]***, and Kroeger*** [18] ***are included for comparison. Arrow indicates that specimen failure did not occur when the test was completed.***

The results in Figure 34 and Figure 35 indicate that unsaturated steam causes greater degradation of the creep resistance of Hi-Nicalon™ S fiber tows than saturated steam. As mentioned in section 3.4, a silicic acid-saturated steam environment provides a more realistic representation of the conditions experienced by SiC fibers within a SiC/SiC composite operating in combustion environment. Thus the improved creep performance in saturated steam is an encouraging result that bodes well for use of SiC/SiC composites reinforced with Hi-Nicalon™ S fibers in applications.

4.4 Post-Test Microstructural Analysis of Hi-Nicalon™ S Fiber Tows

The post-test microstructures of the Hi-Nicalon™ S fiber tow specimens were characterized using optical microscopy and scanning electron microscopy (SEM). The purpose of the microstructural investigation is to assess the damage and failure mechanisms operating in fiber tow specimens. The optical and scanning electron microscopes that were used in this work are shown in Figure 36 and Figure 40, respectively.

4.4.1 Optical Microscopy

The optical microscope shown in Figure 36 was used to examine the surface of two specimens tested in air and of one specimen tested in saturated steam. In the case of the specimens tested in air, we examined the center portion of the specimen gage section (i.e. the portion located in the center of the hot zone). In the case of the specimen tested in saturated steam, we examined the portion of the fiber located below the fracture surface. Additional details pertaining to the specimens examined with the optical microscope are given in Table 8.

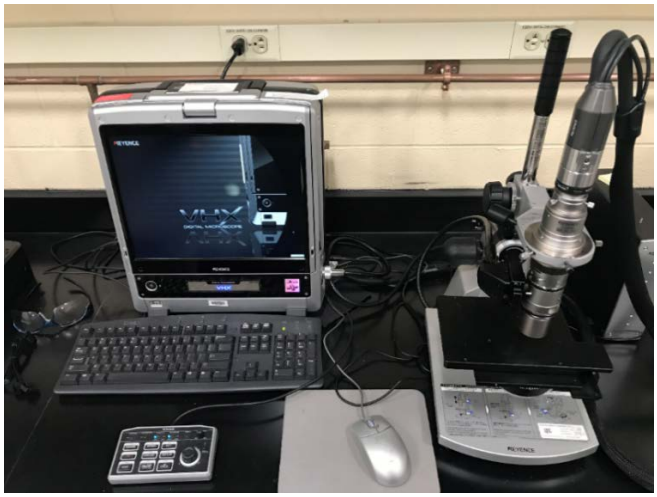

Figure 36 - Keyence VHX Digital microscope in the Air Force Research Laboratory (AFRL) Materials and Manufacturing Directorate.

Table 8 - Hi-Nicalon™ S fiber tow specimens used for analysis with optical microscope.

Specimen ID	Test Environment	Creep Stress (MPa)	Creep Lifetime (hrs)	Sample Location within Fiber Tow
A3	Air	353	100†	Center part of the gage section
A9	Air	600	100†	Center part of the gage section
S12	Sat. Steam	450	13.53	Portion below Fracture Surface

† Creep run-out defined as 100 hours at creep stress. Failure of specimen did not occur when the test was terminated.

This examination was accomplished by placing the specimens under the optical microscope, which utilizes light shining from beneath the specimen as the lenses capture the images, providing reflected light to the lenses rather than transmitted light. As the light reflects off of the fiber tow specimen, if a sufficient amount of oxide layer has developed on the surface then we will see different colored bands of light. These bands are called interference fringes, which are the result of constructive and destructive interference of light as it travels, reflects off a given surface (the fibers), and recombines to highlight a particular color or wavelength of light. Thus, differences in color indicate differences in oxide layer thickness. For SiC, the thickness of the oxide layer must be approximately 60 nm before interference fringes begin to appear [15].

Optical images of the three Hi-Nicalon™ S fiber tow specimens are shown in Figure 37 - Figure 39. The center portions of the gage section two fiber tow specimens

tested in laboratory air shown in Figure 37 and Figure 38. These specimens achieved creep run-out of 100 hours at different levels of creep stress. Note the differences in color of the fibers, suggesting differences in oxide layer thickness.

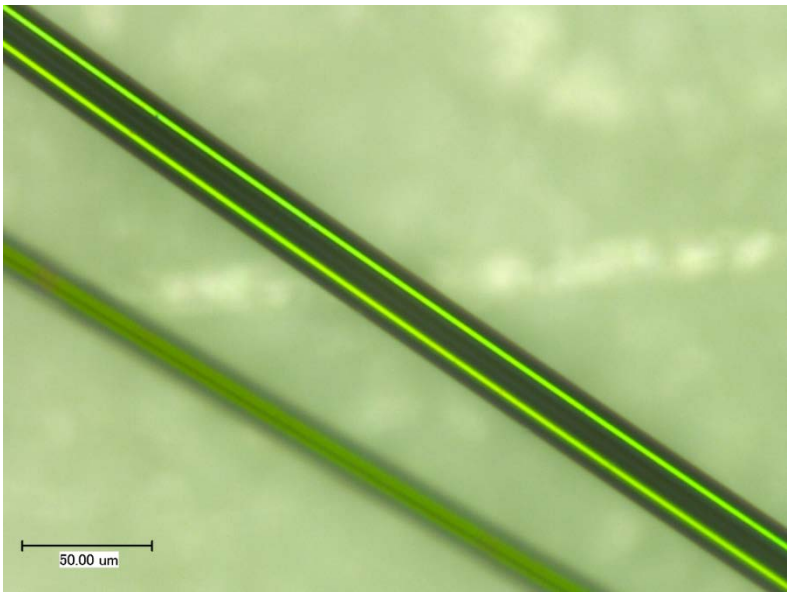

Figure 37 - Optical image of Hi-Nicalon™ S fiber tow specimen "Air 3" at 1000x magnification, examining the center part of the gage section of two fibers subjected to creep in laboratory air.

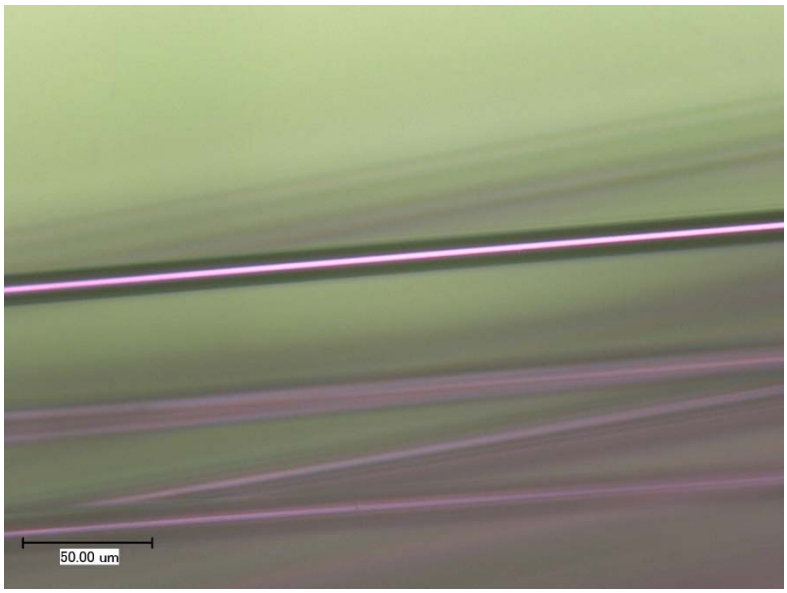

Figure 38 - Optical image of Hi-Nicalon™ S fiber tow specimen "Air 9" at 1000x magnification, examining the center part of the gage section of a fiber subjected to creep in laboratory air.

A fiber from a specimen tested in saturated steam is shown in Figure 39. In this case we examined the section of the fiber located below the fracture surface. Recall that this specimen ruptured after 13.53 hours at 450 MPa in silicic acid-saturated steam. The circular “rainbow” patches seen on the fiber surface suggest that the oxide layer in these regions has begun to crystallize.

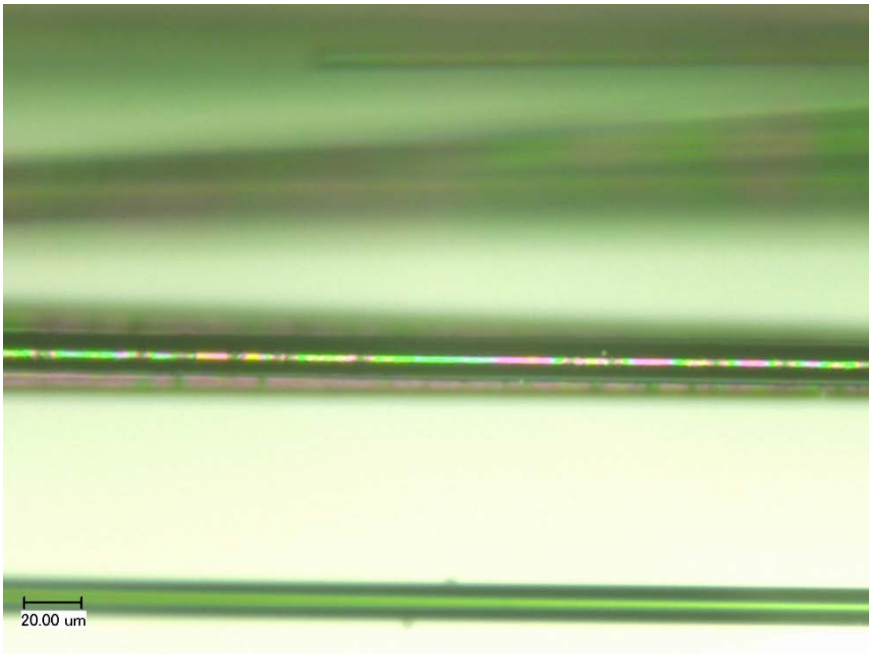

Figure 39 - Optical image of Hi-Nicalon™ S fiber tow specimen "Steam 12" subjected to creep in silicic acid-saturated steam (1000x magnification), examining the section of the fiber located below the fracture surface. The circular “rainbow” patches on the surface of the fiber suggest that the oxide layer has begun to crystallize.

4.4.2 Scanning Electron Microscopy (SEM)

The SEM used to characterize the post-test microstructure of the Hi-Nicalon™ S fiber tow specimens is shown in Figure 40. Ten samples were taken from 4 fiber tows tested in laboratory air, and ten samples were taken from 4 fiber tows tested in saturated steam. The specimens were prepared for examination with an SEM using standard

methods. A detailed description of the SEM sample preparation is given elsewhere [15], [16], [43]. The method for preparing SEM samples is briefly described here.

Figure 40 - Quanta 650 scanning electron microscope (SEM) in the Air Force Research Laboratory (AFRL) Materials and Manufacturing Directorate.

The fiber tows tested in creep were prepared for the SEM examination by securing the fibers onto an aluminum puck with a 45° mounting surface. Prior to mounting the fibers, double-sided carbon tape was applied to the 45° surface of the mounting puck. The fibers were then secured by pressing them against the tape such that the fibers being analyzed protruded 1-5mm above the angled surface. The fibers were then coated with 10 nm of Iridium using an EMS 150T ES coating machine shown in Figure 41 to provide electric conductivity between the fibers and the aluminum puck. Once coated, the fiber specimens were ready to be analyzed in the SEM.

Figure 41 - EMS 150T ES coating machine in the Air Force Research Laboratory (AFRL) Materials and Manufacturing Directorate.

Multiple samples were taken from each fiber tow for SEM examination in order to assess the oxidation modes occurring along the length of the fiber tow specimen. For the fiber tow specimens that had achieved creep run-out of 100 hours, three different sections within the gage section of the fiber tow specimen were examined with the SEM: near the center, near the bottom of the hot zone and near the top of the hot zone. For the fiber tow specimens that failed during creep test, two samples were examined: one located above and another located below the fracture surface. A summary of the specimens prepared for SEM examination is presented in Table 9. All SEM micrographs that were produced in this work are included in Appendix A. Representative SEM Images as well as in the remainder of this section.

Table 9 - Hi-Nicalon™ S fiber tow specimens analyzed using scanning electron microscopy (SEM).

Specimen ID	Test Environment	Stress (MPa)	Creep Lifetime (hrs)	Optical Sample Location within Fiber Tow
A1	Air	3.5	100†	Upper Section
				Center Section
				Lower Section
A3	Air	353	100†	Upper Section
				Center Section
				Lower Section
A9	Air	600	100†	Upper Section
				Center Section
				Lower Section
A10	Air	650	2.24	Above Fracture Surface
				Below Fracture Surface
S1	Sat. Steam	3.5	100†	Upper Section
				Center Section
				Lower Section
S4	Sat. Steam	255	38.04	Above Fracture Surface
				Below Fracture Surface
S12	Sat. Steam	450	13.53	Above Fracture Surface
				Below Fracture Surface
S11	Sat. Steam	650	6.19	Above Fracture Surface
				Below Fracture Surface

† Creep run-out defined as 100 hours at creep stress. Failure of specimen did not occur when the test was terminated.

When Steffens [2] and Shillig [14] tested Hi-Nicalon™ S fiber tows at elevated temperature in steam, they found that steam was chemically altered as it traveled along the SiC fiber tow specimen, extracting silicon from the fiber tow to become saturated with silicic acid ($Si(OH)_4$). As a result, scale thickness and composition varied along the length of the fiber tows indicating a change in oxidation mechanisms. These observations prompted a re-design of the fiber tow test facility to include testing in silicic acid-saturated

steam. Subsequently Piper [16] and Robertson [15] tested Hi-Nicalon™ S fiber tows in silicic acid-saturated steam at 700°C and 800°C respectively. The fiber tows were reported to have a more uniform appearance, with passive oxidation being observed along the length of the fiber tow specimens. The growth of silica scale on the fiber surface produced at 700°C and 800°C was not discernible under the SEM. However, growth of silica scale became increasingly more evident in fiber tows tested in saturated steam at 900°C by Mitchell [17] and 1000°C by Kroeger [18].

This silica scale growth became more apparent at 1100°C in saturated steam; the oxidation rings appear to be more pronounced (Figure 42). Due to the close proximity of the fibers within the fiber tow specimen, the silica scale would occasionally grow and weld multiple fibers together, as evidenced in Figure 43. Smooth fiber surfaces were produced in both air and saturated steam, indicating that passive oxidation had occurred. It was also observed that silica scale had developed on fiber tow specimens that achieved creep run-out of 100 hours at creep stress when tested at 1100°C in laboratory air, although it was not as pronounced as the scale on fibers tested in saturated steam (see Figure 44).

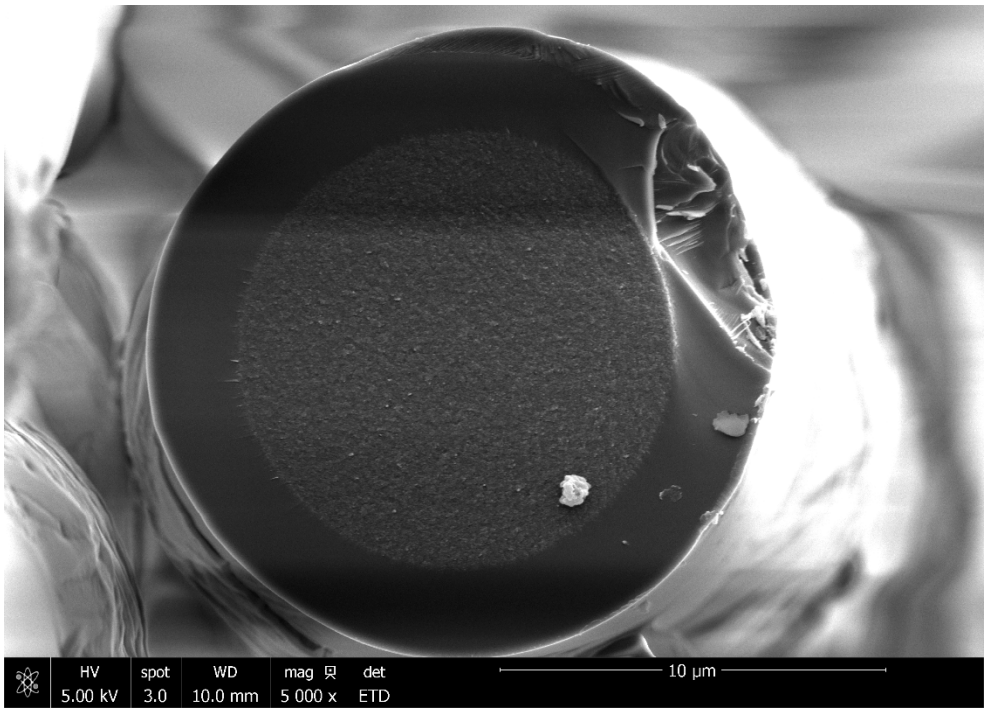

Figure 42 - SEM micrograph of the Hi-Nicalon™ S fiber tow specimen "Steam 4" subjected to 255 MPa at 1100°C in silicic acid-saturated steam for 38.04 hrs. Oxide scale is visible.

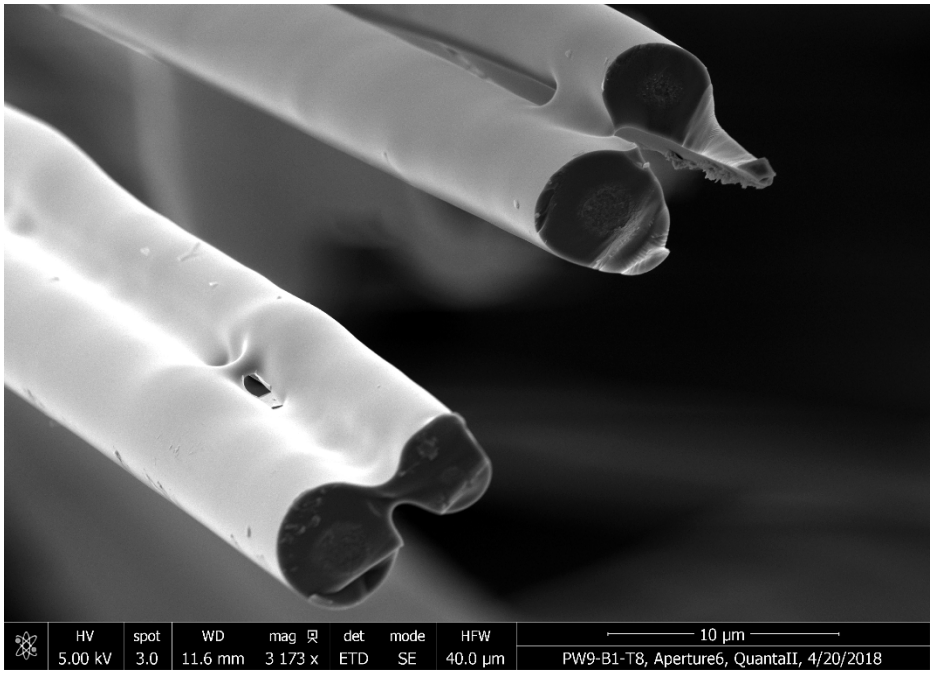

Figure 43 - SEM micrograph of the Hi-Nicalon™ S fiber tow specimen "Steam 1" subjected to 3.5 MPa at 1100°C in silicic acid-saturated steam achieving creep run-out of 100 hours at creep stress. Note regions along the length of the fibers welded together with oxide scale.

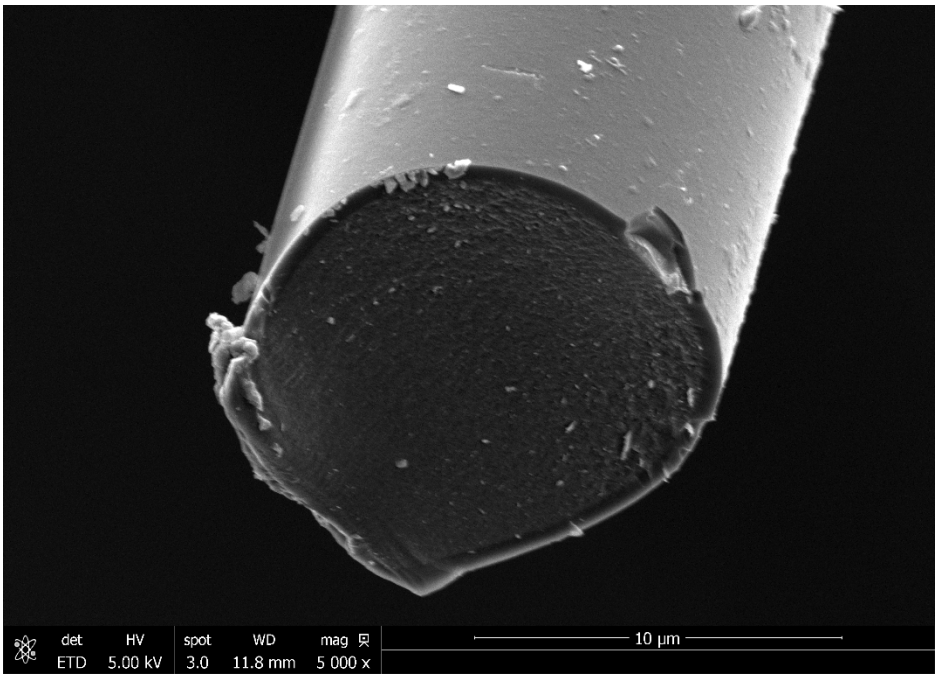

Figure 44 - SEM micrograph of the Hi-Nicalon™ S fiber tow specimen "Air 3" subjected to 353 MPa at 1100°C in laboratory air achieving creep run-out of 100 hours at creep stress. Oxide scale is visible

The thickness of the oxide (SiO_2) scale can be predicted using a modified Deal-Grove model, previously shown in Equation (3). Recalling the solution presented in Equation (6), which could be found provided the initial oxide scale thickness (x_i) is known, this formulation may be simplified further after long periods of time, yielding Equation (18).

$$x^2 = Bt \tag{18}$$

$$B = B_0 \exp\left(-\frac{Q_b}{RT}\right) \tag{19}$$

In this simplified equation, B_0 is a constant and Q_b is the activation energy. For dry air, B_0 is 1.1×10^{-8} m^2/s and Q_b is 245 kJ/mol [54], while for steam, B_0 is 6×10^{-14} m^2/s and Q_b is 80 kJ/mol [38]. By incorporating these parameters within the modified Deal-Grove

model as well as the lifetimes of each test completed in laboratory air and in saturated steam, predictions of the oxide scale thickness could be made. These predictions are presented in Table 10.

Table 10 – Predictions of the oxide scale thickness for creep tests in air and in saturated steam obtained using Deal-Grove kinetics.

	Scale Thickness (μm)	
Time (hrs)	**Dry Air**	**Sat. Steam**
2.24	0.21	-
6.19	-	1.10
13.53	-	1.63
38.04	-	2.73
100.00	1.38	4.42

Predictions of the Deal-Grove model were compared with the scale thickness measurements obtained from the SEM micrographs. The SEM micrograph of the fracture surface of a fiber tested in saturated steam for 38.04 hours shows a scale thickness of approximately 2.42 μm (Figure 42), while the Deal-Grove model predicted a scale thickness of 2.73 μm. A fiber tow specimen tested in laboratory air that achieved creep run-out of 100 hours produced a scale thickness of approximately 0.5 μm (Figure 44), but in this case the model predicts a scale thickness of 1.38 μm. The Deal-Grove model appears to represent the results obtained for fiber tows tested in saturated steam with greater accuracy than the results obtained for fibers tested in laboratory air. Nevertheless, the discrepancies between experimental and predicted oxide scale values may be the result of several circumstances.

First it should be noted that there are numerous oxidation kinetics models besides the Deal-Grove model that was used in this work. Furthermore, different models produce different predictions of scale growth. Some models over predict the scale growth while others under predict it. Each model behaves differently depending on various conditions such as the activation energy, environment, and the presence of amorphous and crystalline scale [54]. Second, the oxidation of SiC to SiO_2 is affected by the presence of contaminants. Given the use of alumina tubing to transport the steam and the alumina susceptor housing the fiber tow specimen in this work, the saturated steam may be contaminated with aluminum particles, thus decreasing the oxidation of the fibers.

A few fiber tow specimens that were analyzed via SEM showed dark areas running along the length of the fiber surface, sometimes faint and barely visible as shown in Figure 45. These regions are likely a result of contact between fibers during testing. Similar observations were previously reported by Piper [16], Robertson [15], Mitchell [17], and Kroeger [18]. Energy-dispersive X-ray spectroscopy (EDS) data was collected from these light and dark regions by Piper [16]. He found that the darker regions had lower oxygen content than the lighter regions, suggesting that contact between the fibers was limiting the exposure of the fiber surfaces to oxidation.

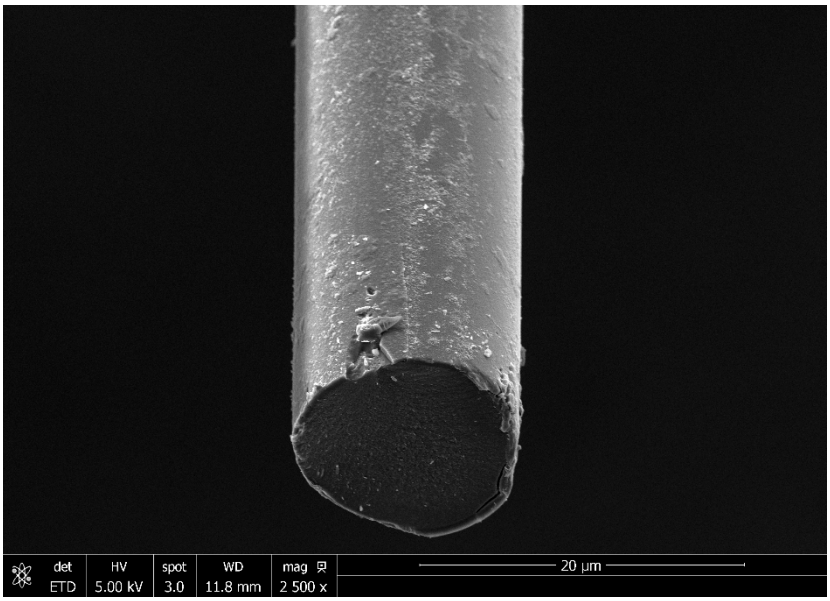

Figure 45 - SEM micrograph from Hi-Nicalon™ S fiber tow specimen "Air 1" subjected to 3.5 MPa at 1100°C in laboratory air achieving creep run-out of 100 hours at creep stress. The dark line along the fiber is indicative of contact between fibers.

While some fibers tested at 1100°C in this work showed evidence of contact between fibers similar to that in Figure 45, in the majority of cases the signs of contact were significantly more dramatic than the dark and mottled areas seen along the length of the fibers tested at lower temperatures. Instead, long gouges or pitting within the developed oxide scale, or the remnants of another fiber's scale, were often present on a fiber surface. Given the significant increase in silica scale growth at 1100°C, it is assumed these are regions where the oxide scales of multiple fibers first welded together and then pulled away (see Figure 46 - Figure 48).

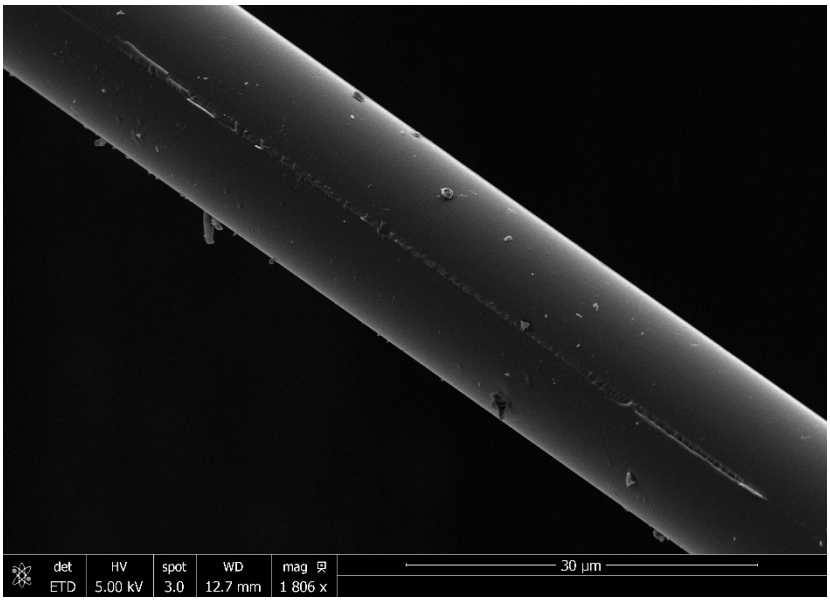

Figure 46 - SEM micrograph of Hi-Nicalon™ S fiber tow specimen "Air 9" subjected to 600 MPa at 1100°C in laboratory air achieving creep run-out of 100 hours at creep stress. The gouged line along the fiber is indicative of contact between fibers.

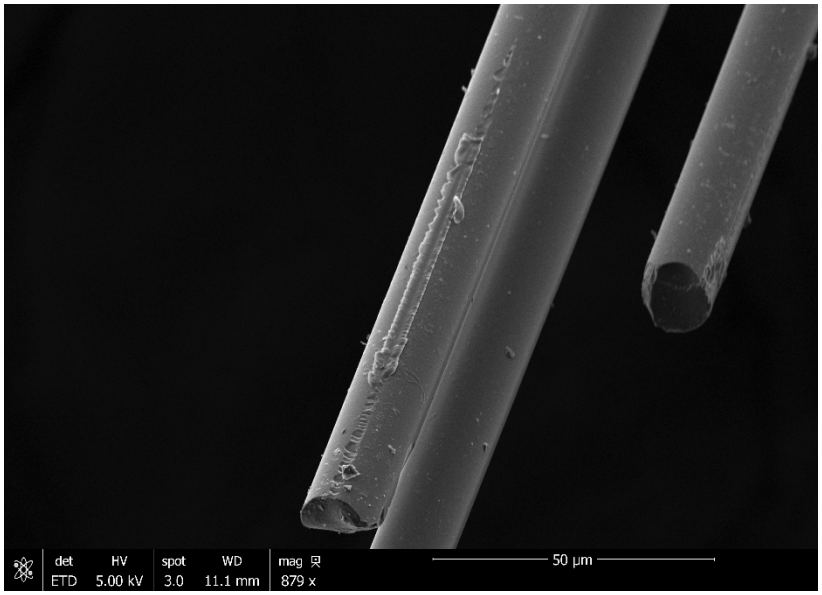

Figure 47 – SEM micrograph of Hi-Nicalon™ S fiber tow specimen "Air 3" subjected to 353 MPa at 1100°C in laboratory air achieving creep run-out of 100 hours at creep stress. The pitted line and remnants of oxide scale along the fiber is indicative of contact between fibers.

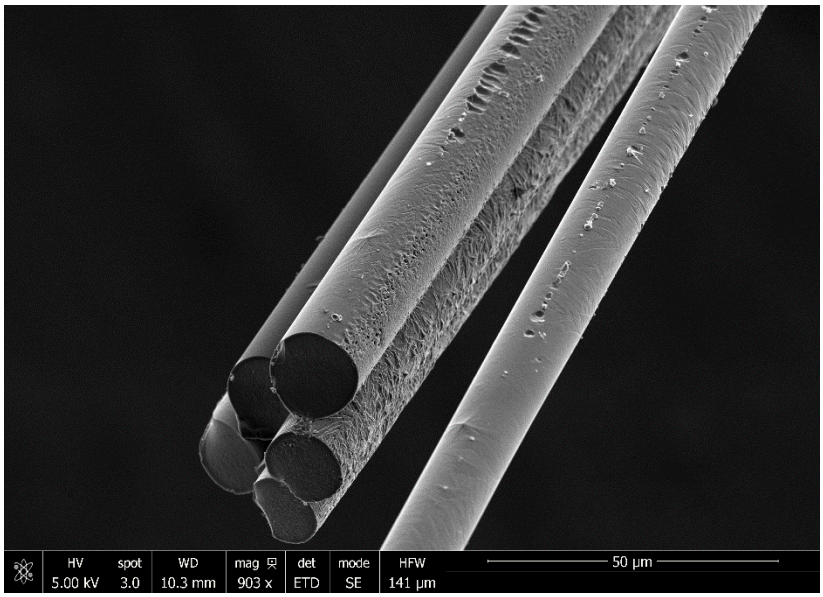

Figure 48 - SEM micrograph of Hi-Nicalon™ S fiber tow specimen "Steam 12" subjected to 450 MPa at 1100°C in silicic acid-saturated steam for 13.53 hours. The pitted lines along the length of the fibers are indicative of contact between fibers.

Given the complexity of the manufacturing process of SiC fibers, microstructural defects and/or contaminants within the fiber tows can be expected. These flaws provide ample opportunity for cracks to initiate and grow, eventually leading to failure of the fiber. Examples of this phenomenon can be seen on the fracture surfaces of some tested fibers, as demonstrated in Figure 49. Fractures were sometimes observed propagating through multiple fibers, as shown in Figure 50. These fibers appear to have been bonded together as the silica scale of each fiber developed, prior to fracture. Note that in this case the silica scale is not as thick as those shown in previous images (Figure 42 and Figure 43), due to the shorter lifetime of this particular fiber tow. The fiber tows tested in saturated steam which achieved longer creep lifetimes developed thicker silica scales on the fiber surface, conceivably providing protection to the fiber tow and delaying failure.

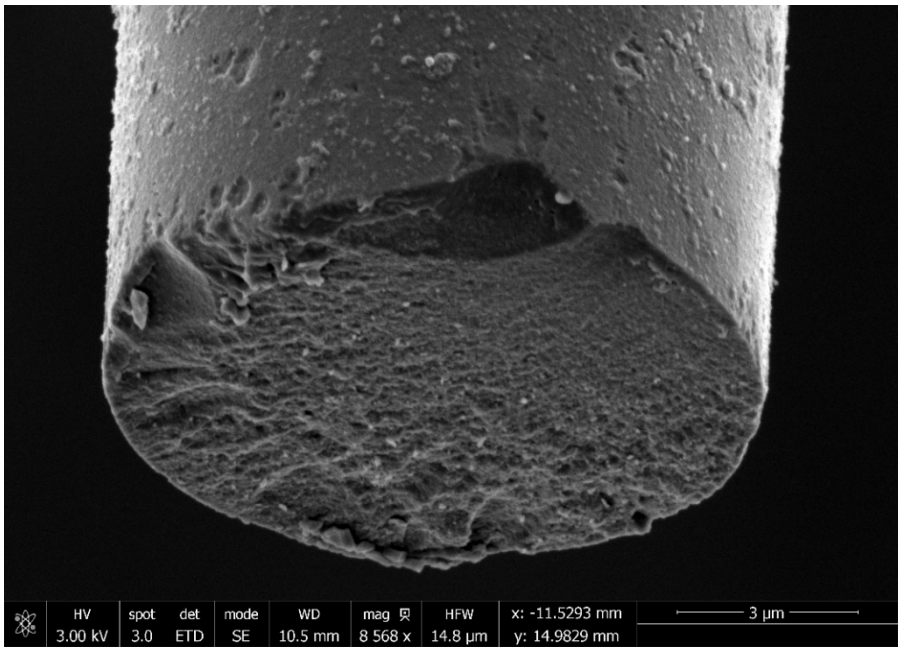

Figure 49 - SEM micrograph of Hi-Nicalon™ S fiber tow specimen "Air 10" examining the fracture surface of a fiber subjected to 650 MPa at 1100°C in laboratory air for 2.24 hrs.

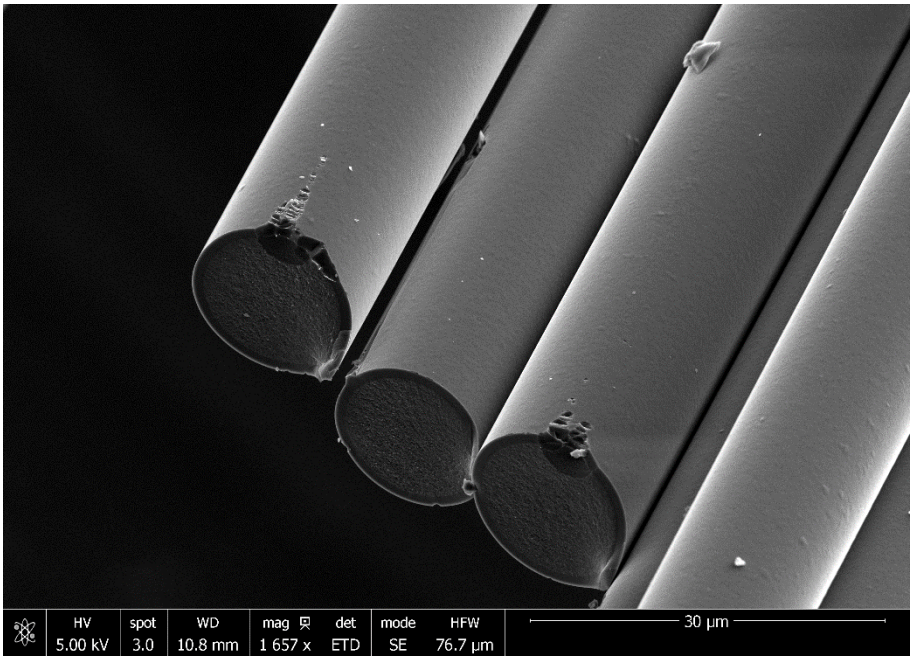

Figure 50 - SEM micrograph of Hi-Nicalon™ S fiber tow specimen "Steam 12" examining the fracture surface of multiple fibers subjected to 450 MPa at 1100°C in silicic acid-saturated steam for 13.53 hrs.

All fiber tows tested in saturated steam developed both amorphous and crystalline scales on the fiber surfaces. The extent of scale appears to be largely dependent on the creep lifetime of the fiber tows. The amorphous scale is glassy in appearance and is distinguishable as a ring grown around the fiber, as seen in previous images. The growth of crystallized scale can be seen on the exterior surface of the fiber, appearing as circular patches or blisters. Examples of crystallized scale are presented in Figure 51 and Figure 52, highlighting the initial and more developed stages of the crystallization process.

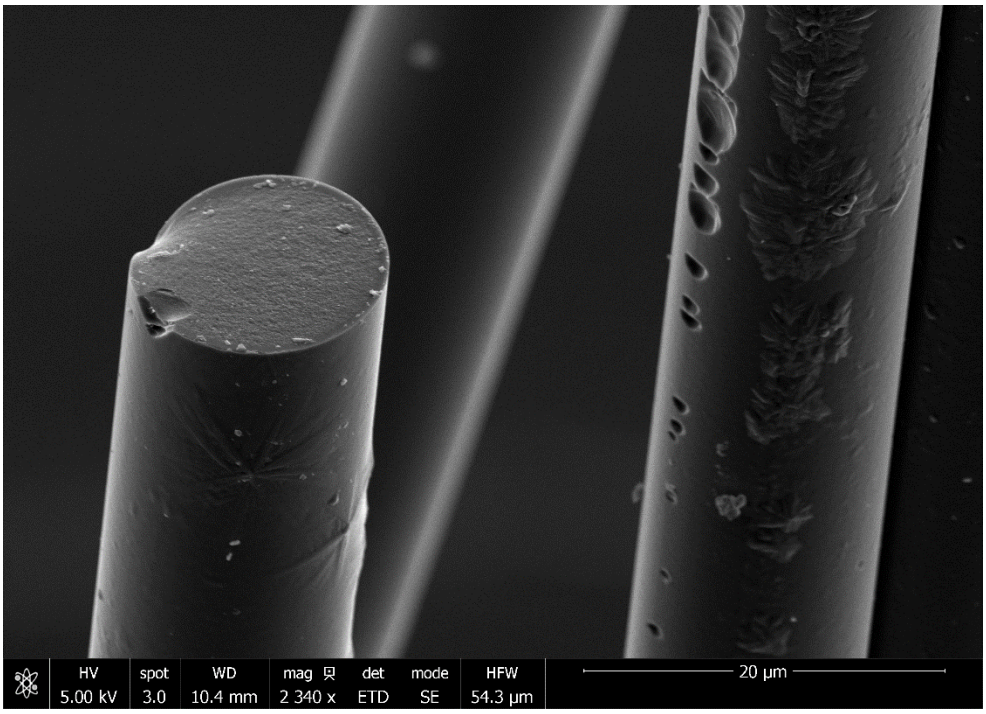

Figure 51 - SEM micrograph of Hi-Nicalon™ S fiber tow specimen "Steam 11" examining the fracture surface of a fiber subjected to 650 MPa at 1100°C in silicic acid-saturated steam. Note the early stages of crystallized scale growth.

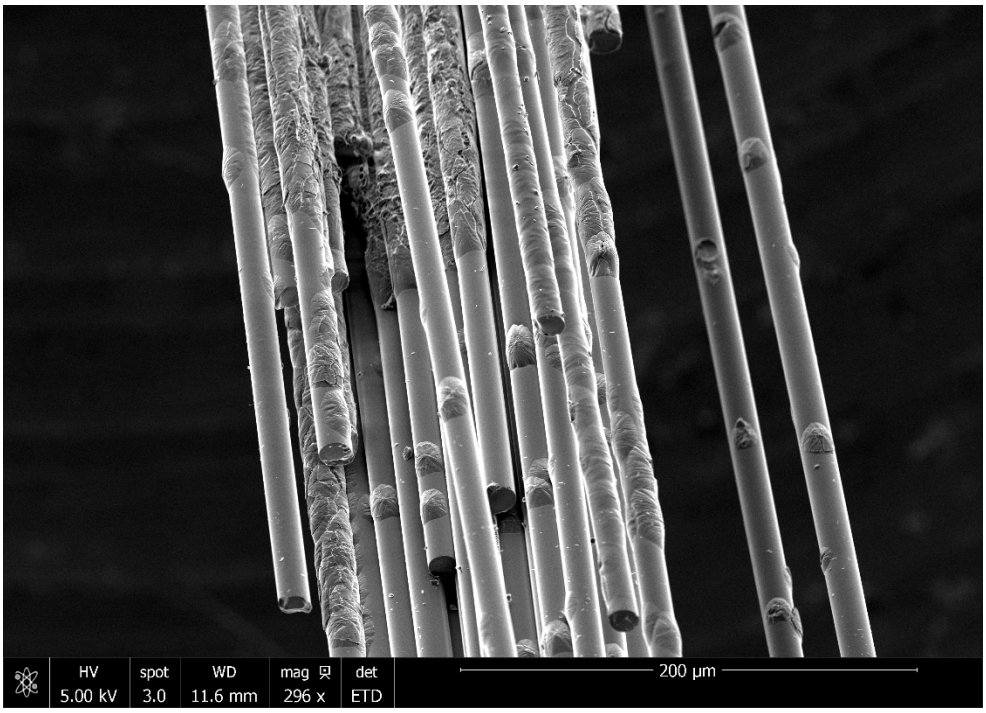

Figure 52 - SEM micrograph of Hi-Nicalon™ S fiber tow specimen "Steam 4" examining the varying degrees of crystallization along the surface of a group of fibers subjected to 255 MPa at 1100°C in silicic acid-saturated steam.

The fiber tows which had failed in saturated steam appeared to predominantly fail in locations where the scale had crystallized, as evidenced in Figure 53. These failure locations within regions of crystallized scale on the fiber surface were also observed by Kroeger [18] for Hi-Nicalon™ S fiber tows tested at 1000°C in saturated steam.

Figure 53 - SEM micrograph of Hi-Nicalon™ S fiber tow specimen "Steam 4" examining the fracture surface of a fiber subjected to 255 MPa at 1100°C in silicic acid-saturated steam. Note the defined amorphous and crystallized scale growth.

V. Conclusions and Recommendations

5.1 Conclusions

The creep behavior of Hi-Nicalon™ S fiber tows was investigated at 1100°C in creep tests performed in laboratory air and in silicic acid-saturated steam. The creep stresses ranged from 3.5 to 650 MPa for both laboratory air and silicic acid-saturated steam. Creep run-out was defined as 100 hours at creep stress, and was achieved at 600 MPa in laboratory air and 3.5 MPa in silicic-acid saturated steam. The silicic acid-saturated steam environment considerably degraded the creep performance of the fiber tows. In silicic acid-saturated steam, creep lifetimes were reduced by one order of magnitude while the steady-state creep rates increased by one order of magnitude.

Results obtained in this effort were compared to the results of prior work completed at AFIT at 800-1100°C in laboratory air, steam, and saturated steam environments. The presence of saturated steam increased creep rates by an order of magnitude for all temperatures studied. However, creep rates obtained in saturated steam were one order of magnitude lower than creep rates found in steam for temperatures below 1000°C. For temperatures above 1000°C, creep rates in saturated steam were only 5 times lower than creep rates obtained in steam. Creep lifetimes produced in saturated steam were an order of magnitude lower than creep lifetimes achieved in laboratory air, but an order of magnitude higher than creep lifetimes obtained in unsaturated steam. These results revealed that at elevated temperatures unsaturated steam was significantly more damaging to the creep performance of Hi-Nicalon™ S fiber tows than silicic acid-saturated steam.

The post-test microstructural analysis of the Hi-Nicalon™ S fiber tows revealed passive oxidation of fibers tested at 1100°C in both laboratory air and in saturated steam. Additionally, evidence of silica scale growth was observed on specimens tested at 1100°C in both laboratory air and in silicic acid-saturated steam. Notably specimens tested in saturated steam developed much thicker scale than those tested in laboratory air. For specimens tested in saturated steam, evidence of crystallized scale growth was present on numerous fibers, particularly on the fiber fracture surface and surrounding regions.

5.2 Recommendations

The creep behavior of Hi-Nicalon™ S fiber tows has been investigated at 700°C [16], 800°C [15], 900°C [17], and 1000°C [18] in laboratory air and silicic acid-saturated steam. The growth of silica scale became more pronounced at temperatures ≥ 1000°C. Further investigation of the effects of silicic acid-saturated steam on creep behavior of Hi-Nicalon™ S fiber tows at temperatures above 1100°C is highly encouraged.

It should be noted that initially it was difficult to heat the saturated steam to 1100°C and to maintain saturated steam at 1100°C in a consistent manner. Future efforts at higher temperatures would benefit from improving the steam heat-up process by changing or upgrading the hardware. An upgrade of the current model of steam generator to the newer HGA-H model (Micropyretics Heaters International), which yields a higher maximum steam output temperature.

Further investigation of the tested fibers using transmission electron microscopy (TEM) is recommended. This method would allow for improved magnification and fidelity

in examining the existence and growth of oxide layer on the surface of the fibers. The results of TEM analysis may also provide additional data that may be compared with predictions made using oxidation kinetics models, such as the Deal-Grove model.

In this endeavor, as well as in all prior work completed at AFIT, we assume that the deformation behavior being investigated is in fact due to creep and not to progressive fiber failure. Future efforts could focus on assessing the validity of this assumption. Such endeavors may consider including acoustic emission capability in the test set-up in order to capture individual fiber failures.

Appendix A. Representative SEM Images

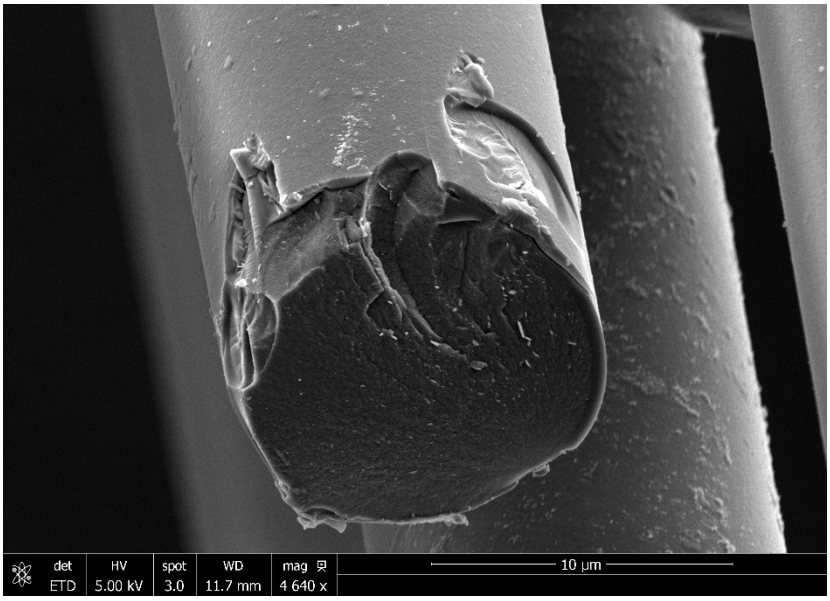

Figure 54 - SEM micrograph of Hi-Nicalon™ S fiber tow specimen "Air 1" examining the silica scale thickness of a fiber along the lower portion of the fiber tow (σ_{cr} = 3.5 MPa, t_f = 100† hrs).

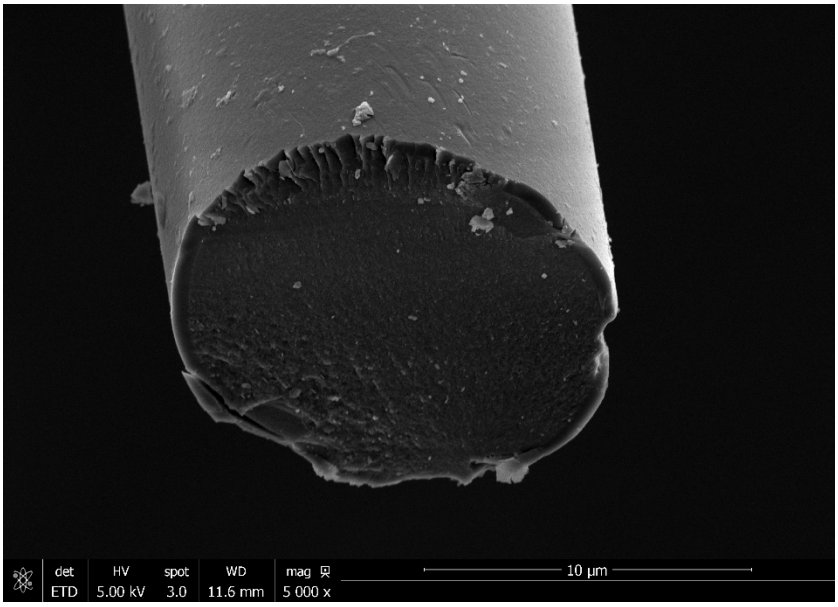

Figure 55 - SEM micrograph of Hi-Nicalon™ S fiber tow specimen "Air 1" examining the silica scale thickness of a fiber along the lower portion of the fiber tow (σ_{cr} = 3.5 MPa, t_f = 100† hrs).

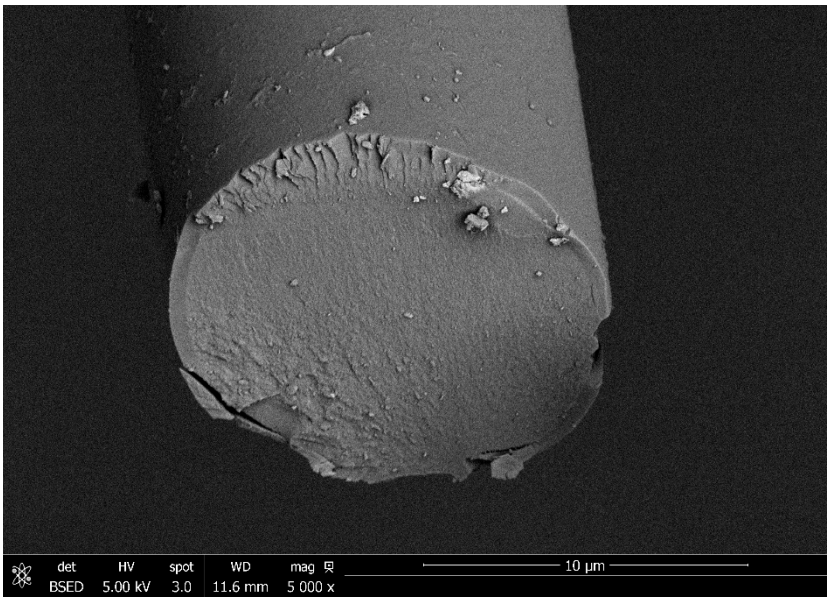

Figure 56 – SEM electron backscatter deflection micrograph of Hi-Nicalon™ S fiber tow specimen "Air 1" examining the silica scale thickness of a fiber along the lower portion of the fiber tow *(σ_{cr} = 3.5 MPa, t_f = 100† hrs)*.

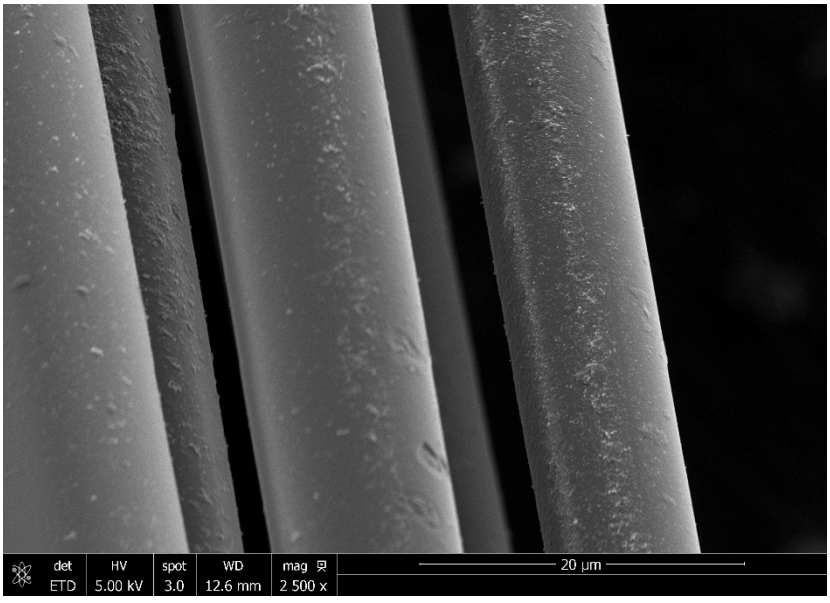

Figure 57 - SEM micrograph of Hi-Nicalon™ S fiber tow specimen "Air 1" examining evidence of fiber to fiber contact along the lengths of a fiber along the lower portion of the fiber tow *(σ_{cr} = 3.5 MPa, t_f = 100† hrs)*.

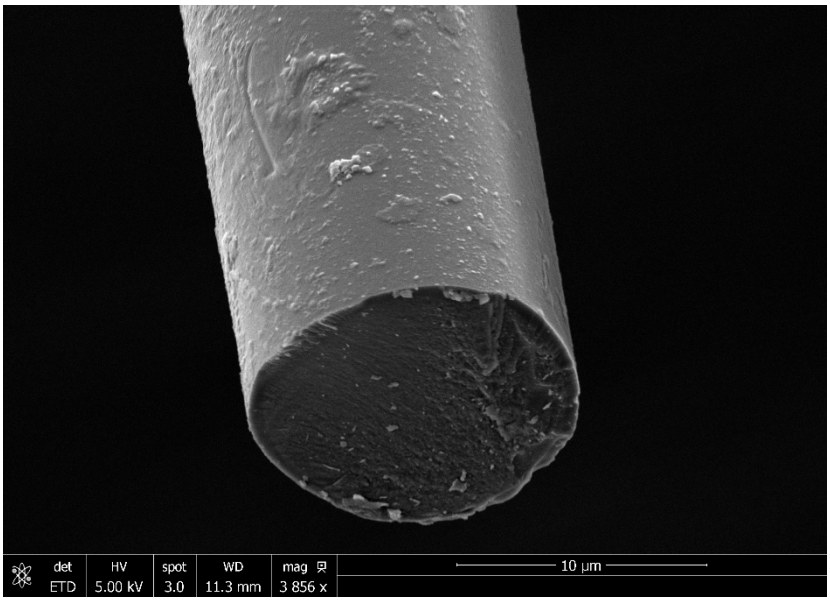

Figure 58 - SEM micrograph of Hi-Nicalon™ S fiber tow specimen "Air 1" examining the silica scale thickness of a fiber along the midpoint of the fiber tow (σ_{cr} = 3.5 MPa, t_f = 100† hrs).

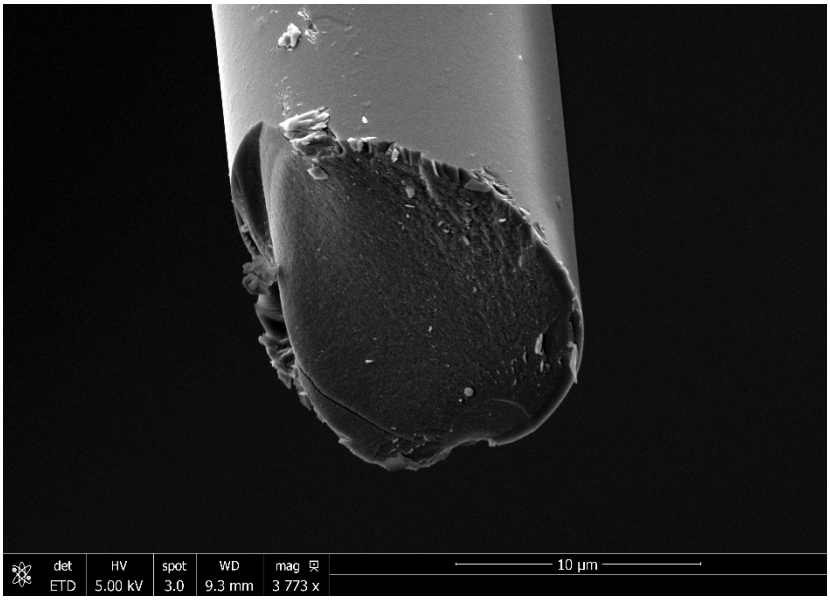

Figure 59 - SEM micrograph of Hi-Nicalon™ S fiber tow specimen "Air 1" examining the silica scale thickness of a fiber along the midpoint of the fiber tow (σ_{cr} = 3.5 MPa, t_f = 100† hrs).

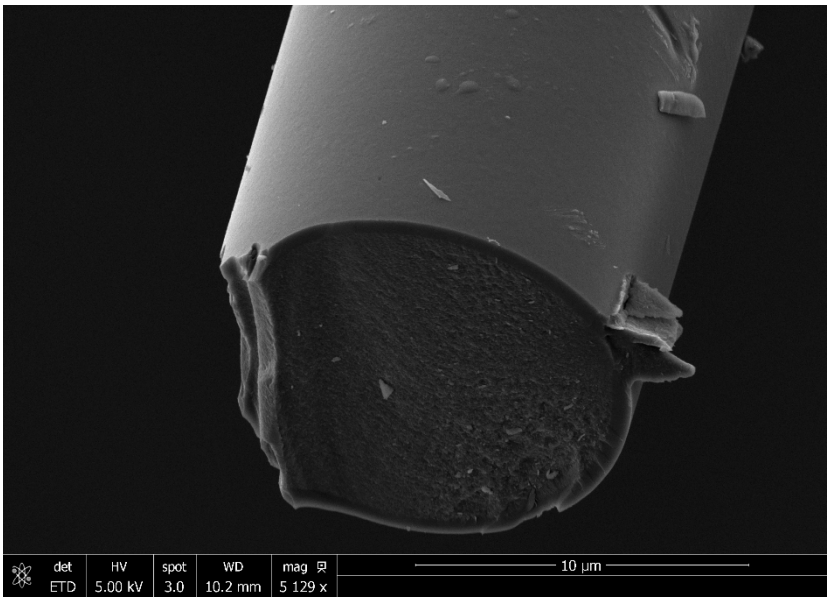

Figure 60 - SEM micrograph of Hi-Nicalon™ S fiber tow specimen "Air 1" examining the silica scale thickness of a fiber along the midpoint of the fiber tow (σ_{cr} = 3.5 MPa, t_f = 100† hrs).

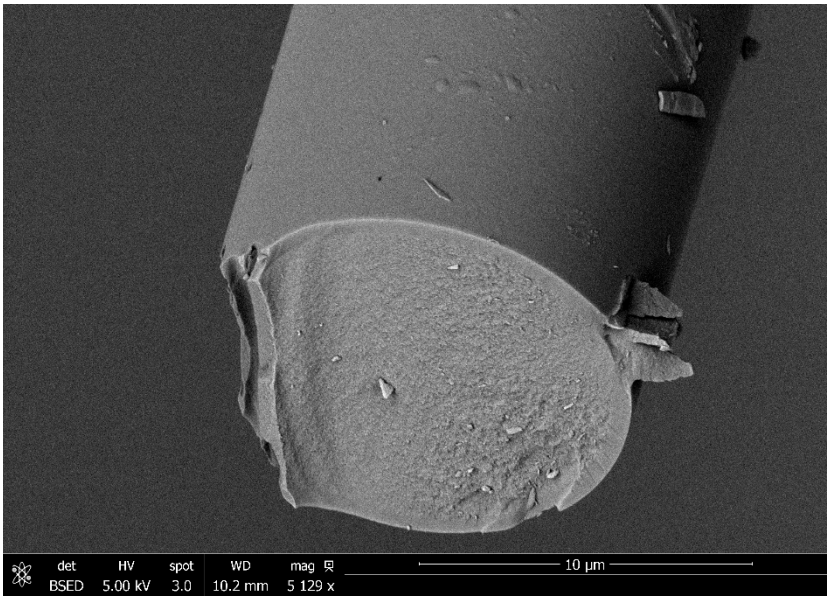

Figure 61 - SEM electron backscatter deflection micrograph of Hi-Nicalon™ S fiber tow specimen "Air 1" examining the silica scale thickness of a fiber along the midpoint of the fiber tow (σ_{cr} = 3.5 MPa, t_f = 100† hrs).

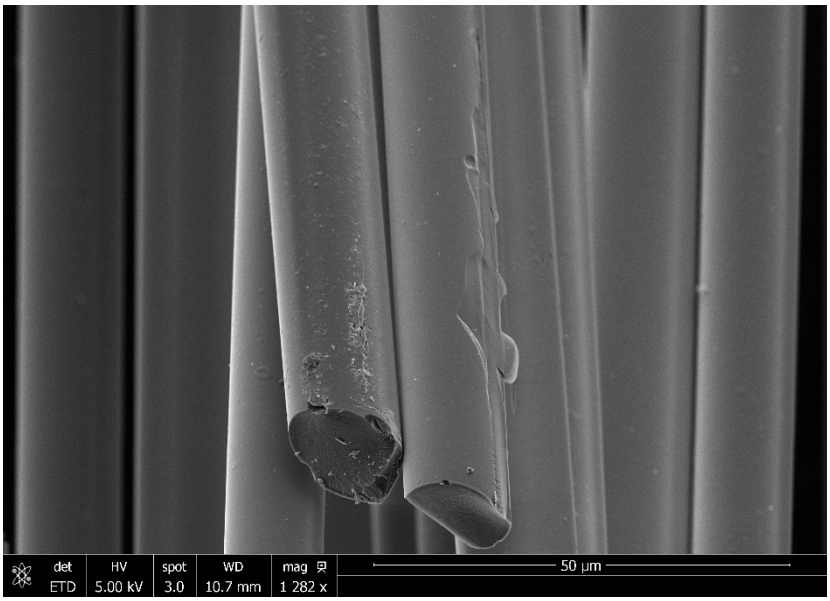

Figure 62 - SEM micrograph of Hi-Nicalon™ S fiber tow specimen "Air 1" examining evidence of fiber to fiber contact on multiple fibers along the midpoint of the fiber tow (σ_{cr} = 3.5 MPa, t_f = 100† hrs).

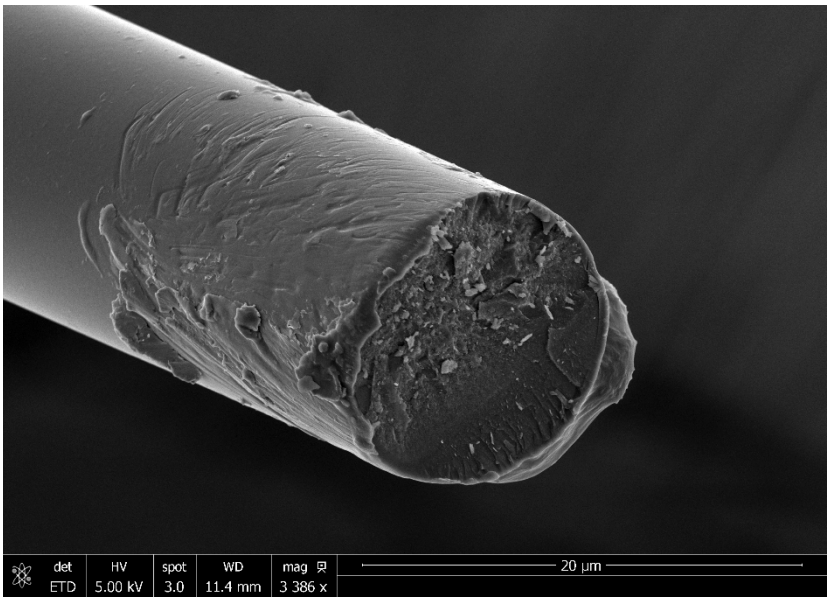

Figure 63 - SEM micrograph of Hi-Nicalon™ S fiber tow specimen "Air 1" examining the silica scale thickness of a fiber along the upper portion of the fiber tow (σ_{cr} = 3.5 MPa, t_f = 100† hrs).

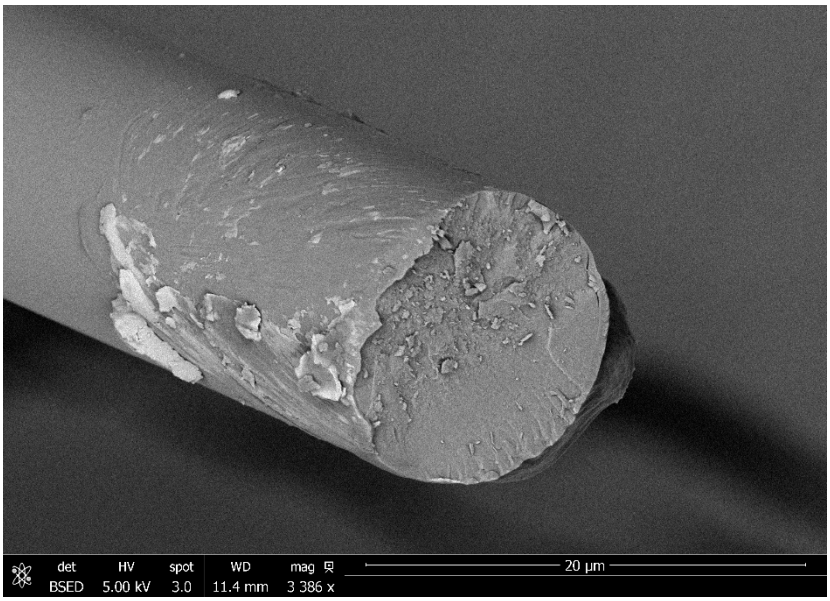

Figure 64 - SEM electron backscatter deflection micrograph of Hi-Nicalon™ S fiber tow specimen "Air 1" examining the silica scale thickness of a fiber along the upper portion of the fiber tow (σ_{cr} = 3.5 MPa, t_f = 100† hrs).

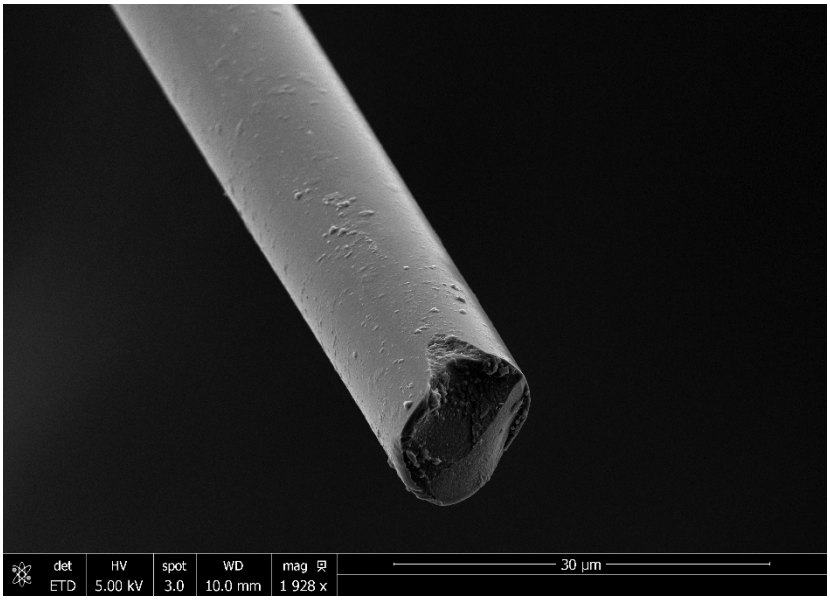

Figure 65 - SEM micrograph of Hi-Nicalon™ S fiber tow specimen "Air 1" examining the silica scale thickness of a fiber along the upper portion of the fiber tow (σ_{cr} = 3.5 MPa, t_f = 100† hrs).

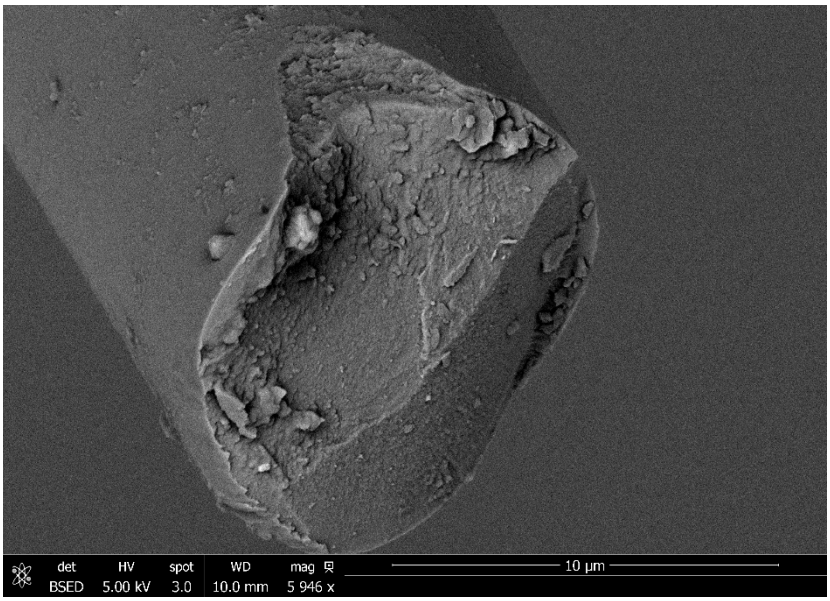

Figure 66 - SEM electron backscatter deflection micrograph of Hi-Nicalon™ S fiber tow specimen "Air 1" examining the silica scale thickness of a fiber along the upper portion of the fiber tow (σ_{cr} = 3.5 MPa, t_f = 100† hrs).

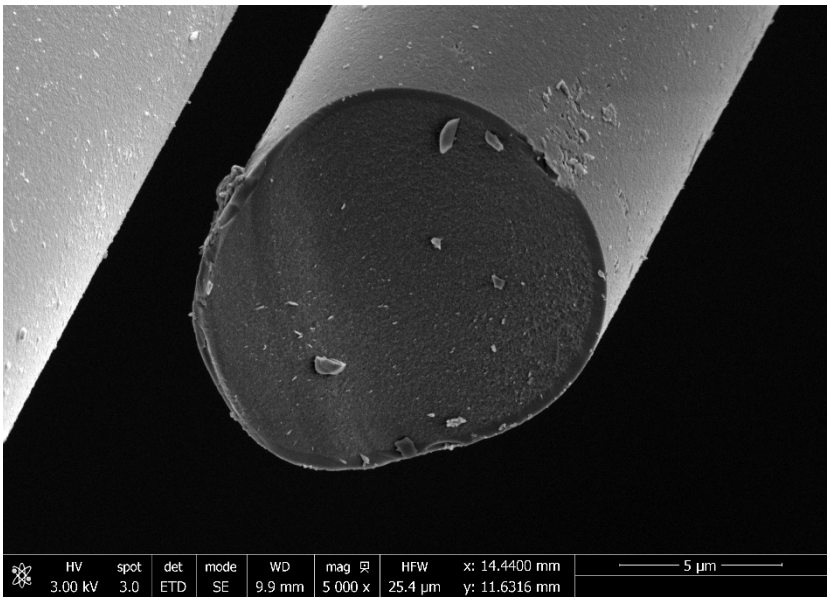

Figure 67 - SEM micrograph of Hi-Nicalon™ S fiber tow specimen "Air 3" examining the silica scale thickness of a fiber along the lower portion of the fiber tow (σ_{cr} = 353 MPa, t_f = 100† hrs).

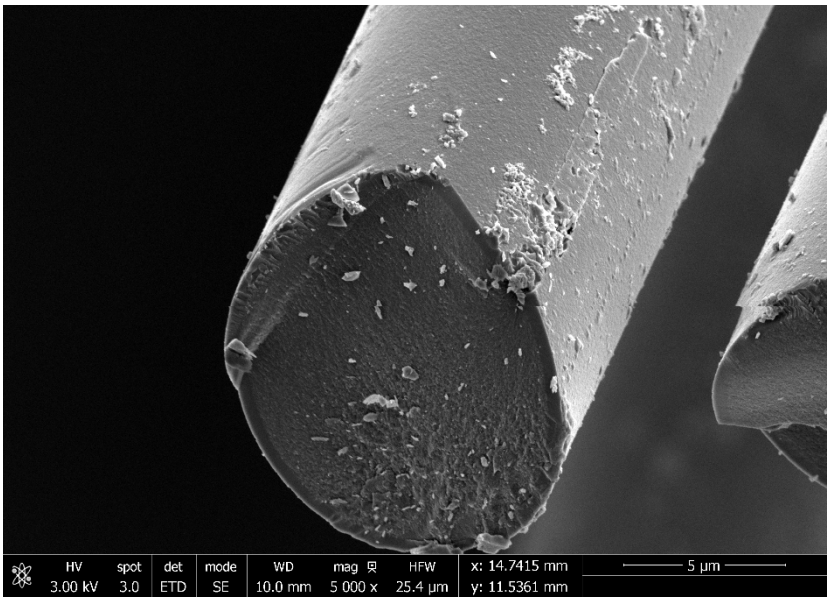

Figure 68 - SEM micrograph of Hi-Nicalon™ S fiber tow specimen "Air 3" examining the silica scale thickness of a fiber along the lower portion of the fiber tow (σ_{cr} = 353 MPa, t_f = 100† hrs).

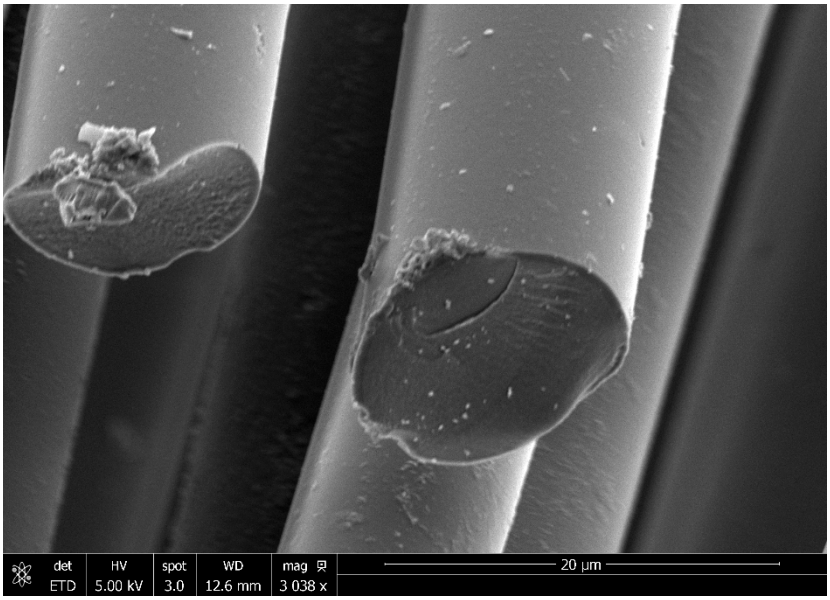

Figure 69 - SEM micrograph of Hi-Nicalon™ S fiber tow specimen "Air 3" examining the silica scale thickness of a fiber along the midpoint of the fiber tow (σ_{cr} = 353 MPa, t_f = 100† hrs).

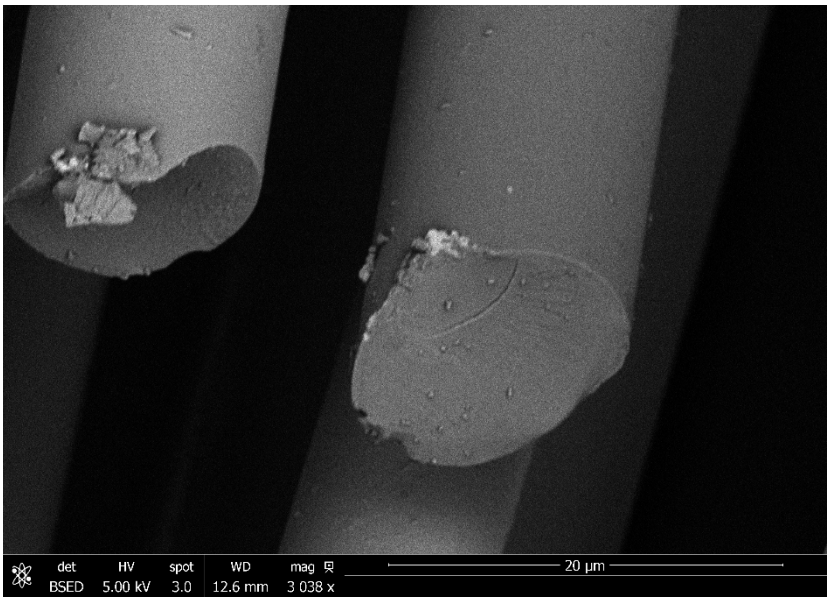

Figure 70 - SEM electron backscatter deflection micrograph of Hi-Nicalon™ S fiber tow specimen "Air 3" examining the silica scale thickness of a fiber along the midpoint of the fiber tow (σ_{cr} = 353 MPa, t_f = 100† hrs).

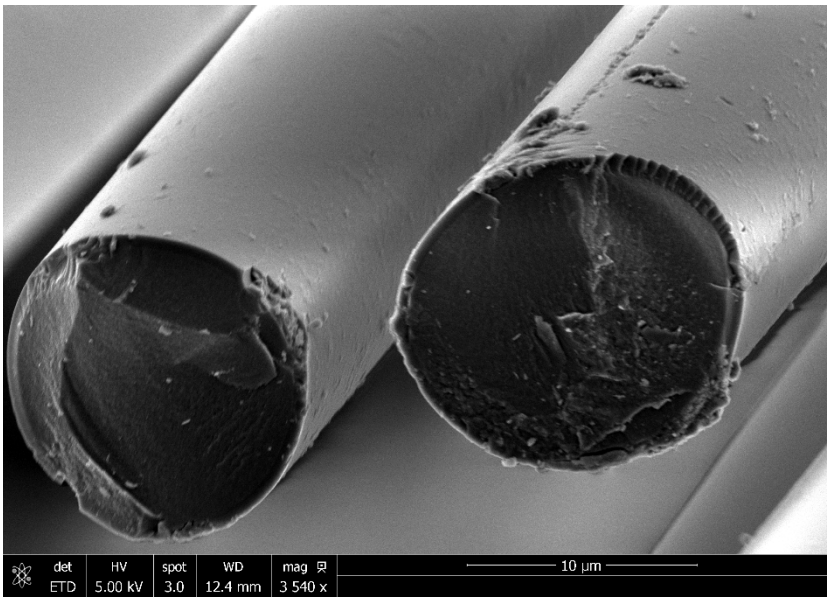

Figure 71 - SEM micrograph of Hi-Nicalon™ S fiber tow specimen "Air 3" examining the silica scale thickness of a pair of fibers along the midpoint of the fiber tow (σ_{cr} = 353 MPa, t_f = 100† hrs).

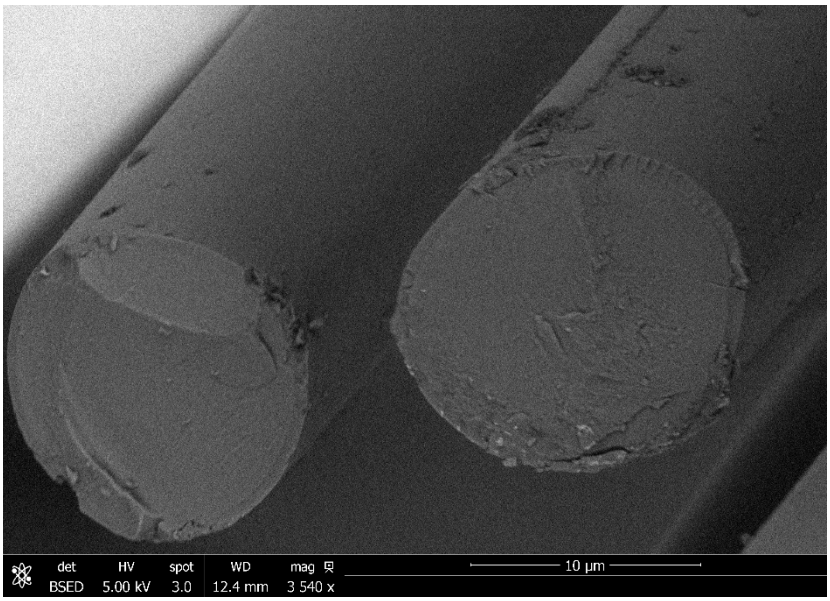

Figure 72 – SEM electron backscatter deflection micrograph of Hi-Nicalon™ S fiber tow specimen "Air 3" examining the silica scale thickness of a pair of fibers along the midpoint of the fiber tow (σ_{cr} = 353 MPa, t_f = 100† hrs).

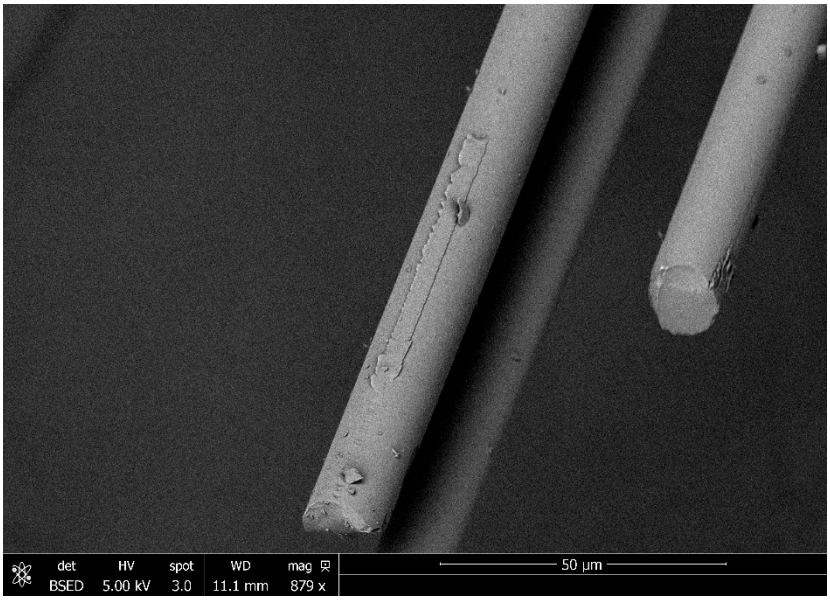

Figure 73 - SEM electron backscatter deflection micrograph of Hi-Nicalon™ S fiber tow specimen "Air 3" examining a fiber surface where contact between fibers has ripped off a portion of the silica scale along the upper portion of the fiber tow (σ_{cr} = 353 MPa, t_f = 100† hrs).

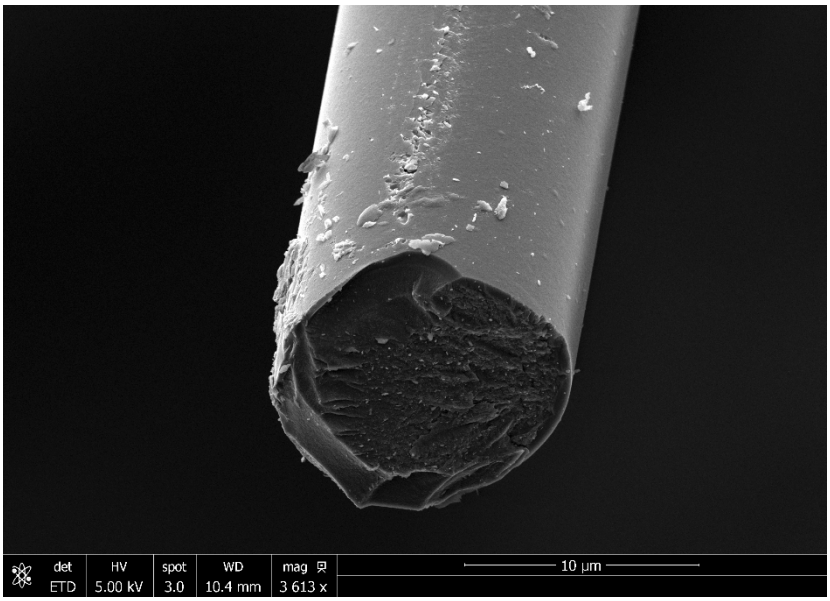

Figure 74 - SEM micrograph of Hi-Nicalon™ S fiber tow specimen "Air 3" examining the silica scale thickness of a fiber along the upper portion of the fiber tow (σ_{cr} = 353 MPa, t_f = 100† hrs).

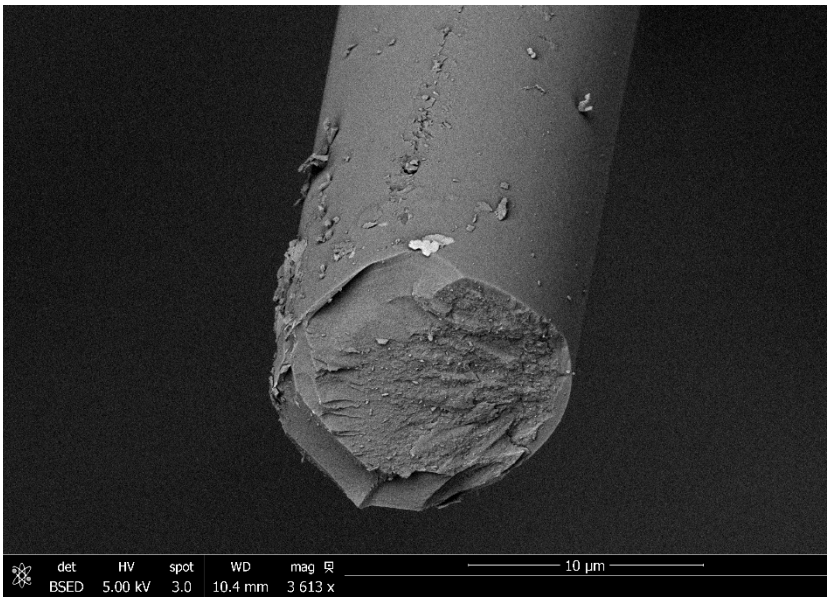

Figure 75 - SEM electron backscatter deflection micrograph of Hi-Nicalon™ S fiber tow specimen "Air 3" examining the silica scale thickness of a fiber along the upper portion of the fiber tow (σ_{cr} = 353 MPa, t_f = 100† hrs).

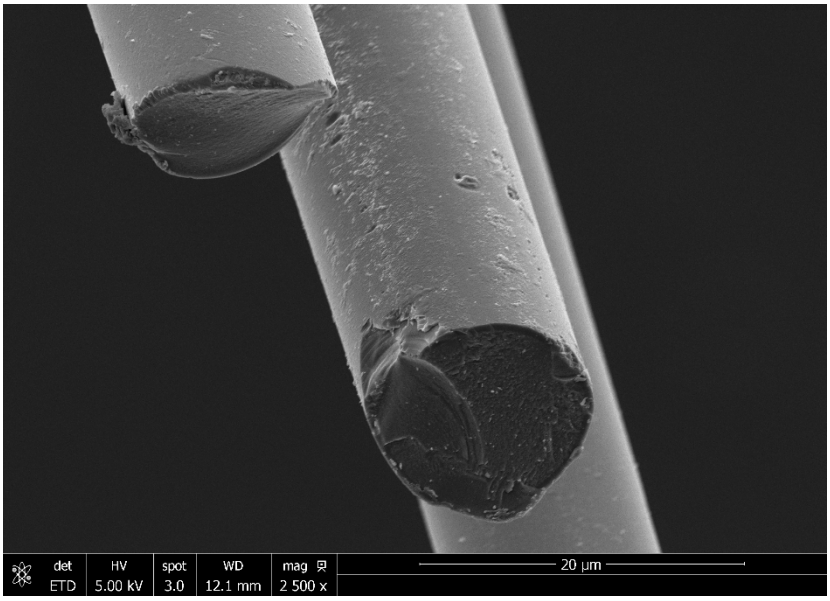

Figure 76 - SEM micrograph of Hi-Nicalon™ S fiber tow specimen "Air 9" examining the silica scale thickness and traces of fiber to fiber contact on a fiber along the lower portion of the fiber tow (σ_{cr} = 600 MPa, t_f = 100† hrs).

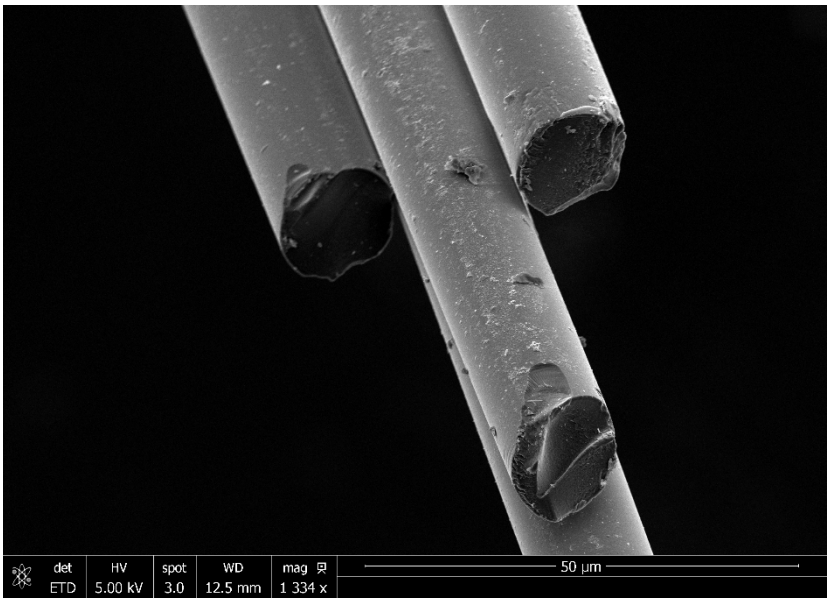

Figure 77 - SEM micrograph of Hi-Nicalon™ S fiber tow specimen "Air 9" examining traces of fiber to fiber contact on fibers along the lower portion of the fiber tow (σ_{cr} = 600 MPa, t_f = 100† hrs).

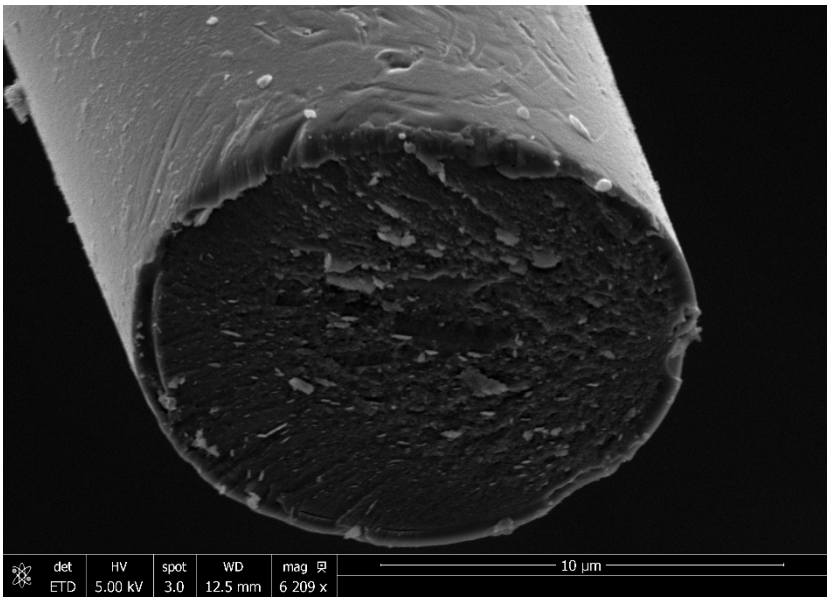

Figure 78 - SEM micrograph of Hi-Nicalon™ S fiber tow specimen "Air 9" examining the silica scale thickness on a fiber along the lower portion of the fiber tow (σ_{cr} = 600 MPa, t_f = 100† hrs).

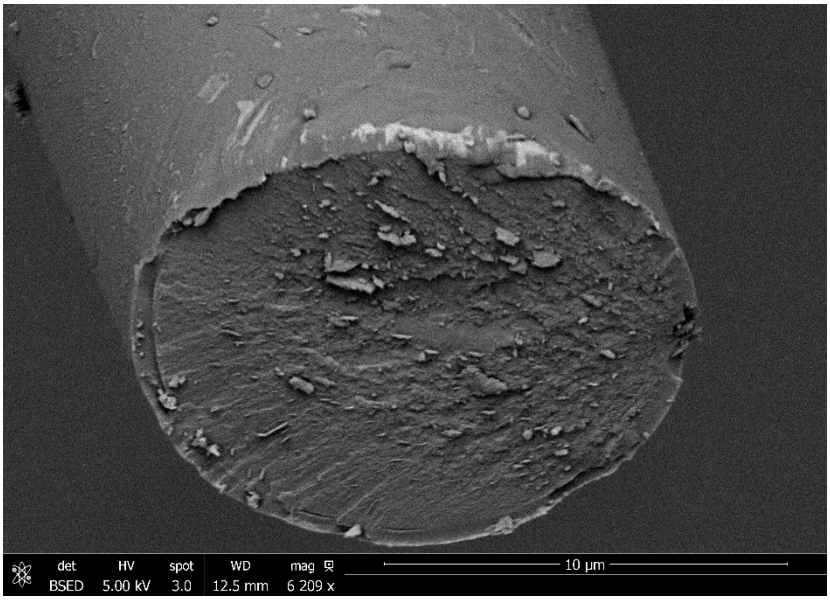

Figure 79 - SEM electron backscatter deflection micrograph of Hi-Nicalon™ S fiber tow specimen "Air 9" examining the silica scale thickness on a fiber along the lower portion of the fiber tow (σ_{cr} = 600 MPa, t_f = 100† hrs).

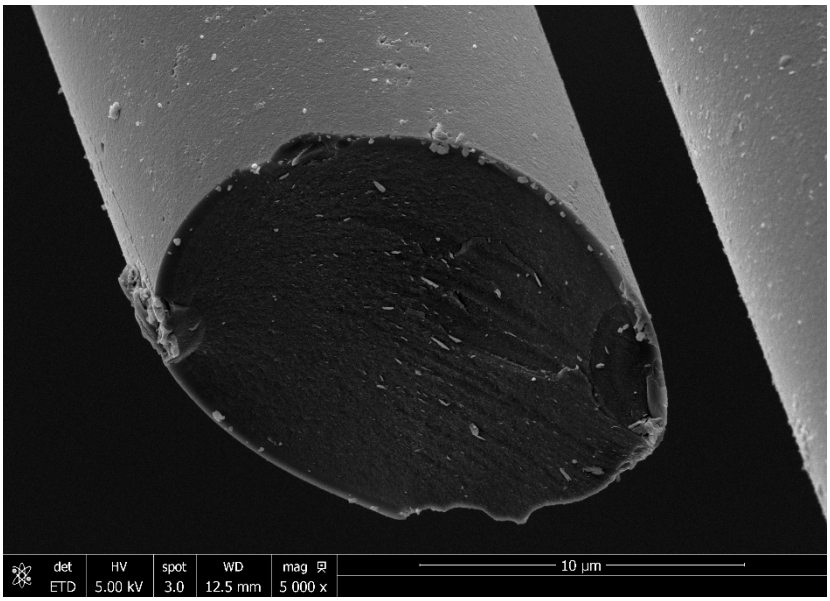

Figure 80 - SEM micrograph of Hi-Nicalon™ S fiber tow specimen "Air 9" examining the silica scale thickness on a fiber along the lower portion of the fiber tow (σ_{cr} = 600 MPa, t_f = 100† hrs).

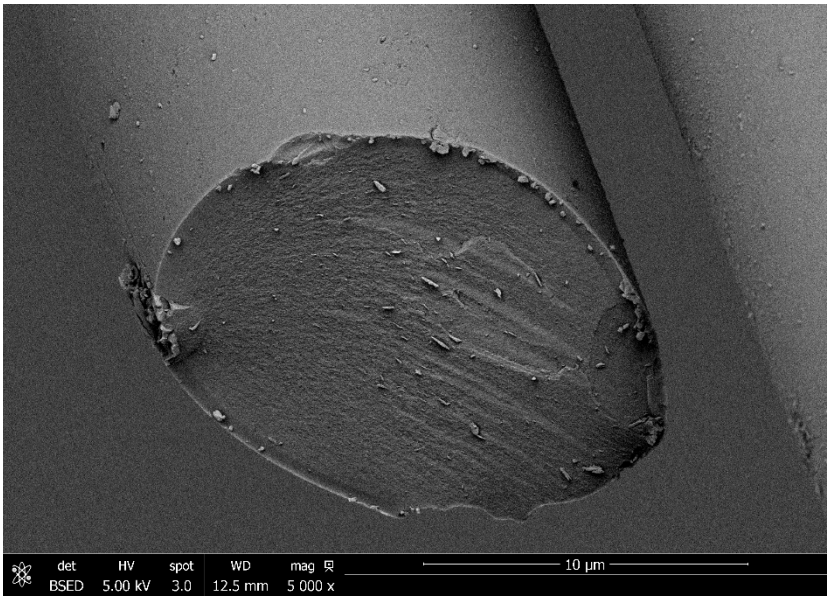

Figure 81 - SEM electron backscatter deflection micrograph of Hi-Nicalon™ S fiber tow specimen "Air 9" examining the silica scale thickness on a fiber along the lower portion of the fiber tow (σ_{cr} = 600 MPa, t_f = 100† hrs).

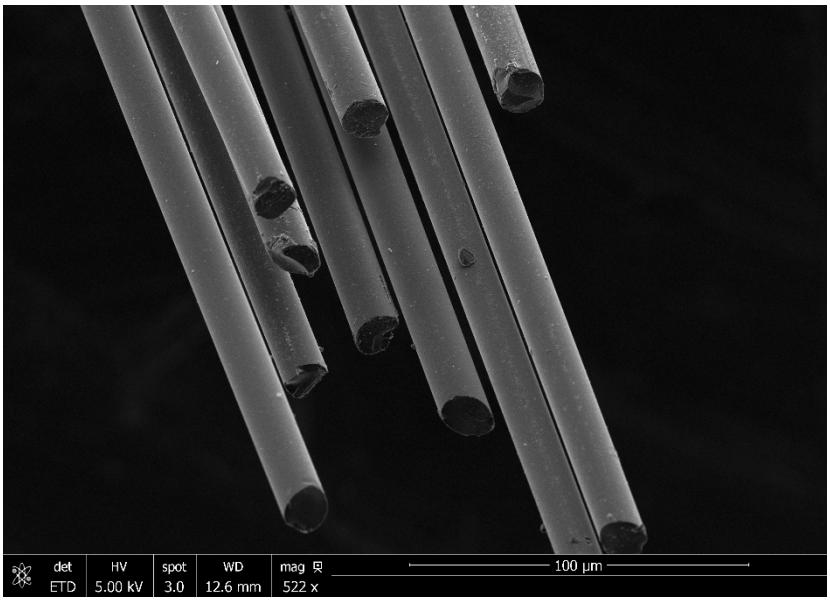

Figure 82 - SEM micrograph of Hi-Nicalon™ S fiber tow specimen "Air 9" examining traces of fiber to fiber contact on a small bundle of fibers along the lower portion of the fiber tow (σ_{cr} = 600 MPa, t_f = 100† hrs).

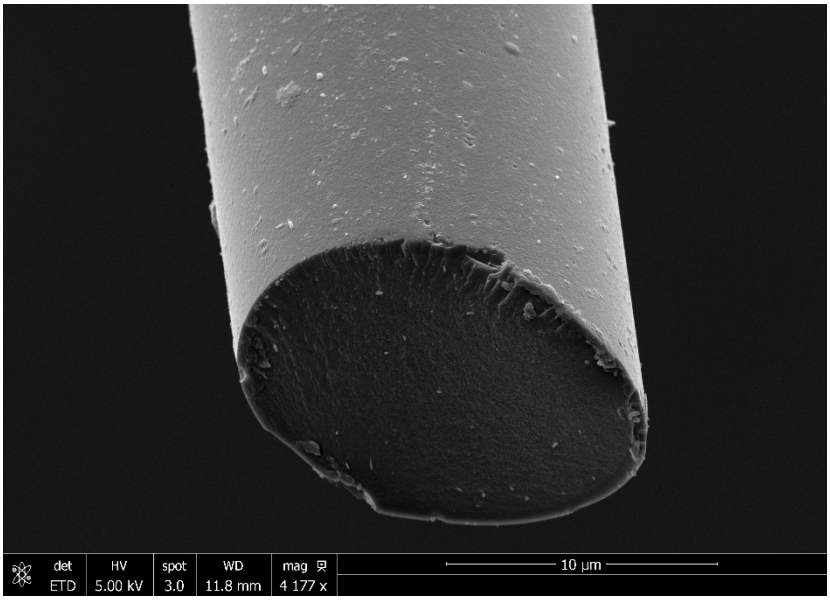

Figure 83 - SEM micrograph of Hi-Nicalon™ S fiber tow specimen "Air 9" examining the silica scale thickness on a fiber along the lower portion of the fiber tow (σ_{cr} = 600 MPa, t_f = 100† hrs).

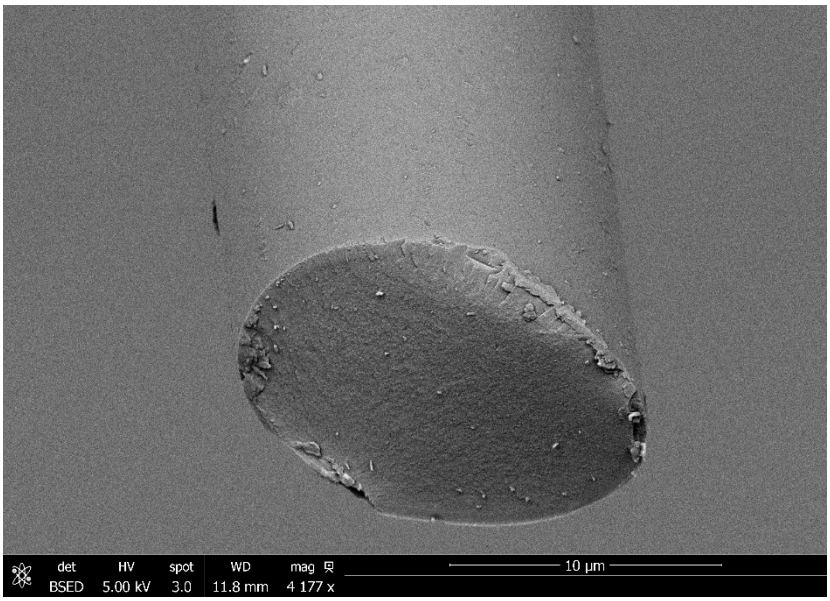

Figure 84 - SEM electron backscatter deflection micrograph of Hi-Nicalon™ S fiber tow specimen "Air 9" examining the silica scale thickness on a fiber along the lower portion of the fiber tow (σ_{cr} = 600 MPa, t_f = 100† hrs).

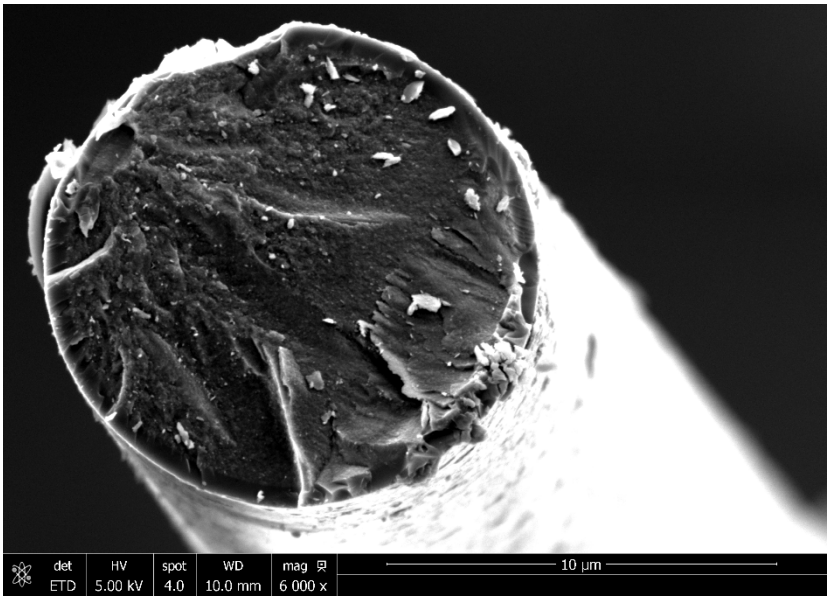

Figure 85 - SEM micrograph of Hi-Nicalon™ S fiber tow specimen "Air 9" examining the silica scale thickness on a fiber along the midpoint of the fiber tow (σ_{cr} = 600 MPa, t_f = 100† hrs).

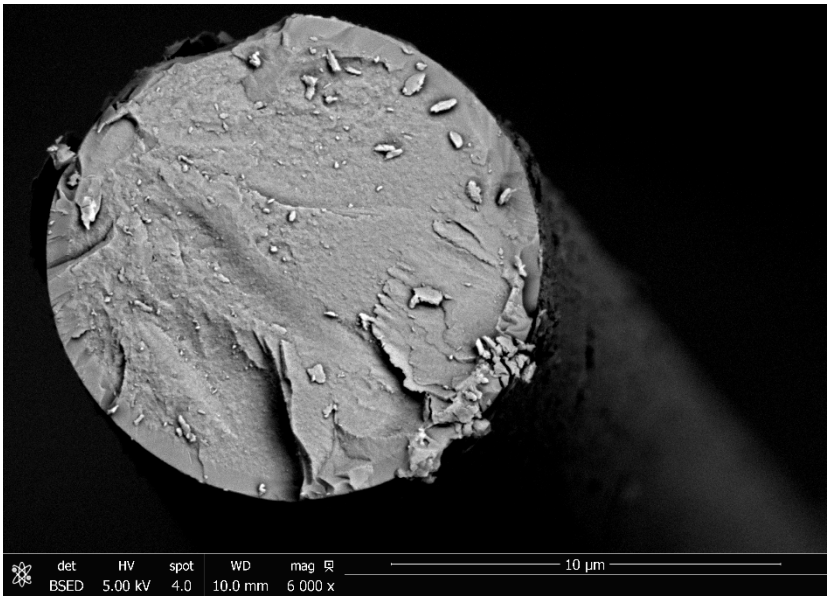

Figure 86 - SEM electron backscatter deflection micrograph of Hi-Nicalon™ S fiber tow specimen "Air 9" examining the silica scale thickness on a fiber along the midpoint of the fiber tow (σ_{cr} = 600 MPa, t_f = 100† hrs).

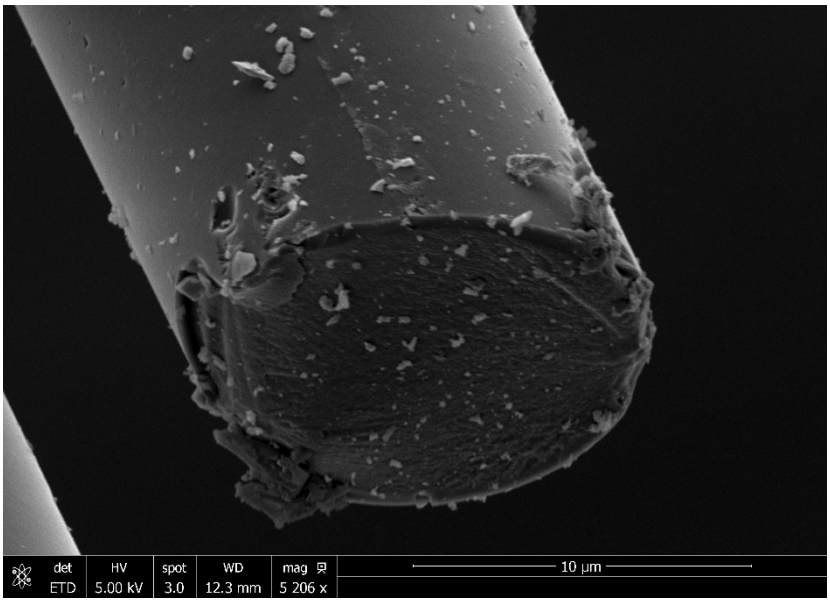

Figure 87 - SEM micrograph of Hi-Nicalon™ S fiber tow specimen "Air 9" examining the silica scale thickness on a fiber along the midpoint of the fiber tow (σ_{cr} = 600 MPa, t_f = 100† hrs).

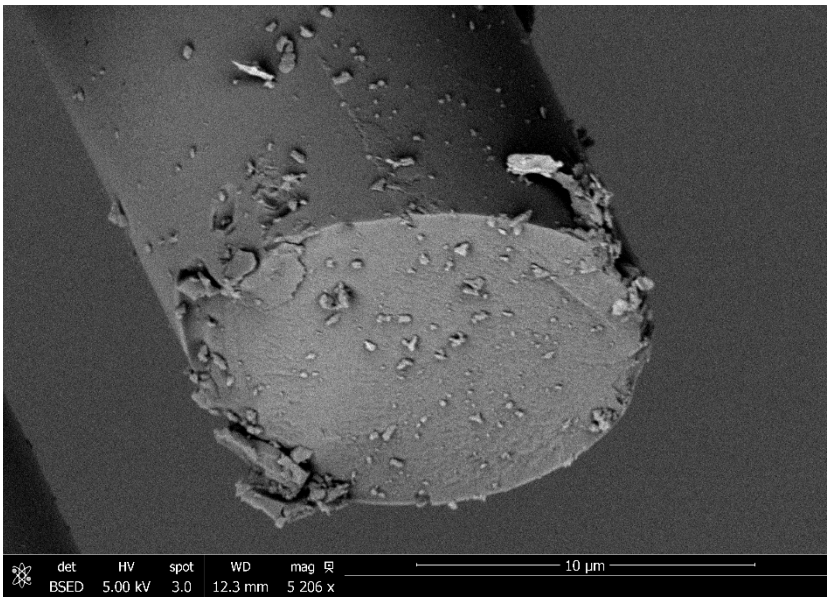

Figure 88 - SEM electron backscatter deflection micrograph of Hi-Nicalon™ S fiber tow specimen "Air 9" examining the silica scale thickness on a fiber along the midpoint of the fiber tow (σ_{cr} = 600 MPa, t_f = 100† hrs).

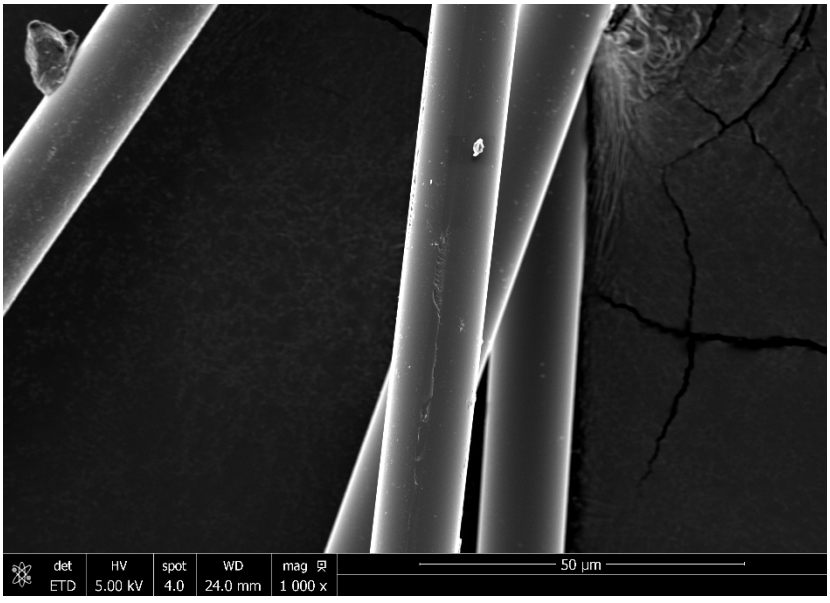

Figure 89 - SEM micrograph of Hi-Nicalon™ S fiber tow specimen "Air 9" examining evidence of fiber to fiber contact on a fiber along the midpoint of the fiber tow (σ_{cr} = 600 MPa, t_f = 100† hrs).

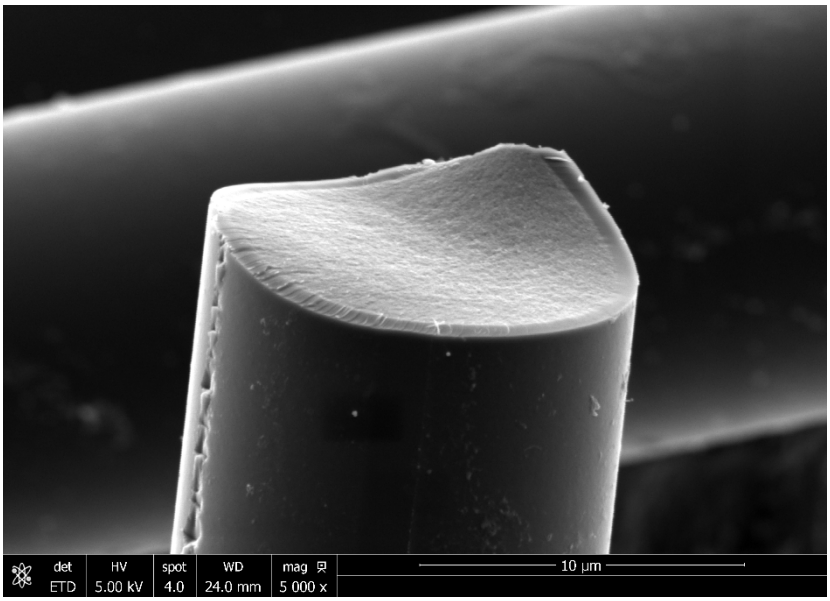

Figure 90 - SEM micrograph of Hi-Nicalon™ S fiber tow specimen "Air 9" examining the silica scale thickness on a fiber along the midpoint of the fiber tow (σ_{cr} = 600 MPa, t_f = 100† hrs).

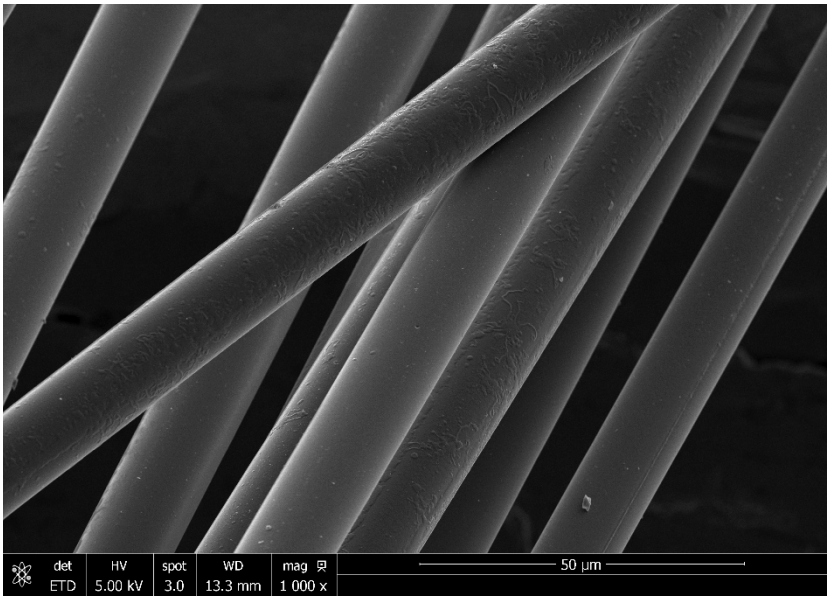

Figure 91 - SEM micrograph of Hi-Nicalon™ S fiber tow specimen "Air 9" examining the surfaces on multiple fibers along the upper portion of the fiber tow (σ_{cr} = 600 MPa, t_f = 100† hrs).

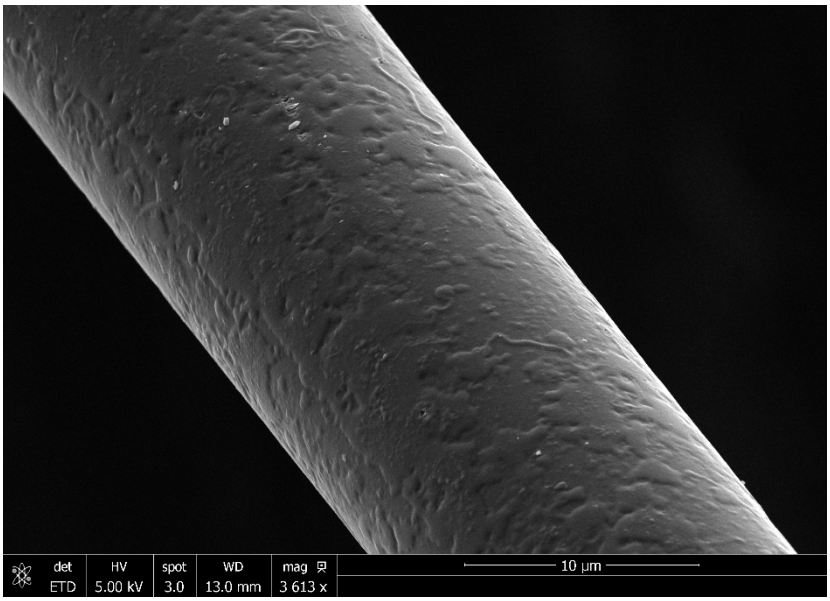

Figure 92 - SEM micrograph of Hi-Nicalon™ S fiber tow specimen "Air 9" examining the surface of a fiber along the upper portion of the fiber tow (σ_{cr} = 600 MPa, t_f = 100† hrs).

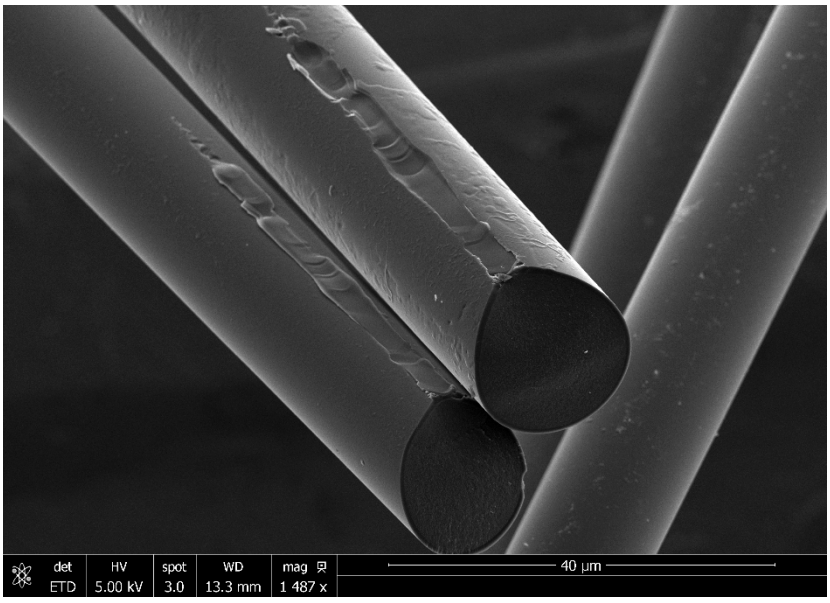

Figure 93 - SEM micrograph of Hi-Nicalon™ S fiber tow specimen "Air 9" examining the silica scale thickness of multiple fibers along the upper portion of the fiber tow. Note the locations where these fibers had been bonded to other fibers and pulled away (σ_{cr} = 600 MPa, t_f = 100† hrs).

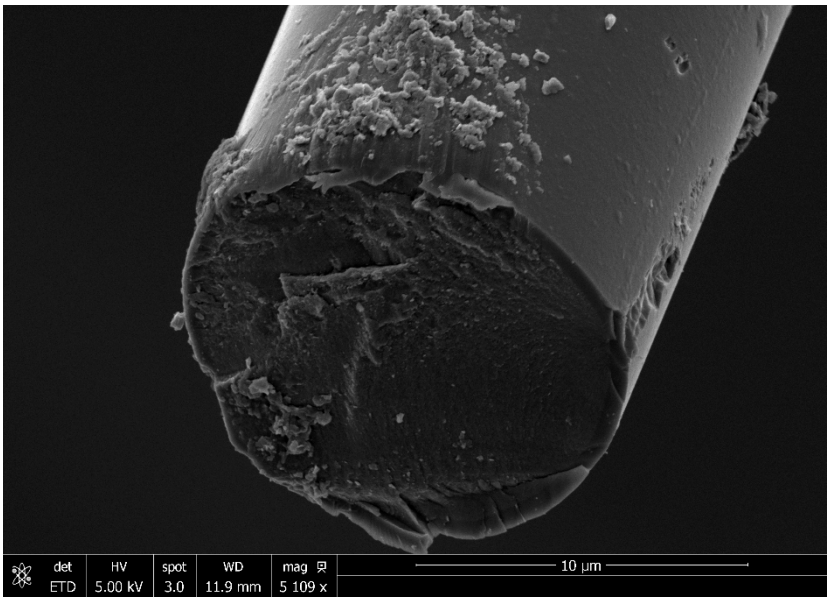

Figure 94 - SEM micrograph of Hi-Nicalon™ S fiber tow specimen "Air 9" examining the silica scale thickness of a fiber along the upper portion of the fiber tow (σ_{cr} = 600 MPa, t_f = 100† hrs).

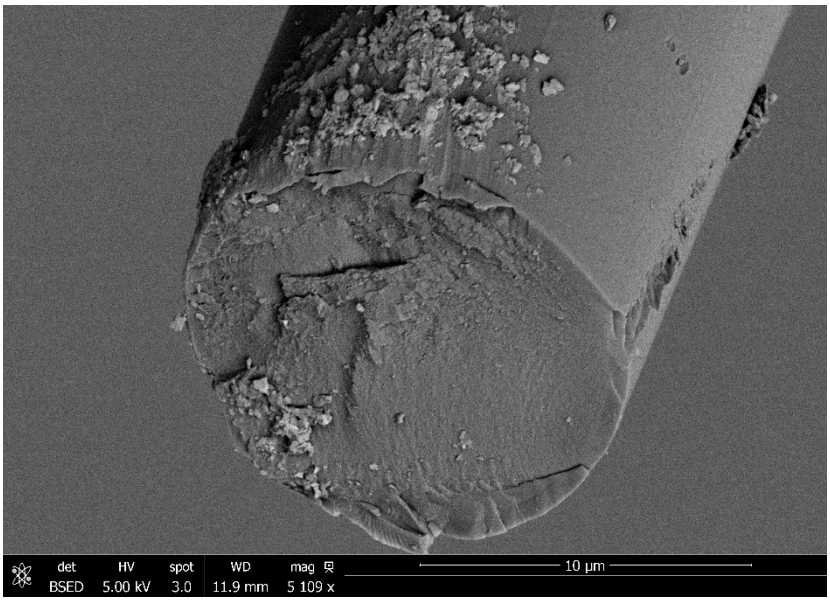

Figure 95 - SEM electron backscatter deflection micrograph of Hi-Nicalon™ S fiber tow specimen "Air 9" examining the silica scale thickness of a fiber along the upper portion of the fiber tow (σ_{cr} = 600 MPa, t_f = 100† hrs).

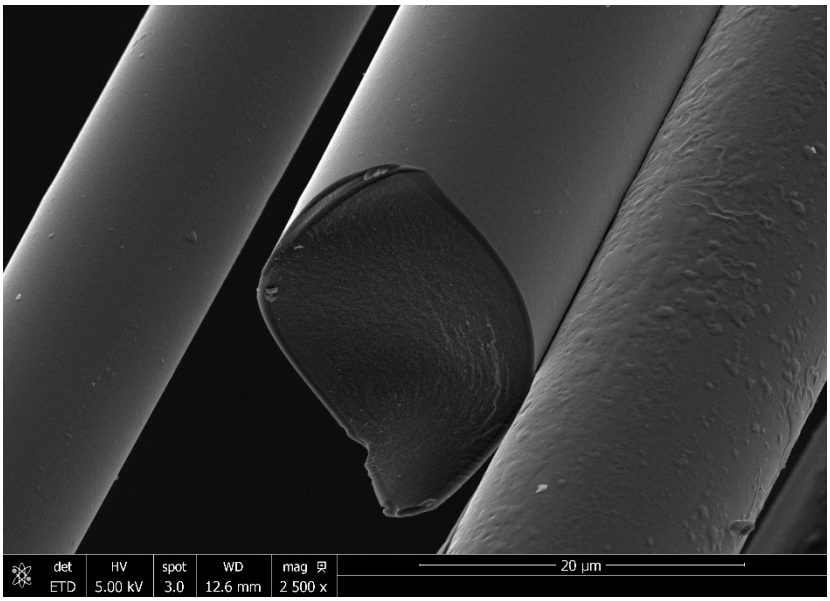

Figure 96 - SEM micrograph of Hi-Nicalon™ S fiber tow specimen "Air 9" examining the silica scale thickness of a fiber along the upper portion of the fiber tow. Note differences in fiber surface content (σ_{cr} = 600 MPa, t_f = 100† hrs).

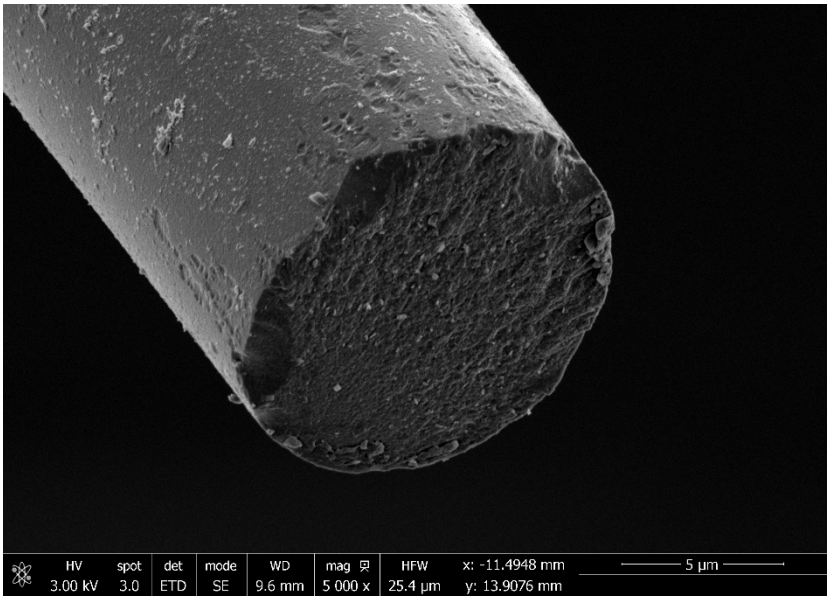

Figure 97 - SEM micrograph of Hi-Nicalon™ S fiber tow specimen "Air 10" examining the fracture surface of a fiber along the upper portion of the fiber tow (σ_{cr} = 650 MPa, t_f = 2.24 hrs).

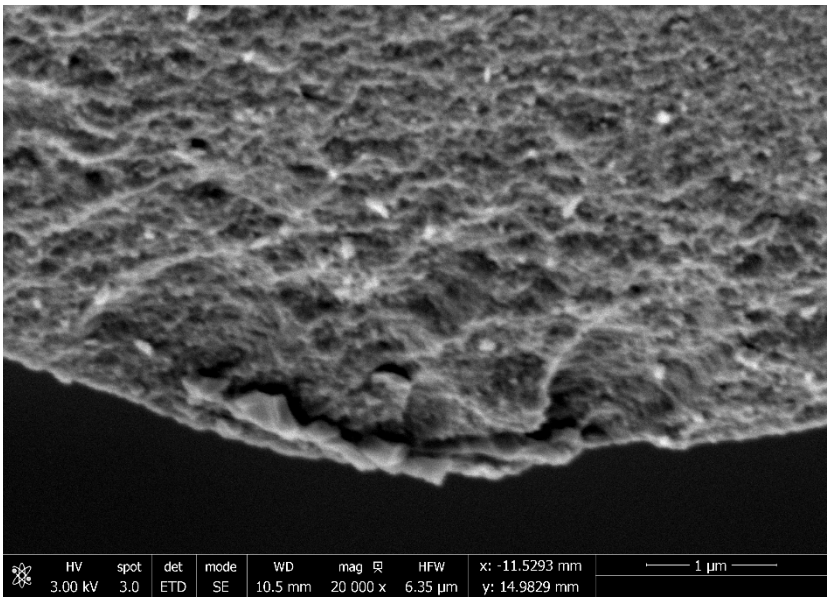

Figure 98 - SEM micrograph of Hi-Nicalon™ S fiber tow specimen "Air 10" examining features on the fracture surface of a fiber along the upper portion of the fiber tow (σ_{cr} = 650 MPa, t_f = 2.24 hrs).

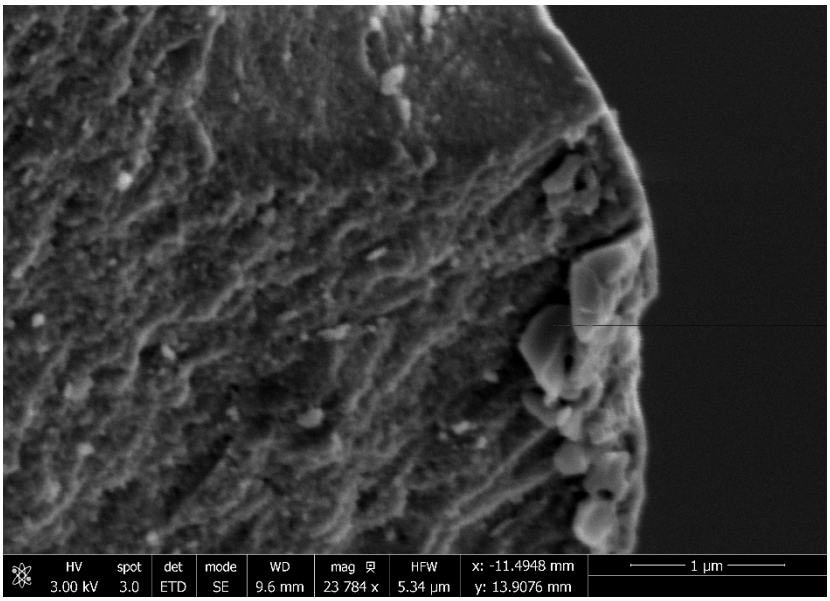

Figure 99 - SEM micrograph of Hi-Nicalon™ S fiber tow specimen "Air 10" examining features on the fracture surface of a fiber along the upper portion of the fiber tow (σ_{cr} = 650 MPa, t_f = 2.24 hrs).

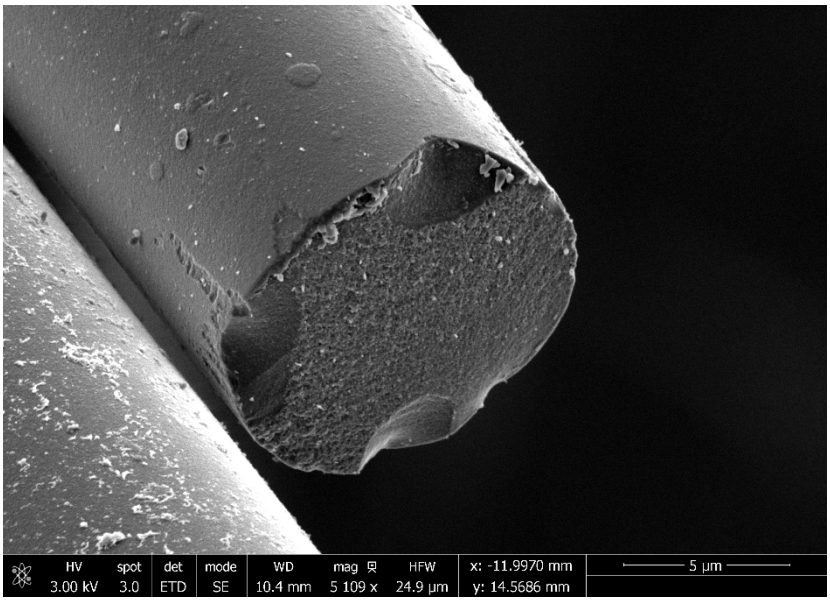

Figure 100 - SEM micrograph of Hi-Nicalon™ S fiber tow specimen "Air 10" examining the fracture surface of a fiber along the upper portion of the fiber tow (σ_{cr} = 650 MPa, t_f = 2.24 hrs).

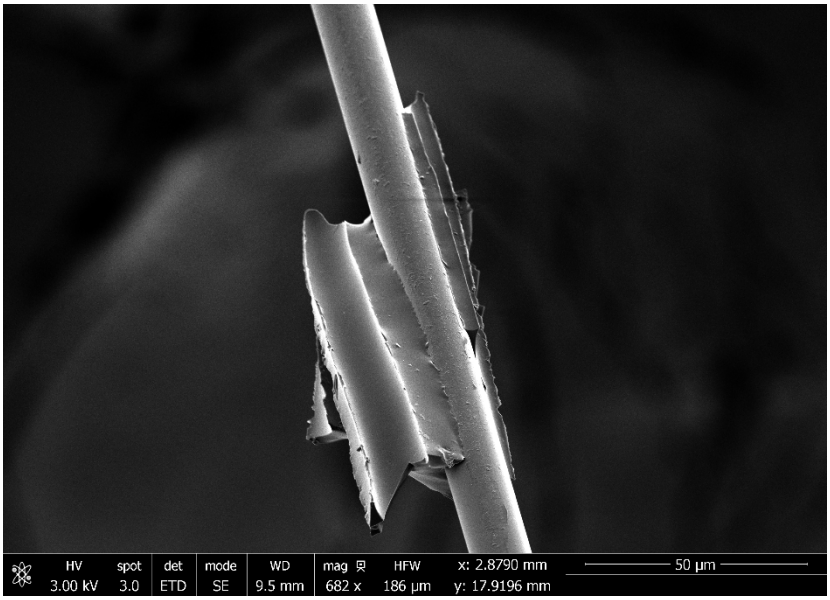

Figure 101 - SEM micrograph of Hi-Nicalon™ S fiber tow specimen "Air 10" examining features on the surface of a fiber along the lower portion of the fiber tow (σ_{cr} = 650 MPa, t_f = 2.24 hrs).

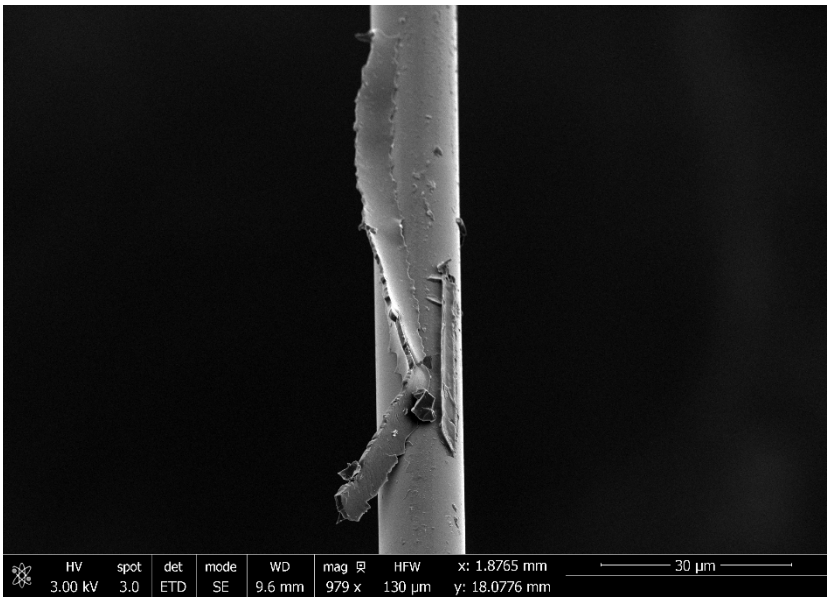

Figure 102 - SEM micrograph of Hi-Nicalon™ S fiber tow specimen "Air 10" examining features on the surface of a fiber along the lower portion of the fiber tow (σ_{cr} = 650 MPa, t_f = 2.24 hrs).

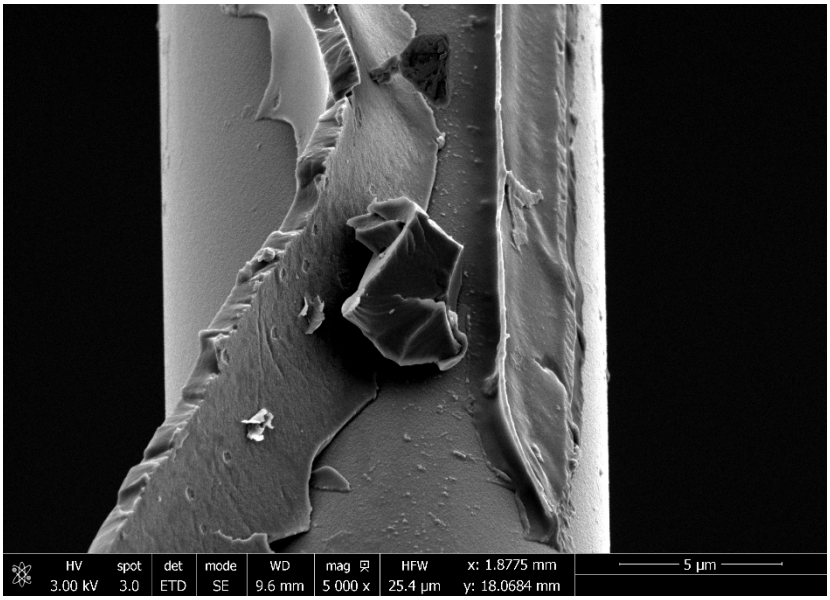

Figure 103 - SEM micrograph of Hi-Nicalon™ S fiber tow specimen "Air 10" examining features on the surface of a fiber along the lower portion of the fiber tow (σ_{cr} = 650 MPa, t_f = 2.24 hrs).

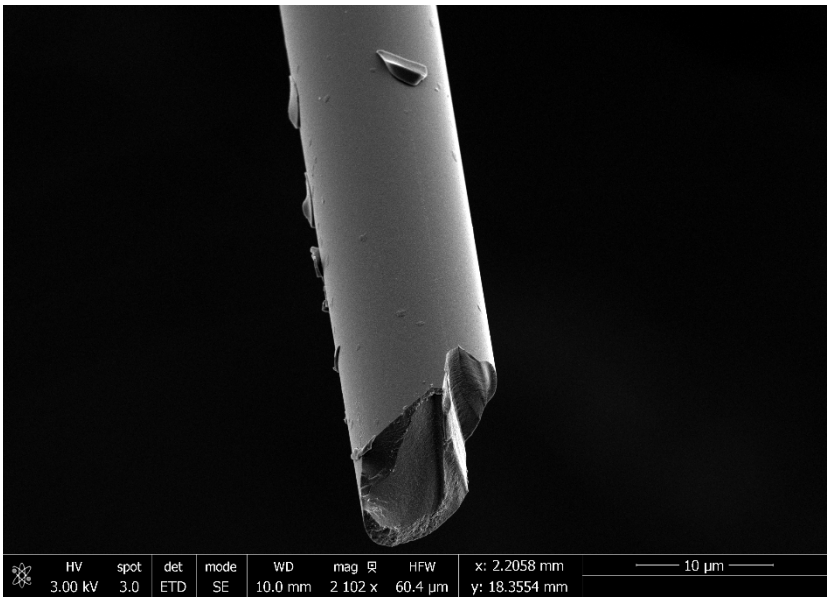

Figure 104 - SEM micrograph of Hi-Nicalon™ S fiber tow specimen "Air 10" examining the fracture surface of a fiber along the lower portion of the fiber tow (σ_{cr} = 650 MPa, t_f = 2.24 hrs).

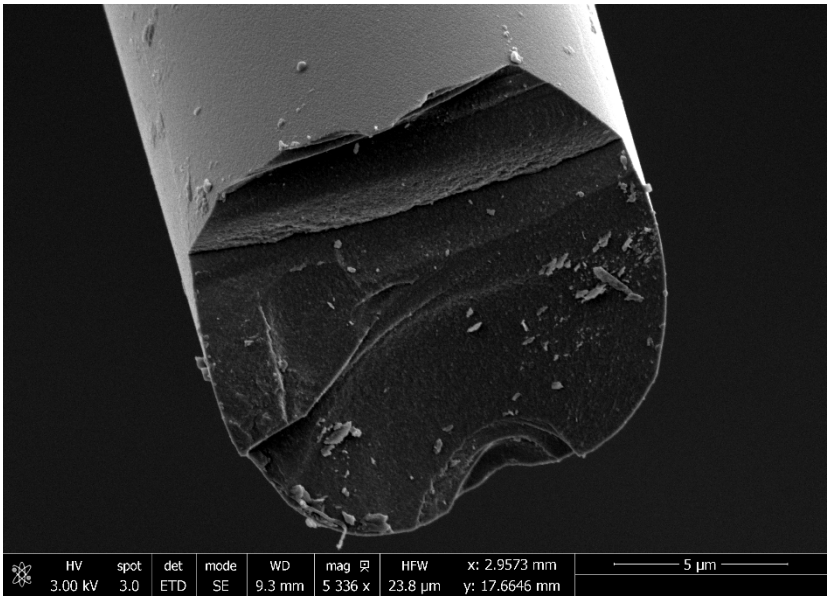

Figure 105 - SEM micrograph of Hi-Nicalon™ S fiber tow specimen "Air 10" examining the fracture surface of a fiber along the lower portion of the fiber tow (σ_{cr} = 650 MPa, t_f = 2.24 hrs).

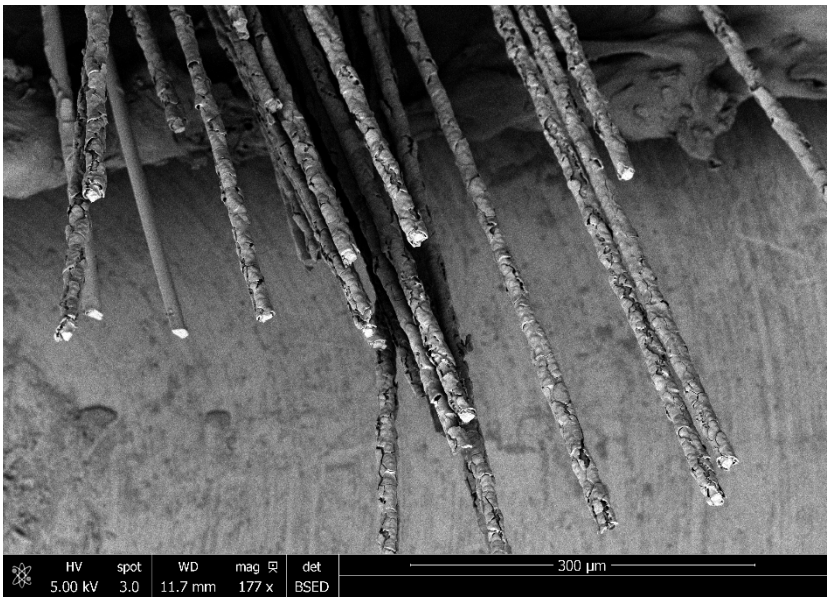

Figure 106 - SEM electron backscatter deflection micrograph of Hi-Nicalon™ S fiber tow specimen "Steam 1" examining a group of fibers along the lower portion of the fiber tow. Note the considerable buildup of what appears to be silica scale due to duration of saturated steam exposure (σ_{cr} = 3.5 MPa, t_f = 100† hrs).

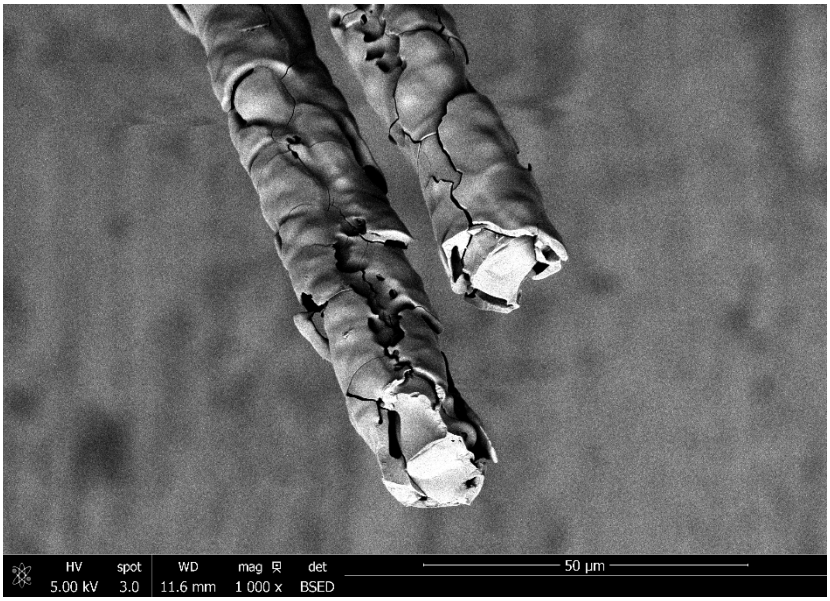

Figure 107 - SEM electron backscatter deflection micrograph of Hi-Nicalon™ S fiber tow specimen "Steam 1" examining fibers along the lower portion of the fiber tow. Note the considerable buildup of what appears to be silica scale due to duration of saturated steam exposure (σ_{cr} = 3.5 MPa, t_f = 100† hrs).

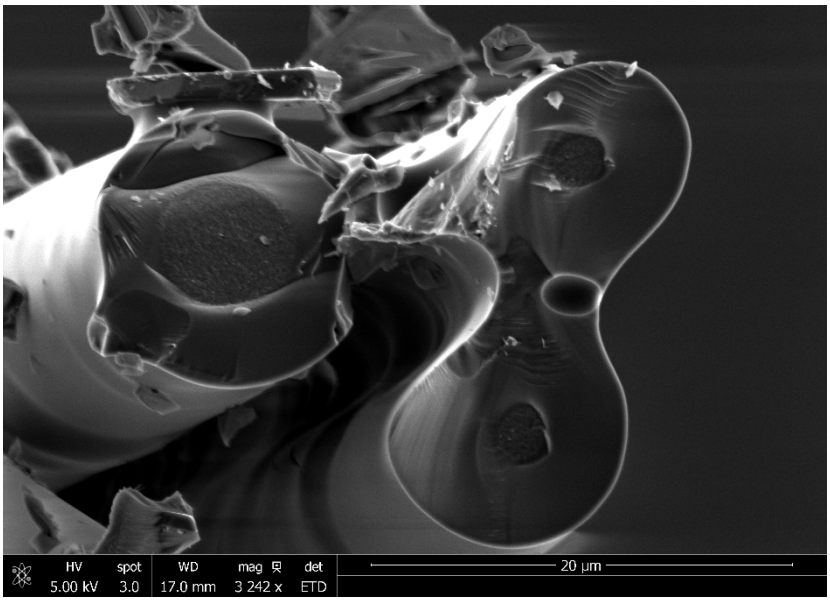

Figure 108 - SEM micrograph of Hi-Nicalon™ S fiber tow specimen "Steam 1" examining fibers along the lower portion of the fiber tow. Note the some of the fibers have almost been completely consumed by silica scale due to duration of saturated steam exposure (σ_{cr} = 3.5 MPa, t_f = 100† hrs).

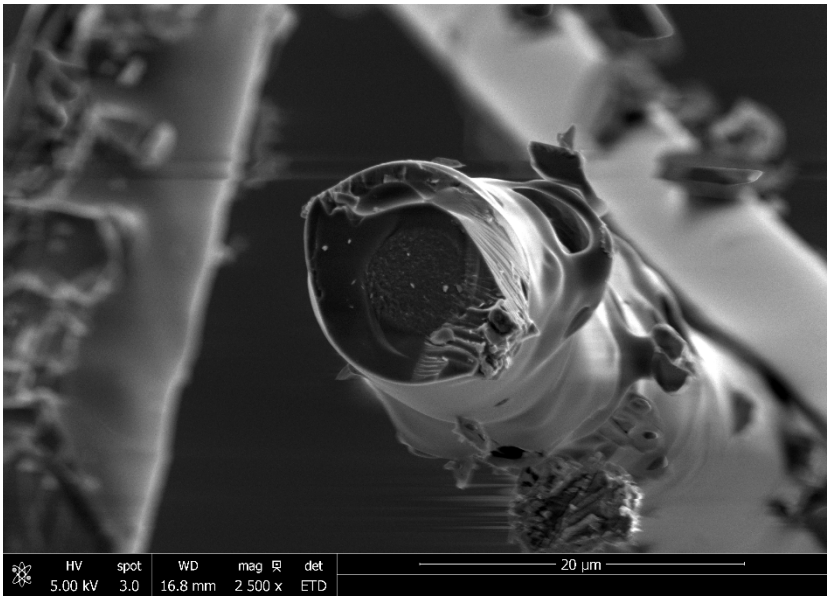

Figure 109 - SEM micrograph of Hi-Nicalon™ S fiber tow specimen "Steam 1" examining a fiber along the lower portion of the fiber tow. Note the thick amount of oxide scale as well as the "mushroom" like nodules along the fiber length (σ_{cr} = 3.5 MPa, t_f = 100† hrs).

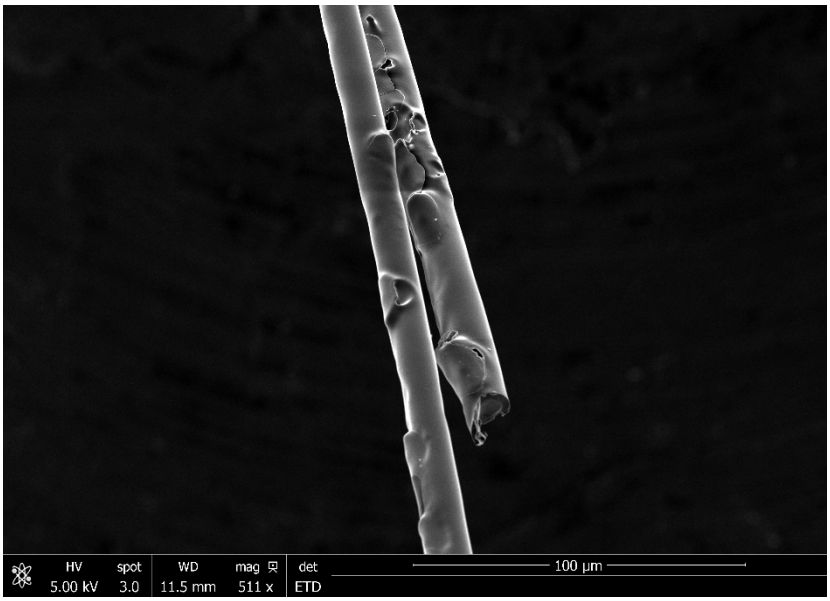

Figure 110 - SEM micrograph of Hi-Nicalon™ S fiber tow specimen "Steam 1" examining a fiber along the lower portion of the fiber tow. Note the buildup along the fibers exterior surface (σ_{cr} = 3.5 MPa, t_f = 100† hrs).

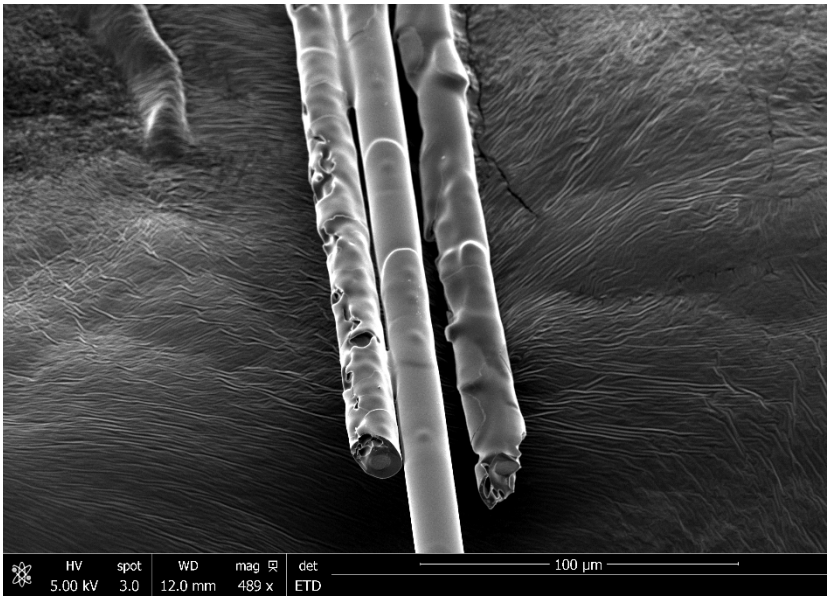

Figure 111 - SEM micrograph of Hi-Nicalon™ S fiber tow specimen "Steam 1" examining fibers along the lower portion of the fiber tow. Note the excessive buildup of silica scale as well as cavitation present (σ_{cr} = 3.5 MPa, t_f = 100† hrs).

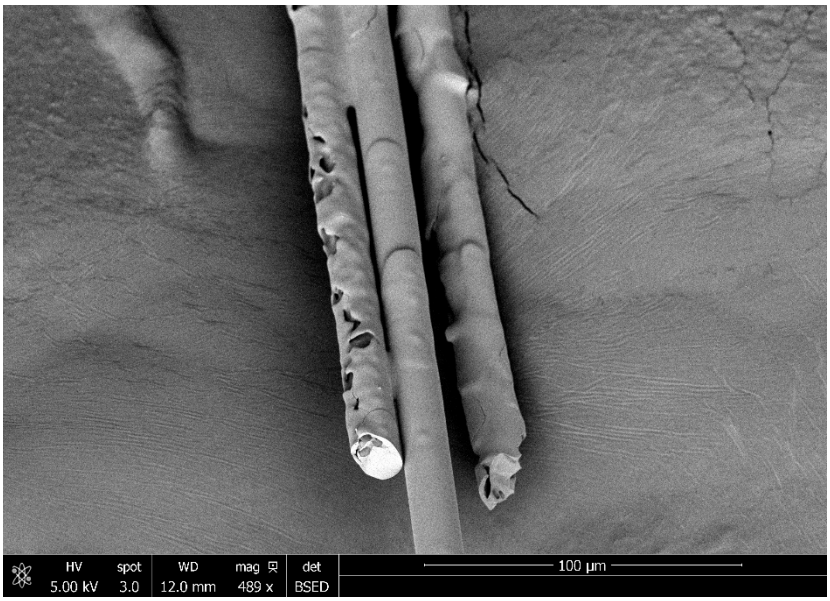

Figure 112 - SEM electron backscatter deflection micrograph of Hi-Nicalon™ S fiber tow specimen "Steam 1" examining fibers along the lower portion of the fiber tow. Note the excessive buildup of silica scale as well as cavitation present (σ_{cr} = 3.5 MPa, t_f = 100† hrs).

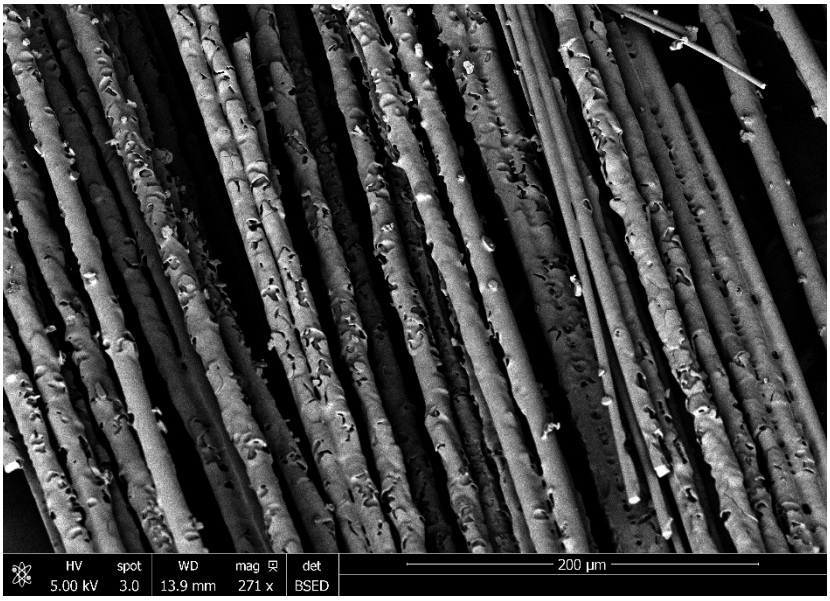

Figure 113 - SEM electron backscatter deflection micrograph of Hi-Nicalon™ S fiber tow specimen "Steam 1" examining a group of fibers along the lower portion of the fiber tow. Note the nodules and pitting along the fibers surfaces (σ_{cr} = 3.5 MPa, t_f = 100† hrs).

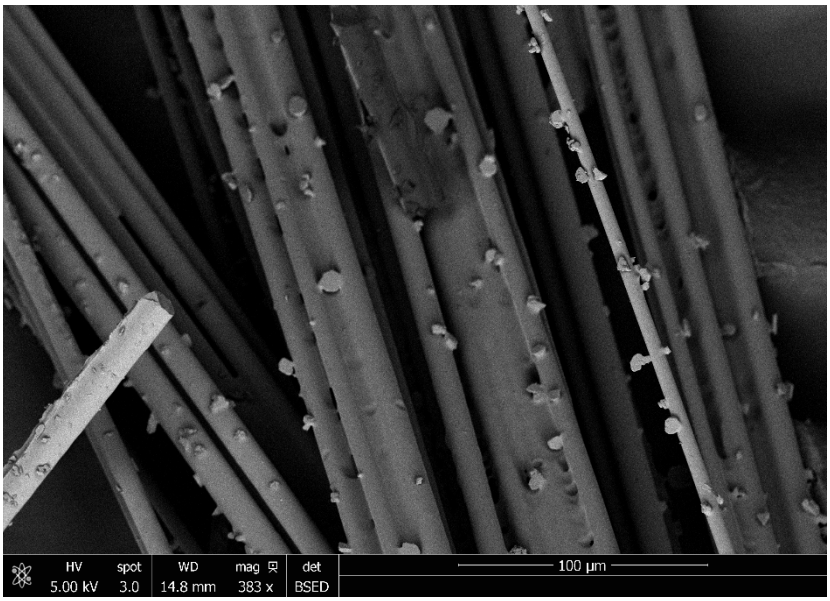

Figure 114 - SEM electron backscatter deflection micrograph of Hi-Nicalon™ S fiber tow specimen "Steam 1" examining a group of fibers along the lower portion of the fiber tow. Note the nodules along the fibers surfaces (σ_{cr} = 3.5 MPa, t_f = 100† hrs).

Figure 115 - SEM electron backscatter deflection micrograph of Hi-Nicalon™ S fiber tow specimen "Steam 1" examining a fiber along the lower portion of the fiber tow. Note the cavitation within the silica scale (σ_{cr} = 3.5 MPa, t_f = 100† hrs).

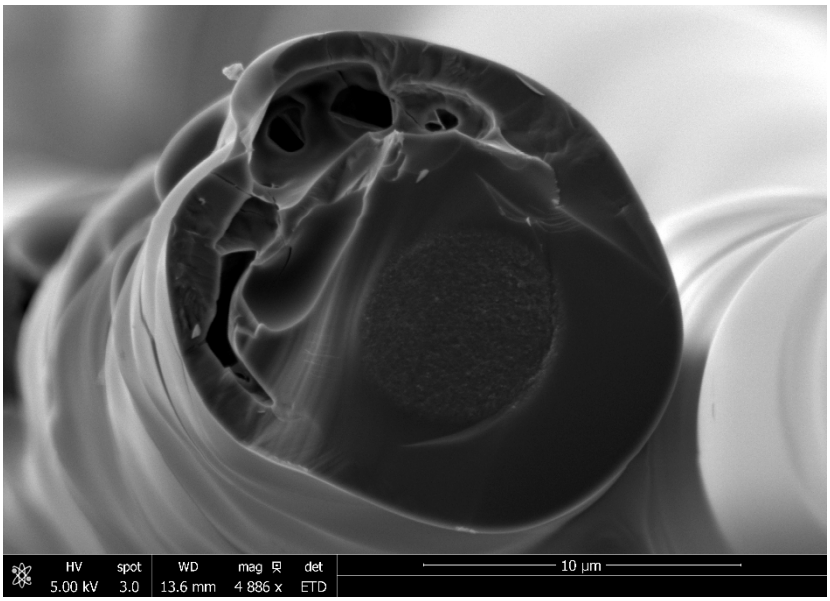

Figure 116 - SEM micrograph of Hi-Nicalon™ S fiber tow specimen "Steam 1" examining a fiber along the lower portion of the fiber tow. Note the cavitation within the silica scale (σ_{cr} = 3.5 MPa, t_f = 100† hrs).

Figure 117 - SEM micrograph of Hi-Nicalon™ S fiber tow specimen "Steam 1" examining fibers along the lower portion of the fiber tow. Note the thickness of the silica scale as well as cavitation (σ_{cr} = 3.5 MPa, t_f = 100† hrs).

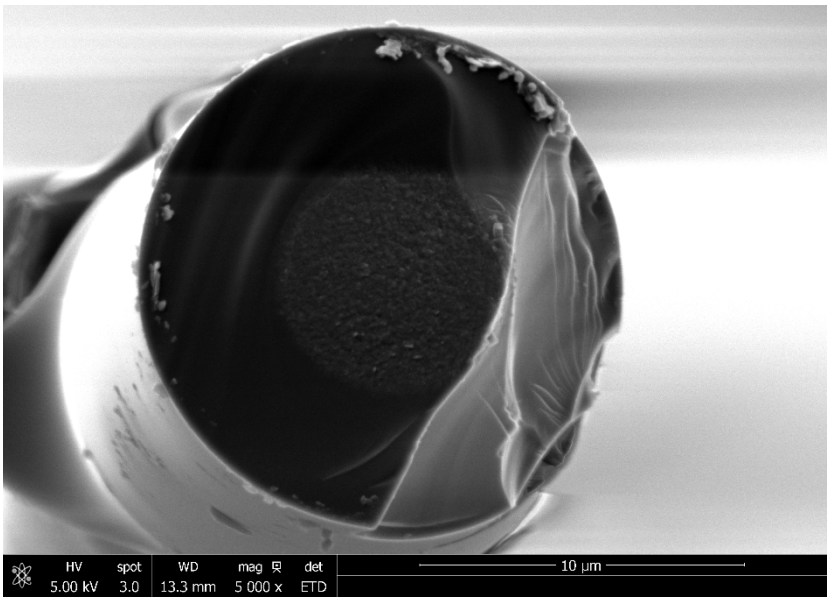

Figure 118 - SEM micrograph of Hi-Nicalon™ S fiber tow specimen "Steam 1" examining a fiber along the lower portion of the fiber tow. Note the thickness of the silica scale (σ_{cr} = 3.5 MPa, t_f = 100† hrs).

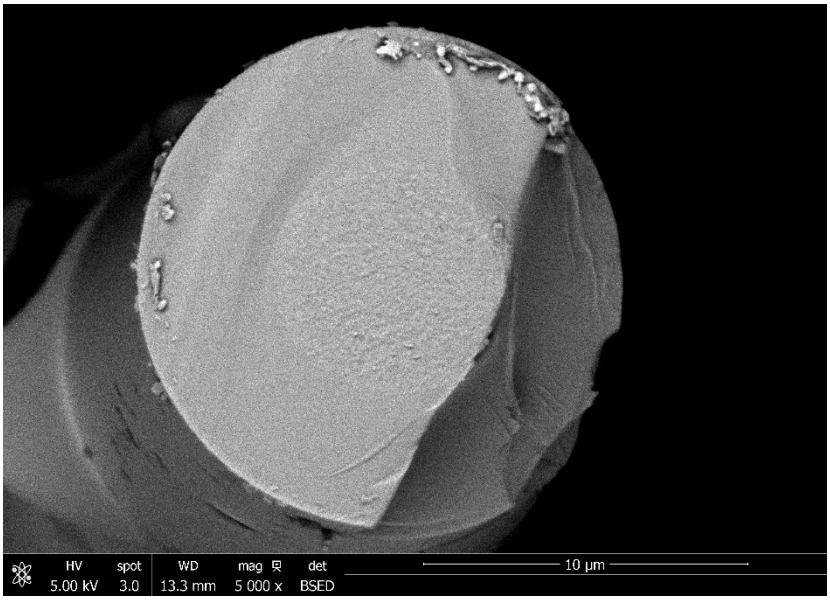

Figure 119 - SEM electron backscatter deflection micrograph of Hi-Nicalon™ S fiber tow specimen "Steam 1" examining a fiber along the lower portion of the fiber tow. Note the thickness of the silica scale (σ_{cr} = 3.5 MPa, t_f = 100† hrs).

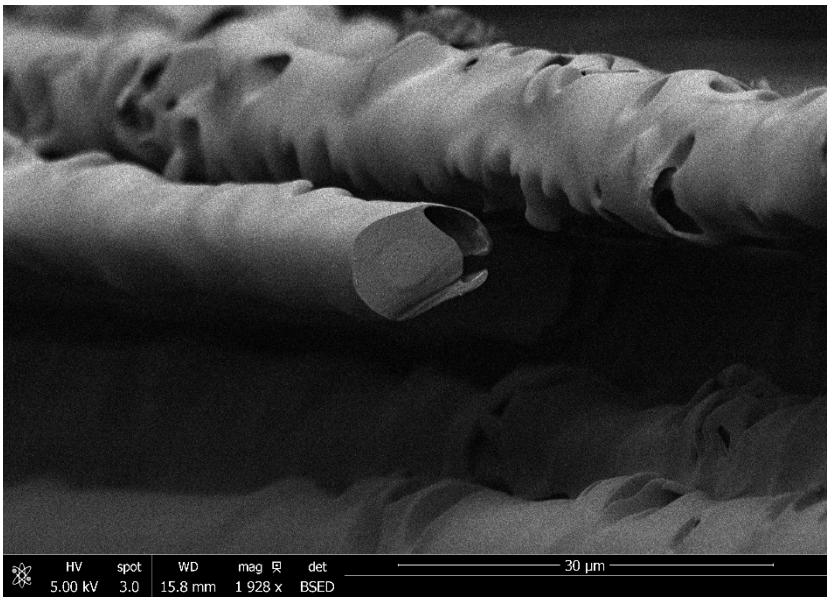

Figure 120 – SEM electron backscatter deflection micrograph of Hi-Nicalon™ S fiber tow specimen "Steam 1" examining fibers along the lower portion of the fiber tow. Note the thickness of the silica scale and cavitation present along the fiber surface (σ_{cr} = 3.5 MPa, t_f = 100† hrs).

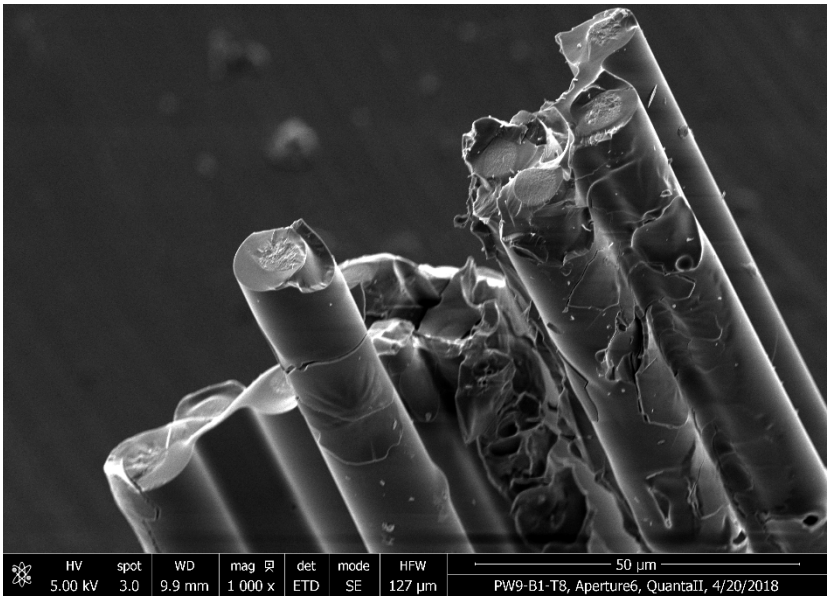

Figure 121 - SEM micrograph of Hi-Nicalon™ S fiber tow specimen "Steam 1" examining fibers along the midpoint of the fiber tow. Note the excessive silica scale growth, welding multiple fibers together (σ_{cr} = 3.5 MPa, t_f = 100† hrs).

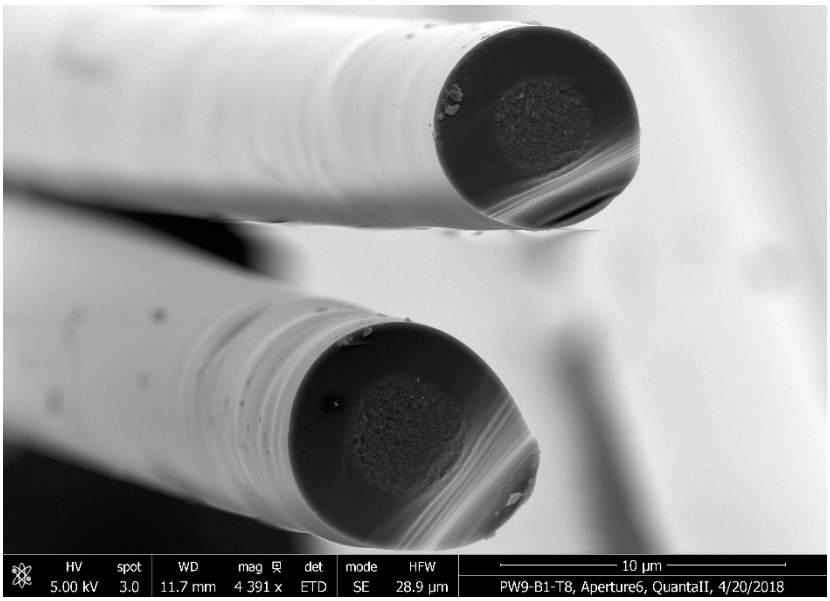

Figure 122 - SEM micrograph of Hi-Nicalon™ S fiber tow specimen "Steam 1" examining fibers along the midpoint of the fiber tow. Note the thickness of the silica scale (σ_{cr} = 3.5 MPa, t_f = 100† hrs).

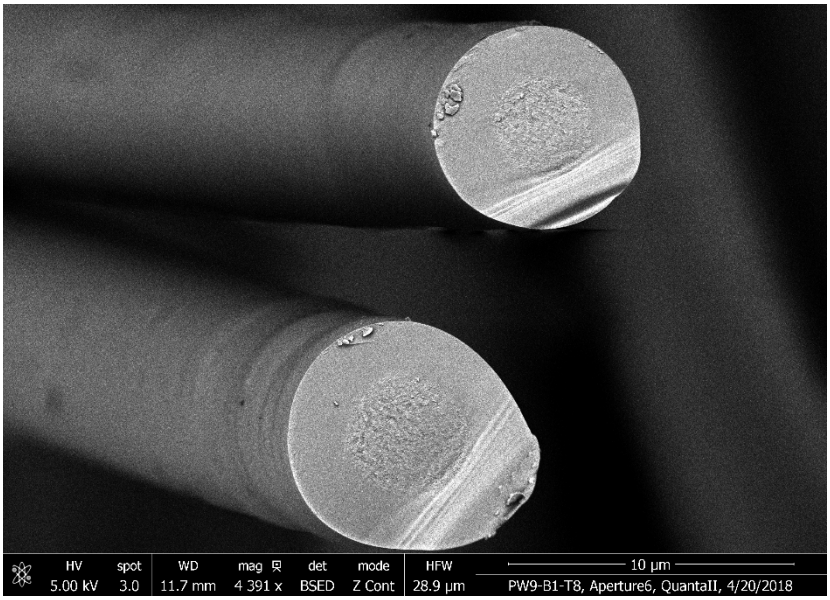

Figure 123 – SEM electron backscatter deflection micrograph of Hi-Nicalon™ S fiber tow specimen "Steam 1" examining fibers along the midpoint of the fiber tow. Note the thickness of the silica scale (σ_{cr} = 3.5 MPa, t_f = 100† hrs).

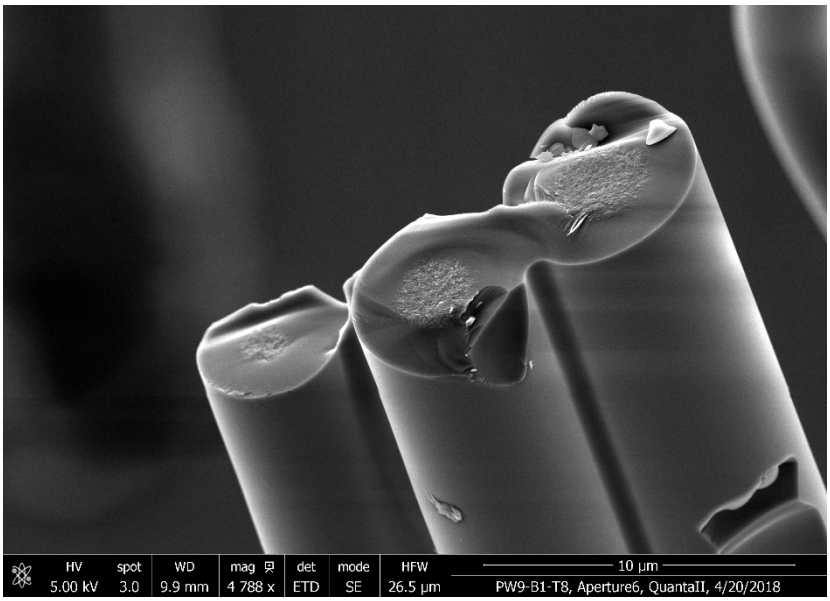

Figure 124 - SEM micrograph of Hi-Nicalon™ S fiber tow specimen "Steam 1" examining fibers along the midpoint of the fiber tow. Note the thickness of the silica scale that has welded the fibers together (σ_{cr} = 3.5 MPa, t_f = 100† hrs).

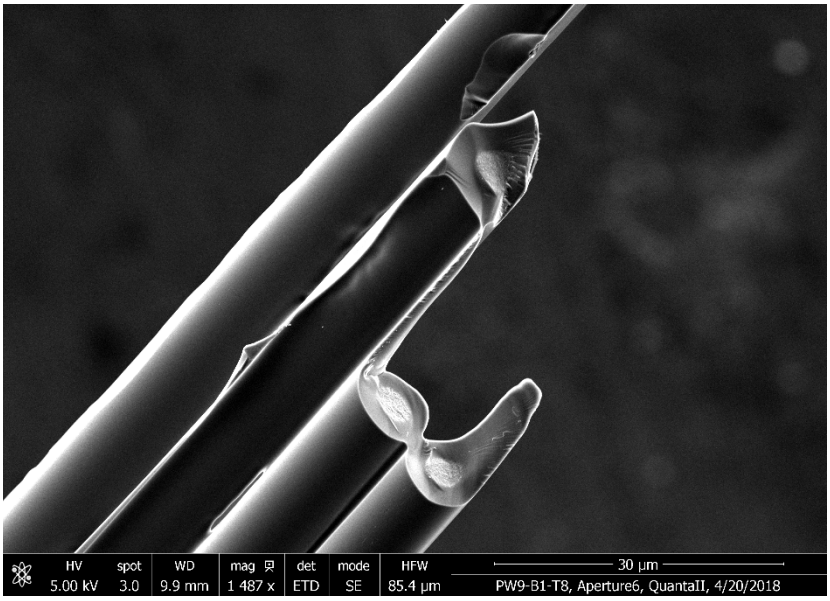

Figure 125 - SEM micrograph of Hi-Nicalon™ S fiber tow specimen "Steam 1" examining fibers along the midpoint of the fiber tow. Note the thickness of the silica scale that has welded the fibers together (σ_{cr} = 3.5 MPa, t_f = 100† hrs).

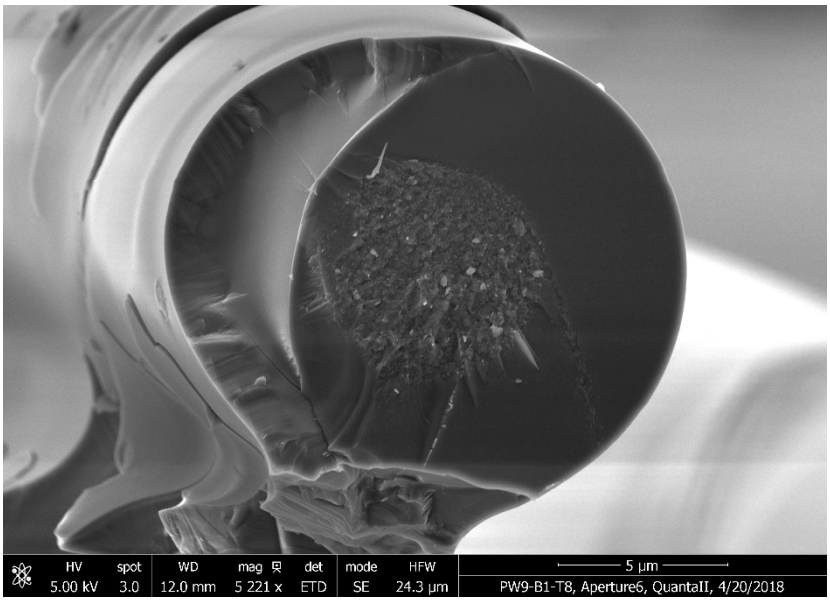

Figure 126 - SEM micrograph of Hi-Nicalon™ S fiber tow specimen "Steam 1" examining a fiber along the midpoint of the fiber tow. Note the thickness of the silica scale that has almost consumed the fiber (σ_{cr} = 3.5 MPa, t_f = 100† hrs).

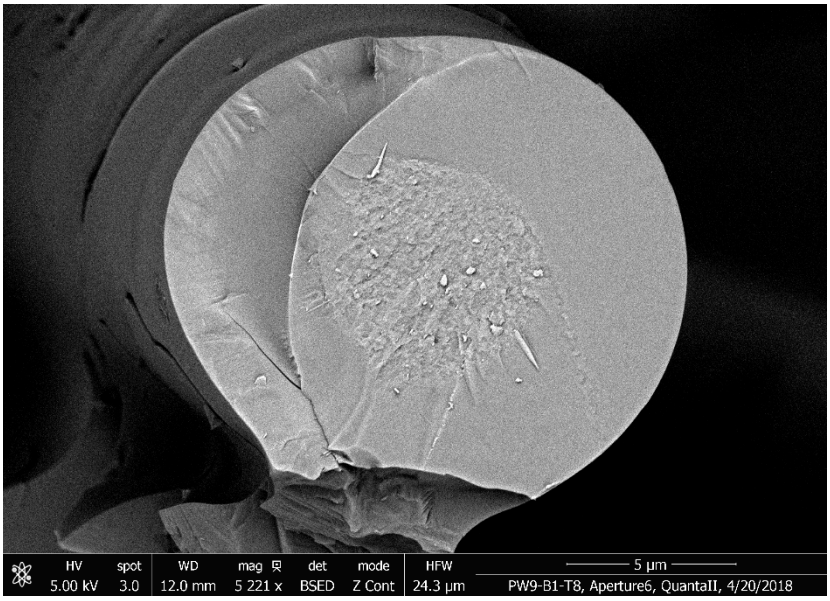

Figure 127 - SEM electron backscatter deflection micrograph of Hi-Nicalon™ S fiber tow specimen "Steam 1" examining a fiber along the midpoint of the fiber tow. Note the thickness of the silica scale that has almost consumed the fiber (σ_{cr} = 3.5 MPa, t_f = 100† hrs).

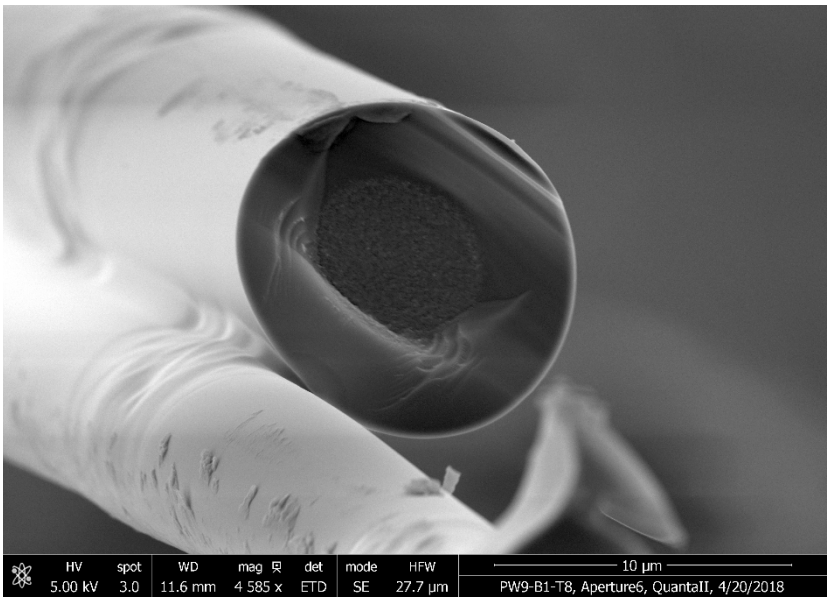

Figure 128 - SEM micrograph of Hi-Nicalon™ S fiber tow specimen "Steam 1" examining a fiber along the midpoint of the fiber tow. Note the thickness of the silica scale (σ_{cr} = 3.5 MPa, t_f = 100† hrs).

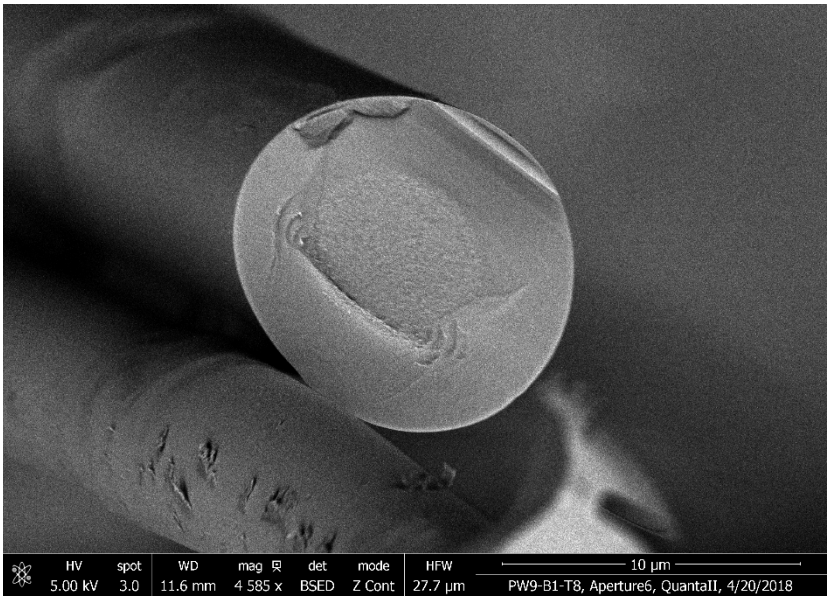

Figure 129 - SEM electron backscatter deflection micrograph of Hi-Nicalon™ S fiber tow specimen "Steam 1" examining a fiber along the midpoint of the fiber tow. Note the thickness of the silica scale (σ_{cr} = 3.5 MPa, t_f = 100† hrs).

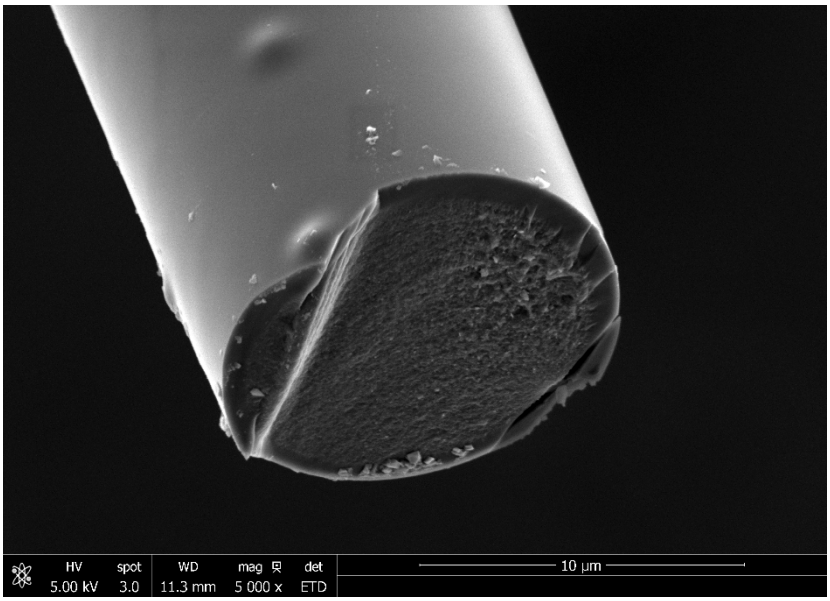

Figure 130 - SEM micrograph of Hi-Nicalon™ S fiber tow specimen "Steam 1" examining a fiber along the upper portion of the fiber tow (σ_{cr} = 3.5 MPa, t_f = 100† hrs).

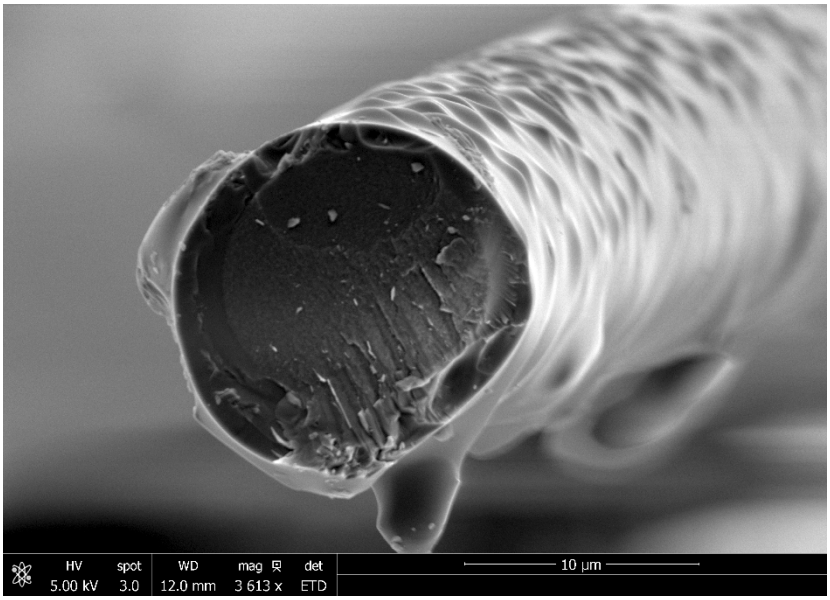

Figure 131 - SEM micrograph of Hi-Nicalon™ S fiber tow specimen "Steam 1" examining a fiber along the upper portion of the fiber tow. Note signs of dewetting along the fiber surface (σ_{cr} = 3.5 MPa, t_f = 100† hrs).

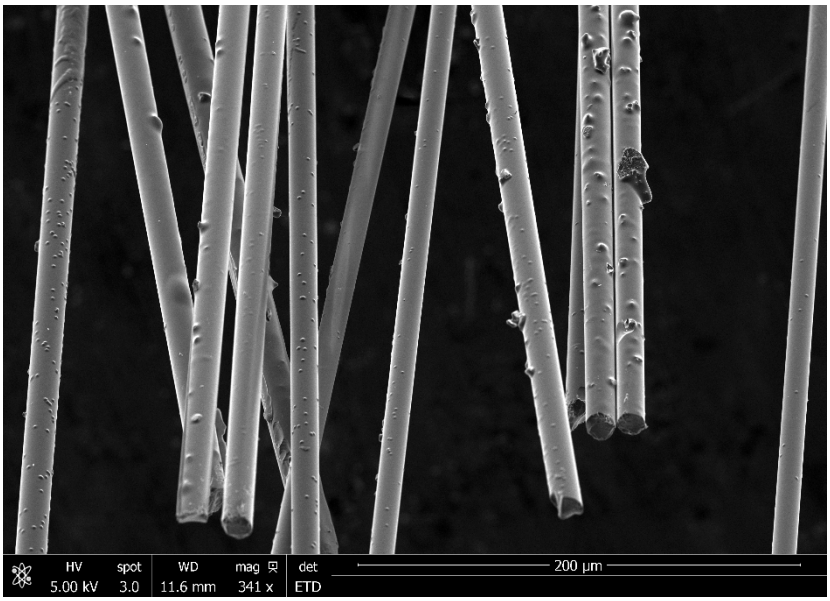

Figure 132 - SEM micrograph of Hi-Nicalon™ S fiber tow specimen "Steam 1" examining a group of fibers along the upper portion of the fiber tow. Note signs of dewetting and nodules along the fiber surfaces (σ_{cr} = 3.5 MPa, t_f = 100† hrs).

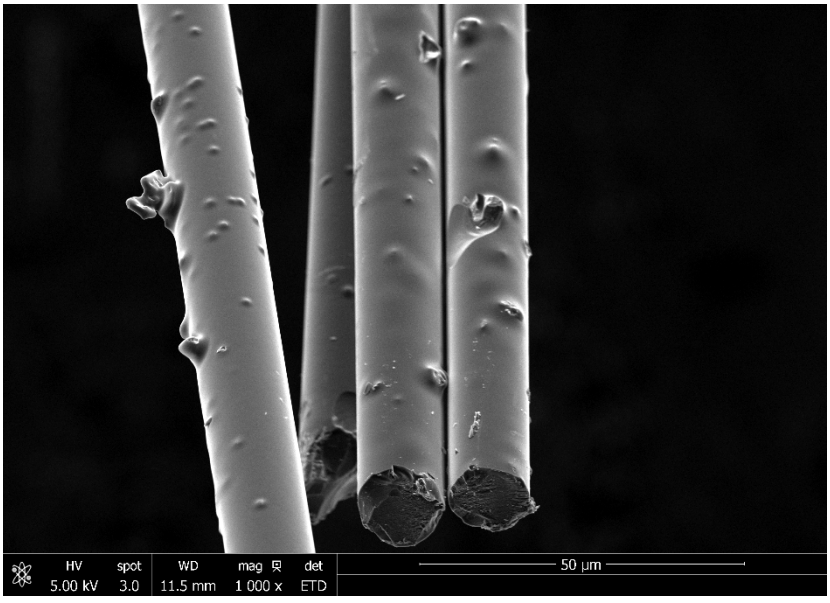

Figure 133 - SEM micrograph of Hi-Nicalon™ S fiber tow specimen "Steam 1" examining a group of fibers along the upper portion of the fiber tow. Note signs of dewetting and nodules along the fiber surfaces (σ_{cr} = 3.5 MPa, t_f = 100† hrs).

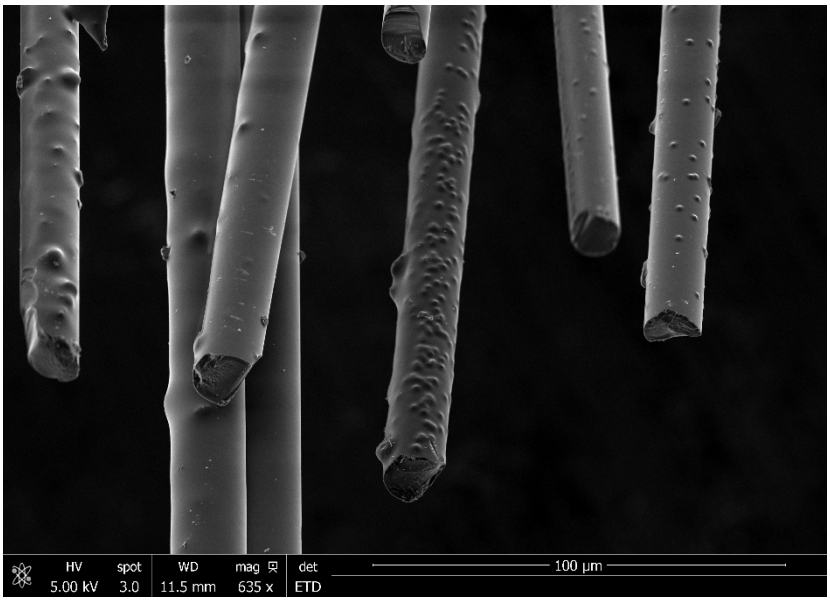

Figure 134 - SEM micrograph of Hi-Nicalon™ S fiber tow specimen "Steam 1" examining a group of fibers along the upper portion of the fiber tow. Note signs of dewetting along the fiber surfaces (σ_{cr} = 3.5 MPa, t_f = 100† hrs).

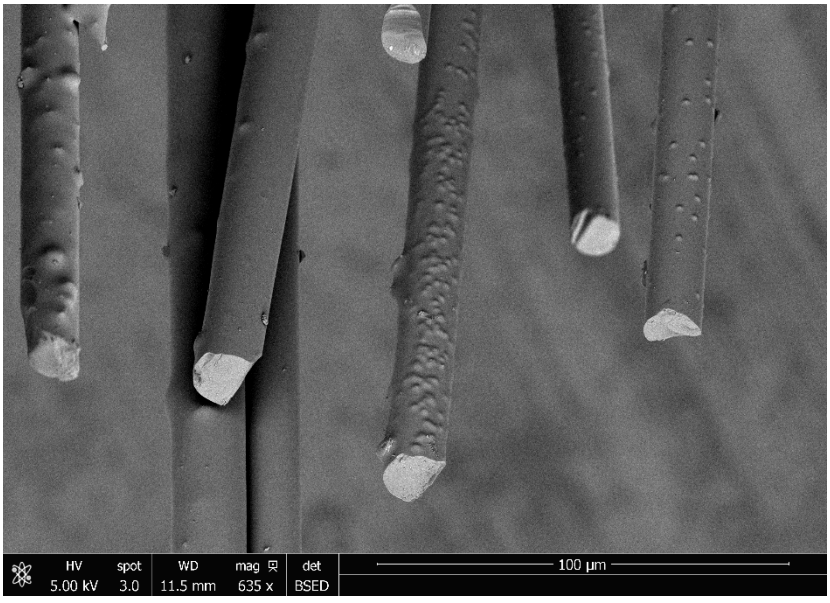

Figure 135 - SEM electron backscatter deflection micrograph of Hi-Nicalon™ S fiber tow specimen "Steam 1" examining a group of fibers along the upper portion of the fiber tow. Note signs of dewetting along the fiber surfaces (σ_{cr} = 3.5 MPa, t_f = 100† hrs).

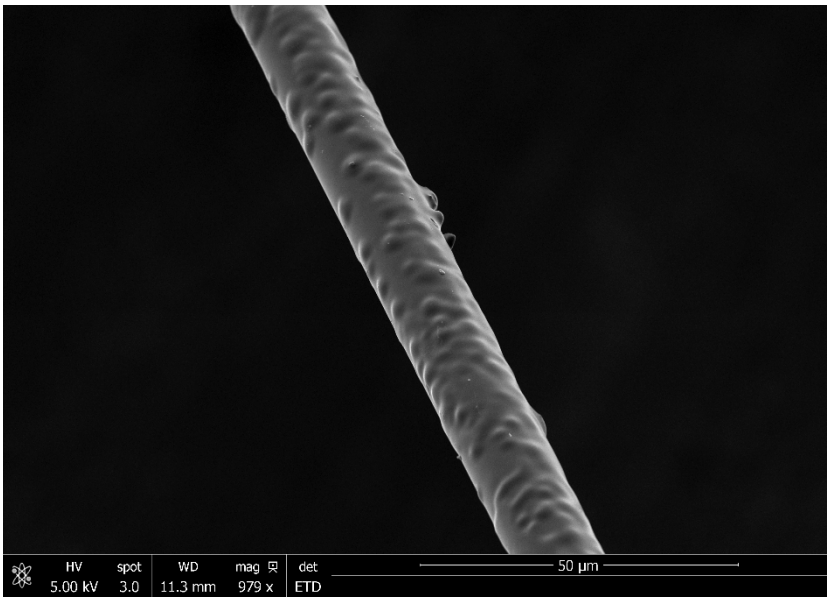

Figure 136 - SEM micrograph of Hi-Nicalon™ S fiber tow specimen "Steam 1" examining a fiber surface along the upper portion of the fiber tow. Note signs of dewetting present (σ_{cr} = 3.5 MPa, t_f = 100† hrs).

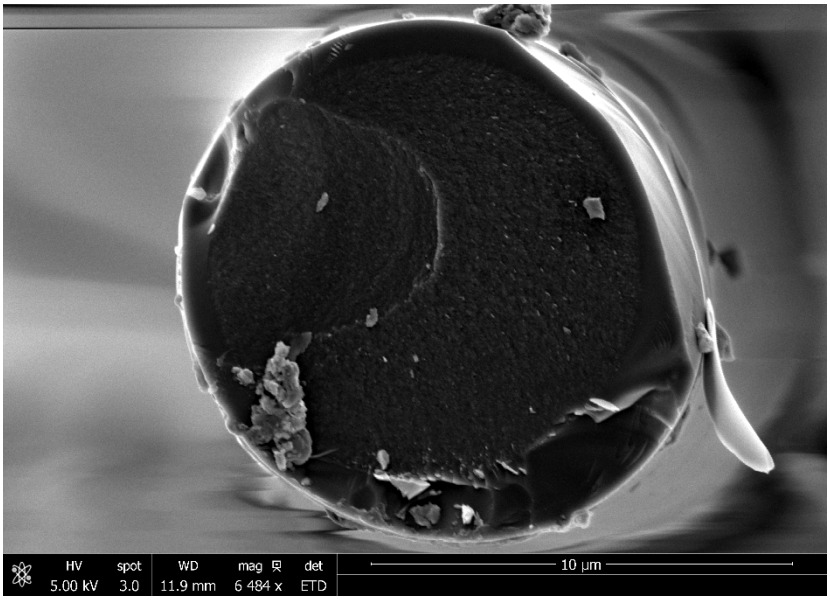

Figure 137 - SEM micrograph of Hi-Nicalon™ S fiber tow specimen "Steam 1" examining a fiber along the upper portion of the fiber tow. Note the asymmetrical thickness of oxide scale around the fiber (σ_{cr} = 3.5 MPa, t_f = 100† hrs).

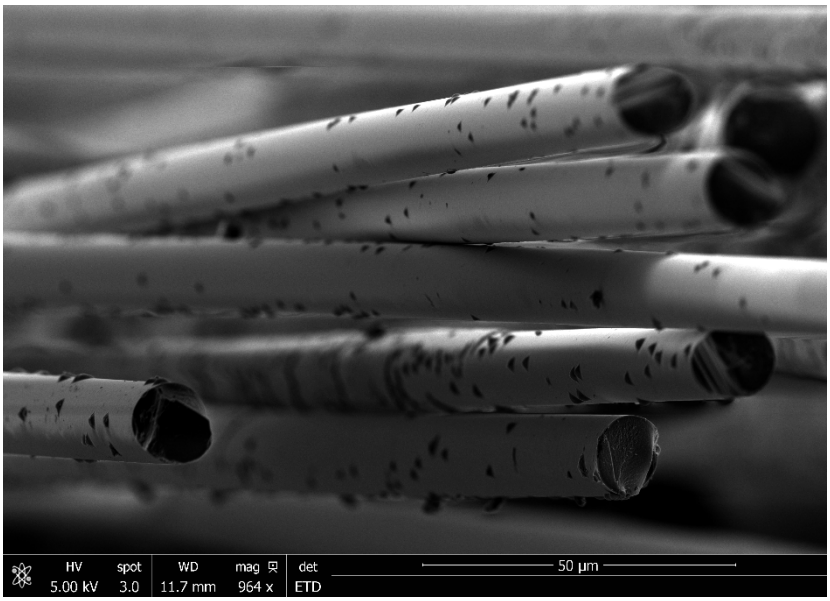

Figure 138 - SEM micrograph of Hi-Nicalon™ S fiber tow specimen "Steam 1" examining the fiber surfaces of a group of fibers along the upper portion of the fiber tow. Note signs of dewetting along the fiber surfaces (σ_{cr} = 3.5 MPa, t_f = 100† hrs).

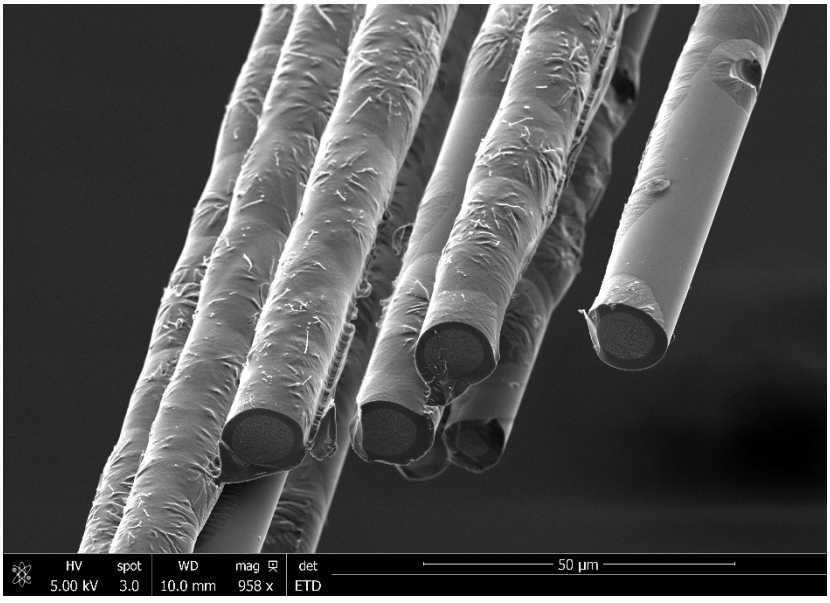

Figure 139 - SEM micrograph of Hi-Nicalon™ S fiber tow specimen "Steam 4" examining the fracture surfaces of a group of fibers along the lower portion of the fiber tow. Note areas of silica amorphous and crystallized scale growth (σ_{cr} = 255 MPa, t_f = 38.04 hrs).

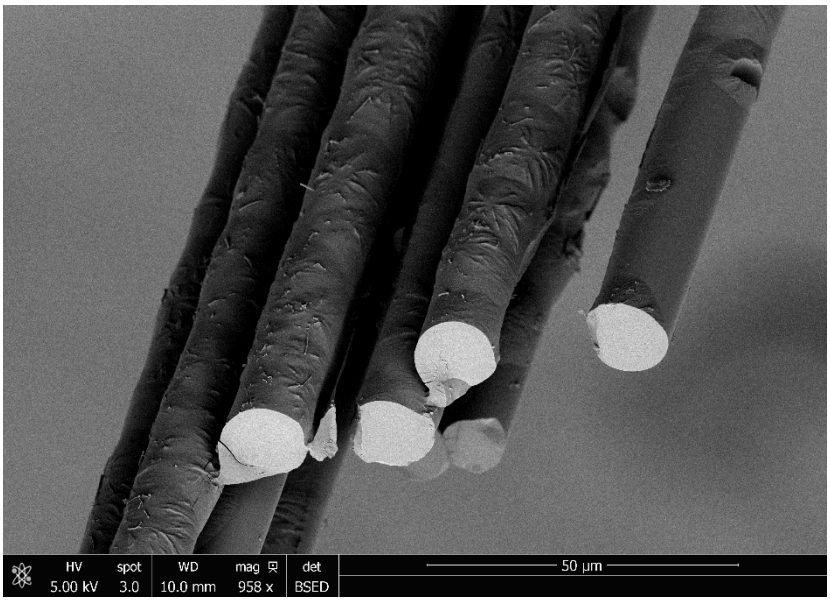

Figure 140 - SEM electron backscatter deflection micrograph of Hi-Nicalon™ S fiber tow specimen "Steam 4" examining the fracture surfaces of a group of fibers along the lower portion of the fiber tow. Note areas of silica amorphous and crystallized scale growth (σ_{cr} = 255 MPa, t_f = 38.04 hrs).

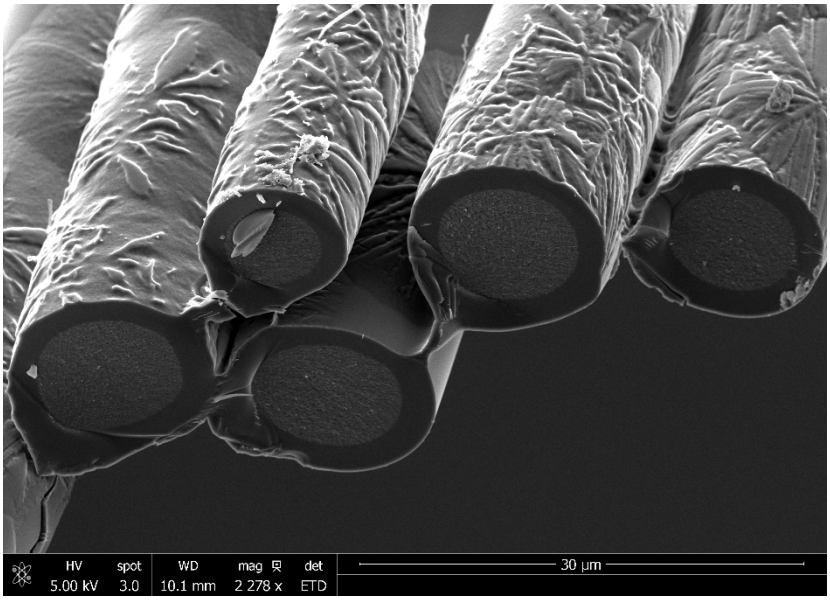

Figure 141 - SEM micrograph of Hi-Nicalon™ S fiber tow specimen "Steam 4" examining the fracture surfaces of a group of fibers along the lower portion of the fiber tow. Note crystallized scale growth along the fiber surfaces (σ_{cr} = 255 MPa, t_f = 38.04 hrs).

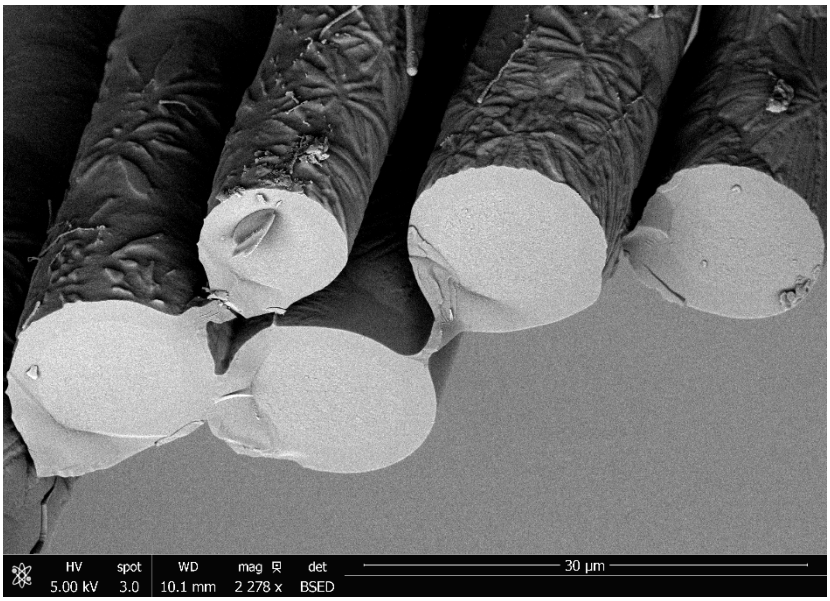

Figure 142 - SEM electron backscatter deflection micrograph of Hi-Nicalon™ S fiber tow specimen "Steam 4" examining the fracture surfaces of a group of fibers along the lower portion of the fiber tow. Note crystallized scale growth along the fiber surfaces (σ_{cr} = 255 MPa, t_f = 38.04 hrs).

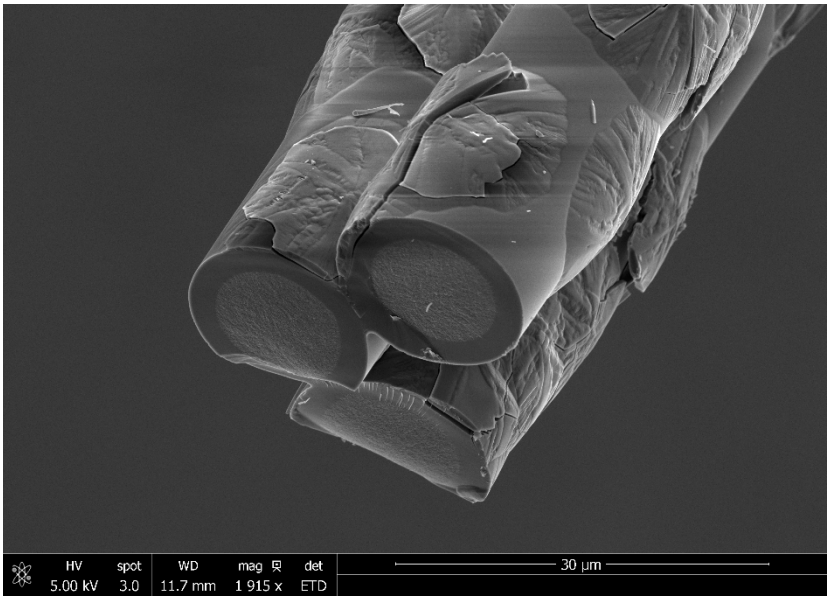

Figure 143 - SEM micrograph of Hi-Nicalon™ S fiber tow specimen "Steam 4" examining the fracture surfaces of a group of fibers along the lower portion of the fiber tow. Note areas of silica amorphous and crystallized scale growth (σ_{cr} = 255 MPa, t_f = 38.04 hrs).

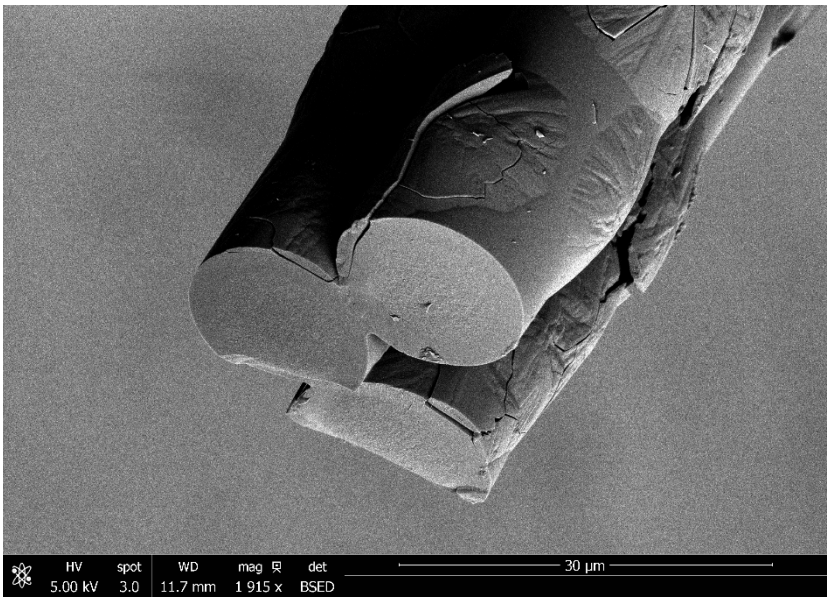

Figure 144 – SEM electron backscatter deflection micrograph of Hi-Nicalon™ S fiber tow specimen "Steam 4" examining the fracture surfaces of a group of fibers along the lower portion of the fiber tow. Note areas of silica amorphous and crystallized scale growth (σ_{cr} = 255 MPa, t_f = 38.04 hrs).

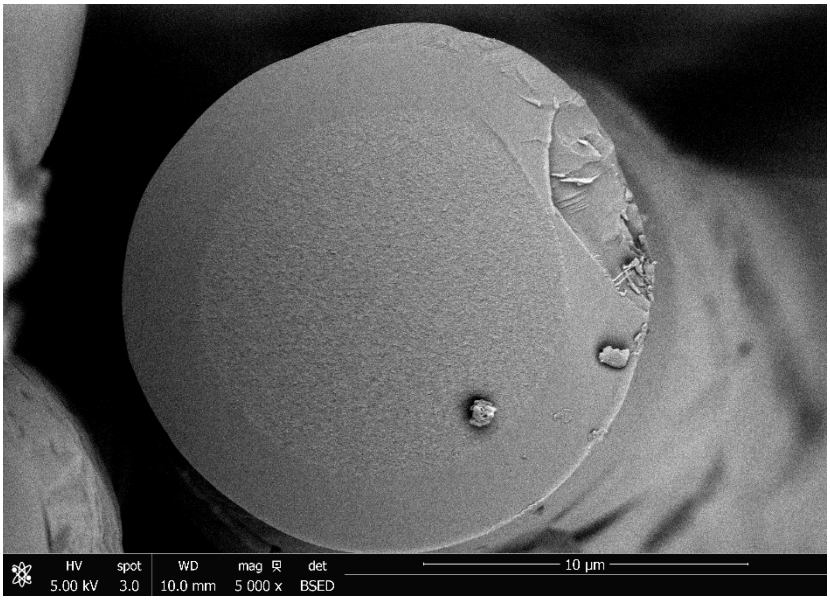

Figure 145 - SEM electron backscatter deflection micrograph of Hi-Nicalon™ S fiber tow specimen "Steam 4" examining the fracture surface of a fiber along the lower portion of the fiber tow. Note the thickness of the silica scale (σ_{cr} = 255 MPa, t_f = 38.04 hrs).

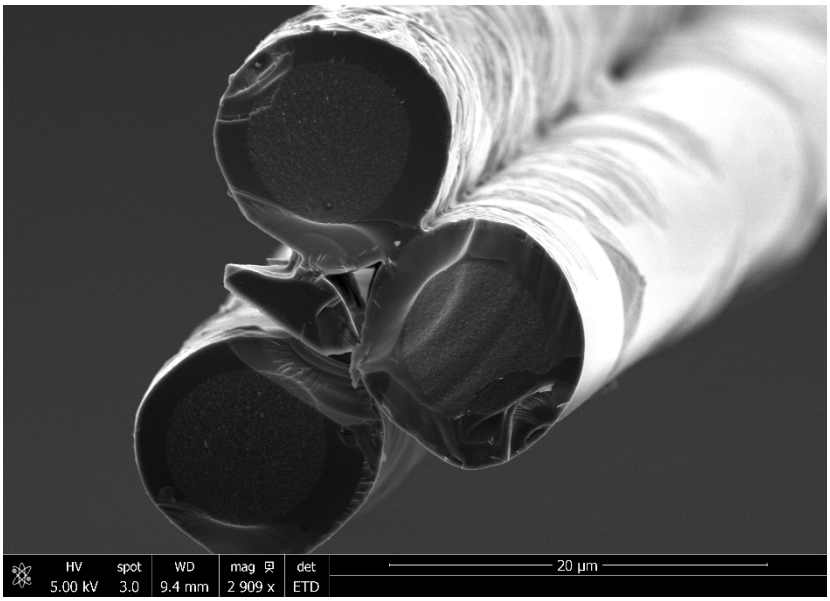

Figure 146 - SEM micrograph of Hi-Nicalon™ S fiber tow specimen "Steam 4" examining the fracture surfaces of a group of fibers along the lower portion of the fiber tow. Note areas of silica scale thickness (σ_{cr} = 255 MPa, t_f = 38.04 hrs).

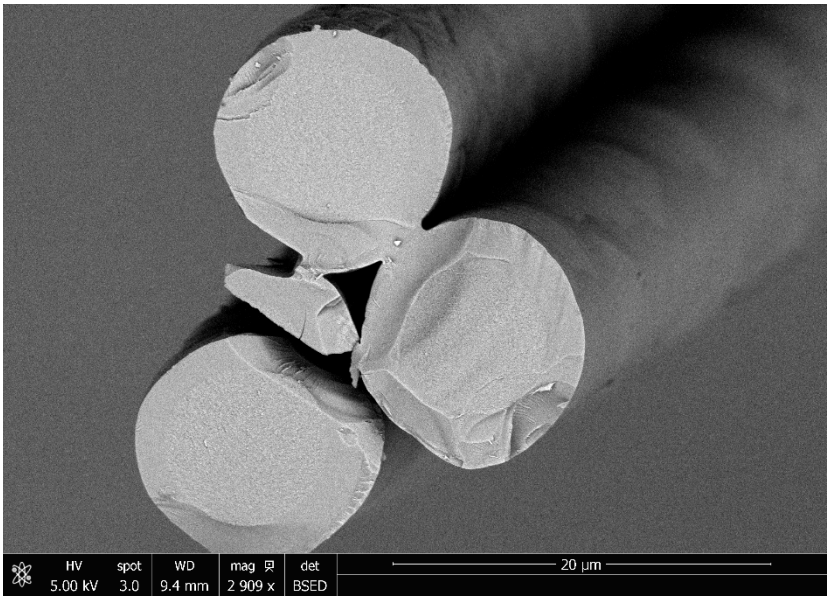

Figure 147 - SEM electron backscatter deflection micrograph of Hi-Nicalon™ S fiber tow specimen "Steam 4" examining the fracture surfaces of a group of fibers along the lower portion of the fiber tow. Note areas of silica scale thickness (σ_{cr} = 255 MPa, t_f = 38.04 hrs).

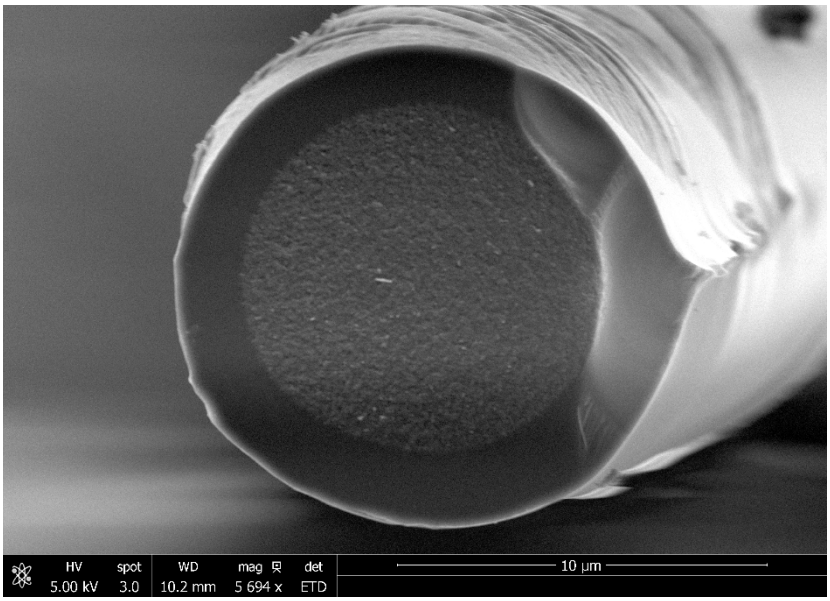

Figure 148 - SEM micrograph of Hi-Nicalon™ S fiber tow specimen "Steam 4" examining the fracture surfaces of a fiber along the lower portion of the fiber tow. Note the thickness of the silica scale (σ_{cr} = 255 MPa, t_f = 38.04 hrs).

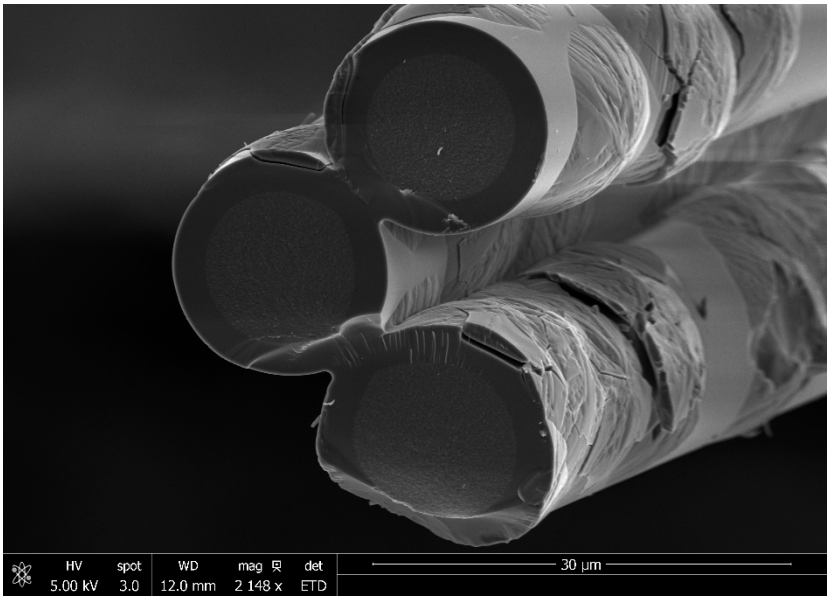

Figure 149 - SEM micrograph of Hi-Nicalon™ S fiber tow specimen "Steam 4" examining the fracture surfaces of a group of fibers along the lower portion of the fiber tow. Note the thickness and areas of silica amorphous and crystallized scale growth (σ_{cr} = 255 MPa, t_f = 38.04 hrs).

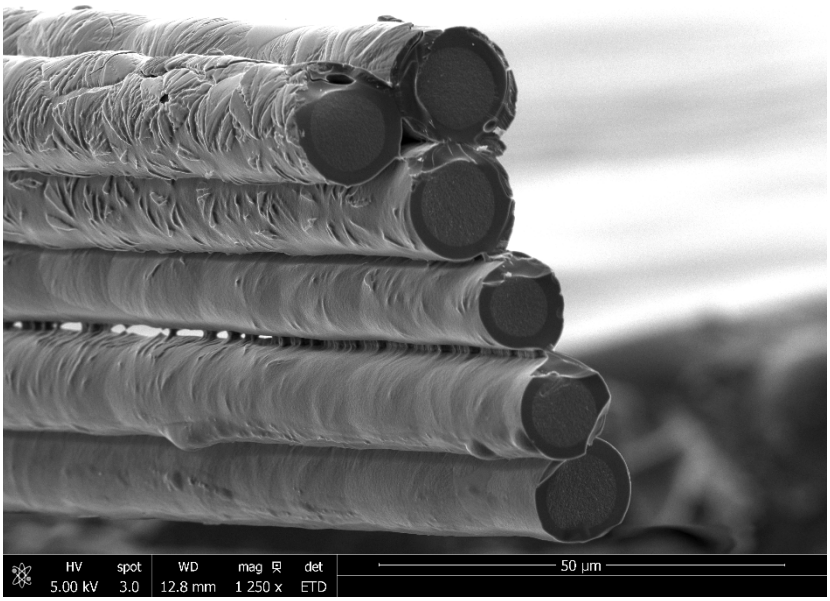

Figure 150 - SEM micrograph of Hi-Nicalon™ S fiber tow specimen "Steam 4" examining the fracture surfaces of a group of fibers along the lower portion of the fiber tow. Note the thickness and areas of silica amorphous and crystallized scale growth (σ_{cr} = 255 MPa, t_f = 38.04 hrs).

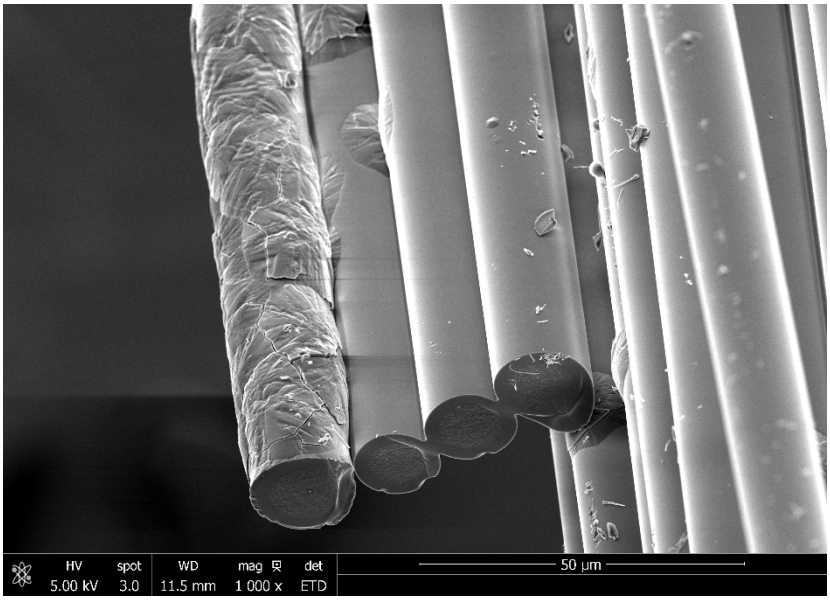

Figure 151 - SEM micrograph of Hi-Nicalon™ S fiber tow specimen "Steam 4" examining the fracture surfaces of a group of fibers along the upper portion of the fiber tow. Note the thickness and areas of silica amorphous and crystallized scale growth (σ_{cr} = 255 MPa, t_f = 38.04 hrs).

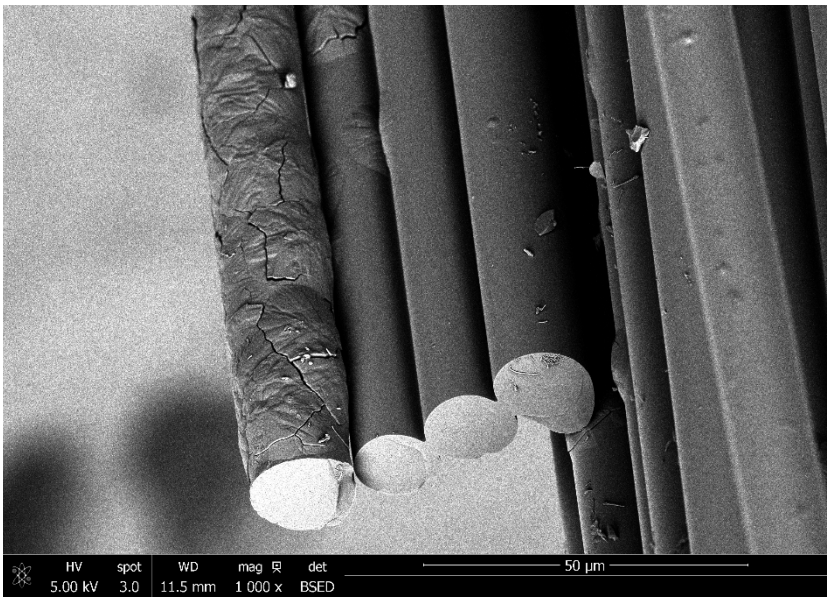

Figure 152 - SEM electron backscatter deflection micrograph of Hi-Nicalon™ S fiber tow specimen "Steam 4" examining the fracture surfaces of a group of fibers along the upper portion of the fiber tow. Note the thickness and areas of silica amorphous and crystallized scale growth (σ_{cr} = 255 MPa, t_f = 38.04 hrs).

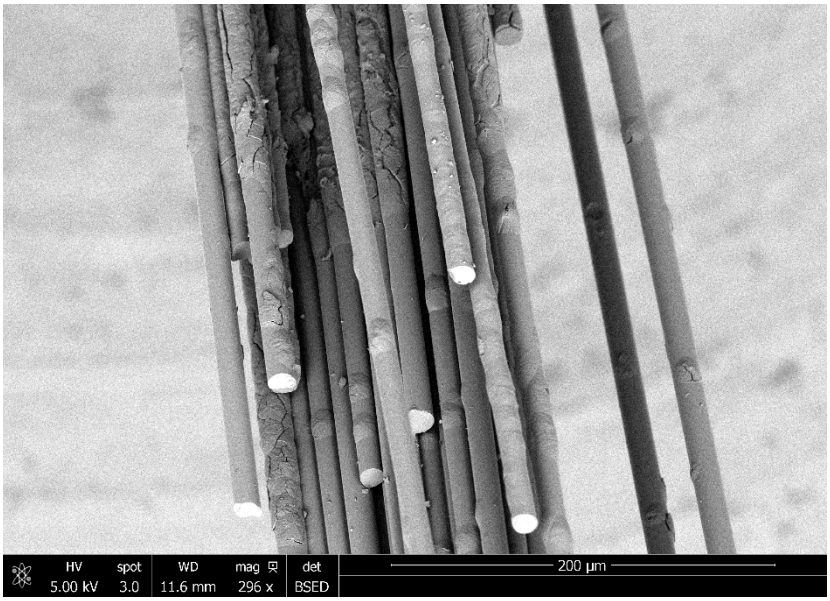

Figure 153 - SEM electron backscatter deflection micrograph of Hi-Nicalon™ S fiber tow specimen "Steam 4" examining the fiber and fracture surfaces of a group of fibers along the upper portion of the fiber tow. Note the areas of silica amorphous and crystallized scale growth (σ_{cr} = 255 MPa, t_f = 38.04 hrs).

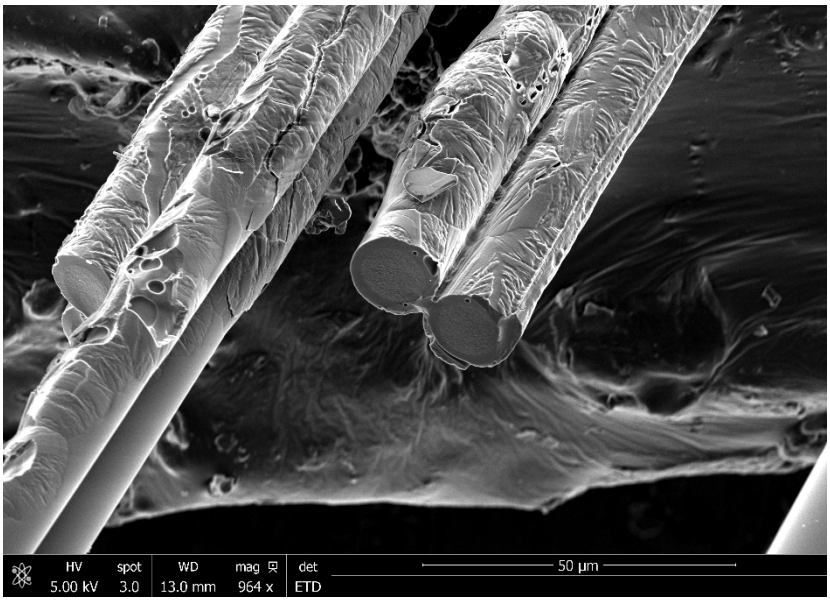

Figure 154 - SEM micrograph of Hi-Nicalon™ S fiber tow specimen "Steam 4" examining the fiber and fracture surfaces of a group of fibers along the upper portion of the fiber tow. Note the areas of silica amorphous and crystallized scale growth (σ_{cr} = 255 MPa, t_f = 38.04 hrs).

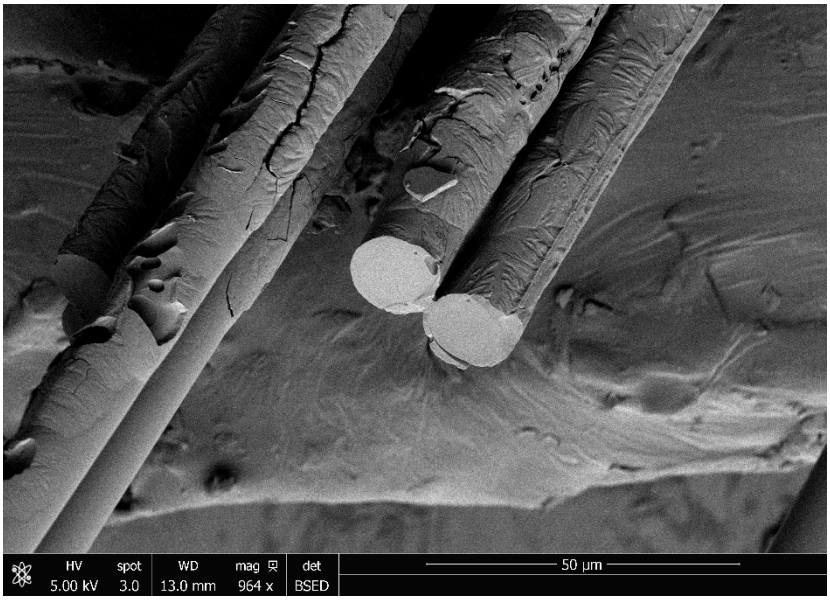

Figure 155 - SEM electron backscatter deflection micrograph of Hi-Nicalon™ S fiber tow specimen "Steam 4" examining the fiber and fracture surfaces of a group of fibers along the upper portion of the fiber tow. Note the areas of silica amorphous and crystallized scale growth (σ_{cr} = 255 MPa, t_f = 38.04 hrs).

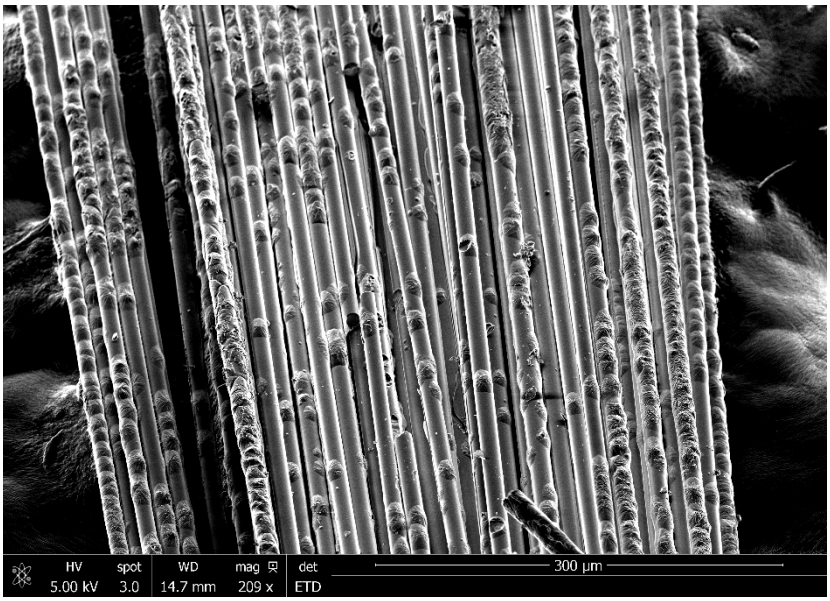

Figure 156 - SEM micrograph of Hi-Nicalon™ S fiber tow specimen "Steam 4" examining a group of fibers along the upper portion of the fiber tow. Note the areas of silica amorphous and crystallized scale growth (σ_{cr} = 255 MPa, t_f = 38.04 hrs).

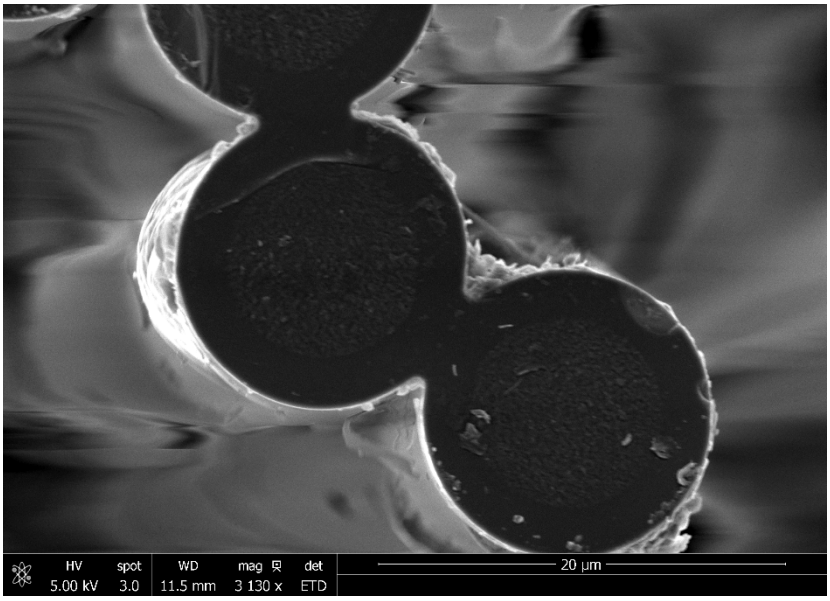

Figure 157 - SEM micrograph of Hi-Nicalon™ S fiber tow specimen "Steam 4" examining the fracture surfaces of multiple fibers along the upper portion of the fiber tow. Note the thickness of the silica scale (σ_{cr} = 255 MPa, t_f = 38.04 hrs).

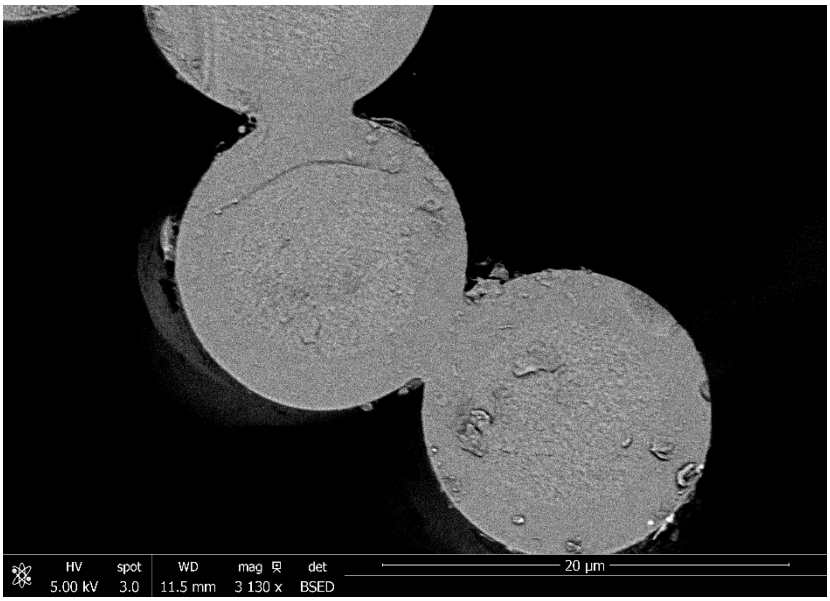

Figure 158 - SEM electron backscatter deflection micrograph of Hi-Nicalon™ S fiber tow specimen "Steam 4" examining the fracture surfaces of multiple fibers along the upper portion of the fiber tow. Note the thickness of the silica scale (σ_{cr} = 255 MPa, t_f = 38.04 hrs).

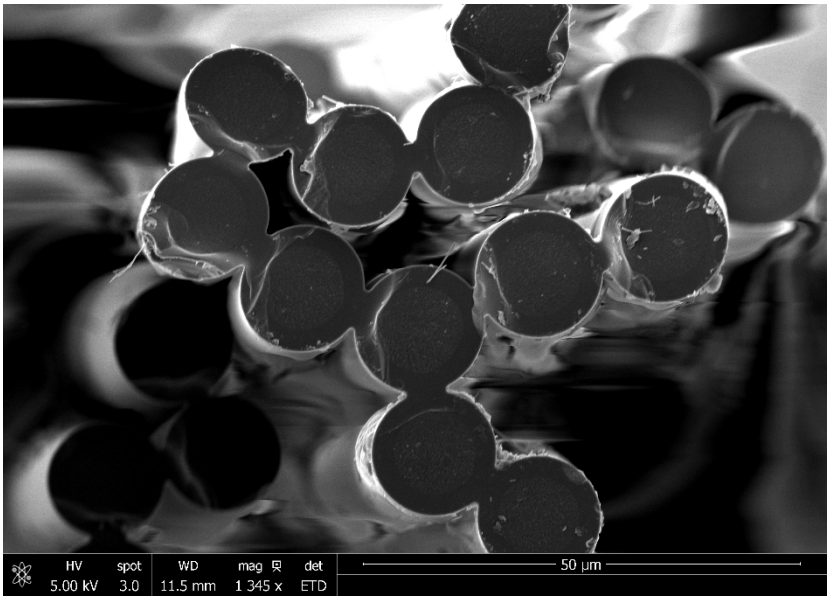

Figure 159 - SEM micrograph of Hi-Nicalon™ S fiber tow specimen "Steam 4" examining the fracture surfaces of a group of fibers along the upper portion of the fiber tow. Note the thickness of the silica scale (σ_{cr} = 255 MPa, t_f = 38.04 hrs).

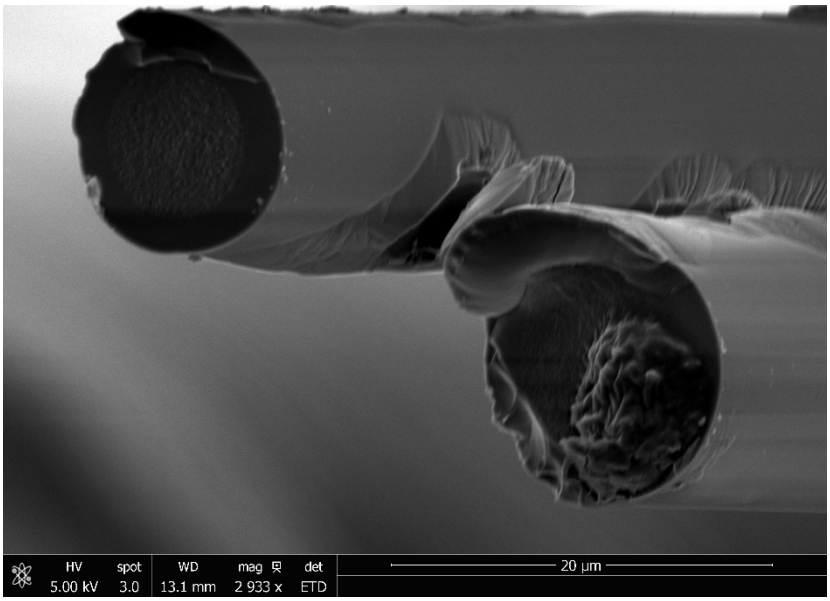

Figure 160 - SEM micrograph of Hi-Nicalon™ S fiber tow specimen "Steam 4" examining the fracture surfaces of multiple fibers along the upper portion of the fiber tow. Note the unknown growth on the fracture surface of the fiber, suggesting progressive fiber failure (σ_{cr} = 255 MPa, t_f = 38.04 hrs).

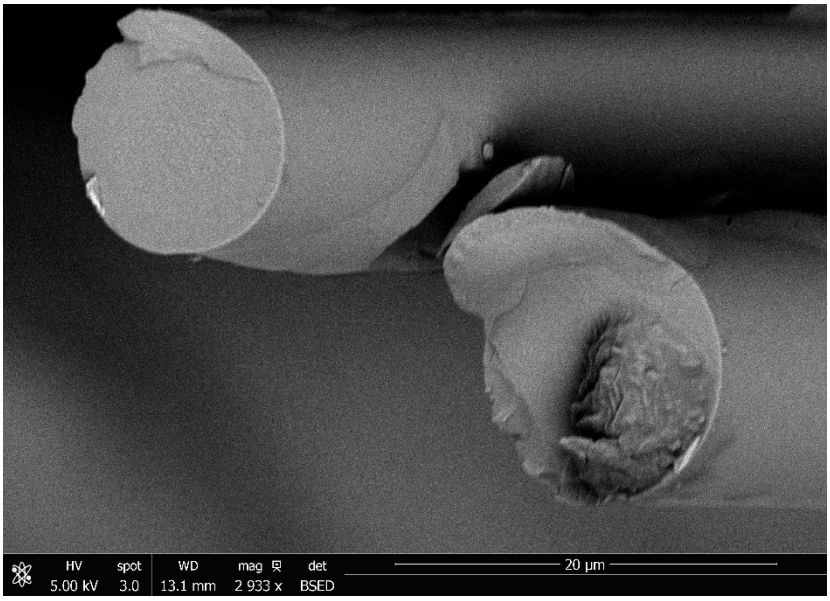

Figure 161 - SEM electron backscatter deflection micrograph of Hi-Nicalon™ S fiber tow specimen "Steam 4" examining the fracture surfaces of multiple fibers along the upper portion of the fiber tow. Note the unknown growth on the fracture surface of the fiber, suggesting progressive fiber failure (σ_{cr} = 255 MPa, t_f = 38.04 hrs).

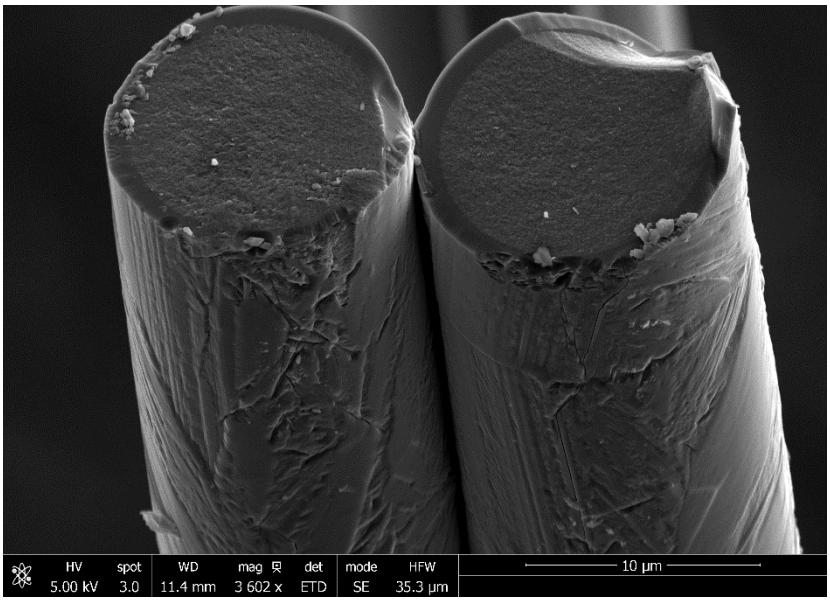

Figure 162 – SEM micrograph of Hi-Nicalon™ S fiber tow specimen "Steam 12" examining the fracture surfaces of multiple fibers along the lower portion of the fiber tow (σ_{cr} = 450 MPa, t_f = 13.53 hrs).

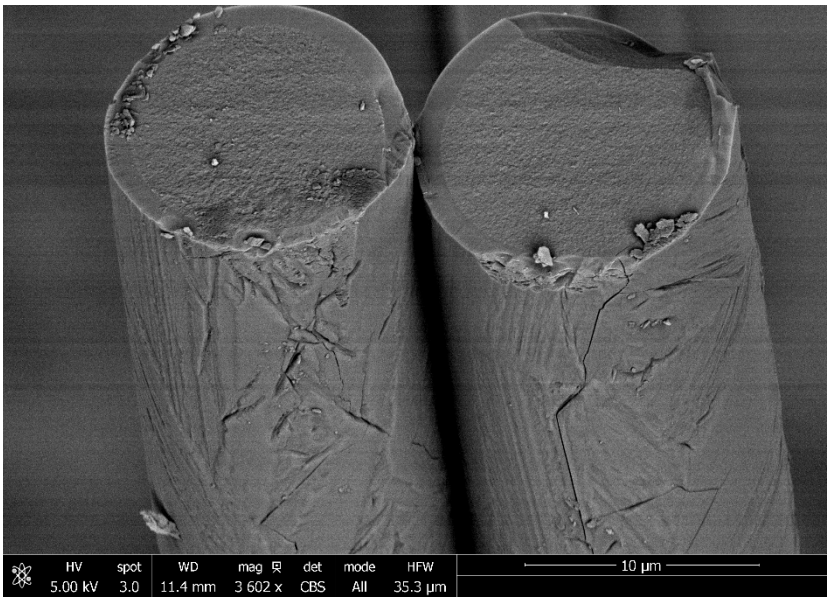

Figure 163 - SEM electron backscatter deflection micrograph of Hi-Nicalon™ S fiber tow specimen "Steam 12" examining the fracture surfaces of multiple fibers along the lower portion of the fiber tow (σ_{cr} = 450 MPa, t_f = 13.53 hrs).

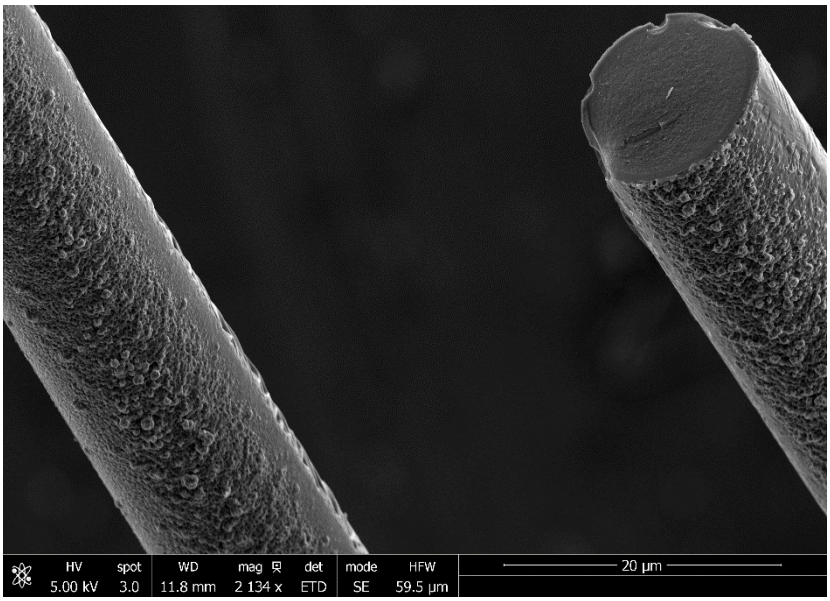

Figure 164 - SEM micrograph of Hi-Nicalon™ S fiber tow specimen "Steam 12" examining rogue fibers along the lower portion of the fiber tow. Note the unknown growth along the exterior surface of the fibers (σ_{cr} = 450 MPa, t_f = 13.53 hrs).

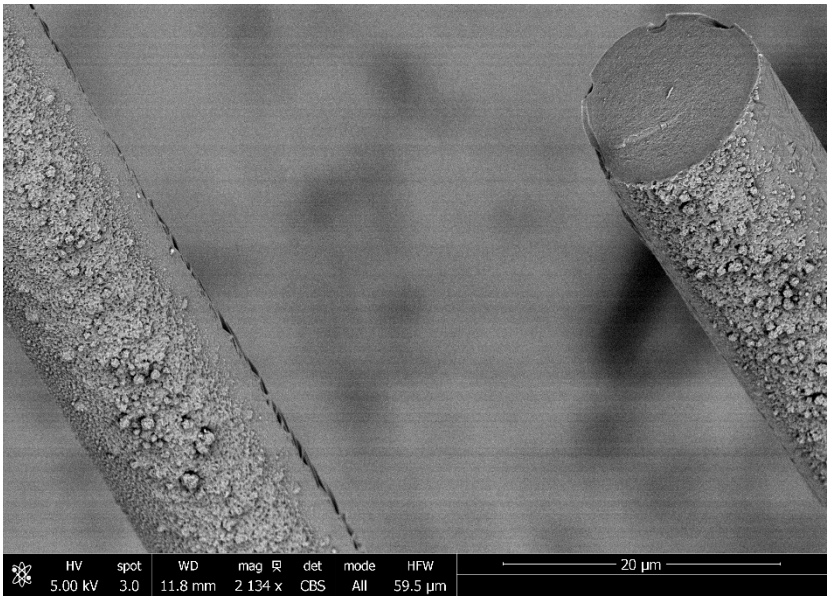

Figure 165 - SEM electron backscatter deflection micrograph of Hi-Nicalon™ S fiber tow specimen "Steam 12" examining rogue fibers along the lower portion of the fiber tow. Note the unknown growth along the exterior surface of the fibers (σ_{cr} = 450 MPa, t_f = 13.53 hrs).

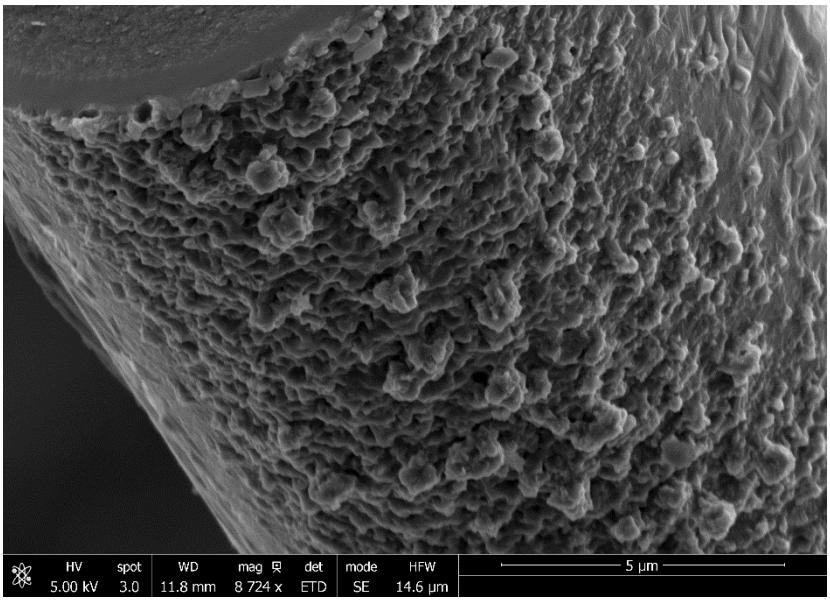

Figure 166 - SEM micrograph of Hi-Nicalon™ S fiber tow specimen "Steam 12" examining the exterior surface along a rogue fiber along the lower portion of the fiber tow (σ_{cr} = 450 MPa, t_f = 13.53 hrs).

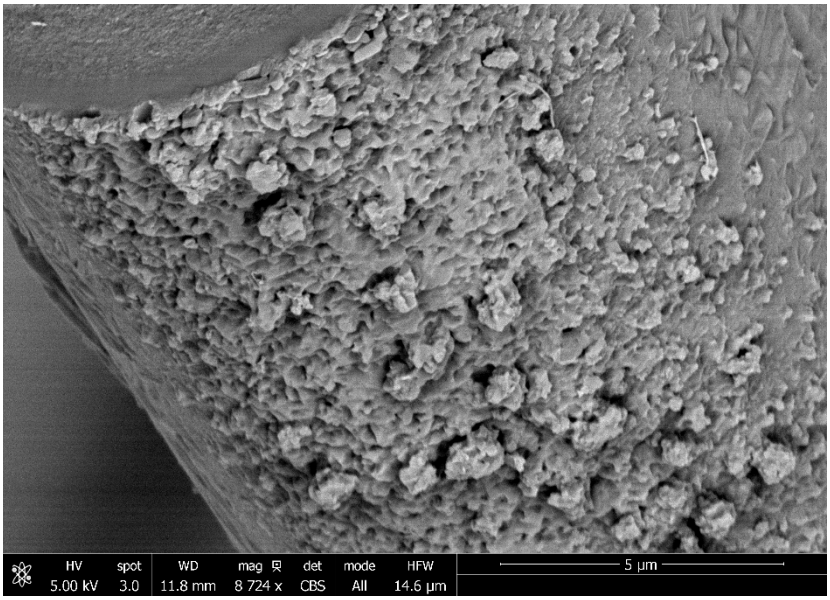

Figure 167 - SEM electron backscatter deflection micrograph of Hi-Nicalon™ S fiber tow specimen "Steam 12" examining the exterior surface along a rogue fiber along the lower portion of the fiber tow (σ_{cr} = 450 MPa, t_f = 13.53 hrs).

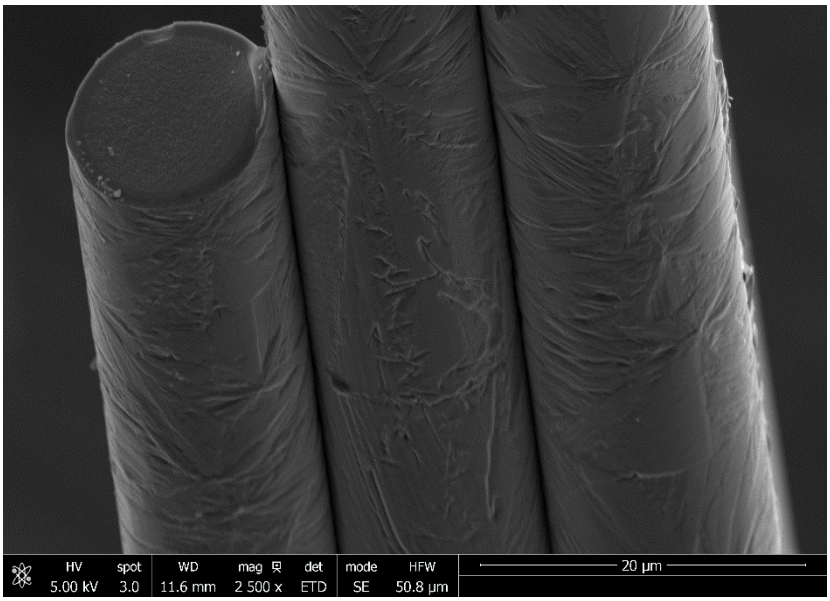

Figure 168 - SEM micrograph of Hi-Nicalon™ S fiber tow specimen "Steam 12" examining the exterior surface of fractured fibers along the lower portion of the fiber tow. Note the crystallized silica scale along the fiber surface (σ_{cr} = 450 MPa, t_f = 13.53 hrs).

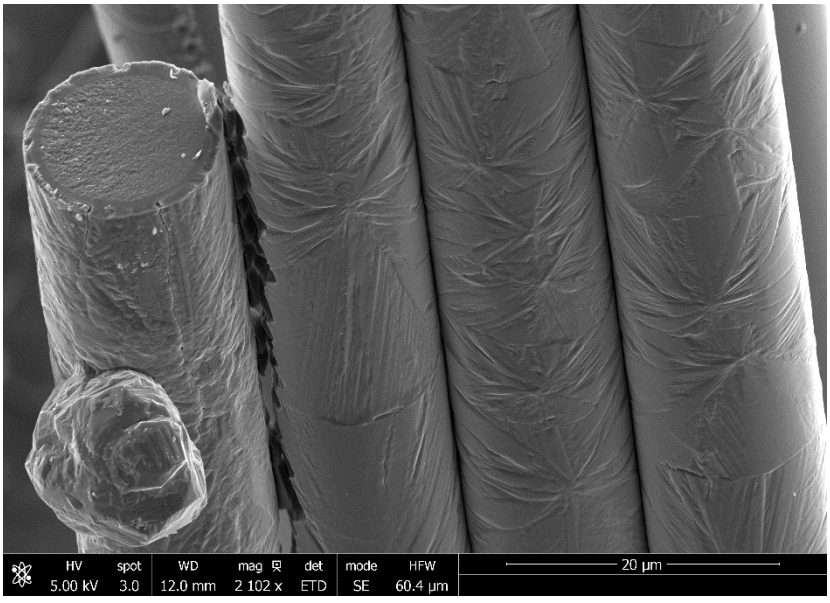

Figure 169 - SEM micrograph of Hi-Nicalon™ S fiber tow specimen "Steam 12" examining the exterior surface of fractured fibers along the lower portion of the fiber tow. Note the crystallized silica scale along the fiber surface (σ_{cr} = 450 MPa, t_f = 13.53 hrs).

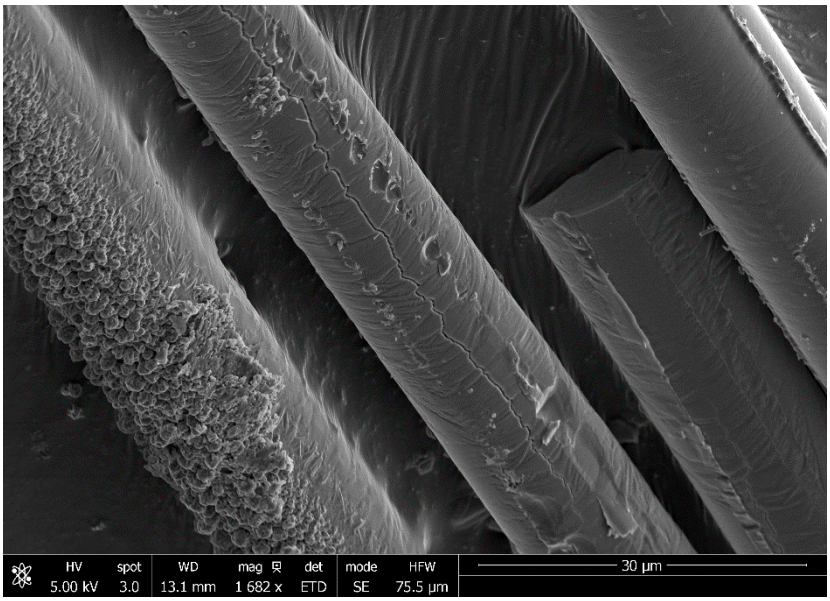

Figure 170 - SEM micrograph of Hi-Nicalon™ S fiber tow specimen "Steam 12" examining the exterior surfaces of a group of fractured fibers along the lower portion of the fiber tow. Note the rogue fiber present (σ_{cr} = 450 MPa, t_f = 13.53 hrs).

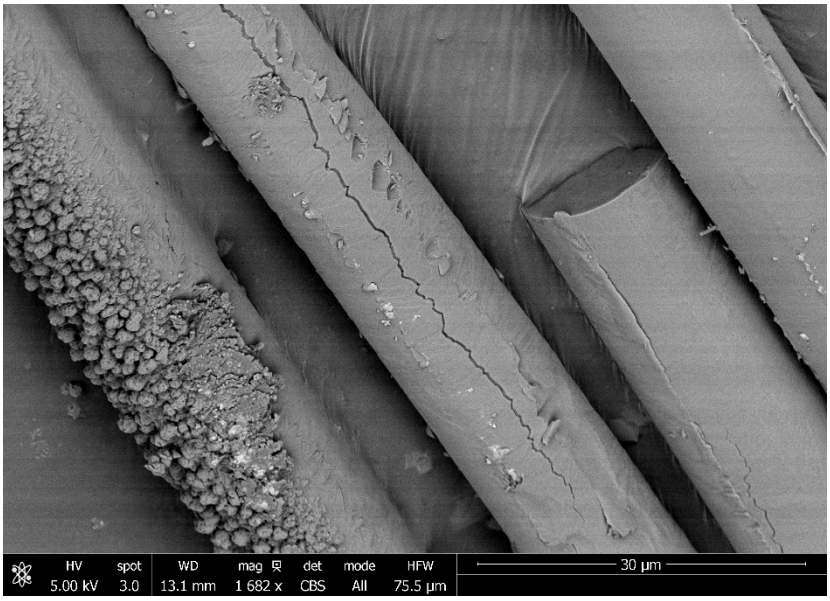

Figure 171 - SEM electron backscatter deflection micrograph of Hi-Nicalon™ S fiber tow specimen "Steam 12" examining the exterior surfaces of a group of fractured fibers along the lower portion of the fiber tow. Note the rogue fiber present (σ_{cr} = 450 MPa, t_f = 13.53 hrs).

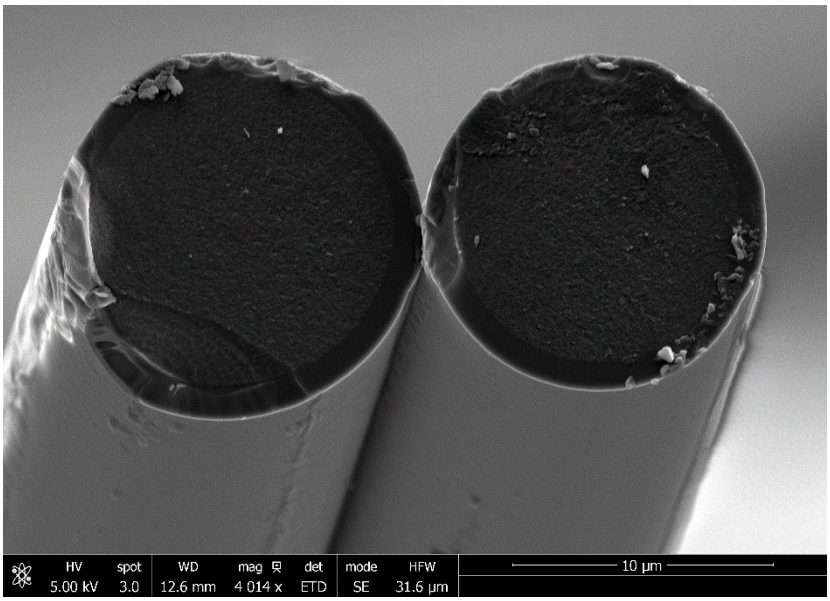

Figure 172 - SEM micrograph of Hi-Nicalon™ S fiber tow specimen "Steam 12" examining the fracture surfaces of a pair of fibers along the lower portion of the fiber tow. Note the thickness of silica scale (σ_{cr} = 450 MPa, t_f = 13.53 hrs).

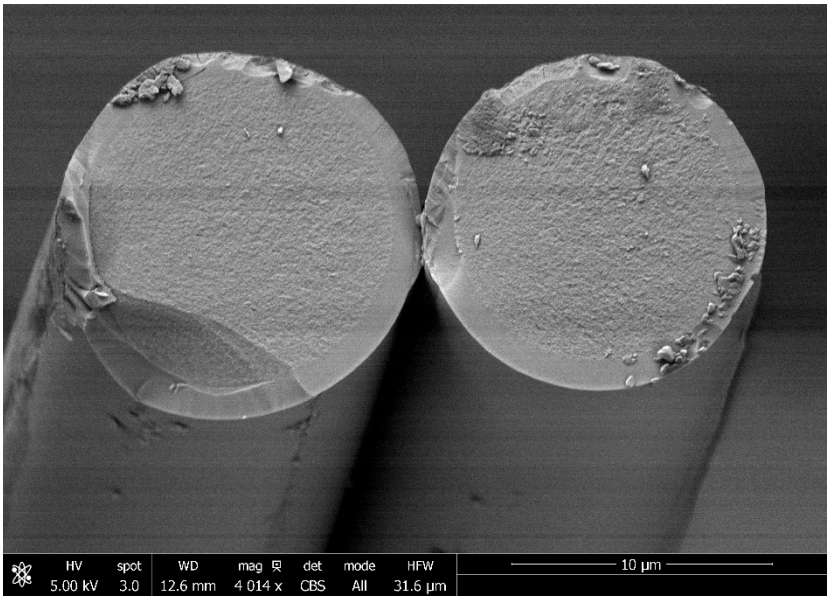

Figure 173 - SEM electron backscatter deflection micrograph of Hi-Nicalon™ S fiber tow specimen "Steam 12" examining the fracture surfaces of a pair of fibers along the lower portion of the fiber tow. Note the thickness of silica scale (σ_{cr} = 450 MPa, t_f = 13.53 hrs).

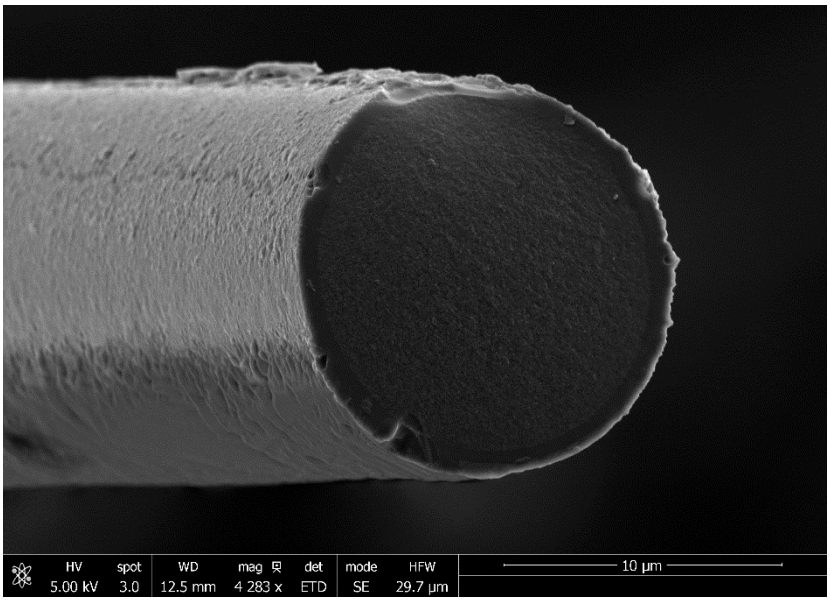

Figure 174 - SEM micrograph of Hi-Nicalon™ S fiber tow specimen "Steam 12" examining the fracture surface of a fiber along the lower portion of the fiber tow. Note the thickness of silica scale (σ_{cr} = 450 MPa, t_f = 13.53 hrs).

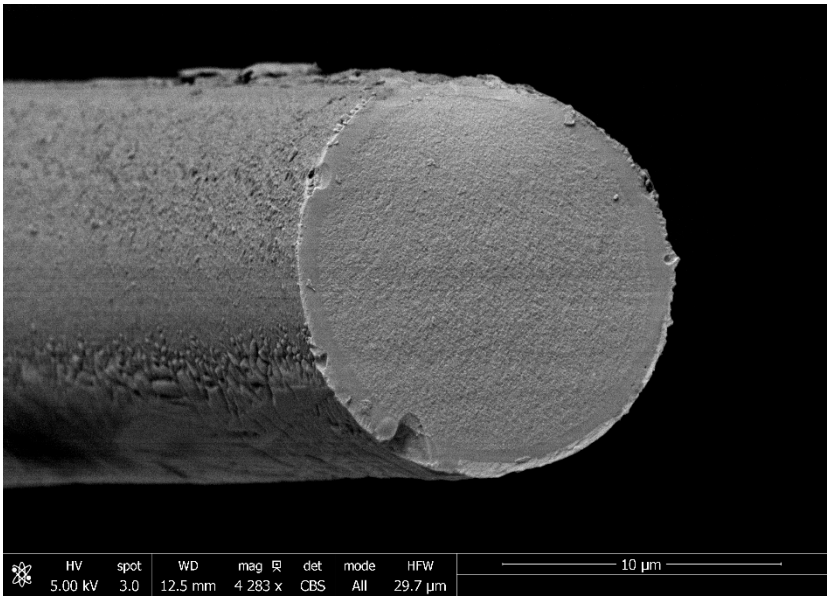

Figure 175 - SEM electron backscatter deflection micrograph of Hi-Nicalon™ S fiber tow specimen "Steam 12" examining the fracture surface of a fiber along the lower portion of the fiber tow. Note the thickness of silica scale (σ_{cr} = 450 MPa, t_f = 13.53 hrs).

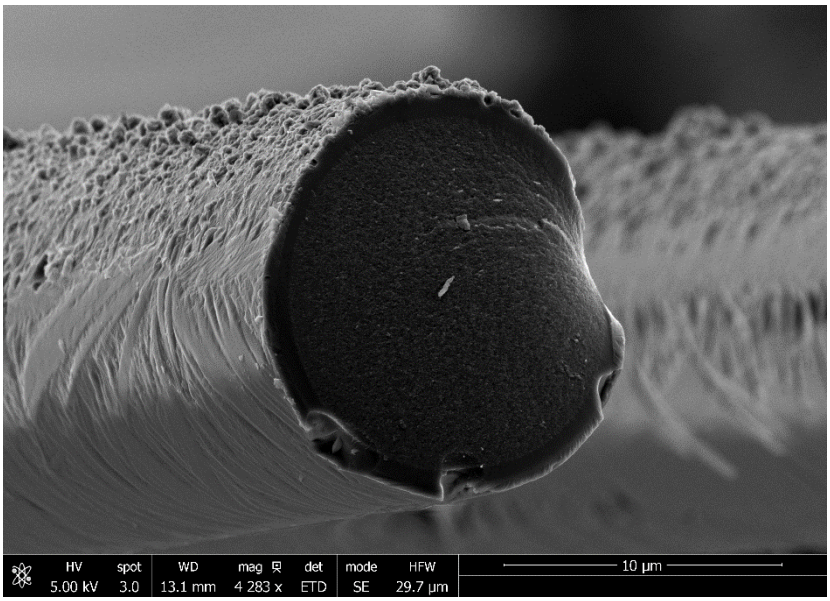

Figure 176 – SEM micrograph of Hi-Nicalon™ S fiber tow specimen "Steam 12" examining the fracture surface of a fiber along the lower portion of the fiber tow. Note the different features present along the exterior fiber surface (σ_{cr} = 450 MPa, t_f = 13.53 hrs).

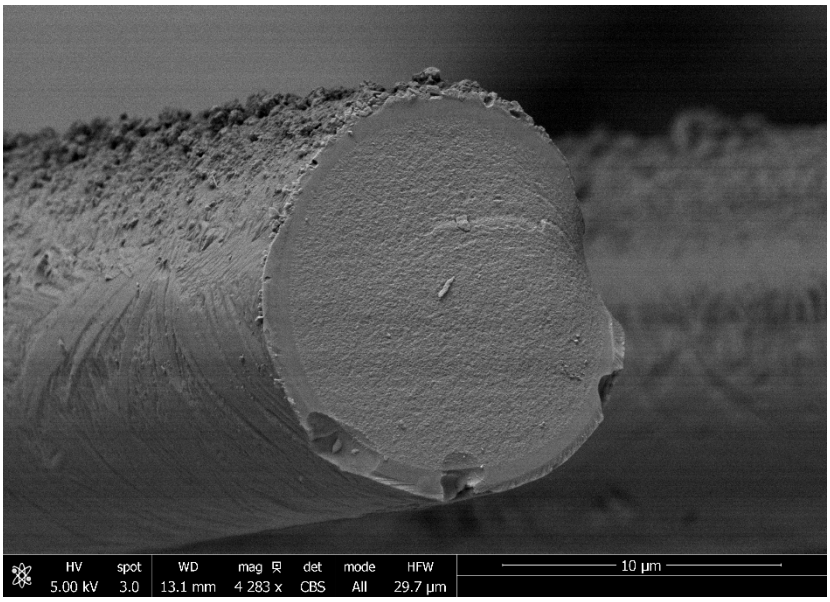

Figure 177 - SEM electron backscatter deflection micrograph of Hi-Nicalon™ S fiber tow specimen "Steam 12" examining the fracture surface of a fiber along the lower portion of the fiber tow. Note the different features present along the exterior fiber surface (σ_{cr} = 450 MPa, t_f = 13.53 hrs).

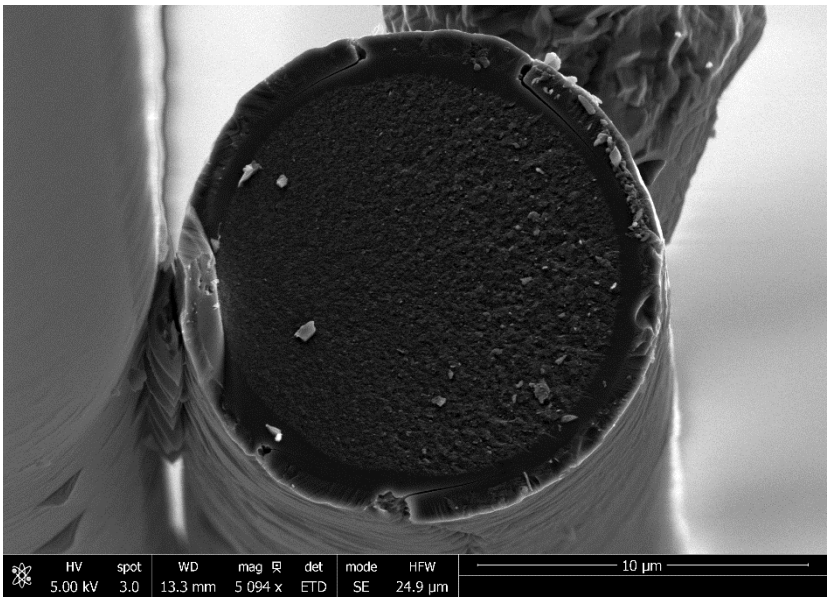

Figure 178 - SEM micrograph of Hi-Nicalon™ S fiber tow specimen "Steam 12" examining the fracture surface of a fiber along the lower portion of the fiber tow. Note the thickness of silica scale (σ_{cr} = 450 MPa, t_f = 13.53 hrs).

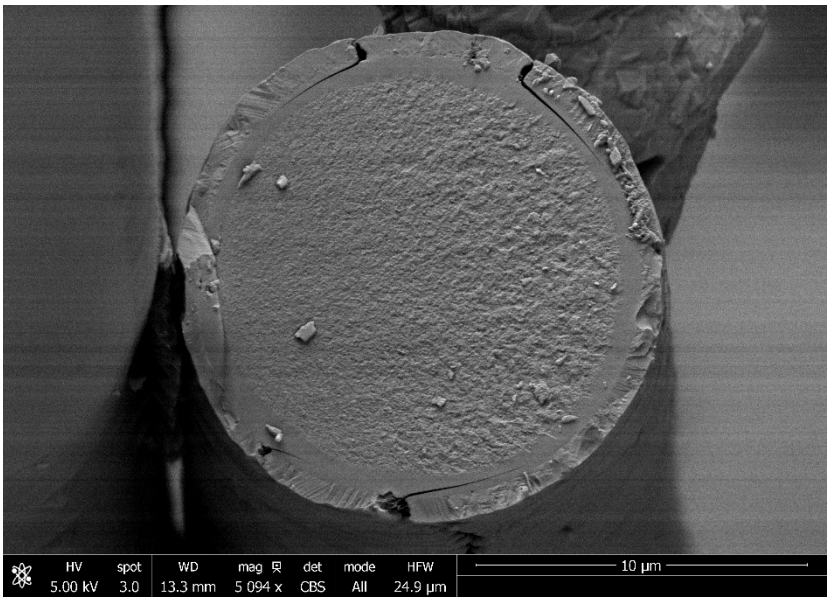

Figure 179 - SEM electron backscatter deflection micrograph of Hi-Nicalon™ S fiber tow specimen "Steam 12" examining the fracture surface of a fiber along the lower portion of the fiber tow. Note the thickness of silica scale (σ_{cr} = 450 MPa, t_f = 13.53 hrs).

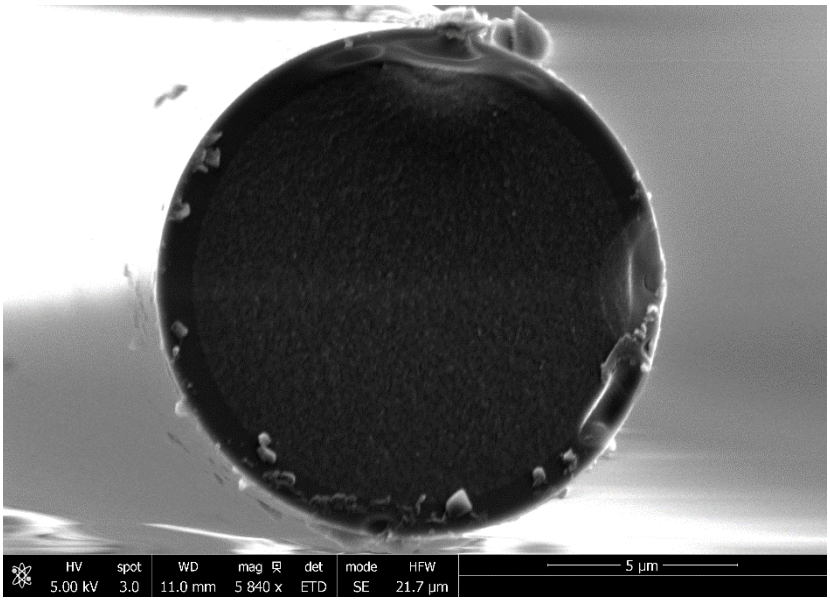

Figure 180 - SEM micrograph of Hi-Nicalon™ S fiber tow specimen "Steam 12" examining the fracture surface of a fiber along the upper portion of the fiber tow. Note the thickness of silica scale (σ_{cr} = 450 MPa, t_f = 13.53 hrs).

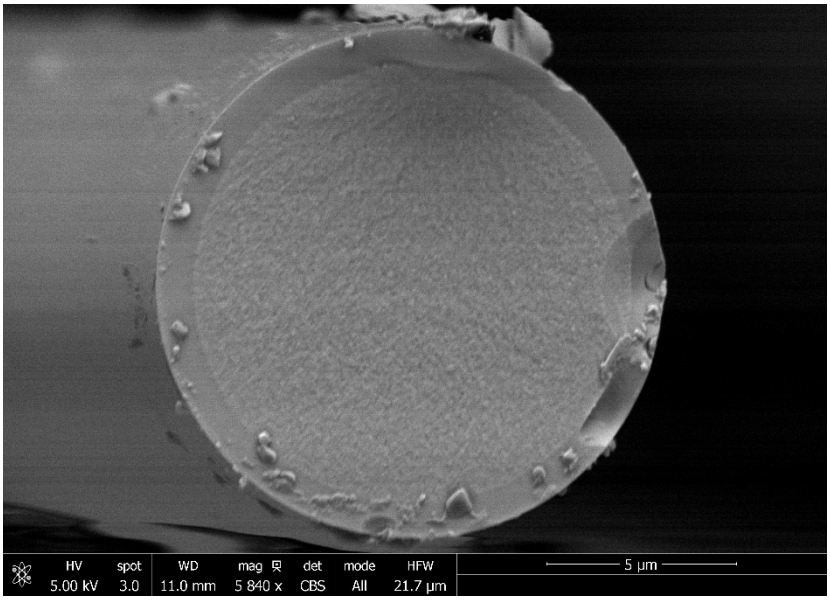

Figure 181 - SEM electron backscatter deflection micrograph of Hi-Nicalon™ S fiber tow specimen "Steam 12" examining the fracture surface of a fiber along the upper portion of the fiber tow. Note the thickness of silica scale (σ_{cr} = 450 MPa, t_f = 13.53 hrs).

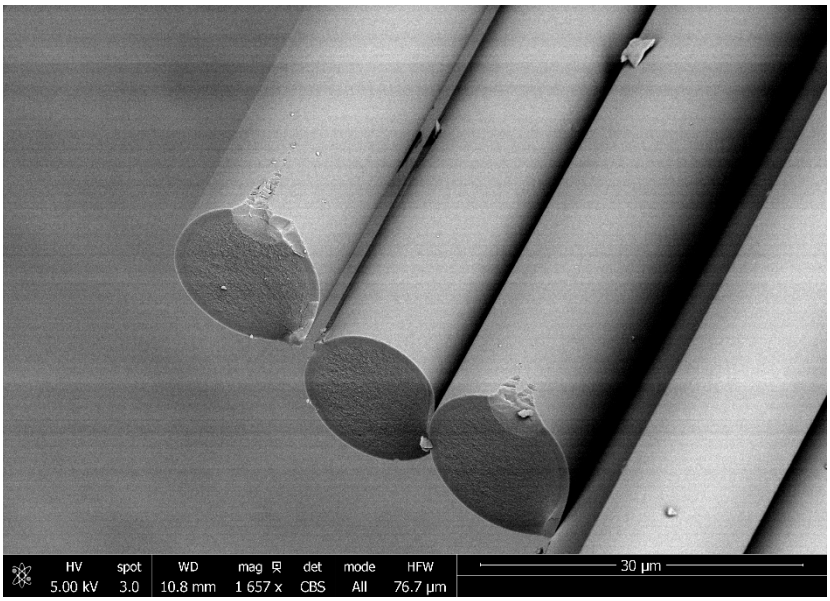

Figure 182 - SEM electron backscatter deflection micrograph of Hi-Nicalon™ S fiber tow specimen "Steam 12" examining the fracture surfaces of a group of fibers along the upper portion of the fiber tow (σ_{cr} = 450 MPa, t_f = 13.53 hrs).

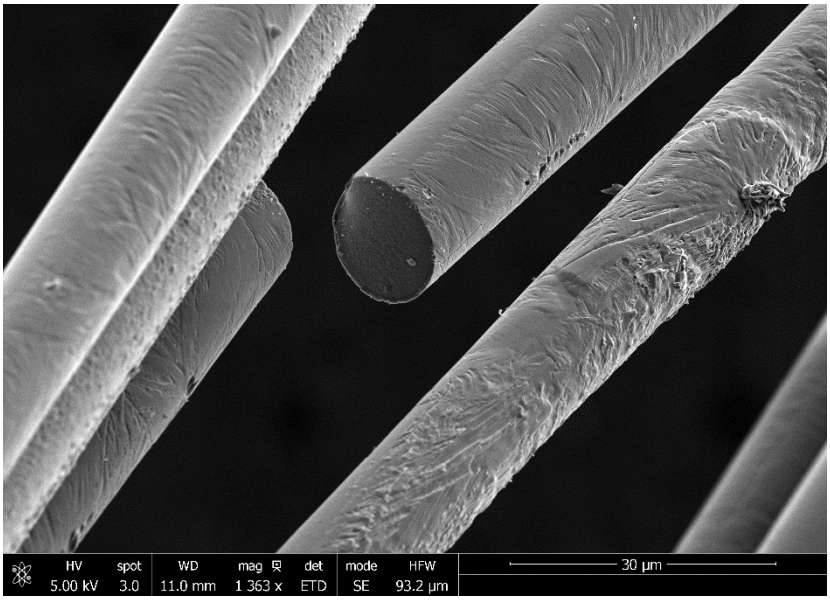

Figure 183 - SEM micrograph of Hi-Nicalon™ S fiber tow specimen "Steam 12" examining the fracture surface and exterior surfaces of a group of fibers along the upper portion of the fiber tow. Note the crystallized scale growth along the fiber surface (σ_{cr} = 450 MPa, t_f = 13.53 hrs).

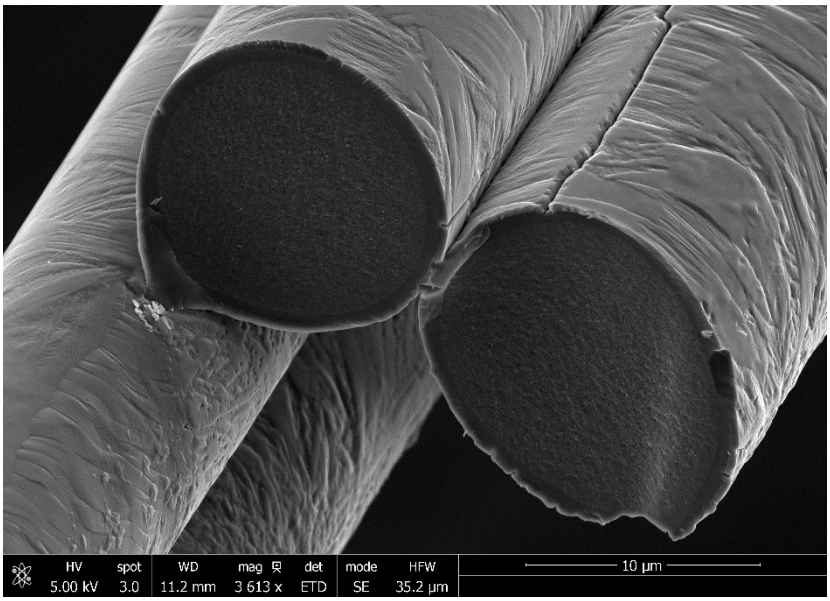

Figure 184 - SEM micrograph of Hi-Nicalon™ S fiber tow specimen "Steam 12" examining the fracture surfaces of a group of fibers along the upper portion of the fiber tow. Note the crystallized scale, scale thickness, and fiber to fiber contact (σ_{cr} = 450 MPa, t_f = 13.53 hrs).

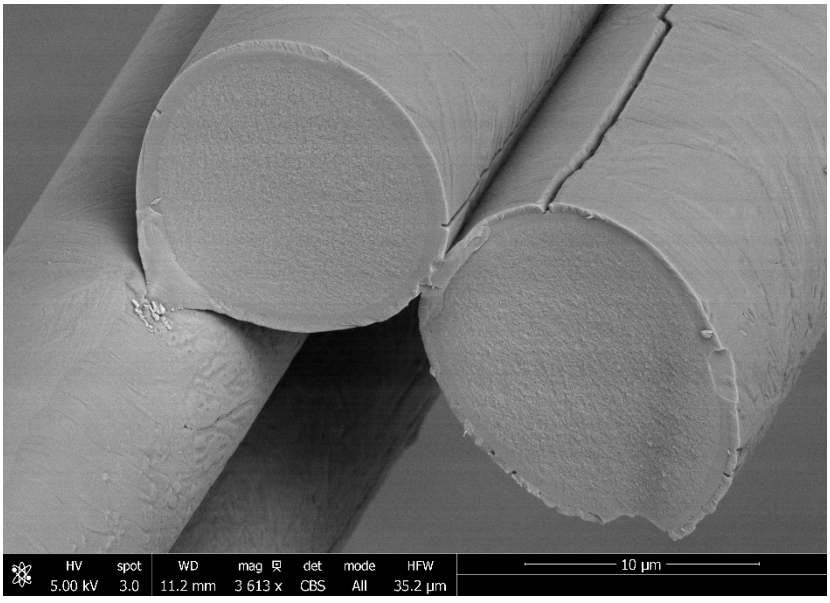

Figure 185 - SEM electron backscatter deflection micrograph of Hi-Nicalon™ S fiber tow specimen "Steam 12" examining the fracture surfaces of a group of fibers along the upper portion of the fiber tow. Note the crystallized scale, scale thickness, and fiber to fiber contact (σ_{cr} = 450 MPa, t_f = 13.53 hrs).

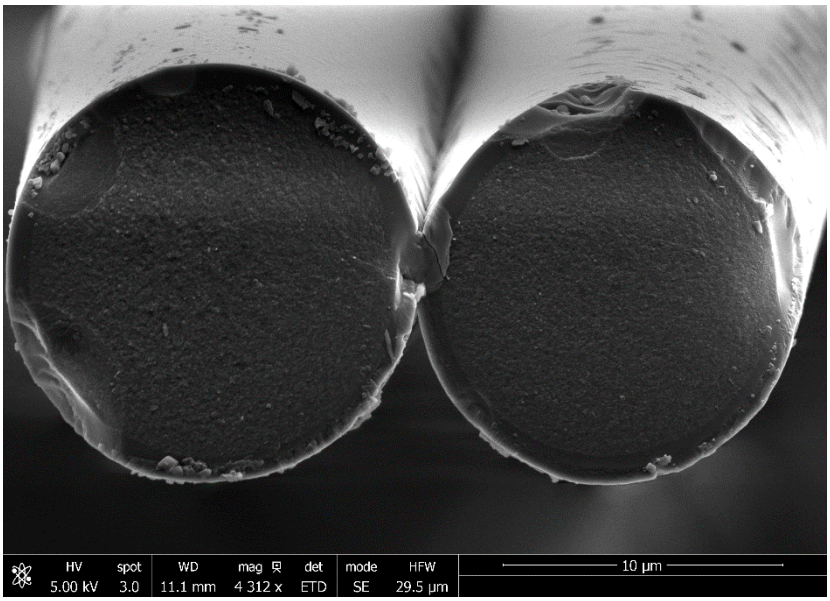

Figure 186 – SEM micrograph of Hi-Nicalon™ S fiber tow specimen "Steam 12" examining the fracture surface of a pair of fibers along the upper portion of the fiber tow (σ_{cr} = 450 MPa, t_f = 13.53 hrs).

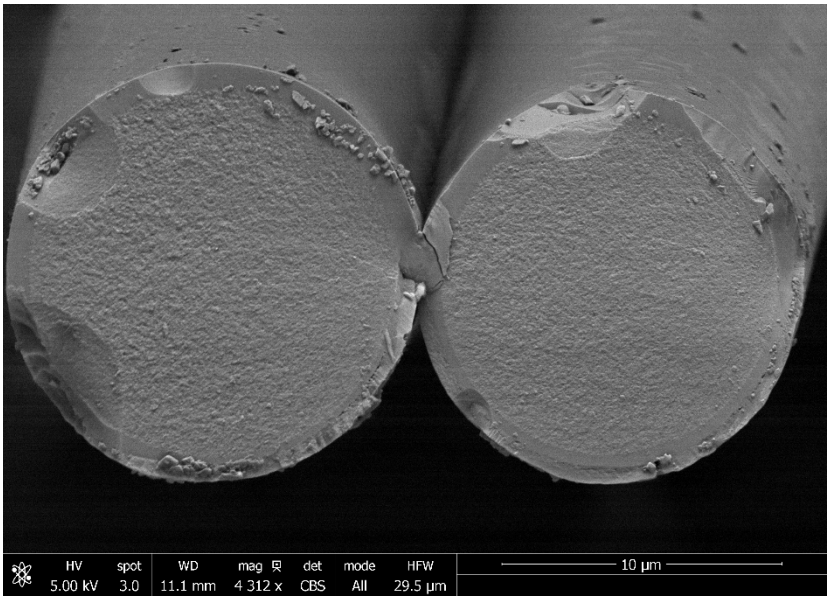

Figure 187 - SEM electron backscatter deflection micrograph of Hi-Nicalon™ S fiber tow specimen "Steam 12" examining the fracture surface of a pair of fibers along the upper portion of the fiber tow (σ_{cr} = 450 MPa, t_f = 13.53 hrs).

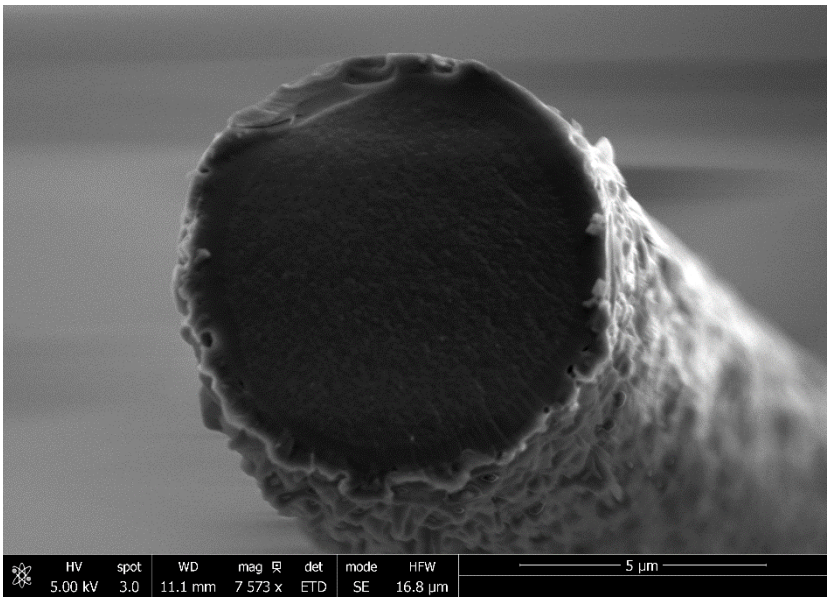

Figure 188 - SEM micrograph of Hi-Nicalon™ S fiber tow specimen "Steam 12" examining the fracture surface of a fiber along the upper portion of the fiber tow. Note the features growing on the exterior fiber surface (σ_{cr} = 450 MPa, t_f = 13.53 hrs).

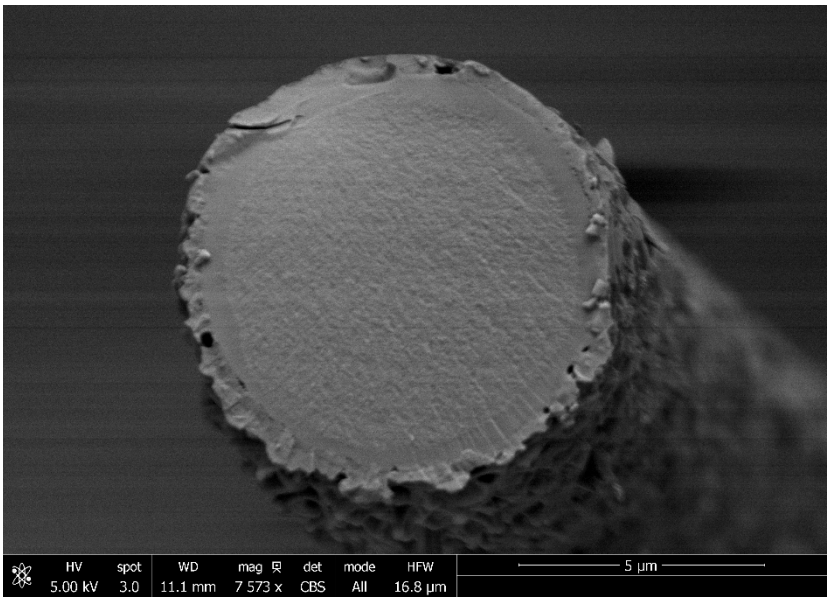

Figure 189 - SEM electron backscatter deflection micrograph of Hi-Nicalon™ S fiber tow specimen "Steam 12" examining the fracture surface of a fiber along the upper portion of the fiber tow. Note the features growing on the exterior fiber surface (σ_{cr} = 450 MPa, t_f = 13.53 hrs).

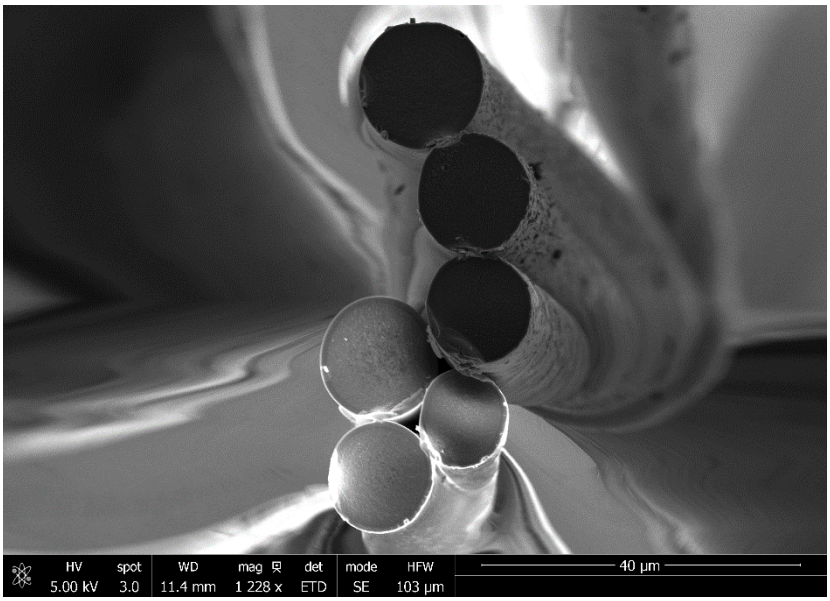

Figure 190 - SEM micrograph of Hi-Nicalon™ S fiber tow specimen "Steam 12" examining the fracture surfaces of a group of bonded fibers along the upper portion of the fiber tow (σ_{cr} = 450 MPa, t_f = 13.53 hrs).

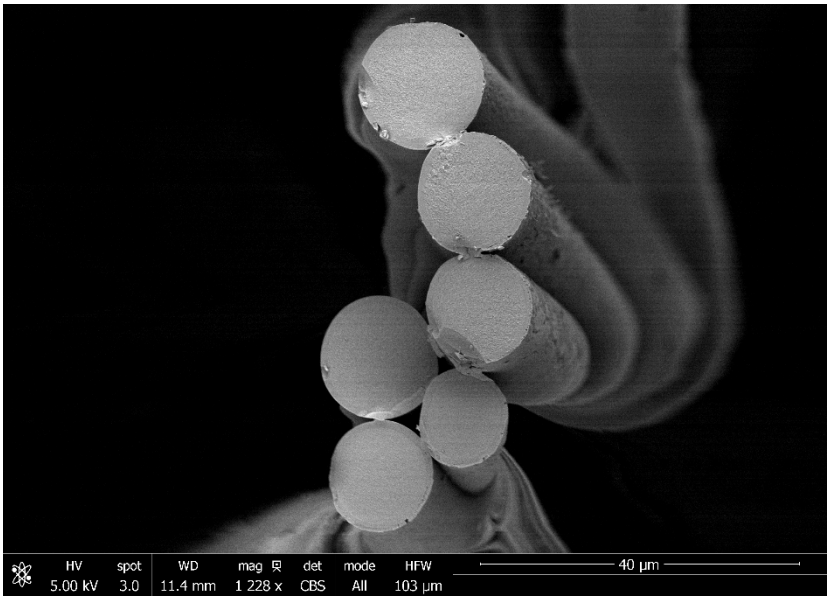

Figure 191 - SEM electron backscatter deflection micrograph of Hi-Nicalon™ S fiber tow specimen "Steam 12" examining the fracture surfaces of a group of bonded fibers along the upper portion of the fiber tow (σ_{cr} = 450 MPa, t_f = 13.53 hrs).

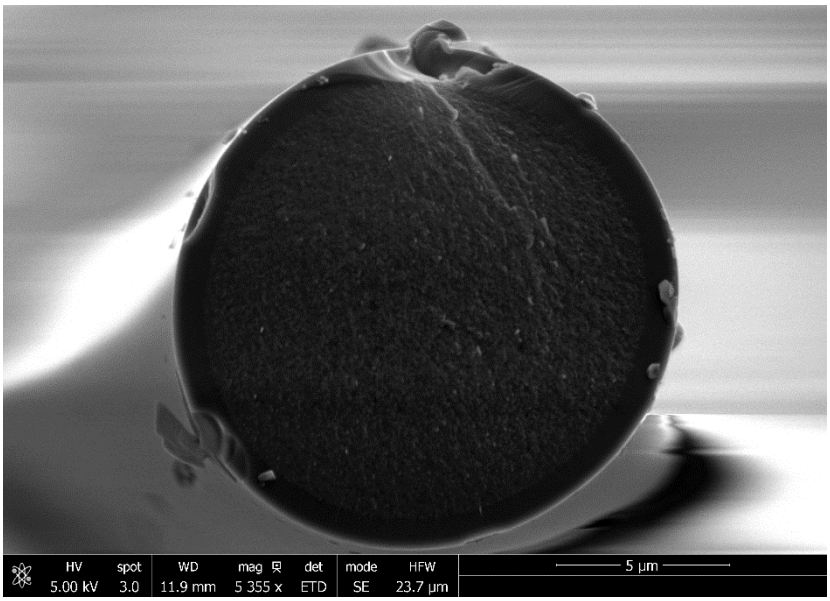

Figure 192 - SEM micrograph of Hi-Nicalon™ S fiber tow specimen "Steam 12" examining the fracture surface of a fiber along the upper portion of the fiber tow (σ_{cr} = 450 MPa, t_f = 13.53 hrs).

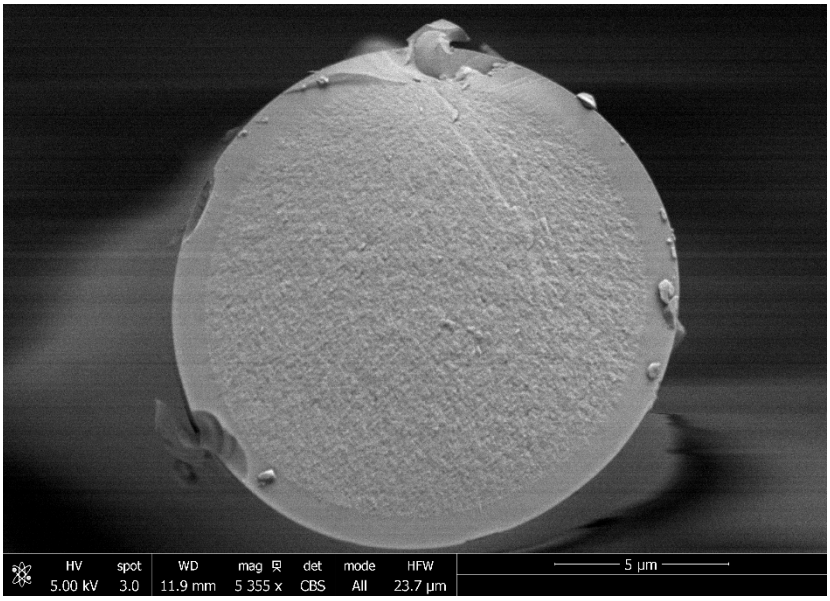

Figure 193 - SEM electron backscatter deflection micrograph of Hi-Nicalon™ S fiber tow specimen "Steam 12" examining the fracture surface of a fiber along the upper portion of the fiber tow (σ_{cr} = 450 MPa, t_f = 13.53 hrs).

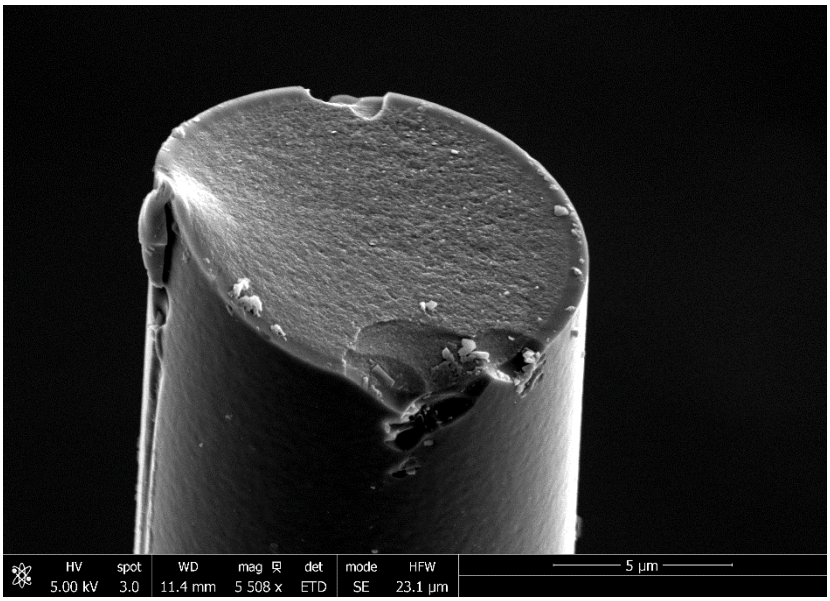

Figure 194 - SEM micrograph of Hi-Nicalon™ S fiber tow specimen "Steam 11" examining the fracture surface of a fiber along the lower portion of the fiber tow (σ_{cr} = 650 MPa, t_f = 6.19 hrs).

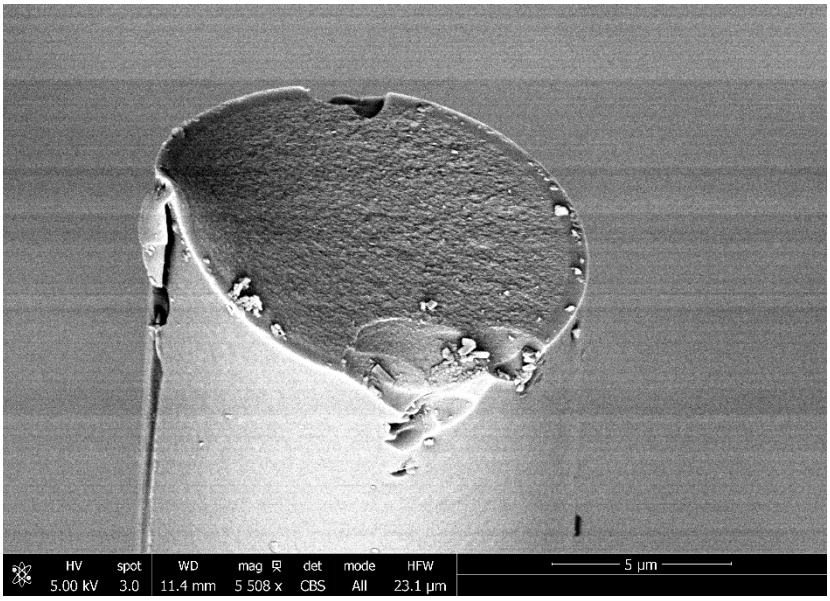

Figure 195 - SEM electron backscatter deflection micrograph of Hi-Nicalon™ S fiber tow specimen "Steam 11" examining the fracture surface of a fiber along the lower portion of the fiber tow (σ_{cr} = 650 MPa, t_f = 6.19 hrs).

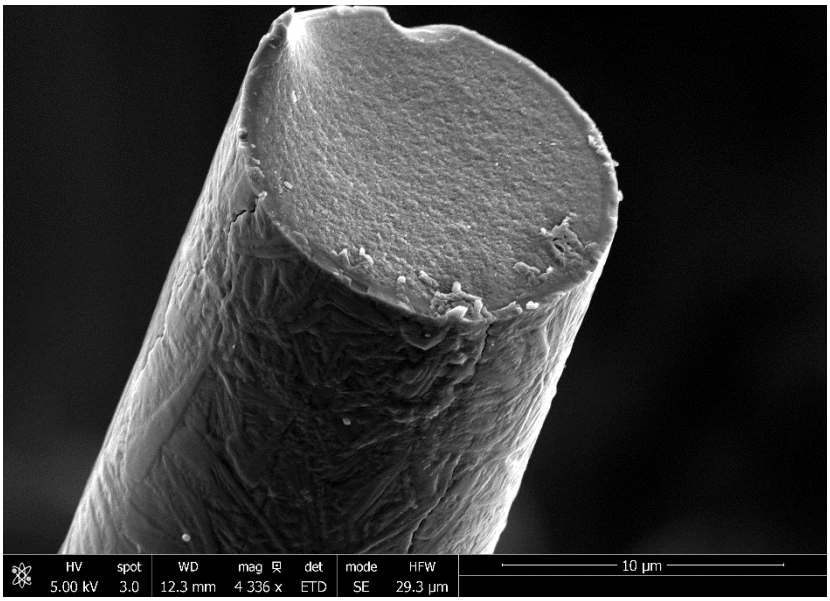

Figure 196 - SEM micrograph of Hi-Nicalon™ S fiber tow specimen "Steam 11" examining the fracture surface of a fiber along the lower portion of the fiber tow (σ_{cr} = 650 MPa, t_f = 6.19 hrs).

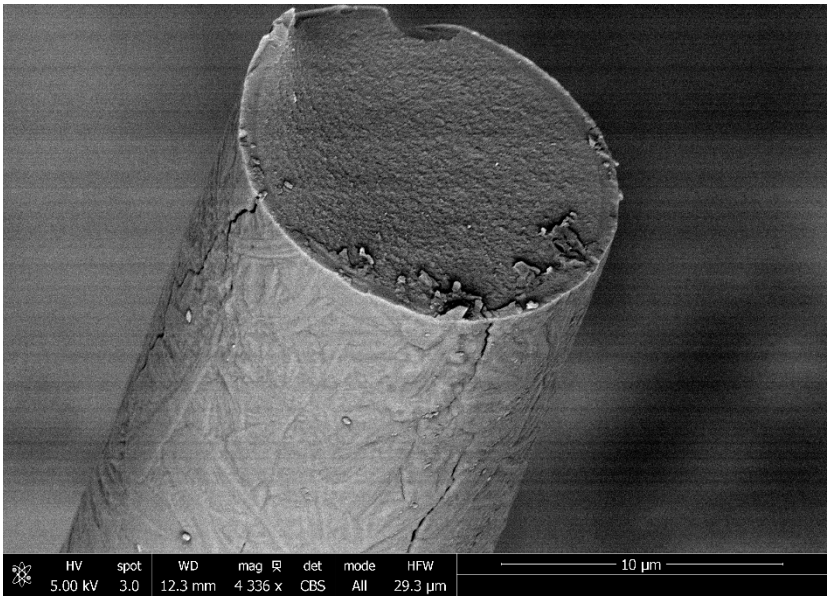

Figure 197 - SEM electron backscatter deflection micrograph of Hi-Nicalon™ S fiber tow specimen "Steam 11" examining the fracture surface of a fiber along the lower portion of the fiber tow (σ_{cr} = 650 MPa, t_f = 6.19 hrs).

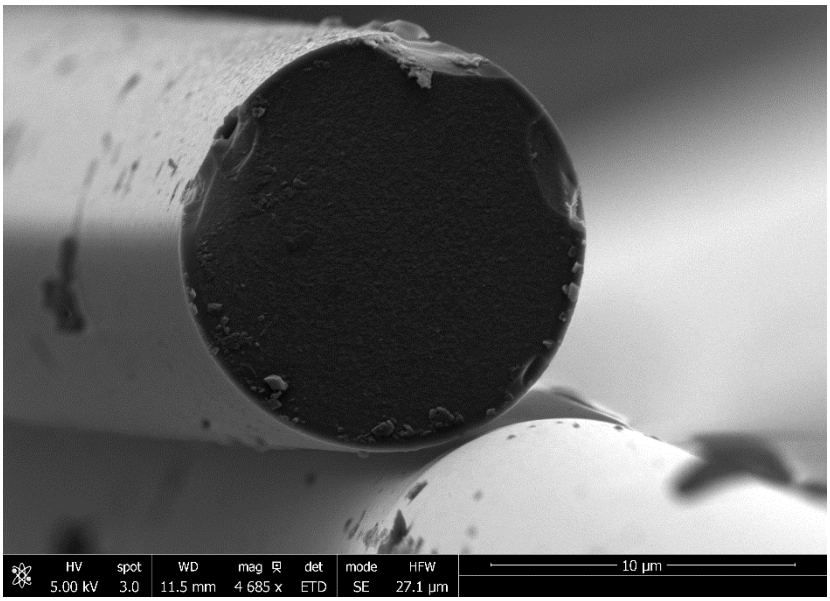

Figure 198 - SEM micrograph of Hi-Nicalon™ S fiber tow specimen "Steam 11" examining the fracture surface of a fiber along the lower portion of the fiber tow (σ_{cr} = 650 MPa, t_f = 6.19 hrs).

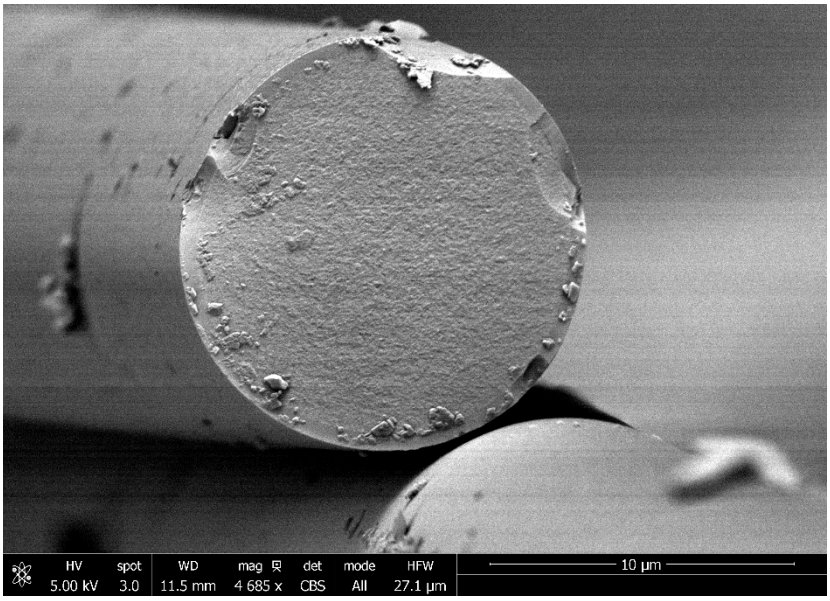

Figure 199 - SEM electron backscatter deflection micrograph of Hi-Nicalon™ S fiber tow specimen "Steam 11" examining the fracture surface of a fiber along the lower portion of the fiber tow (σ_{cr} = 650 MPa, t_f = 6.19 hrs).

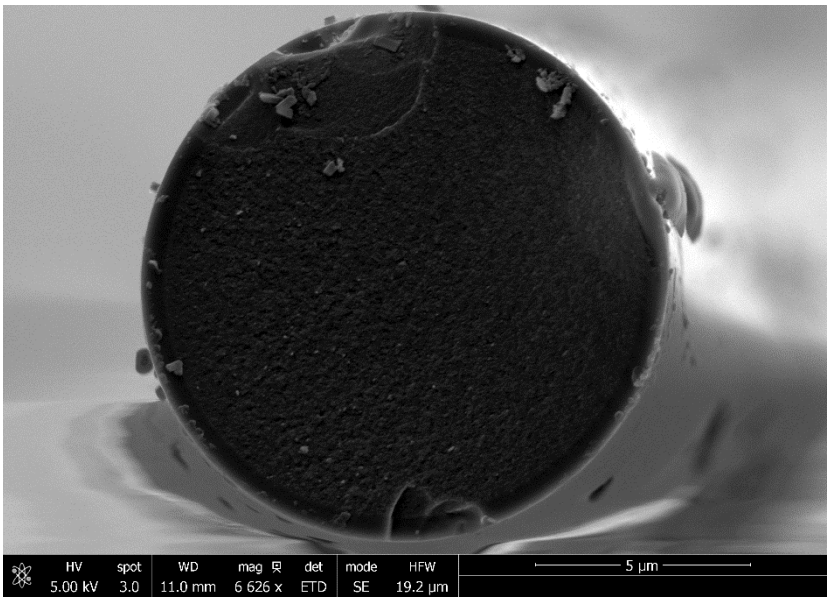

Figure 200 - SEM micrograph of Hi-Nicalon™ S fiber tow specimen "Steam 11" examining the fracture surface of a fiber along the lower portion of the fiber tow (σ_{cr} = 650 MPa, t_f = 6.19 hrs).

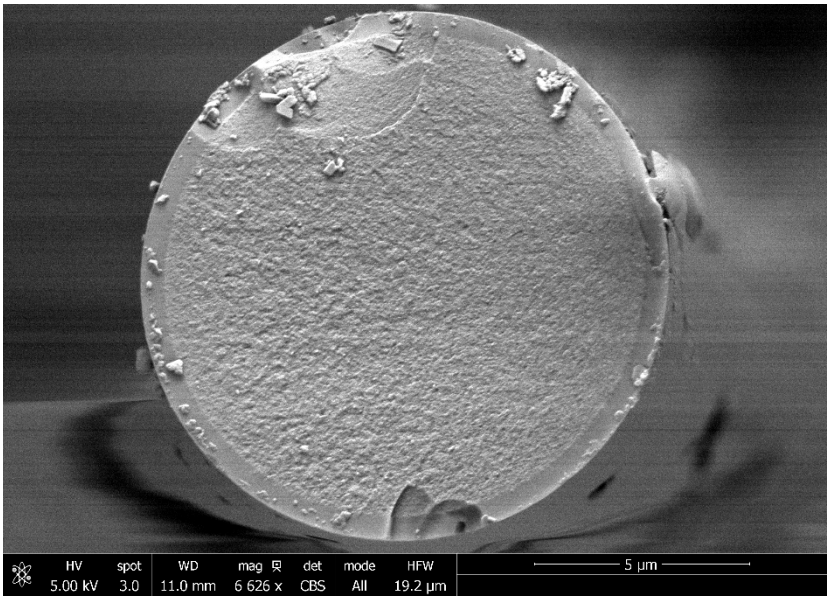

Figure 201 - SEM electron backscatter deflection micrograph of Hi-Nicalon™ S fiber tow specimen "Steam 11" examining the fracture surface of a fiber along the lower portion of the fiber tow (σ_{cr} = 650 MPa, t_f = 6.19 hrs).

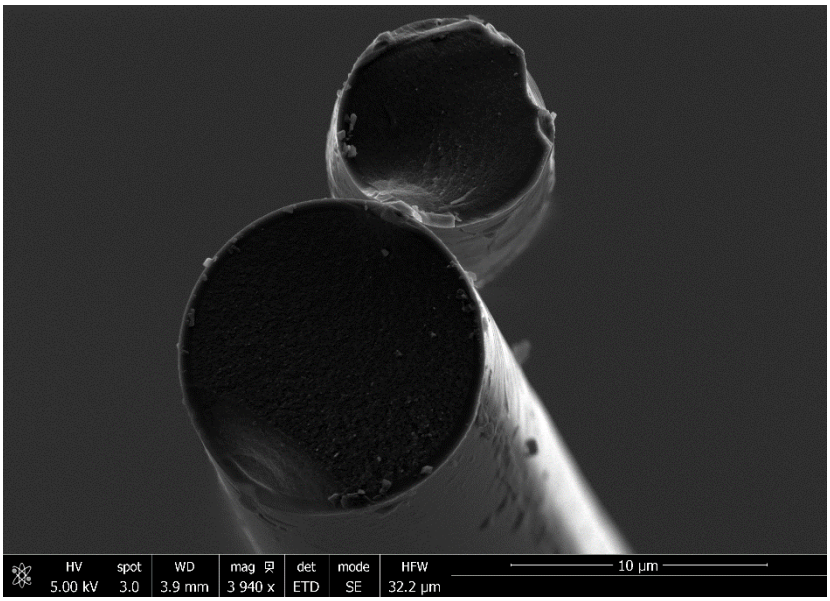

Figure 202 - SEM micrograph of Hi-Nicalon™ S fiber tow specimen "Steam 11" examining the fracture surfaces of bonded fibers along the lower portion of the fiber tow (σ_{cr} = 650 MPa, t_f = 6.19 hrs).

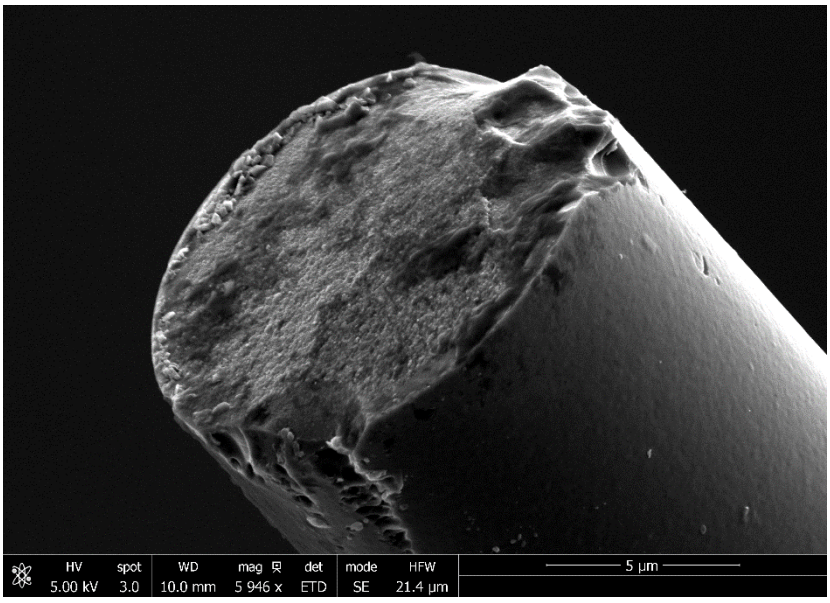

Figure 203 - SEM micrograph of Hi-Nicalon™ S fiber tow specimen "Steam 11" examining the fracture surface of a fiber along the upper portion of the fiber tow. Note growths on the fiber fracture surface (σ_{cr} = 650 MPa, t_f = 6.19 hrs).

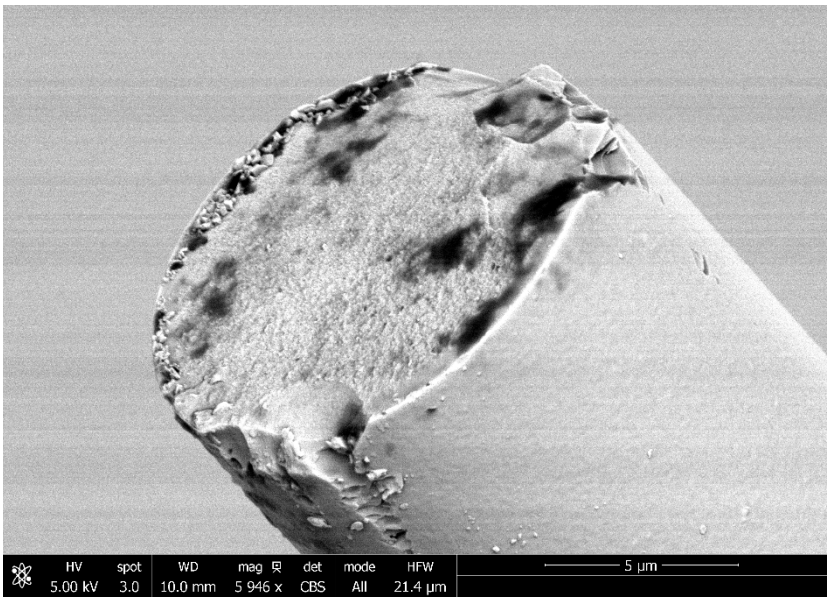

Figure 204 - SEM electron backscatter deflection micrograph of Hi-Nicalon™ S fiber tow specimen "Steam 11" examining the fracture surface of a fiber along the upper portion of the fiber tow. Note growths on the fiber fracture surface (σ_{cr} = 650 MPa, t_f = 6.19 hrs).

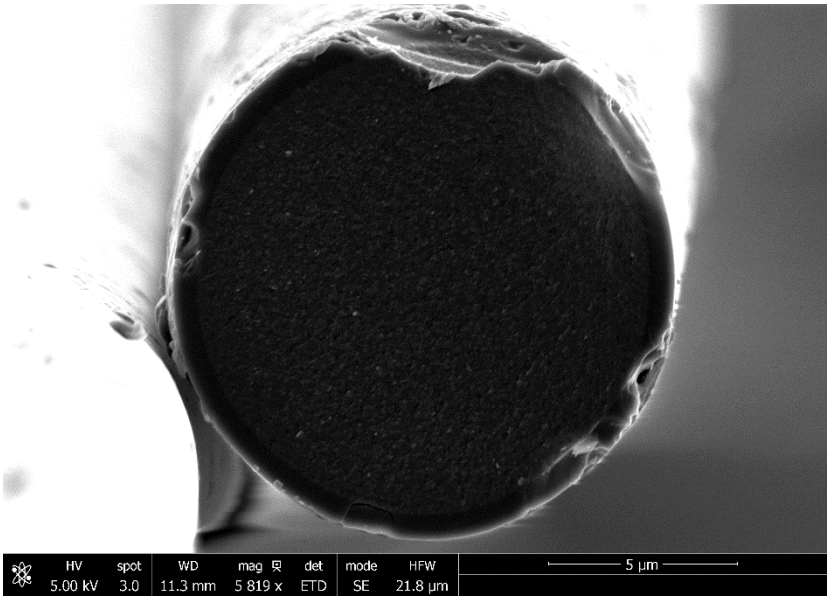

Figure 205 - SEM micrograph of Hi-Nicalon™ S fiber tow specimen "Steam 11" examining the fracture surface of a fiber along the upper portion of the fiber tow (σ_{cr} = 650 MPa, t_f = 6.19 hrs).

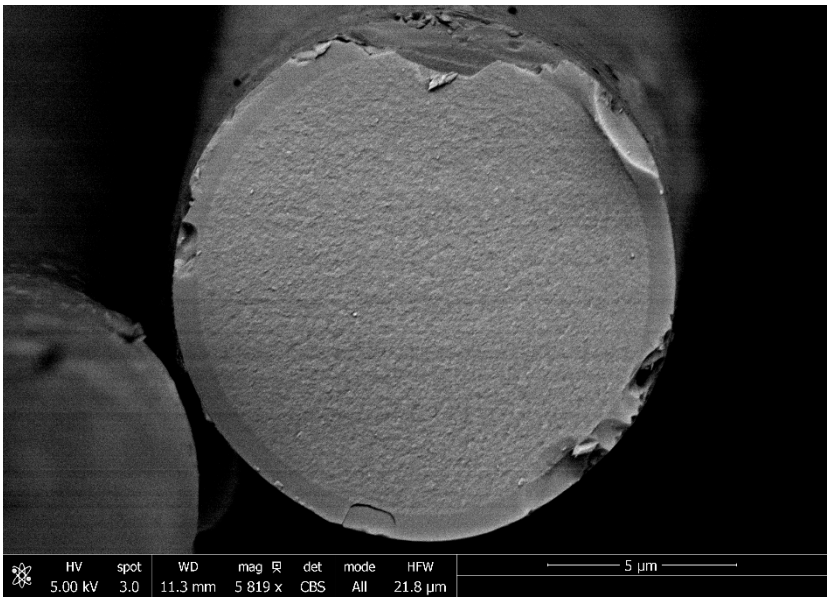

Figure 206 - SEM electron backscatter deflection micrograph of Hi-Nicalon™ S fiber tow specimen "Steam 11" examining the fracture surface of a fiber along the upper portion of the fiber tow (σ_{cr} = 650 MPa, t_f = 6.19 hrs).

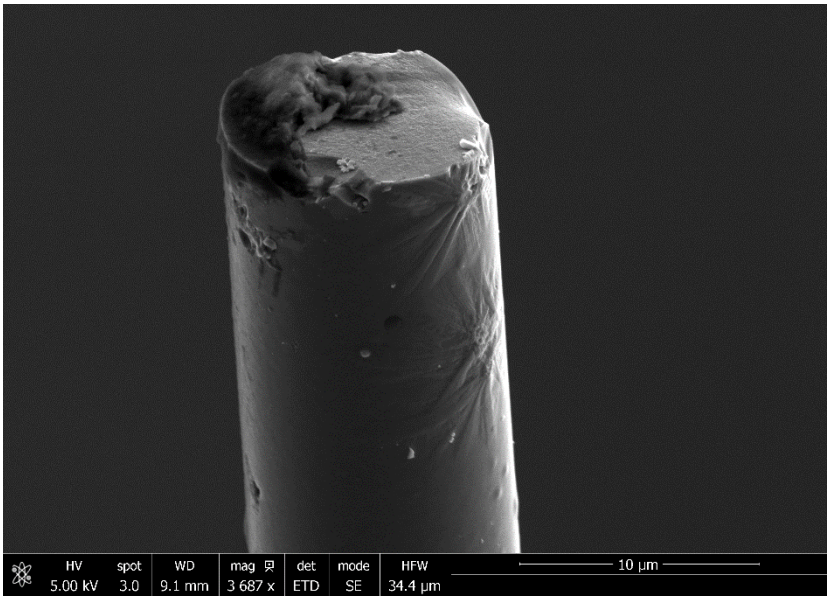

Figure 207 - SEM micrograph of Hi-Nicalon™ S fiber tow specimen "Steam 11" examining the fracture surface of a fiber along the upper portion of the fiber tow. Note the unknown growth on the fracture surface and formation of crystallized scale on the exterior fiber surface (σ_{cr} = 650 MPa, t_f = 6.19 hrs).

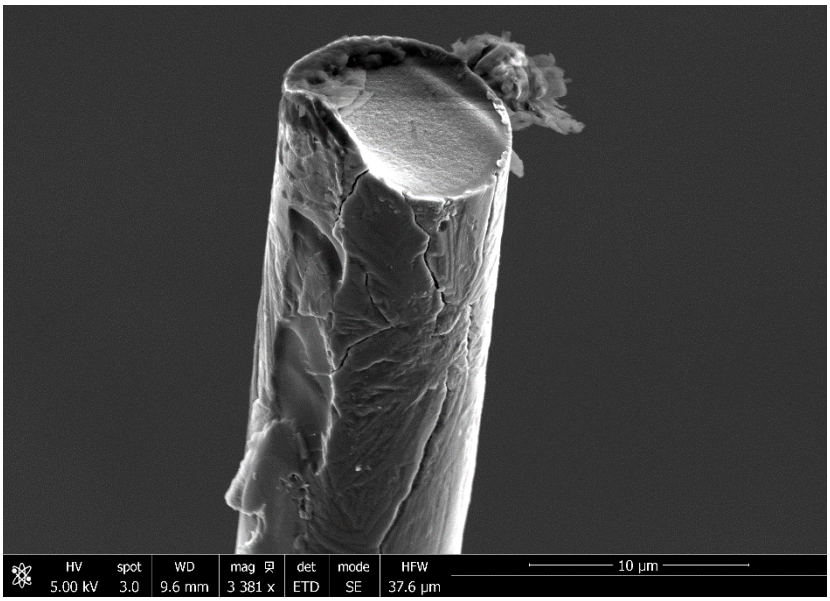

Figure 208 - SEM micrograph of Hi-Nicalon™ S fiber tow specimen "Steam 11" examining the fracture surface of a fiber along the upper portion of the fiber tow. Note the unknown growth on the fracture surface (σ_{cr} = 650 MPa, t_f = 6.19 hrs).

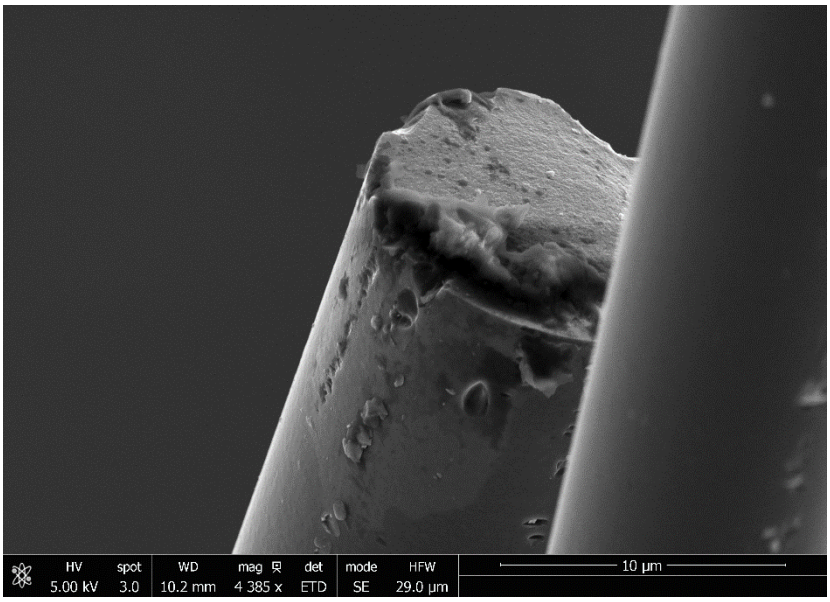

Figure 209 - SEM micrograph of Hi-Nicalon™ S fiber tow specimen "Steam 11" examining the fracture surface of a fiber along the upper portion of the fiber tow. Note the unknown growth on the fracture surface (σ_{cr} = 650 MPa, t_f = 6.19 hrs).

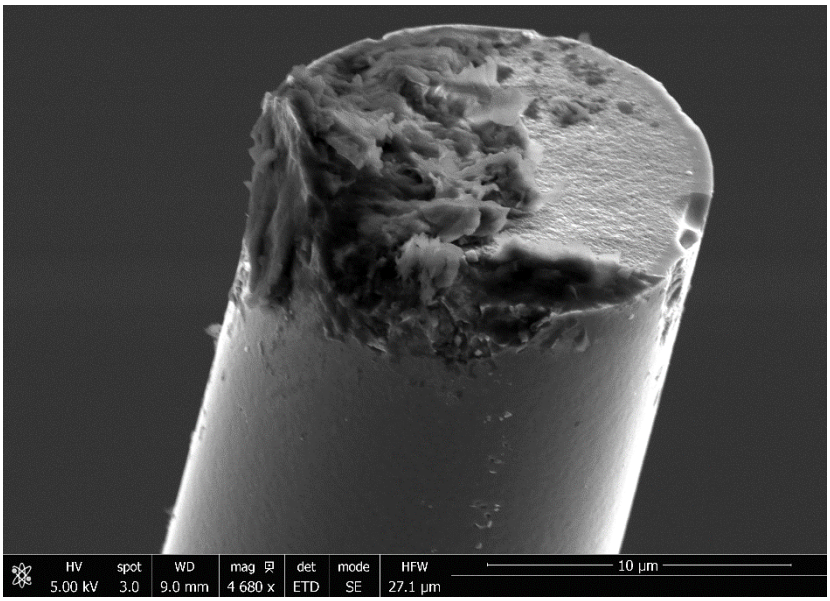

Figure 210 - SEM micrograph of Hi-Nicalon™ S fiber tow specimen "Steam 11" examining the fracture surface of a fiber along the upper portion of the fiber tow. Note the unknown growth on the fracture surface (σ_{cr} = 650 MPa, t_f = 6.19 hrs).

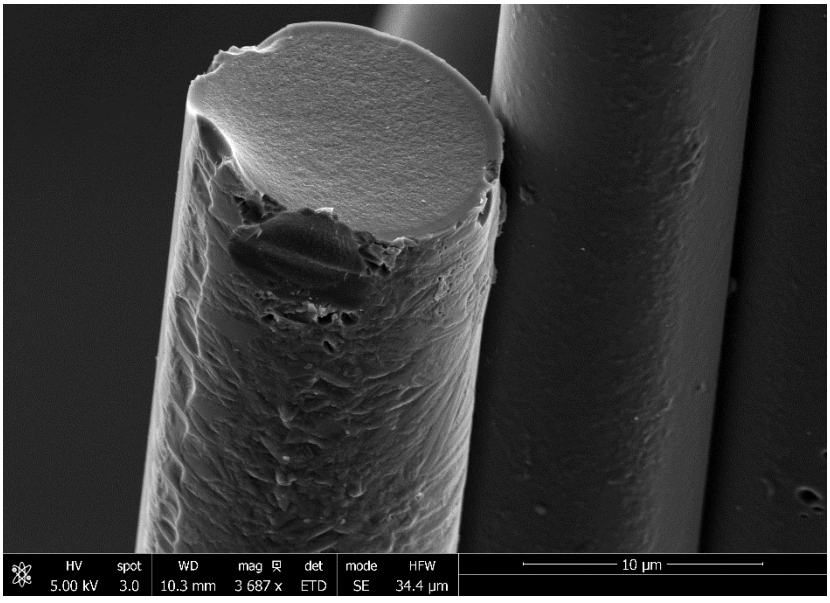

Figure 211 - SEM micrograph of Hi-Nicalon™ S fiber tow specimen "Steam 11" examining the fracture surface of a fiber along the upper portion of the fiber tow (σ_{cr} = 650 MPa, t_f = 6.19 hrs).

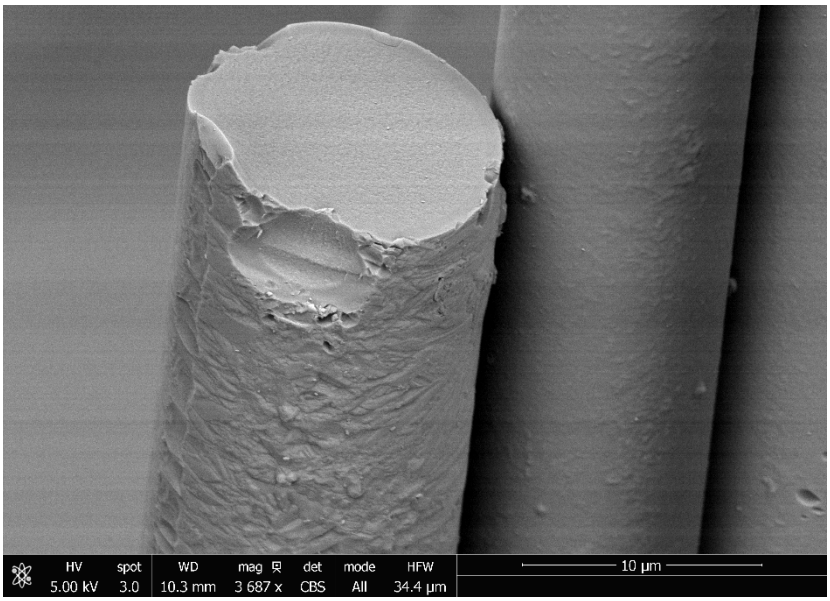

Figure 212 - SEM electron backscatter deflection micrograph of Hi-Nicalon™ S fiber tow specimen "Steam 11" examining the fracture surface of a fiber along the upper portion of the fiber tow (σ_{cr} = 650 MPa, t_f = 6.19 hrs).

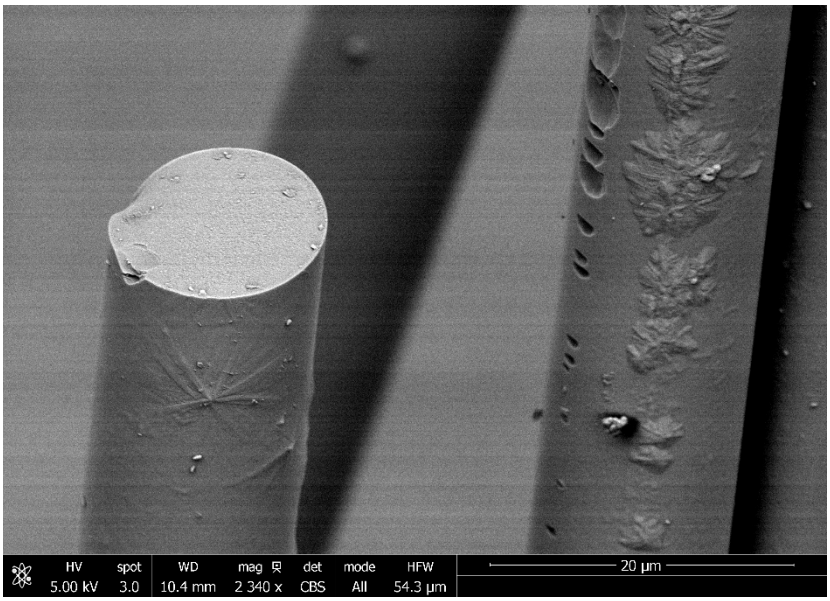

Figure 213 - SEM electron backscatter deflection micrograph of Hi-Nicalon™ S fiber tow specimen "Steam 11" examining the fracture and exterior surfaces of fibers along the upper portion of the fiber tow. Note different stages of crystallization along the exterior fiber surface (σ_{cr} = 650 MPa, t_f = 6.19 hrs).

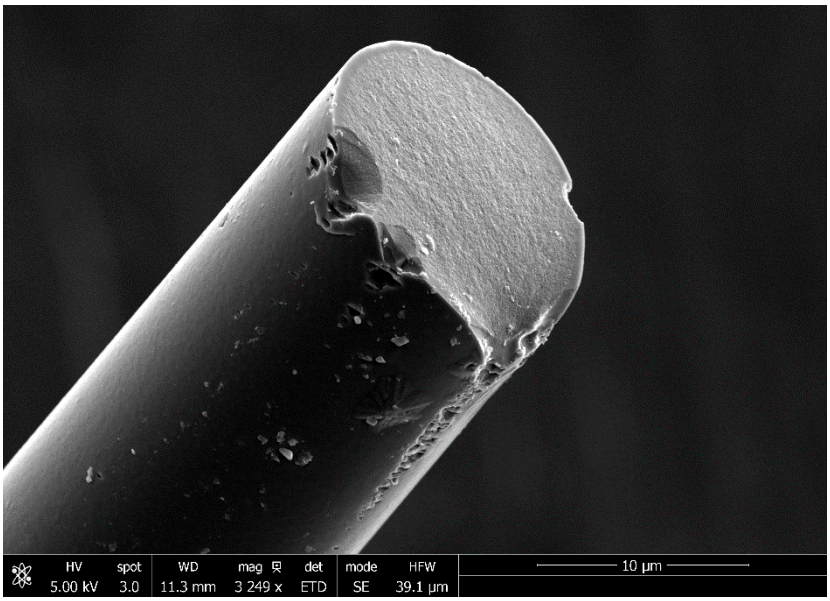

Figure 214 - SEM micrograph of Hi-Nicalon™ S fiber tow specimen "Steam 11" examining the fracture surface of a fiber along the upper portion of the fiber tow (σ_{cr} = 650 MPa, t_f = 6.19 hrs).

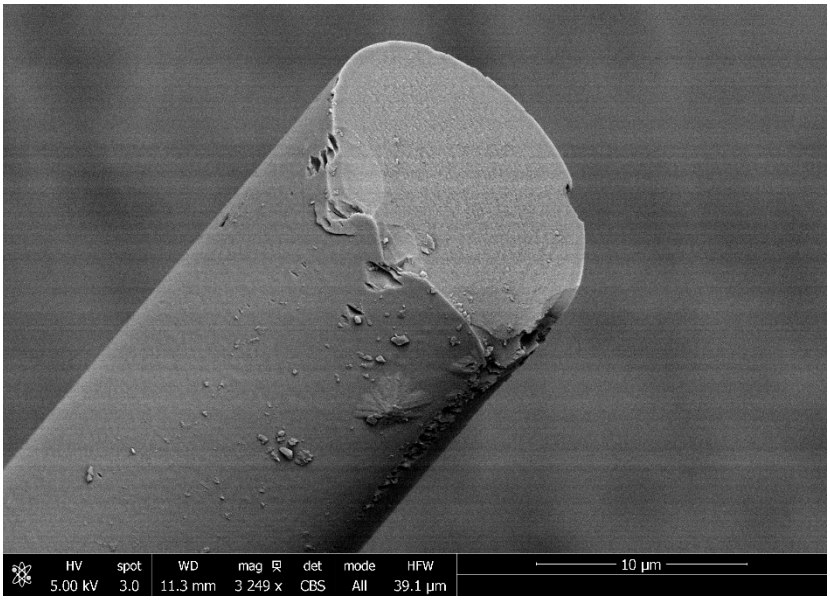

Figure 215 - SEM electron backscatter deflection micrograph of Hi-Nicalon™ S fiber tow specimen "Steam 11" examining the fracture surface of a fiber along the upper portion of the fiber tow (σ_{cr} = 650 MPa, t_f = 6.19 hrs).

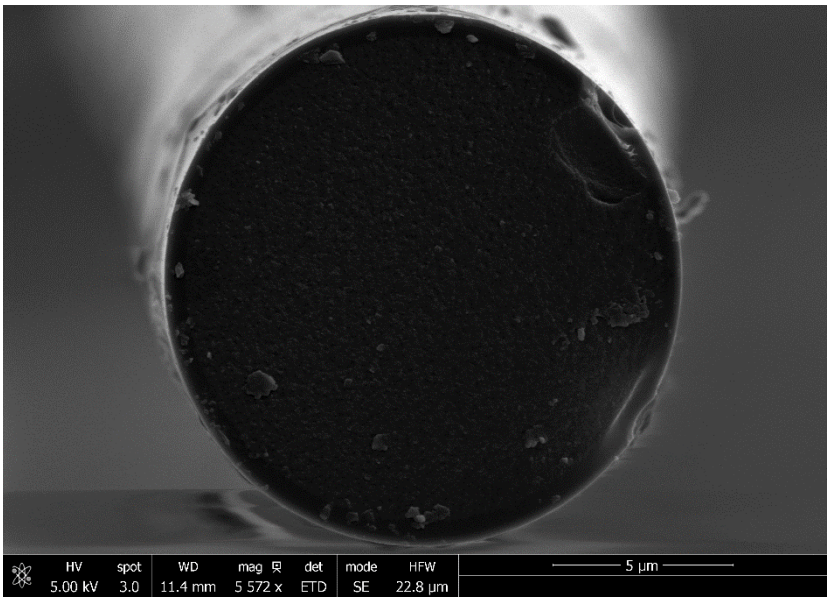

Figure 216 - SEM micrograph of Hi-Nicalon™ S fiber tow specimen "Steam 11" examining the fracture surface of a fiber along the upper portion of the fiber tow (σ_{cr} = 650 MPa, t_f = 6.19 hrs).

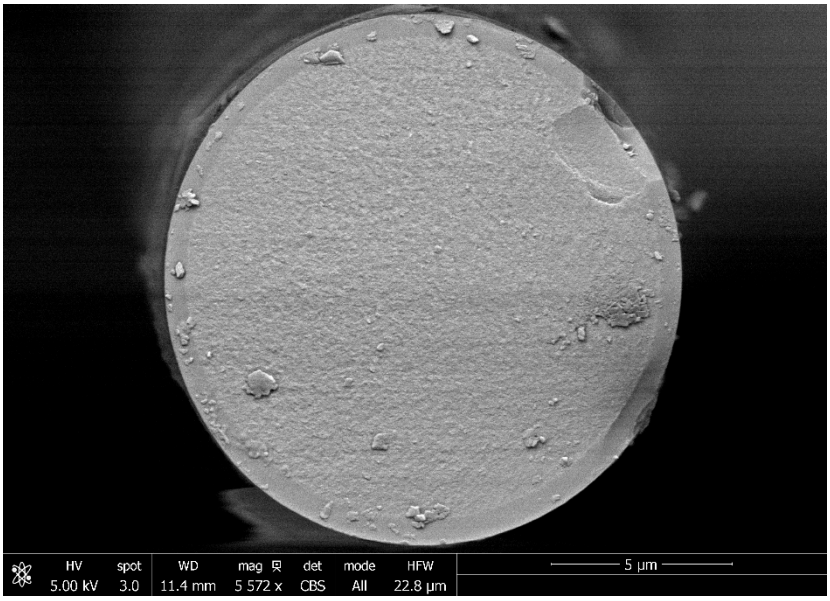

Figure 217 - SEM electron backscatter deflection micrograph of Hi-Nicalon™ S fiber tow specimen "Steam 11" examining the fracture surface of a fiber along the upper portion of the fiber tow (σ_{cr} = 650 MPa, t_f = 6.19 hrs).

Bibliography

[1] F. Press, “Advanced Materials and Competitiveness,” *Metall. Trans. B*, vol. 21B, pp. 415–418, 1990.

[2] B. Steffens, “Creep of Hi-Nicalon S Ceramic Fiber Tows at Elevated Temperature in Air and in Steam,” Air Force Institute of Technology (AU), 2012.

[3] K. K. Chawla, *Ceramic Matrix Composites*. New York: Springer, 1998.

[4] I. M. Daniel and O. Ishai, *Engineering Mechanics of Composite Materials*, 2nd ed. New York: Oxford University Press, 2006.

[5] “Exodus,” in *The Holy Bible: King James Version*, Salt Lake City: The Church of Jesus Christ of Latter-Day Saints, 2013, pp. 85–86.

[6] T. Johnson, “History of Composites,” 2013.

[7] American Composites Manufacturers Association, “History of the Composite Industry,” 2013.

[8] A. Fraher, *Thinking Through Crisis: Improving Teamwork and Leadership in High-Risk Fields*. Cambridge University Press, 2011.

[9] W. G. Roeseler, B. Sarh, and M. U. Kismarton, “Composite Structures: The First 100 Years,” in *16th International Conference on Composite Materials*, 2007, pp. 1–10.

[10] H. Clauser, “Advanced Composite Materials,” *Sci. Am.*, vol. 229, no. 1, pp. 36–44, 1973.

[11] D. Tenney, J. Davis Jr, R. Pipes, and N. Johnston, “NASA Composite Materials Development: Lessons Learned and Future Challenges,” *NATO RTO AVT-154*

Work. Support Compos. Syst., vol. LF99-9370, 2009.

[12] T. Ishikawa, “Advances in Inorganic Fibers,” *Polym. Inorg. Fibers*, vol. 178, pp. 109–144, 2005.

[13] C. J. Armani, “Creep Performance of Oxide Ceramic Fiber Materials at Elevated Temperature in Air and in Steam,” Air Force Institute of Technology (AU), 2011.

[14] T. R. Shillig, “Creep of Hi-Nicalon S Fiber Tows at Elevated Temperature in Air and in Steam,” Air Force Institute of Technology (AU), 2013.

[15] S. J. Robertson, “Creep of Hi-Nicalon S Ceramic Fiber Tows at 800 deg C in Air and in Silicic Acid-Saturated Steam,” Air Force Institute of Technology (AU), 2015.

[16] M. W. Piper, “Creep of Hi-Nicalon S Ceramic Fiber Tows at 700°C Elevated Temperature in Air and in Silicic Acid-Saturated Steam,” Air Force Institute of Technology (AU), 2016.

[17] R. K. Mitchell, “Creep of Hi-Nicalon S Ceramic Fiber Tows at 900°C Elevated Temperature in Air and in Silicic Acid-Saturated Steam,” Air Force Institute of Technology (AU), 2017.

[18] B. G. Kroeger, “Creep of Hi-Nicalon S Ceramic Fiber Tows at 1000°C in Air and in Silicic Acid-Saturated Steam,” Air Force Institute of Technology (AU), 2018.

[19] S. Schmidt, S. Beyer, H. Knabe, H. Immich, and R. Meistring, “Advanced Ceramic Matrix Composite Materials for Current and Future Propulsion Technology Applications,” *Acta Astronaut.*, vol. 55, no. 3, pp. 409–420, 2004.

[20] Department of Defense, “Ceramic Matrix Composites,” in *Composite Materials*

Handbook, Vol. 5., US Army Research Laboratory, 2002, pp. 43–46.

[21] Committee on Advanced Fibers for High-Temperature Ceramic Composites, *Ceramic Fibers and Coatings: Advanced Materials for the Twenty-First Century*. National Academies Press, 1998.

[22] F. Matthews and R. Rawlings, *Composite Materials: Engineering and Science*. Cambridge, England: Chapman & Hall, 1994.

[23] J. Lamon, S. Mazerat, and M. R'Mili, "Reinforcement of Ceramic Matrix Composites: Properties of SiC-Based Filaments and Tows," in *Ceramic Matrix Composites: Materials, Modeling and Technology*, N. P. Bansal and J. Lamon, Eds. John Wiley & Sons, Inc., 2015, pp. 1–26.

[24] J. A. DiCarlo and H.-M. Yun, "Non-oxide (Silicon Carbide) Fibers," in *Handbook of Ceramic Composites*, Springer US, 2005, pp. 33–52.

[25] A. Bunsell and A. Piant, "A review of the development of three generations of small diameter silicon carbide fibres," *J. Mater. Sci.*, vol. 41, pp. 823–839, 2006.

[26] S. Yajima, J. Hayashi, and M. Omori, "Continuous silicon carbide fiber of high tensile strength," *Chem. Lett.*, 1975.

[27] M. Yamamura, T., Hurushima, T., Kimoto, "High Tech Ceramics," *Mater. Sci. Monogr. 38A*, p. 737, 1988.

[28] G. Simon and A. R. Bunsell, "Mechanical and structural characterization of the Nicalon silicon carbide fibre," *J. Mater. Sci.*, vol. 19, no. 11, pp. 3649–3657, Nov. 1984.

[29] M. Takeda, Y. Imai, H. Ichikawa, T. Ishikawa, T. Seguchi, and K. Okamura,

"Properties of the Low Oxygen Content SiC Fiber on High Temperature Heat Treatment," *Proc. 15th Annu. Conf. Compos. Adv. Ceram. Mater. Part 1 2 Ceram. Eng. Sci. Proc.*, vol. 12, no. 7/8, 1991.

[30] M. Takeda, Y. Imai, H. Ichikawa, T. Ishikawa, N. Kasai, T. Seguchi, and K. Okamura, "Thermomechanical Analysis of the Low Oxygen Silicon Carbide Fibers Derived from Polycarbosilane," *Proc. 17th Annu. Conf. Compos. Adv. Ceram. Mater. Part 1 2 Ceram. Eng. Sci. Proc.*, vol. 14, no. 7/8, 1993.

[31] N. Hochet, M. H. Berger, and A. R. Bunsell, "Microstructural evolution of the latest generation of small-diameter SiC-based fibres tested at high temperatures," *J. Microsc.*, vol. 185, no. 2, pp. 243–258, Feb. 1997.

[32] I. H. . Shames and F. A. A. Cozzarelli, *Elastic and Inelastic Stress Analysis*. Philadelphia: PA: Taylor & Francis Group, 1997.

[33] J. Wachtman, W. Cannon, and M. Matthewson, *Mechanical Properties of Ceramics*, 2nd ed. New York: John Wiley & Sons, Inc., 2009.

[34] J. Pelleg, *Creep in Ceramics*. Springer International Publishing, 2017.

[35] D. Green, *An Introduction to the Mechanical Properties of Ceramics*. Cambridge University Press, 1998.

[36] R. S. Hay, G. E. Fair, R. Bouffioux, E. Urban, J. Morrow, A. Hart, and M. Wilson, "Hi-Nicalon^{TM}-S SiC Fiber Oxidation and Scale Crystallization Kinetics," *J. Am. Ceram. Soc.*, vol. 94, no. 11, pp. 3983–3991, Nov. 2011.

[37] R. Hay, G. Fair, A. Hart, S. Potticary, and R. Bouffioux, "Kinetics of Passive Oxidation of Hi-Nicalon-S SiC fibers in Wet Air: Relationships between SiO2

Scale Thickness, Crystallization, and Fiber Strength," in *Mechanical Properties and Performance of Engineering Ceramics and Composites VII*, D. Singh, J. Salem, M. Halbig, and S. Mathur, Eds. Hoboken, NJ: John Wiley & Sons, Inc., 2012.

[38] R. S. Hay and R. Corns, "Passive Oxidation Kinetics for Glass and Cristobalite Formation on Hi-Nicalon^{TM}-S SiC Fibers in Steam," Air Force Research Laboratory, Materials and Manufacturing Directorate, WPAFB, OH, 2018.

[39] B. E. Deal and A. S. Grove, "General Relationship for the Thermal Oxidation of Silicon," *J. Appl. Phys.*, vol. 36, no. 12, pp. 3770–3778, Dec. 1965.

[40] R. S. Hay, G. E. Fair, R. Bouffioux, E. Urban, J. Morrow, A. Hart, and M. Wilson, "Relationships Between Fiber Strength, Passive Oxidation and Scale Crystallization Kinetics of Hi-Nicalon^{TM}-S SiC Fibers," *J. Am. Ceram. S*, vol. 32, pp. 39–54, 2011.

[41] R. S. Hay, G. E. Fair, R. Bouffioux, E. Urban, J. Morrow, A. Hart, and M. Wilson, "Relationships Between Fiber Strength, Passive Oxidation and Scale Crystallization Kinetics of Hi-Nicalon^{TM}-S SiC Fibers," in *Mechanical Properties and Performance of Engineering Ceramics and Composites VI: Ceramix Engineering and Science Proceedings*, vol. 32, 2011, pp. 37–51.

[42] Y. Song, S. Dhar, L. C. Feldman, G. Chung, and J. R. Williams, "Modified Deal Grove model for the thermal oxidation of silicon carbide," *J. Appl. Phys.*, vol. 95, no. 9, pp. 4953–4957, May 2004.

[43] K. B. Sprinkle, "Creep of Sylramic-iBN Fiber Tows at Elevated Temperature in

Air and in Silicic Acid-Saturated Steam," Air Force Institute of Technology (AU), 2015.

[44] L. Nippon Carbon Co., "Silicon Carbide Continuous Fibers," *Nippon Carbon Co., Ltd*. [Online]. Available: http://www.carbon.co.jp/english/products/silicon_carbide/. [Accessed: 31-Aug-2017].

[45] I. COI Ceramics, "HI-NICALON^{TM} Type S CERAMIC FIBER," *ATK Space Systems Inc*. [Online]. Available: http://www.coiceramics.com/pdfs/hi-nicalon-types_1-17-06.pdf. [Accessed: 31-Aug-2017].

[46] L. NGS Advanced Fiber Co., "Product NGS Advanced Fibers," *NGS Advanced Fiber Co., Ltd*, 2017. [Online]. Available: http://www.ngs-advanced-fibers.com/eng/item/index.html. [Accessed: 31-Aug-2017].

[47] J. A. DiCarlo, "Property Goals and Test Methods for High Temperature Ceramic Fibre Reinforcement," *Ceram. Int.*, vol. 23, no. 4, pp. 283–289, Jan. 1997.

[48] R. M. Morrell, "A Tensile Creep-Testing Apparatus for Ceramic Materials Using Simple Knife-Edge Universal Joints," *J. Phys. E.*, vol. 5, no. 5, pp. 465–467, May 1972.

[49] F. A. Kandil and B. F. Dyson, "Tensile Creep of Ceramics: The Development of a Testing Facility," *Int. J. High Technol. Ceram.*, vol. 4, no. 2–4, pp. 243–262, Jan. 1988.

[50] W. Gauthier and J. Lamon, "Delayed Failure of Hi-Nicalon and Hi-Nicalon S Multifilament Tows and Single Filaments at Intermediate Temperatures (500°-

800°C)," *J. Am. Ceram. Soc.*, vol. 92, no. 3, pp. 702–709, Mar. 2009.

[51] V. Hammond, "Creep rupture of an oxide/oxide composite fiber," University of Viginia, 2001.

[52] H. M. Yun, J. C. Goldsby, and J. A. DiCarlo, *Tensile Creep and Stress-Rupture Behavior of Polymer Derived SiC Fibers*. Lewis Research Center, 1994.

[53] C. Sauder and J. Lamon, "Tensile Creep Behavior of SiC-Based Fibers With a Low Oxygen Content," *J. Am. Ceram. Soc.*, vol. 90, no. 4, pp. 1146–1156, Apr. 2007.

[54] R. S. Hay and R. J. Chater, "Oxidation kinetics strength of Hi-Nicalon^{TM}-S SiC fiber after oxidation in dry and wet air," *J. Am. Ceram. Soc.*, vol. 100, no. 9, pp. 4110–4130, Sep. 2017.

REPORT DOCUMENTATION PAGE

Form Approved
OMB No. 0704-0188

The public reporting burden for this collection of information is estimated to average 1 hour per response, including the time for reviewing instructions, searching existing data sources, gathering and maintaining the data needed, and completing and reviewing the collection of information. Send comments regarding this burden estimate or any other aspect of this collection of information, including suggestions for reducing the burden, to Department of Defense, Washington Headquarters Services, Directorate for Information Operations and Reports (0704-0188), 1215 Jefferson Davis Highway, Suite 1204, Arlington, VA 22202-4302. Respondents should be aware that notwithstanding any other provision of law, no person shall be subject to any penalty for failing to comply with a collection of information if it does not display a currently valid OMB control number.

PLEASE DO NOT RETURN YOUR FORM TO THE ABOVE ADDRESS.

1. REPORT DATE *(DD-MM-YYYY)*	2. REPORT TYPE	3. DATES COVERED *(From - To)*
14-06-2018	Master's Thesis	Jan 2017 - Jun 2018

4. TITLE AND SUBTITLE

Creep of Hi-Nicalon™ S Ceramic Fiber Tows at 1100°C In Air and In Silicic Acid-Saturated Steam

5a. CONTRACT NUMBER

5b. GRANT NUMBER

5c. PROGRAM ELEMENT NUMBER

6. AUTHOR(S)

Logan M. Gumucio

5d. PROJECT NUMBER

5e. TASK NUMBER

5f. WORK UNIT NUMBER

7. PERFORMING ORGANIZATION NAME(S) AND ADDRESS(ES)

Air Force Institute of Technology
Graduate School of Engineering and Management (AFIT/EN)
2950 Hobson Way
Wright-Patterson AFB, OH 45433-7765

8. PERFORMING ORGANIZATION REPORT NUMBER

AFIT-ENY-MS-18-J-072

9. SPONSORING/MONITORING AGENCY NAME(S) AND ADDRESS(ES)

Air Force Research Laboratory
Dr. Randall S. Hay,
2977 Hobson Way, Building 652
Wright-Patterson AFB, OH 45433
randall.hay@us.af.mil

10. SPONSOR/MONITOR'S ACRONYM(S)

AFRL/RXCCM

11. SPONSOR/MONITOR'S REPORT NUMBER(S)

12. DISTRIBUTION/AVAILABILITY STATEMENT

DISTRIBUTION STATEMENT A:
Distribution Statement A: Approved For Public Release; Distribution Unlimited.

13. SUPPLEMENTARY NOTES

This material is declared a work of the U.S. Government and is not subject to copyright protection in the United States.

14. ABSTRACT

Innovations in SiC based ceramic matrix composites (CMCs) have yielded exceptional high-temperature properties and performance in aggressive oxidizing environments. These material characteristics provide potential avenues for future advancements in many applications where current metallic alloys perform near their operating temperature limits in a harsh environment. As steam (typically present in these environments) enters through cracks in the matrix of a SiC/SiC composite, it leaches Si and becomes saturated with silicic acid, Si(OH)4, prior to attacking the reinforcing SiC fibers. Therefore, it is paramount that a thorough understanding of the performance and durability of SiC fibers be obtained under these conditions. This research effort investigated the creep behavior of Hi-Nicalon™ S SiC fibers at 1100°C in air and in silicic acid-saturated steam. The fiber tows that were tested consist of approximately 500 fiber filaments with an average diameter of 12 µm. Creep tests were performed with creep stresses ranging from 3.5 to 650 MPa in both air and in silicic acid-saturated steam. Regions of primary and secondary creep were observed in all tests, with the transition from primary to secondary creep occurring within the first hour of each test. Creep run-out was defined as 100 hours at creep stress and was achieved at 600 MPa in air, but only at 3.5 MPa in saturated steam. The creep rates achieved in saturated steam were approximately an order of magnitude higher than those achieved in air. Post-test analysis revealed passive oxidation of the fibers tested in air and in saturated steam. Crystallized scale growth was found on fibers tested in saturated steam.

15. SUBJECT TERMS

Creep, SiC, Hi-Nicalon™ S Fiber Tow, Silicic Acid-Saturated Steam, ceramic matrix composite (CMC), oxidation

16. SECURITY CLASSIFICATION OF:			17. LIMITATION OF ABSTRACT	18. NUMBER OF PAGES	19a. NAME OF RESPONSIBLE PERSON
a. REPORT	b. ABSTRACT	c. THIS PAGE			Dr. Marina B. Ruggles-Wrenn, AFIT/ENY
U	U	U	UU	220	19b. TELEPHONE NUMBER *(Include area code)* (937) 255-3636 x1234 Marina.Ruggles-Wrenn@af

Reset

Standard Form 298 (Rev. 8/98)
Prescribed by ANSI Std. Z39.18